JPL Publication 88-38

# Proceedings of the Airborne Visible/Infrared Imaging Spectrometer (AVIRIS) Performance Evaluation Workshop

## June 6, 7, and 8, 1988

Gregg Vane
Editor

September 15, 1988

NASA
National Aeronautics and
Space Administration

Jet Propulsion Laboratory
California Institute of Technology
Pasadena, California

This publication was prepared by the Jet Propulsion Laboratory, California Institute of Technology, under a contract with the National Aeronautics and Space Administration.

## ABSTRACT

The Airborne Visible/Infrared Imaging Spectrometer (AVIRIS) Performance Evaluation Workshop was held at the Jet Propulsion Laboratory on June 6, 7, and 8, 1988. The major focus of the Workshop was the assessment of data quality by the AVIRIS project and 18 NASA-sponsored performance evaluation investigators. Twenty one presentations were made to 119 workshop attendees from 7 countries. Written summaries of 16 of the presentations are published in these proceedings. The AVIRIS performance evaluation period began in June 1987 with flight data collection in the eastern United States, and continued in the western U.S. into October 1987, after which the instrument was returned to JPL for post-flight calibration. At the start of the performance evaluation period, the sensor met all of the spatial, spectral and radiometric performance requirements except in the fourth spectrometer where the signal-to-noise ratio was below the required value. By the end of the flight season, sensor performance had deteriorated due to failure of 2 critical parts and due to some design deficiencies which were discovered as a result of extensive flight operations in the air. The independent assessment by the NASA performance evaluation investigators confirmed the assessment by the AVIRIS project, which was the basis for the flight hardware rework plan that was already well under way by the time the workshop was convened. Although much of the flight data collected during the June to October 1987 period was of only moderate to poor quality, some exciting scientific results were derived and are presented in these proceedings. These include the mapping of the spatial variation of atmospheric precipitable water, detection of environmentally induced shifts in the chlorophyll red edge, detection of spectral features related to pigment, leaf water and ligno-cellulose absorptions in plants, and the identification of many minerals in a variety of geological settings. The work done by the research community on the data collected in 1987 should pave the way for rapid progress in terrestrial imaging spectroscopy when AVIRIS is returned to operations in the near future.

# FOREWORD

In the text and figure captions of some of the papers in the Proceedings, reference is made to color slides; these 35-mm slides are located in a pocket at the end of the Proceedings. They are sometimes color versions of the referenced black-and-white figures within the Proceedings. A limited number of copies were printed with the color slides included.

Contents

# AVIRIS PERFORMANCE DURING THE 1987 FLIGHT SEASON: AN AVIRIS PROJECT ASSESSMENT AND SUMMARY OF THE NASA-SPONSORED PERFORMANCE EVALUATION

GREGG VANE, WALLACE M. PORTER, JOHN H. REIMER, THOMAS G. CHRIEN, and ROBERT O. GREEN, Jet Propulsion Laboratory, California Institute of Technology, Pasadena, California 91109

## ABSTRACT

Results are presented of the assessment of AVIRIS performance during the 1987 flight season by the AVIRIS project and the earth scientists who were chartered by NASA to conduct an independent data quality and sensor performance evaluation. The AVIRIS evaluation program began in late June 1987 with the sensor meeting most of its design requirements except for signal-to-noise ratio in the fourth spectrometer, which was about half of the required level. Several events related to parts failures and design flaws further reduced sensor performance over the flight season. Substantial agreement was found between the assessments by the project and the independent investigators of the effects of these various factors. A summary of the engineering work that is being done to raise AVIRIS performance to its required level is given. In spite of degrading data quality over the flight season, several exciting scientific results were obtained from the data. These include the mapping of the spatial variation of atmospheric precipitable water, detection of environmentally-induced shifts in the spectral red edge of stressed vegetation, detection of spectral features related to pigment, leaf water and ligno-cellulose absorptions in plants, and the identification of many diagnostic mineral absorption features in a variety of geological settings.

## INTRODUCTION

The AVIRIS Performance Evaluation Workshop held at JPL on June 6, 7, and 8, 1988, was the culmination of an intensive assessment of data quality and sensor performance. The evaluation was sponsored by NASA and conducted by the AVIRIS project and an independent group of NASA-selected scientists. Development of the AVIRIS flight and ground data

processing systems began in 1984 in response to an unsolicited proposal to NASA the previous year. Engineering flights were conducted with the sensor in the winter and spring of 1987 in conjunction with extensive laboratory testing of the sensor in the AVIRIS calibration laboratory at JPL. By June 1987, the sensor was performing close to the design goals, meeting most requirements. The notable exception was the signal-to-noise ratio (SNR) in the fourth spectrometer, which was only about half the design requirement. However, because flight data from AVIRIS spectrometer D were shown to be adequate for meeting the original science requirements, i.e., the detection of subtle spectral features such as the OH absorption doublet at 2.2 μm in the spectrum of the clay mineral kaolinite, the decision was made to conduct the data quality and sensor performance evaluation program during the summer of 1987 as planned, and defer further improvements, such as increasing SNR, to the following winter. Flights were begun in late June at the East coast NASA Wallops Island facility on the U-2 aircraft and continued on the West coast at NASA Ames from late July through October when AVIRIS was returned to JPL for post-flight season calibration, checkout and upgrade. During the 4 months of operations aboard the aircraft, several events occurred which compromised the performance of the sensor. These events were related both to parts failures and design flaws that were undetectable through laboratory testing of the sensor. As a result of what was learned during the in-flight testing of AVIRIS, the upgrade program planned for late 1987 was enlarged and extended through 1988.

In this paper, we summarize the performance characteristics of AVIRIS at the beginning of the in-flight assessment program, describe the problems that occurred during the 1987 operations and how they affected data quality, summarize the findings of the independent performance evaluation investigators whose reports are published in these proceedings, and briefly describe the upgrade program that is under way at JPL to bring AVIRIS performance to the required level.

## AVIRIS PERFORMANCE DURING THE FIRST FLIGHT SEASON

AVIRIS is a "whisk-broom" imaging spectrometer employing a scanning foreoptic connected by optical fibers to 4 spectrometers, each with a line array of detector elements at its focus. Data encoded at 10 bits are recorded at the rate of 17 Mbps on an on-board tape recorder. Also recorded are data from an on-board calibrator and various engineering data from the sensor. Flight data are subsequently processed at JPL at a dedicated computer facility. The instrument and ground data processing facility are described in detail in a suite of papers by the AVIRIS engineers in Vane (1987a and b). A brief description of the instrument is given in Appendix 1 of these proceedings by Vane et al. (1988).

Figure 1 is an artist's sketch of the flight hardware in the NASA U-2 aircraft (see slide No. 1).

Performance at the Start of the Flight Season

At the start of flight operations in late June, 1987, three engineering flights, including the first field calibration experiment, and 3 laboratory calibrations had been performed on AVIRIS. Table 1 summarizes the sensor performance at the start of flight operations as determined in the laboratory.

Table 1. AVIRIS performance at the start of the 1987 flight season

| Parameter | Requirement | Achieved |
|---|---|---|
| Spectral Coverage | 0.4 to 2.4 μm | 0.410 to 2.451 μm |
| Spectral Sampling | 10 nm | 9.6 to 10.0 μm |
| Spectral Bandwidth | 10 nm | 9.0 to 11.6 μm |
| SNR (Albedo = 0.5) | 100:1 at 0.7 μm | 110:1 |
| | 50:1 at 2.2 μm | 20:1 |
| IFOV | 1 mrad | 0.95 mrad |
| Swath from U-2 | 10 km | 10.5 km |
| Spatial Oversampling | 15% | 17% |
| Internal Image Geometry | | |
| Cum. Error over Scan | 0.5 mrad | 0.26 mrad |
| Pixel-to-Pixel Error | 0.1 mrad | 0.06 mrad |
| Signal Level Stability | 3% | 2.4 to 7.7% |
| Calibration | | |
| Spectral | 5 nm | 0.8 to 2.1 nm |
| Radiometric (absolute) | 10% | 7.3% |

The areas of sensor performance not meeting the requirements were SNR at 2.2 μm and signal level stability. The required and achieved SNR performance cited in Table 1 is referred to a standard scene radiance determined by an albedo of 0.5 at mid-latitude, mid-summer, with an atmosphere of 23 km visibility with rural aerosols (see Green et al., 1988, for a more detailed description of the AVIRIS reference radiance model). The achieved performance was measured in the laboratory with a calibrated integrating sphere whose radiance output was normalized to the AVIRIS reference radiance. While the SNR requirement of 50:1 was not being met at the start of the flight season, engineering flight data over Cuprite, Nevada showed that the sensor performance at that wavelength was adequate for detecting the kaolinite doublet under the conditions at Cuprite (Vane, 1987c). Signal level stability in Table 1 refers to the stability of the radiometric response function, which is different for

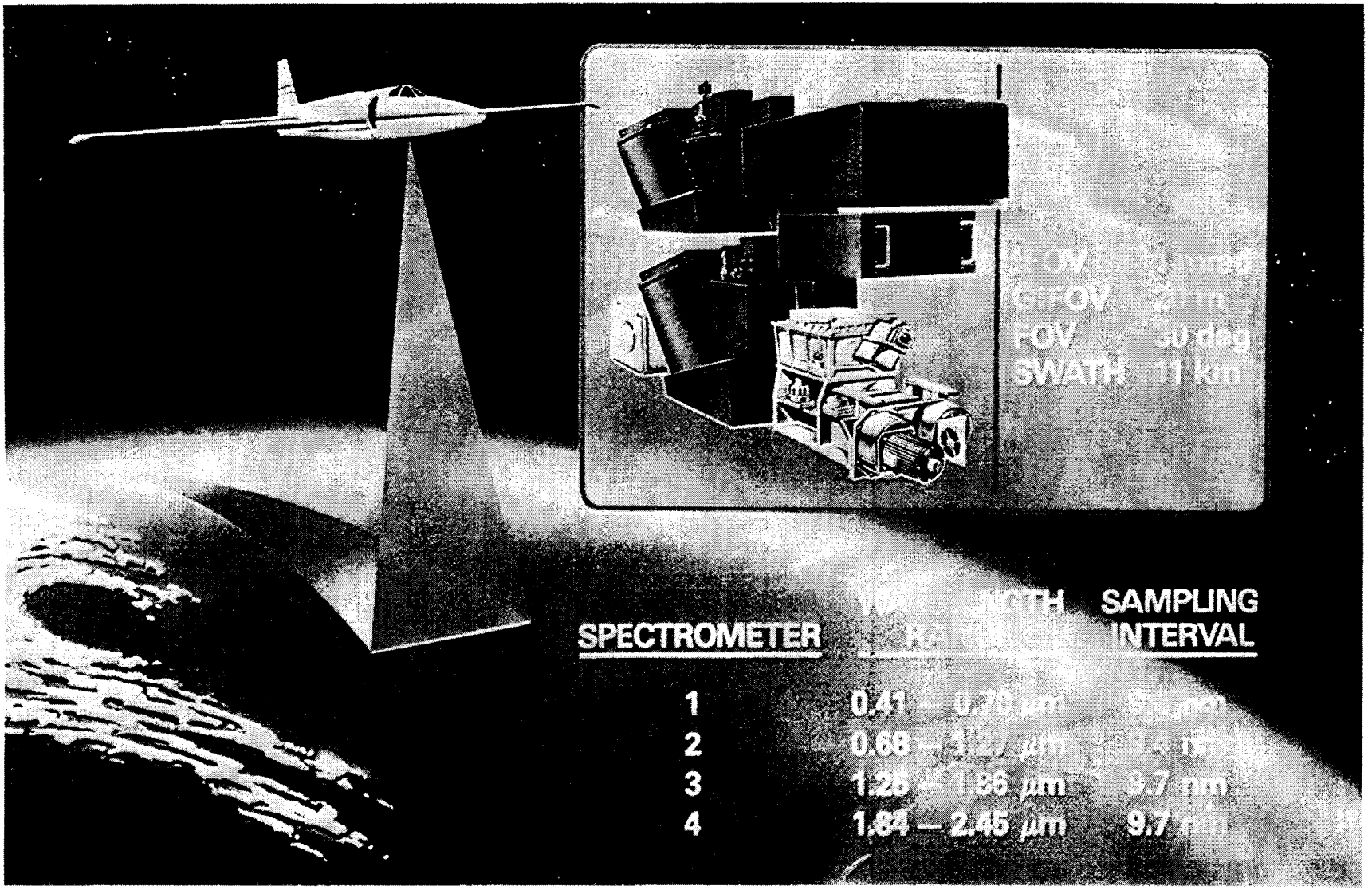


Characteristics of AVIRIS

each spectrometer because of the small differences in their thermal and opto-mechanical configurations. In the pre-flight season laboratory testing of AVIRIS, we found that spectrometer D with a stability of 2.4%, met the requirement, which was derived from the absolute radiometric calibration requirement, while spectrometers A, B and C, at 3.5%, 7.7%, and 4.2% respectively, did not meet the requirement for radiometric response function stability (Vane et al., 1987). Spectral coverage overlap between the spectrometers, plus the on-board calibrator, could be used to tie the radiometry of spectrometers A, B, and C to the more stable spectrometer D if desired, however.

Three other areas affecting data quality and sensor performance were also known at the start of the flight season. Fixed pattern noise was present in the data from all spectrometers and had been studied through a Fourier transform analysis. Only in spectrometer D, however, was its amplitude great enough to be observable to the eye, and there only in highly stretched images of uniform targets such as the interior of the AVIRIS integrating sphere. Spectrometer D was also known to have 2 noisy detector elements in its 64-element line array. Their locations were at spectral channels 181 and 210, or 2.026 and 2.312 μm, respectively. Finally, vignetting was present in the foreoptics of about 8% at the left edge of the field of view. These and the areas discussed above were to be addressed in the upgrade program at the end of the flight season.

## Evolution of AVIRIS Performance Over the Flight Season

As a result of the extensive operation of AVIRIS aboard the U-2, coupled with a field calibration experiment at the end of the season, a post-flight season laboratory calibration and the subsequent tear-down of the instrument, a great deal was learned about sensor performance by the AVIRIS project by the time of the Performance Evaluation Workshop. In particular, several additional areas of performance weakness that developed over the flight season were identified, their causes determined and solutions identified. Appendix 1 contains 2 papers that were presented at the Orlando, Florida meeting of the Society of Photo-Optical Instrumentation Engineers (SPIE) April 6, 7, and 8, 1988, that detail what was learned through the field calibration experiment and post-flight season laboratory calibration (Conel et al., 1988a, and Vane et al., 1988, respectively). We summarize the results here as they pertain to radiometric stability, spectral performance and SNR. Details of the engineering work being done to address these problems is discussed in the last section of the paper.

Radiometric stability. Variations of 50% or more were seen in the radiometric response of the sensor relative to the AVIRIS reference radiance model. The causes were (1) an inadequate spectrometer thermal control system, (2) warpage

of the AVIRIS instrument rack, (3) detachment of optical fibers to 2 of the spectrometers, (4) failure of a component in the signal chain electronics, and (5) breakage of a blocking filter in one of the spectrometers. Because of the close match between the size of the cone of light falling on the AVIRIS detectors and the detector dimensions, thermal control of the spectrometer bodies is critical to maintaining alignment and, therefore, constant signal level. The thermal control system used during the first flight season held the spectrometer bodies to within 3 degrees C of a pre-set temperature, which resulted in the laboratory stability performance noted earlier. The much colder aircraft environment caused larger fluctuations in temperature, however, and therefore signal levels. Warpage of the instrument rack in the aircraft apparently resulted because of a design deficiency by the manufacturer. The warpage was transmitted to at least spectrometer D, resulting in a degradation of optical alignment. In the post-flight season inspection of the instrument, it was discovered that the optical fibers to spectrometers A and B had become detached because of an epoxy failure. This resulted in both a signal loss in each spectrometer and a degradation of spectral resolution discussed below. During the flight season, sudden shifts in brightness were occasionally noted in the images from the various spectrometers. This was traced to the potentiometers in the preamplifier circuits which null the dark current offset of the detector signal prior to signal processing, in order to keep detector dark current levels on scale. This had the additional effect of making it appear that the output of some detector elements was zero when the offset drift was negative. Table 2 summarizes the spectral channels affected by this problem, which show up in the data as having dark current values of zero. Finally, the breakage of the $KH_2PO_4$ crystal (KDP) filter in spectrometer B early in the flight season, caused additional fluctuations in the response of that spectrometer. These 5 factors taken together on an individual spectrometer basis are thought to explain most of the instrument response instabilities seen during the 1987 flight season. See Vane et al. (1988) in Appendix 1 for a much more thorough discussion.

Table 2. AVIRIS spectral channels with dark current of zero

| Flight | Date | Channel Number |
|---|---|---|
| 4 | 6/25 | 162, 163, 166, 168, 169, 173, 189, 200, 214, 216 |
| 5 | 7/4 | 162, 168, 173 |

Table 2. (contd)

| Flight | Date | Channel Number |
|---|---|---|
| 6 | 7/9 | 162, 168, 173 |
| 7 | 7/13[a] | 162-166, 168, 169, 173-178, 180, 182, 184, 189, 194, 197, 200, 201, 205, 208, 209, 211, 213, 214, 216, 223 |
| 9 | 7/24 | 162, 168 |
| 10 | 7/30 | 162, 168 |
| 11 | 8/1 | 162, 168 |
| 12 | 9/14 | 20, 24, 26, 28, 32, 162, 163, 168, 169, 173 |
| 13 | 9/18[a] | 20, 24, 26, 28, 32, 34, 40, 64, 72, 80,162, 163, 165, 168, 169, 173, 176, 189, 205 |
| 15 | 10/13[b] | none |
| 16 | 10/14[b] | none |
| 17 | 10/15[b] | none |
| 18 | 10/19[b] | none |
| 19 | 10/21[b] | none |

[a]Potentiometers adjusted and/or replaced after these flights.
[b]Although no channels had dark current values of zero, small line-to-line offsets were still occurring.

Spectral performance. Item numbers (2) and (3) above also affected the spectral alignment and bandwidths of the AVIRIS spectrometers. Warpage of spectrometer D induced by distortion of the instrument rack probably accounts for the 3 nm shift in spectral alignment measured in the post-flight season laboratory calibration (Vane et al., 1988) and subsequently measured in the flight data from flight number 10 on July 30, 1987 (Green et al., 1988). Detachment of the optical fibers to spectrometers A and B caused a broadening of the spectral response functions and shifts in the spectral alignments of both spectrometers. Vane et al. (1988) report post-flight season bandwidths of 17 and 14 nm and spectral alignment shifts of 6 and 2 nm toward the blue for spectrometers A and B respectively. Green et al. (1988) report from the flight data of July 30, 1987, spectral bandwidths of 15 and 17 nm and alignment shifts of 0 and 4 nm toward the blue for A and B respectively. We take the discrepancy between these 2 independent determinations to be an indication of the dynamic nature of the spectral response of these two spectrometers because of the detached and therefore moveable optical fibers. A similar disagreement between the in-flight radiometric response and the pre- and post-flight season radiometry is noted by Conel et al. (1988a).

Signal-to-noise performance. All of the factors discussed above which affect instrument output signal levels also affect SNR. In addition, increases in electronic noise were noted over the flight season. One source was the failing potentiometers which by the end of the flight season were causing line-by-line variations in offsets. Additionally, this effect nullifies the gain one would normally get by averaging spatial pixels to enhance SNR by the square root of the number of pixels averaged. We also noted an increase in the Gaussian noise level in spectrometer D, and increases in fixed pattern noise in all spectrometers, but again, especially in spectrometer D. Most of the preamplifier and clock driver boards were reworked several times to improve performance before the flight season began to optimize noise performance. This probably weakened the boards, making them more susceptible to such noise paths as vibration of various electronic components on the boards. As a result of these factors, the SNR of spectrometer D was as low as 10:1 by the end of the flight season, normalized to the AVIRIS reference radiance model.

## AVIRIS Ground Data Processing Facility Performance

The AVIRIS Ground Data Processing Facility consists of a dedicated VAX 11-780 computer, an Ampex HBR3000 high density digital tape drive, 2 9-track 6250 bpi tape drives, and dedicated hard disk drives, printers, display devices, terminals, an optical disk drive, a matrix film recorder, and an interlan ethernet interface. The purpose of the facility is to convert flight data on high density tapes (HDTs) to 9-track 6250 bpi archival computer compatible tapes (CCTs) and quick-look hardcopy images (archival processing), to provide engineering data to the instrument team for timely monitoring of instrument performance, to process requested data from the archive through spatial and spectral subsetting and radiometric and geometric rectification (retrieval processing), and to provide analytical processing support for visiting scientists. Also, selected scenes specified by the AVIRIS experiment scientist are archived on optical disk for distribution to anyone who wishes a copy. The system and its functions are described in detail by Reimer et al. (1987). During the 1987 flight season, the AVIRIS Ground Data Processing Facility performed flawlessly.

During 1987, the equivalent of 795 full 6250 bpi CCTs of data were collected and processed as a result of the performance evaluation program and the pre- and post-flight season project engineering evaluation activities. The design goal for the facility was to complete retrieval processing in no more than 3 weeks of elapsed time from receipt of the processing request from the investigator. This goal was achieved. In addition, 10 investigators spent an average of 3 days each analyzing their flight data at the AVIRIS Ground Data Processing Facility. Table 3 summarizes the data processing statistics for 1987. The flow of data from

acquisition to distribution of processed products is: (1) Data acquisition aboard the NASA U-2, (2) mailing HDT to AVIRIS Ground Data Processing Facility at JPL, (3) archival processing at JPL, (4) mailing a copy of the quick-look hardcopy images and a retrieval processing request form to the investigator, (5) investigator returns retrieval request form to JPL indicating which data are to be processed and to what level, and (6) JPL mails processed data on 6250 bpi CCT to investigator.

Table 3. AVIRIS 1987 data processing statistics

| | |
|---|---|
| Data Quantity Collected | 33 HDTs |
| Data Quantity Archived (Archival Processing) | 795 CCTs |
| Data Quantity Processed (Retrieval Processing) | 339 CCTs |
| Number of Investigators Who Received Data | 58 |
| Data Processing Times (Average) | |
| From Acquisition through Archival Processing | 6 weeks |
| From Archival Processing to Receipt of Retrieval Processing Request Form | 7 weeks |
| From Receipt of Request Form to Mailing of Fully Processed Data on CCTs | 3 weeks |

## RESULTS OF THE INDEPENDENT PERFORMANCE EVALUATION OF AVIRIS

In the following section of the paper we summarize the work presented in these proceedings of 15 of the investigations sponsored by NASA to assess AVIRIS data quality and sensor performance. In addition to assessing data quality, many of the investigations attempted to use AVIRIS data to address scientific problems.

Conel et al. (1988b) used AVIRIS data from Mountain Pass, California to assess the potential for recovering atmospheric water abundance in the vertical column below the sensor at the spatial resolution of AVIRIS. Using a band ratio method and the 940 nm atmospheric water band and the 870 nm continuum radiance, they were able to successfully produce a map of the areal distribution of total precipitable water over the region which conforms well to topography. Independent validation of the AVIRIS-derived column abundance at one point in the region was supplied by a calibrated spectral hygrometer. The accuracy of the AVIRIS determination is estimated to be 10%. For average conditions over Mountain Pass, the uncertainty in AVIRIS-derived water column abundance is +/- 0.12 cm. Signal-to-noise was enhanced by averaging spatially 2 by 2 pixels.

Kieffer et al. (1988) analyzed AVIRIS data from several sites to assess instrument stability and response. Although the data were clearly noisy and the instrument response function was unstable at the times of data acquisition, they showed that valuable spectral signatures can still be extracted and analyzed. Two methods are described for extracting spectral information from the Kelso Dunes, California, both of which successfully identified at least three distinct spectral signatures, although positive identification of a specific material was not possible. They also describe their assessment of coherent and random noise and two techniques used for minimizing these and atmospheric effects.

Curran and Dungan (1988) have developed a new procedure for estimating SNR which they call the "geostatistical" method, and have applied it to 5 AVIRIS data sets to illustrate its utility to the investigator for determining where the zones of maximum information lie for a specific ground cover type. They define zones of maximum information as those spectral regions of highest SNR. The procedure is based on removal of periodic noise by "notch filtering" in the frequency domain and the isolation of sensor noise and intra-pixel variability using the semi-variogram.

Clark et al. (1988) used data from several ground calibration sites at Cripple Creek and Canon City, Colorado to reduce their flight data to ground reflectance. SNR performance was computed on selected spectra extracted from the calibrated images. The data were very noisy, although Fourier transform analysis revealed the absence of periodic noise in the data. Random offsets in signal and dark current levels were noted, leading the investigators to drop the standard procedure of the 101 scan line dark current smoothing in favor of a line-by-line correction. Images of spectral absorption band depth selected to be diagnostic of the presence of certain minerals and vegetation were computed. The resulting images showing the presence of goethite, kaolinite and lodgepole pine trees agreed well with field checks of the test sites. Clark et al. point out however, that successful identification of these materials in areas of lower abundance or higher vegetation cover will require higher SNR performance than AVIRIS had in October 1987.

Kruse et al. (1988a) have developed techniques for the automated extraction and characterization of absorption features from reflectance spectra and have successfully applied these techniques to AVIRIS and Geophysical and Environmental Research Imaging Spectrometer (GERIS) data. Maxima in the spectra are identified automatically, and a continuum of straight line segments is fit between these points The continuum is removed from the spectrum by division, the minima of the resulting spectrum are determined, and the 10 strongest features are extracted. From these, the wavelength position, depth, full width at half the maximum depth, and asymmetry for each of the 10

features are determined and tabulated. The routines are written in Fortran and C languages. When applied to AVIRIS data from the Grapevine Mountains of Nevada, many of the strongest features located were noise, but AVIRIS spectra from known areas of sericite and dolomite were also found.

A second study by Kruse et al. (1988b) used the internal average relative (IAR) reflectance approach and a U. S. Geological Survey (Flagstaff) developed analysis program called QLook to analyze the Grapevine Mountains data as well as the Colorado data sets studied by Clark et al. At the Grapevine Mountains both muscovite and carbonate were accurately identified and mapped in the imagery, but low SNR precluded differentiation between calcite and limestone and muscovite and montmorillonite, which had been previously done with AIS. The noise problems with the Colorado data were accentuated by the IAR technique because of the moderate vegetation cover. This approach to information extraction was less successful than that used by Clark et al. described above. The conclusion by Kruse et al. was the same as Clark et al., however: Higher SNR is required if AVIRIS is to be effectively utilized in more challenging geological settings.

Rock et al. (1988) were interested in testing the efficacy of AVIRIS data for detection of environmentally-induced shifts in the spectra of vegetation at the chlorophyll well and red edge. They used radiometrically corrected data from Bishop, California, which were flat field corrected using a grus pit of weathered products from granitic rock and having no vegetation present. A normalization technique was developed and applied to remove the large variations in the height of the near infrared plateau and depth of the chlorophyll well characteristic of the different types of vegetation in the area. Both native and cultivated vegetation sites were studied in areas sufficiently large and uniform that several pixels could be averaged to enhance SNR. When applied to data from fields of green uncut alfalfa and fields of freshly cut green but drying alfalfa, a distinct shift in wavelength toward the blue end of the spectrum was observed in the position of the red edge of the cut alfalfa relative to the red edge position of the uncut alfalfa. The investigators also conclude that AVIRIS spectra may be useful in detecting small amounts (20 to 30% cover) of semi-arid and arid vegetation ground cover.

Elvidge (1988) used laboratory and field reflectance data from 3 large, uniform targets of high, intermediate and low brightness for correcting AVIRIS data from Jasper Ridge, California to percent reflectance. The area studied is a large natural vegetation preserve which contains most of the major plant communities found along the central California coast. Highly linear relationships were found between the digital numbers and reflectance for the 3 calibration targets in the first two spectrometers. However, changes in instrument response in the last 2 spectrometers induced by factors discussed earlier in this paper caused the DN of the bright target at the north end of the flight line to deviate

from a linear fit with the other 2 targets further south along the flight line. Spectrometer C and D data were therefore corrected only with the reflectance data from the 2 southern targets. The results of the analysis of the calibrated data showed distinct reflectance spectra from 5 plant communities, including 4 containing green vegetation and 1 containing a dry annual grassland. Spectral features identified in the data were tied to pigment absorption in the visible spectrum, to the red edge, to leaf water absorptions at 0.97 and 1.19 μm, and to ligno-cellulose absorptions at 2.09, 2.26, and 2.33 μm. A ligno-cellulose vegetation index image was produced from the data having very good correlation with known ligno-cellulose concentrations on the ground.

Swanberg (1988) has completed the first phase of a 2 phase study to assess the utility of AVIRIS data for remotely acquiring information on plant chemistry. She assessed the geometric and radiometric properties of data sets from central Oregon for pixel size, swath width, spectral position and SNR. Her in-flight analysis of image geometry compares well with the laboratory measured values for IFOV and FOV, the small differences being due most likely to topographic effects. The LOWTRAN 6 atmospheric modelling code was used to evaluate spectral position by comparing a 50 pixel averaged AVIRIS spectrum with a LOWTRAN spectrum calculated for a mid-latitude, mid-summer, 0.5 albedo model. From the visual inspection of the two radiance curves, agreement was found to within 1 AVIRIS spectral bandwidth or 10 nm, which is the resolution of such an approach. SNR was calculated at two targets by dividing the mean signal level at each by the standard deviation of the signal. Fifty pixels from a bright, relatively homogeneous beach and 9 pixels from a dark forest site were used to determine the upper and lower bounds respectively, of SNR. Swanberg concludes that for the second phase of her study, which is to analyze AVIRIS spectra for plant chemistry signatures, she will use data only from spectrometers A and B since the SNR of spectrometers C and D is too low in the 1987 data.

Bailey et al. (1988) analyzed AVIRIS data from the Drum Mountains, Utah, to assess sensor performance and the utility of the data for geological mapping in an area of well-exposed diverse rock and alteration types. Their assessment of coherent noise and identification of the low output channnels agrees well with results obtained by the AVIRIS project. To avoid contamination by the low output channels, they chose to work with raw data processed without spectral resampling, and a modified dark current subtraction approach was taken to avoid introducing errors due to the offset shifts noted above. Also, a Gaussian notch filter was successfully applied to remove some of the major noise components. SNR was calculated on a bright hardpan target after these corrections and found to be generally lower than those reported by the project at the start of the flight season, which is in agreement with post-flight season laboratory verification of the overall drop in SNR by the end of the

summer. To assess the spectral content of the data, several analysis approaches were used including those associated with the JPL-developed Spectral Analysis Manager (SPAM) software, and standard image processing and enhancing techniques such as band ratioing, band averaging, and principal components analysis. Mixed results were obtained: Data from spectrometers A and C were adequate for identifying iron-oxide-bearing rocks, but poor SNR in spectrometer D limited the ability to discriminate and identify hydroxyl-bearing rocks and minerals or differentiate carbonate minerals, although the major absorption features associated with these materials were resolved.

The study by Mustard and Pieters (1988) was limited by the fact that AVIRIS missed the prime area in their test site, although useful field studies were conducted to pave the way for future AVIRIS data collection when the sensor is returned to operations with improved performance. The test area is the Kings-Kaweah ophiolite melange in east-central California, which is thought to be an obducted oceanic fracture zone. The eventual goal of the study is to map the distribution and abundance of key mineral components in the melange with AVIRIS to determine the importance of geological processes which are responsible for the formation of fracture zone crust.

Wetland vegetation near San Francisco was the target of interest to Gross et al. (1988) in their assessment of AVIRIS data utility. Using SPAM to analyze JPL-radiometrically corrected data, they concentrated their efforts in the 0.4 to 1.72 μm region, ignoring the spectral region covered by spectrometer D because of low SNR. Averages of 5 by 5 pixels were generally used in constructing spectral curves from the data. Their results suggest that despite low SNR, it is possible to detect differences in the position of the red edge, and that there may be several narrow spectral regions between 0.4 and 1.72 μm where amplitude and slope variations for various vegetation types are sufficiently different to enable them to be distinguished. These include the 0.76-0.77, 0.80-0.84, 1.04-1.09, 1.29-1.33, 1.50-1.52, and 1.57-1.65 μm regions.

Carrere and Abrams (1988) chose the Goldfield Mining District of western Nevada for their test area because of the large suite of hydrothermal alteration minerals in a well-mapped and well-exposed setting. They worked with raw data, correcting them for dark current variations and detector readout delay with software written for that purpose. Atmospheric correction was achieved by applying the flat field technique using a 9 by 9 pixel average from the spectrally bland and spatially homogeneous Chispa andesite as reference. Unambiguous kaolinite and alunite spectra were obtained from the processed data and verified through field and laboratory work. Poor SNR prohibited the production of mineral and alteration zone maps with the techniques available with SPAM or with ratio or clustering techniques, however. Assessment of several aspects of sensor performance

was also conducted, including long-period drift in instrument response over a several minute duration flight line, sudden steps in scene brightness, noise, SNR, and spectral resolution. Their findings on in-flight performance are in good agreement with other results presented at the workshop.

Crowley et al. (1988) studied AVIRIS data quality at the rare-earth-element-bearing carbonatite complex at Mountain Pass, California, a site well-suited for assessment of spectral and radiometric performance because of the presence of minerals with very narrow and deep absorption features, and a large homogeneous, spectrally bland playa and other targets for field calibration. They derived SNR estimates that were in general agreement with the pre-flight season values tabulated earlier in this paper, and characterized periodic noise at several frequencies having strong horizontal and weak vertical, and horizontal only frequency dependencies. Two procedures were used to correct for atmospheric and solar irradiance effects, the flat field and single spectrum techniques. The single spectrum technique consists of dividing a spectrum from a ground target by the corresponding radiometrically calibrated but otherwise uncorrected AVIRIS spectrum, and applying the resulting set of scalars for each spectral channel to the rest of the AVIRIS image. The 3 rare-earth (neodymium) narrow absorption features between 0.7 and 0.94 μm, as well as features due to $CO_3$ and Al-OH were clearly observable in the processed spectra.

Green et al. (1988), in a parallel but largely independent study of the same area used the rare-earth as well as atmospheric absorption features to qualitatively determine in-flight spectral bandwidths and positions, and used the LOWTRAN 7 atmospheric code in conjunction with measurements of atmospheric optical depth and reflectance of Ivanpah Playa and other ground targets, all obtained near the time of overflight, to assess in-flight SNR. Using field-measured reflectance data from the Playa, an asphalt and a graded soil target, an empirical line correction was applied to the data to compensate for solar, atmospheric and instrumental factors. Using the concurrently acquired surface and atmospheric measurements, an improved spectral calibration was performed. Radiometric calibration was done using LOWTRAN 7 modelled radiance over Ivanpah. From these data, shifts in spectral alignment of spectrometers B, C and D were found respectively, of 4 nm and 1 μm toward the blue, and 3 nm toward the red. The spectral bandwidths of spectrometers A and B were found to have broadened to 15 and 17 nm respectively. SNR over Ivanpah Playa normalized to the AVIRIS reference radiance model was found to be lower for spectrometers A and B than measured in the laboratory pre-flight season calibration, which is consistent with the fact that the optical fibers to these spectrometers were detached at the time of the flight, while the in-flight SNR for spectrometers C and D was roughly equivalent to that measured pre-flight in the laboratory. A comparison of the geometric

quality of the AVIRIS imagery was also made relative to a Landsat Thematic Mapper image of the same area. AVIRIS clearly resolves more spatial detail on the surface while showing excellent intra-image geometry. Finally, the neodymium absorption features between 0.7 and 0.94 μm were unambiguously resolved.

## SENSOR PERFORMANCE IMPROVEMENTS

Efforts are under way to improve the performance of AVIRIS for the next field season. The 2 major thrusts in performance improvement are (1) increase in SNR and (2) improved radiometric response stability. Table 4 lists the areas of work and the aspect or aspects of performance that are targeted for improvement.

The first 7 items in Table 1 were completed and the instrument was tested in the laboratory over the summer of 1988, and in-flight in early September, 1988. The results were encouraging: The instrument radiometric response functions were significantly more stable than during the 1987 flights, although anomalies were observed which it is hoped may be partially mitigated by item number 9; signal levels generally were the highest yet achieved from the instrument and matched the modelled levels for all but spectrometer D which, because of the aberrations inherent in its design, has a larger spot size than the other spectrometers, resulting in signal loss off the detectors; and, there was a general improvement in noise, especially coherent noise, which was

Table 4. AVIRIS project activities directed at improving sensor performance.

| | Engineering Activity Undertaken | Performance Issue(s) Addressed |
|---|---|---|
| 1. | Improve spectrometer thermal controllers | Stabilize radiometric response function and spectral alignment |
| 2. | Kinematically mount spectrometers to rack | Reduce heat flow and vibrations from rack and mitigate effects of rack warpage on alignment |
| 3. | Improve optical fiber package | Minimize chance of future defocus of instrument |
| 4. | Implement new fiber positioners | Facilitate optical alignment - maximize signal levels |

Table 4. (contd)

| | Engineering Activity Undertaken | Performance Issue(s) Addressed |
|---|---|---|
| 5. | Remove KDP filter from spectrometer B | Stabilize radiometric response function |
| 6. | Realign foreoptics | Minimize vignetting |
| 7. | Build new pre-amplifier and clock driver boards | Stabilize signal chain performance and reduce noise |
| 8. | Repackage detector drive logic | Reduce signal chain noise |
| 9. | Remove delrin rod between dewar mount and spectrom. | Stabilize spectrometer alignment |

greatly reduced from the levels seen early in the 1987 flight season. However, overall, there was only a modest improvement in SNR as a result of reduced coherent noise and much more stable signal chain electronics performance. After the in-flight testing in September 1988, additional experiments were conducted in the laboratory which showed that (1) signal chain packaging was responsible for much of the remaining system noise, and (2) the delrin rod that is the mechanical interface between each dewar mounting assembly and the spectrometer body is not sufficiently rigid for that application, allowing some movement of the dewar under various conditions that exist in both the lab and flight environments. These rods are being replaced with aluminum. The signal chain packaging was implicated as a noise source through substitution testing of each spectrometer with the breadboard electronics, which when substituted for the flight electronics on the instrument rack, gave noise levels that were 2 to 4 times lower. As a weight saving strategy to meet the requirements for flying on the NASA U-2 aircraft, the detector drive logic was originally packaged in the same box with other logic circuitry using a common power supply and master clock. Moreover, because of its size, the box is located at the other end of the AVIRIS rack from the spectrometers, requiring long electrical cables which are susceptible to noise pick up. The weight constraints of the U-2 have been relieved now that the last of the U-2s has been retired and replaced with the more capable ER-2, so the detector drive logic is being repackaged with its own power supply and clock and located much closer to the spectrometers to minimize cable length. It is hoped that this will result in a significant noise improvement. The engineering team

plans to finish the work in the Spring of 1989 and verify in-flight performance with another field calibration experiment.

## SUMMARY

Judged by most criteria, the 1987 flight season and performance evaluation effort were successful in meeting the objectives of assessing data quality and sensor performance. The results of the evaluation by the AVIRIS project and the independent performance evaluation investigators provided the engineering team with a great deal of information needed to bring AVIRIS performance to its desired levels. In spite of degraded data quality over the course of the summer, some exciting scientific results were also obtained from the program, which bodes well for the future of imaging spectroscopy. If the AVIRIS engineering team is successful in its work over the next few months, the enhanced performance of the sensor and the knowledge gained by the members of the earth science community who participated in the 1987 evaluation program should allow us to launch a vigorous and exciting new phase of earth remote sensing.

## ACKNOWLEDGMENTS

The authors would like to express their deep gratitude to the large number of people who have made possible the progress reported in this paper and in these proceedings: The members of the AVIRIS flight hardware and ground data processing teams for their tireless efforts over the past 4 years; the program sponsors at NASA who have supported this work from the outset; and the enthusiastic members of the earth science community who have worked so hard and creatively to develop the tools for utilizing this new class of data, and who have offered us so much support and encouragement.

The AVIRIS project work summarized in this paper was performed at the Jet Propulsion Laboratory, California Institute of Technology, under contract to the National Aeronautics and Space Administration.

REFERENCES

Bailey, G.B., J.L. Dwyer, and D.J. Meyer. 1988. AVIRIS data characteristics and their effects on spectral discrimination of rocks exposed in the Drum Mountains, Utah: Results of a preliminary study. Proceedings of the AVIRIS Performance Evaluation Workshop. JPL 88-38 (Pasadena, California: The Jet Propulsion Laboratory), these Proceedings.

Carrere, V. and M.J. Abrams. 1988. An assessment of AVIRIS data for hydrothermal alteration mapping in the Goldfield Mining District, Nevada. Proceedings of the AVIRIS Performance Evaluation Workshop. JPL 88-38 (Pasadena, California: The Jet Propulsion Laboratory), these Proceedings.

Clark, R.N., B.J. Middlebrook, G.A. Swayze, K.E. Livo, D.H. Knepper, T.V.V. King and K. Lee. 1988. Calibration and evaluation of AVIRIS data: Cripple Creek in October 1987. Proceedings of the AVIRIS Performance Evaluation Workshop. JPL 88-38 (Pasadena, California: The Jet Propulsion Laboratory), these Proceedings.

Conel, J.E., R.O. Green, R.E. Alley, C.J. Bruegge, V. Carrere, J.S. Margolis, G. Vane, T.G. Chrien, P.N. Slater, S.F. Biggar, P.M. Teillet, R.D. Jackson, and M.S. Moran. 1988a. In-flight radiometric calibration of the Airborne Visible/Infrared Imaging Spectrometer (AVIRIS). Proceedings of the SPIE Conference on Recent Advances in Sensors, Radiometry, and Data Processing for Remote Sensing, v. 924, pp. 179-195. (see also Appendix 1 of these Proceedings)

Conel, J.E., R.O. Green, V. Carrere, J.S. Margolis, R.E. Alley, G. Vane, C.L. Bruegge, and B.L. Gary. 1988b. Atmospheric water mapping with the Airborne Visible/Infrared Imaging Spectrometer (AVIRIS), Mountain Pass, California. Proceedings of the AVIRIS Performance Evaluation Workshop. JPL 88-38 (Pasadena, California: The Jet Propulsion Laboratory), these Proceedings.

Crowley, J., L. Rowan and M. Podwysocki. 1988. Evaluation of AVIRIS data of the Mountain Pass, California Carbonatite Complex. Proceedings of the AVIRIS Performance Evaluation Workshop. JPL 88-38 (Pasadena, California: The Jet Propulsion Laboratory), these Proceedings.

Curran, P.J. and J.L. Dungan. 1988. Zones of information in the AVIRIS spectra. Proceedings of the AVIRIS Performance Evaluation Workshop. JPL 88-38 (Pasadena, California: The Jet Propulsion Laboratory), these Proceedings.

Elvidge, C.D. 1988. Examination of the spectral features of vegetation in 1987 AVIRIS data. Proceedings of the AVIRIS Performance Evaluation Workshop. JPL 88-38 (Pasadena, California: The Jet Propulsion Laboratory), these Proceedings.

Green, R.O., G. Vane and J.E. Conel. 1988. In-flight determination of AVIRIS spectral, radiometric, spatial and signal-to-noise characteristics using atmospheric and

surface measurements from the vicinity of the rare-earth-bearing carbonatite at Mountain Pass, California. Proceedings of the AVIRIS Performance Evaluation Workshop. JPL 88-38 (Pasadena, California: The Jet Propulsion Laboratory), these Proceedings.

Gross, M.F., S.L. Ustin and V. Klemas. 1988. AVIRIS spectra of California wetlands. Proceedings of the AVIRIS Performance Evaluation Workshop. JPL 88-38 (Pasadena, California: The Jet Propulsion Laboratory), these Proceedings.

Kieffer, H.H., E.M. Eliason, K.F. Mullins, L.A. Soderblom, and J.M. Torson. 1988. Radiometric performance of AVIRIS: Assessment for an arid region geological target. Proceedings of the AVIRIS Performance Evaluation Workshop. JPL 88-38 (Pasadena, California: The Jet Propulsion Laboratory), these Proceedings.

Kruse, F.A., W.M. Calvin and O. Seznec. 1988a. Automated extraction of absorption features from Airborne Visible/Infrared Imaging Spectromter (AVIRIS) and Geophysical and Environmental Research Imaging Spectrometer (GERIS) data. Proceedings of the AVIRIS Performance Evaluation Workshop. JPL 88-38 (Pasadena, California: The Jet Propulsion Laboratory), these Proceedings.

Kruse, F.A., D.L. Taranik and K.S. Kierein-Young. 1988b. Preliminary analysis of Airborne Visible/Infrared Imaging Spectrometer (AVIRIS) for mineralogic mapping at sites in Nevada and Colorado. Proceedings of the AVIRIS Performance Evaluation Workshop. JPL 88-38 (Pasadena, California: The Jet Propulsion Laboratory), these Proceedings.

Mustard, J.F. and C.M. Pieters. 1988. Application of imaging spectrometer data to the Kings-Kaweah ophiolite melange. Proceedings of the AVIRIS Performance Evaluation Workshop. JPL 88-38 (Pasadena, California: The Jet Propulsion Laboratory), these Proceedings.

Reimer, J.H., J.R. Heyada, S.C. Carpenter, W.T.S. Deich and M. Lee. 1987. Airborne Visible/Infrared Imaging Spectrometer (AVIRIS) ground data processing system. Proceedings of the SPIE Conference on Imaging Spectroscopy II, v. 834, pp. 79-90.

Rock, B.N., C.D. Elvidge and N.J. Defeo. 1988. Assessment of AVIRIS data from vegetated sites in the Owens Valley, California. Proceedings of the AVIRIS Performance Evaluation Workshop. JPL 88-38 (Pasadena, California: The Jet Propulsion Laboratory), these Proceedings.

Swanberg, N.A. 1988. AVIRIS data quality for coniferous canopy chemistry. Proceedings of the AVIRIS Performance Evaluation Workshop. JPL 88-38 (Pasadena, California: The Jet Propulsion Laboratory), these Proceedings.

Vane, G., editor. 1987a. Proceedings of the SPIE Conference on Imaging Spectroscopy II, 20-21 August 1987, San Diego, California, v. 834, 232 pages.

Vane, G., editor. 1987b. Airborne Visible/Infrared Imaging Spectrometer (AVIRIS): A description of the sensor, ground data processing facility, laboratory calibration and first

results. JPL 87-38 (Pasadena, California: The Jet Propulsion Laboratory), 97 pages.

Vane, G. 1987c. First results from the Airborne Visible/Infrared Imaging Spectrometer (AVIRIS). Proceedings of the SPIE Conference on Imaging Spectroscopy II, v. 834, pp. 166-174.

Vane, G., T.G. Chrien, E.A. Miller and J.H. Reimer. 1987. Spectral and radiometric calibration of the Airborne Visible/Infrared Imaging Spectrometer (AVIRIS). Proceeding of the SPIE Conference on Imaging Spectroscopy II, v. 834, pp. 91-106.

Vane, G., T.G. Chrien, J.H. Reimer, R.O. Green and J.E. Conel. 1988. Comparision of laboratory calibrations of the Airborne Visible/Infrared Imaging Spectrometer at the beginning and end of the first flight season. Proceedings of the SPIE Conference on Recent Advances in Sensors, Radiometry, and Data Processing for Remote Sensing, v. 924, pp. 168-178. (see also Appendix 1 of these Proceedings)

# ATMOSPHERIC WATER MAPPING WITH THE AIRBORNE VISIBLE/INFRARED IMAGING SPECTROMETER (AVIRIS), MOUNTAIN PASS, CALIFORNIA

James E. Conel, Robert O. Green, Veronique Carrere, Jack S. Margolis, Ronald E. Alley, Gregg Vane, Carol J. Bruegge & Bruce L. Gary

Jet Propulsion Laboratory
California Institute of Technology
Pasadena, California 91109

We report observations of the spatial variation of atmospheric precipitable water using the Airborne Visible/Infrared Imaging Spectrometer (AVIRIS) over a desert area in eastern California, derived using a band ratio method and the 940 nm atmospheric water band and 870 nm continuum radiances. The ratios yield total path water from curves of growth supplied by the LOWTRAN 7 atmospheric model. An independent validation of the AVIRIS-derived column abundance at a point is supplied by a spectral hygrometer calibrated with respect to radiosonde observations. Water values conform to topography and fall off with surface elevation. The edge of the water vapor boundary layer defined by topography is thought to have been recovered. The ratio method yields column abundance estimates of good precision and high spatial resolution.

Atmospheric water vapor is an important reservoir in the global hydrosphere having profound implications for the maintenance of fresh water supplies that are essential for life[1], for energetics of the atmosphere[2] and for modelling the Earth's hydrologic cycle[3] and climate[4]. In addition, water vapor line and continuum absorptions affect quantitative interpretation of the spectral reflectance, which is a fundamental parameter derivable from remote sensing observations of the Earth's surface. We describe here preliminary experiments utilizing spectral radiance band ratios of the Airborne Visible/Infrared Imaging Spectrometer (AVIRIS) that yield high-spatial resolution maps of precipitable atmospheric water. The present band ratio method was modeled after a similar method devised by Farmer *et al.*[5] for measurement of atmospheric water on Mars. The band ratio method offers the possibility of significant improvement in determination of column abundances over mid-infrared and microwave remote sensing techniques. Specification of the time and spatial variability of the absolute amount of water vapor, usually carried out remotely for the terrestrial case by observations at mid-infrared or microwave wavelengths[6] (but see also Ref. 7) contributes to our understanding of surface fluxes through local application of the equation-of-continuity for water vapor. The compensation for water vapor in radiance images of the Earth from aircraft or satellites can be carried out by application of theoretical models of radiative transfer based on molecular absorption line compilations[8,9].

AVIRIS provides near nadir spectral radiance measurements of the Earth from 400-2500 nm[10] with a spectral sampling interval and spectal resolution near 10 nm. From its U-2 platform at an altitude of 20 km above terrain the swath width is 11 km and the surface instantaneous field-of-view (IFOV) 20mx20m. The inflight spectral and radiometric performance of this instrument have been evaluated by field experiment[11]

AVIRIS overflew our test site at Mountain Pass, CA (Lat. 35° 28′ N, Long. 115° 32′ W, Figure 1a) on July 30, 1987, 10:15 AM PST, along a flight line oriented N 55° E. Topographically (Figure 1b) the image area to the northeast contains Ivanpah Valley with Ivanpah Lake (dry) occupying the lowest part at an elevation of 2600 ft (794 m). To the southwest the land surface rises over broad sparsely vegetated alluvial slopes to Clark Mountain and the Mescal Range where the maximum elevation is 6493 ft (1980 m). The image is bordered on the southwest by Shadow Valley at an elevation near 4200 feet (1280 m). During the overflight, measurements were made at site A (elevation 4726 ft., 1441 m)of atmospheric optical depth using a Reagan-type solar radiometer[12] (Figure 2), from which aerosol and ozone optical depths were derived by the procedure of Ref. 13. An observation at wavelength 940 nm was used to derive the slant path precipitable water present by cross-calibration with a ratioing spectral hygrometer (wavelengths 935 nm/880 nm) that is independently calibrated in terms of column precipitable water as determined by about one hundred radiosonde plus high altitude aircraft and large zenith angle solar observations. In addition, the surface bidirectional spectral reflectance of targets within the scene was measured with a portable instantaneous display and analysis spectrometer (PIDAS)[14]. PIDAS covers the spectral range 425-2500 nm with sampling intervals better than 5 nm. Reflectances of uniform areas of Ivanpah Lake (Site B, Figure 1a) were used to generate a local inflight radiometric calibration of AVIRIS[11] through the LOWTRAN 7[8] atmospheric model so that the image digital numbers could be converted to spectral radiance $L(\lambda)$ in $\mu w\ cm^{-2} nm^{-1} ster^{-1}$. A standard rural aerosol model was employed with visibility of 23 km, adopted by comparison with the Reagan solar radiometer measurements.

Figure 3 is the radiance at AVIRIS spectral resolution predicted at altitude from Ivanpah Lake according to the LOWTRAN 7 standard mid-latitude summer model using the PIDAS-determined surface reflectance as measured at site B. We used the ratio R(940,870,w) of AVIRIS-determined radiances $\bar{L}(940,w)/\bar{L}(870,w)$ (over-bars are averages of three channels around the wavelength indicated and w is precipitable water in cm) to estimate total path precipitable water (downward slant path of zenith angle ≈ 29° and upward vertical path) on a point by point basis in the image. The ratios were converted to amounts of water by generating a curve-of-growth from the LOWTRAN 7 model for the altitude of site A, including effects of path radiance intrinsic to the

model for the site altitude and flight conditions. The ratio curve-of-growth has the form $R = Aexp(-B/w)$ where $A = 0.8564$ and, $B = 0.5248$, with correlation coefficient- squared $r^2 = 0.9988$. The total precipitable water calculated from the model for Site A is 3.139 pr. cm. This model neglects the pressure effect from variations in topography over the image away from Site A, which amounts to a few percent.

Figure 1c is a map of the distribution of total precipitable water over the image area. In general atmospheric water distribution conforms to the topography. Notable are differences in amount between Ivanpah Valley and Shadow Valley, which differ in elevation by about 1600 feet (490 m), and a broad area of reduced water abundance found on the topographic slope between Ivanpah Lake and Clark Mountain. Highpoints of the landscape correspond to minimums in observed water abundance. We speculate that the sharp decrease in water column abundance found at the toe of the alluvial slope northeast of Clark Mountain may represent the edge of the water vapor boundary layer. The ratio calculation compensates well for albedo variations (bright and dark areas) over the surface, because the channels used are close to each other in wavelength and the corresponding differences in reflectance are small. The ratio R may be affected by water absorptions in the surface reflectance, either in vegetation or as soil moisture. The presence of an uncompensated surface absorption will decrease the apparent ratio and lead to an apparent increase in atmospheric water calculated to be present. The surface water absorption is always displaced to the red, and any effect of its presence minimized by forming the ratio described above. Also, the sparse desert plant cover present (mainly *Larrea*) and dry climatic conditions probably minimize these effects.

We used the solar radiometer measurements in Figure 2, to estimate precipitable water present at Site A according to the radiosonde-based spectral hygrometer scale, for comparison with the LOWTRAN 7-derived scale. The relationship between solar radiometer ratio $R_{sr} = L(940)/L(870)$ and spectral hygrometer ratio $R_{sr} = L(935)/L(880)$ is $R_{sh} = 0.08703 + 1.07992R_{sr}$ with $r^2 = 0.9999$. The line-of-site precipitable water present is determined from $W_{los} = W_0 + (W_0/6.8)^3$, where $W_0 = 13.7/10^{1.38R_{sh}}$, with an uncertainty ± 10%, including systematic and random errors. The values $W_{los}$ were adjusted for pressure by multiplying by $\sqrt{(p_0/p)}$ where $p_0$ is sea-level pressure and p is the pressure at site A. The pressure correction factor used is 1.1. Our ratio $R_{sr} = 0.4886$, which yields 2.78 cm of water from the radiosonde scale. This compares favorably with the LOWTRAN 7 value of 3.14 pr cm from the AVIRIS-determined ratio.

The data from separate bands used to generate the ratio image of Figure 1c contain both coherent and random noise components. To improve signal/noise ratio the separate band data were first averaged areally with a 2x2 square filter thereby decreasing the surface spatial resolution by a factor of four.

Horizontal banding present in the ratio image was removed by adjusting the pixels in each line as the difference between the average value for that line and the average value of all pixels in the surrounding ± 25 lines. Periodic microphonic noise was removed by transforming to the Fourier domain, severly attenuating the microphonic noise frequencies, and performing the inverse transform. The random noise component, determined by analysis of single-band imagery over uniform portions of Ivanpah Lake, was found to be ±2% rms. The curve-of-growth yields a fractional uncertainty $\sigma_w/w = 3.8(\sigma_R/R)/\sqrt{w}$ in the determination of w, where $\sigma_R/R$ is the fractional uncertainty in the ratio, i.e., 4% rms. This gives about ± 0.12 cm of water for average conditions over the Mountain Pass test area.

The present method benefits from a double pass of incident solar radiance through the atmosphere, increasing the observed abundance by approximately $1/\cos\theta$ ($\theta$ = solar zenith angle) over the vertical path alone column abundance. The present method offers improvement in precision of retrieved column abundances over that provided by both infrared and microwave remote sounding techniques[15] which have an estimated accuracy of 0.6 - 0.8 pr. cm with present-day instruments. Analysis of sensitivity to effects of scattering and further field validation exercises are planned.

Acknowledgments

We thank Prof. Fred Shair, Caltech, for many useful discussions. This research was carried out at Jet Propulsion Laboratory, California Institute of Technology under contract from the National Aeronautics and Space Administration.

## REFERENCES


1. Peixoto, J.P. & Oort, A.H. in *Variations in the Global Water Budget* (eds Street-Perrott, A., Beran, M. & Ratcliffe, R.) 5-65 (Reidel, Dordrecht, 1983).

2. Alestalo, M. in *Variations in the Global Water Budget* (eds Street-Perrott, A., Beran, M. & Ratcliffe, R.) 67-79 (Reidel, Dordrecht, 1983).

3. Brutsaert, W. *Evaporation into the Atmosphere* (Reidel, Dordrecht, 1988).

4. Houghton, J.T. & Morel, P. in *The Global Climate* (ed Houghton, J.T.) 1-11 (Cambridge University Press, Cambridge, 1984).

5. Farmer, C.B., Davies D.W., Holland, A.L., LaPorte, D.D. & Doms, P.E. *J. Geophys. Res.* **82(28)**, 4225-4248 (1977).

6. Houghton, J.T., Taylor, F.W. & Rodgers, C.D. *Remote Sounding of Atmospheres* (Cambridge University Press, Camabridge, 1986).

7. Gorodetsky, A.K. & Syachinov, V.I. in *Variations in the Global Water Budget* (Street-Perrott, A., Meran,M., & Ratcliffe, R.) 81-87 (Reidel, Dordrecht, 1983).

8. Kneizys, F.X., Shettle, E.P., Anderson, G.P., Abrew, L.W., Chetwynd, J.H., Shelby, J.E.A., Clough, S.A., & Gallery W.O. *Atmospheric Transmittance/Radiance: Computer Code LOWTRAN 7* (in press) (1988).

9. Tanre, D., Deroo, C., Duhaut, P., Herman, M., Morcrette, J.J. Perbos, J. & Deschamps, P.Y. in *Proc. Third Int. Colloq. on Spectral Signatures of Objects in Remote Sensing ESA SP* 247 315-319 (1985).

10. Vane, G., Chrisp, M., Enmark, H., Macenka, S., & Solomon, J. *Proc 1984 IEEE Int'l Geoscience and Remote Sensing Symposium ESA SP* 215 751-757 (1984).

11. Conel, J.E., Green, R. O., Alley, R.E., Bruegge, C.J., Carrere, V., Margolis, J., Vane, G., Chrien, T.G., Slater, P.N., Biggar, S.F., Teillet, P.M., Jackson, R.D., & Moran M.S. in *Recent Advances in Sensors, Radiometry, and Data Processing for Remote Sensing SPIE* 924 179-195 (1988).

12. Robinson, B.F., Bauer, M.E., Dewitt, D.P., Silva, L.F. & Vanderbilt, V.C. *SPIE* 196 8-15 (1979).

13. King, D.K. & Byrne, D.M. *J. Atm. Sci.* 33 2242-2251 (1976).

14. Goetz, A.F.H. in *Proceedings of the Third Airborne Imaging Spectrometer Data Analysis Workshop* (ed Vane, G.) *JPL Publication*

87-30 8-17 (1987).

15. Isaacs, R.G., Hoffman, R.N. & Kaplan, L.D. *Rev. Geophys.* 24(4) 701-743 (1986).

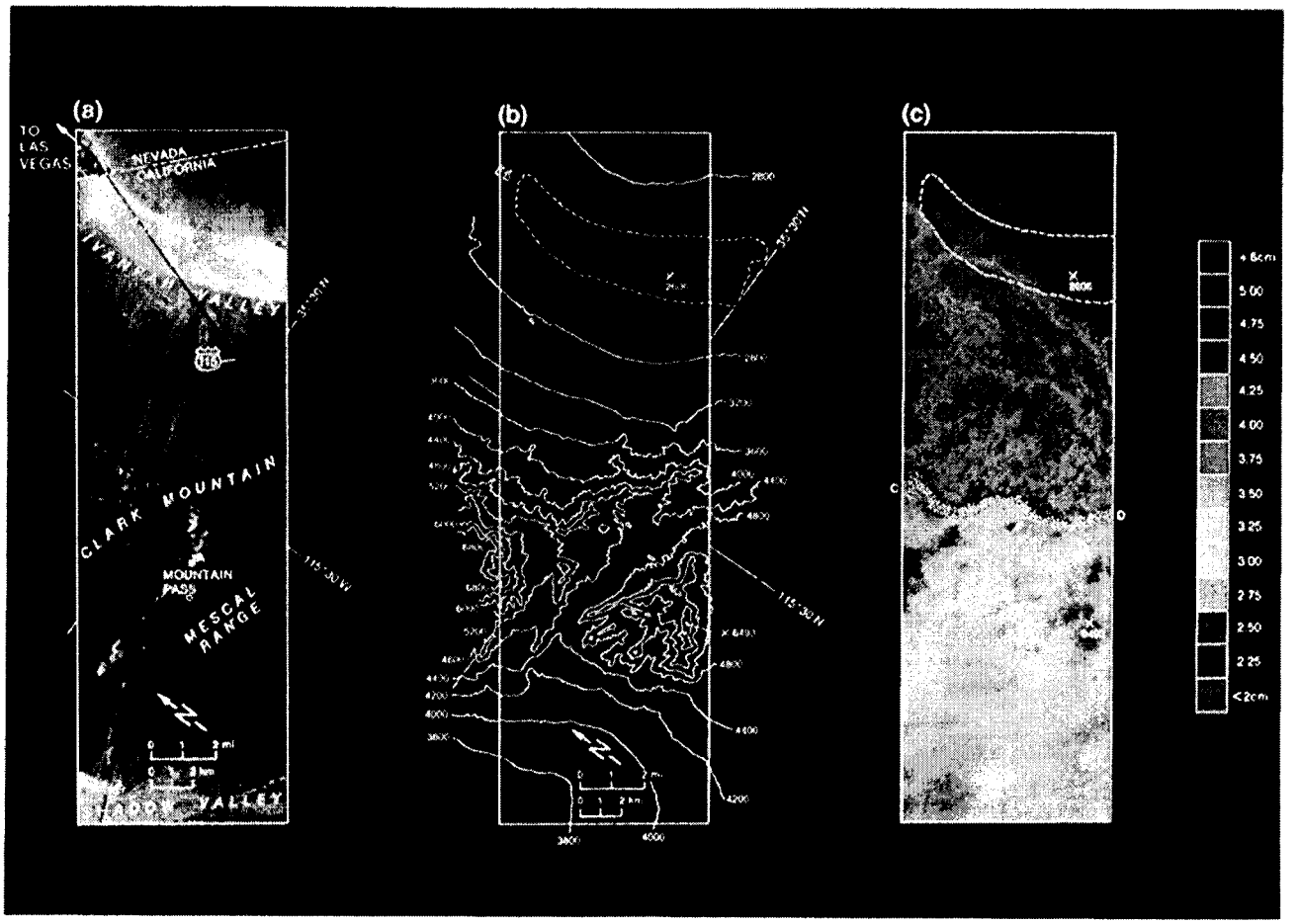


Figure 1. (Refer to slide No. 2.) (a) Three color composite image of the Mountain Pass site using 10 nm channels from AVIRIS, 1537 nm (red), 1051 nm (green), 672 nm (blue). The point (■) labeled A locates station where optical depth was determined; (■) B, a playa target used for inflight calibration of the instrument. (b) generalized topographic map of the site, (c) map of the distribution of precipitable water in cm (color scale at right) determined using the 940 nm atmospheric water band, and the radiance ratio L(940)/ L(870). Stippled region CD marks location of sharp change in mapped water abundance that may represent edge of water vapor boundary layer tapered against the topography.

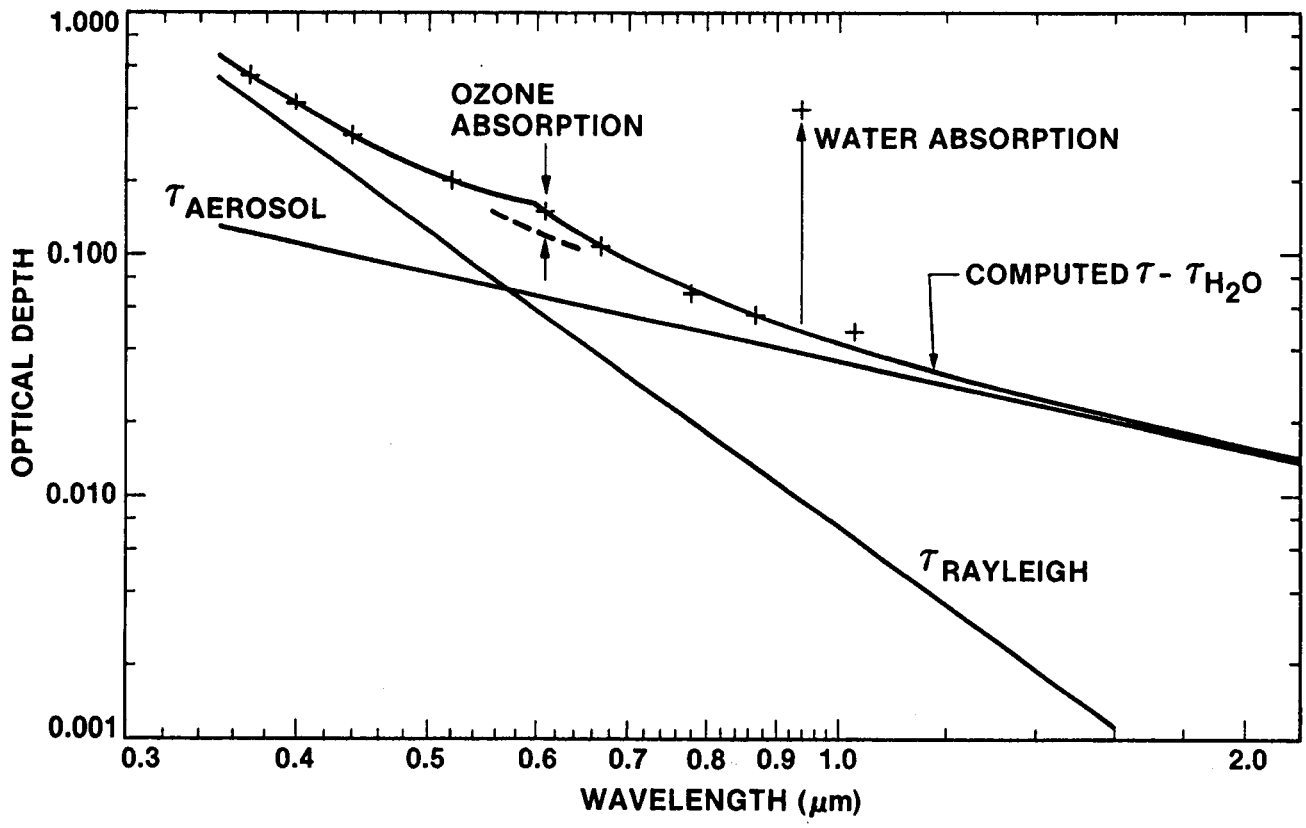


Figure 2. Atmospheric optical depth determined for the clear air conditions of July 30, 1987. (+) are measured points. Rayleigh optical depth $\tau_{RAYLEIGH}$ was computed from the measured atmospheric pressure (856 mb) at time of overflight, 10:15 AM, PST. The line $\tau_{AEROSOL}$ is generated as the best fit to the difference between the observed and Rayleigh optical depths. The ozone optical depth is derived as the difference between observed and sum of Rayleigh and Mie values. The resulting computed optical depth excludes absorption from atmospheric water vapor.

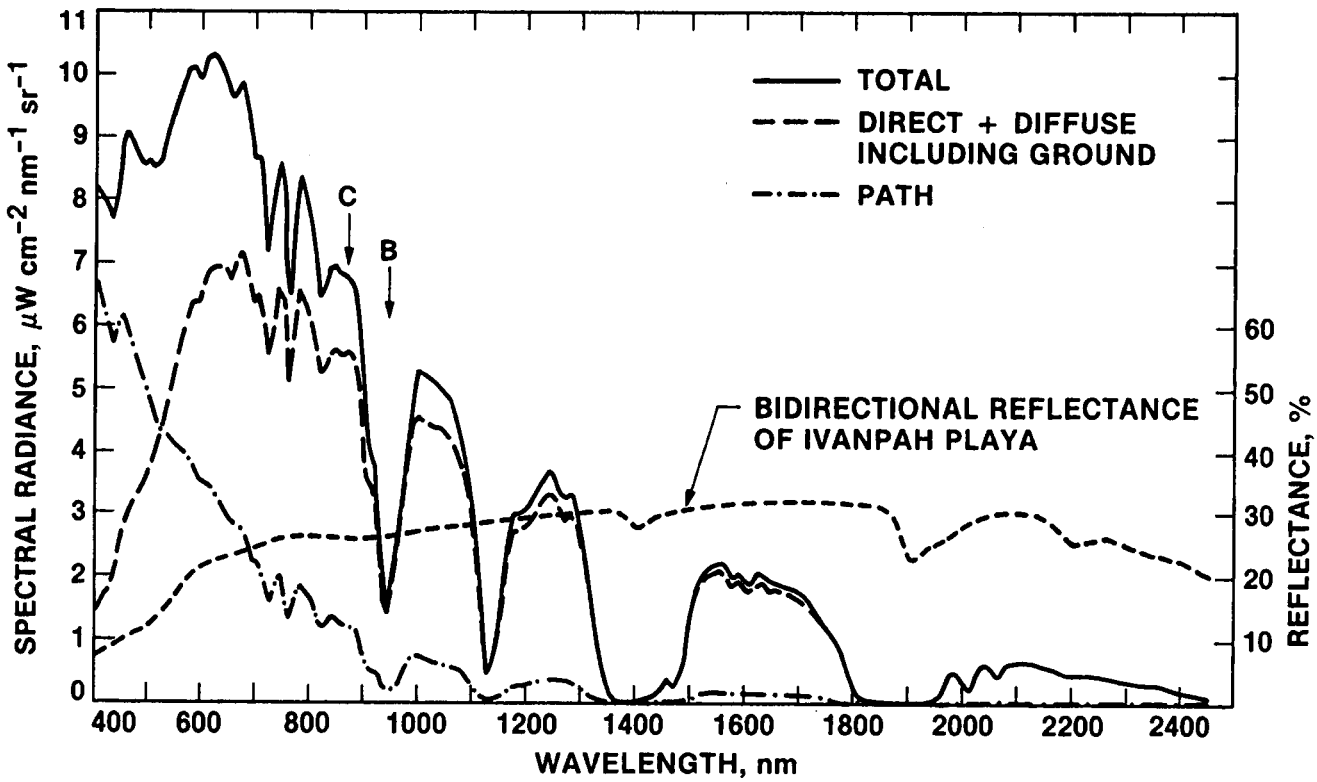


Figure 3. Total radiance, direct plus diffuse ground-reflected radiance, and path radiance generated from LOWTRAN 7 model at AVIRIS observational altitude and spectral resolution over Ivanpah Playa using the spectral reflectance measured at site B (Figure 1a). C and B mark central positions of band clusters used to generate band ratios that are calibrated in terms of atmospheric precipitable water abundances in Figure 1c.

# RADIOMETRIC PERFORMANCE OF AVIRIS: ASSESSMENT FOR AN ARID REGION GEOLOGIC TARGET

HUGH H. KIEFFER, ERIC M. ELIASON, KEVIN F. MULLINS, LAURENCE A. SODERBLOM, AND JAMES M. TORSON; U.S. Geological Survey, Flagstaff, Arizona, USA

ABSTRACT

Data from several AVIRIS flight lines were examined to assess instrument stability and response. Both scene and in-flight calibration data were analyzed statistically. The data clearly indicate that, although the instrument output was noisy and unstable at the time of data acquisition, valuable spectral signatures can still be extracted and analyzed. Some first order calibration corrections can be performed by forcing internal consistency within the data. AVIRIS data are delivered in band-interleaved-by-line format, but we have developed high-efficency routines which access the data as either image or spectral planes and enable effective statistical and visual examination of both AVIRIS scenes and ancillary files.

Two methods were used to extract spectral information from segment 4 of the Kelso Dunes flight. Both successfully identified at least three distinct spectral signatures, but neither has positively identified a specific material.

## INTRODUCTION

First, a detailed statistical analysis was performed on the various calibration files that accompany all AVIRIS flights for several 1987 targets (TABLE 1). Statistical parameters were collected for coherent and random noise patterns, offset and gain drifts, and intensity shifts; some or all of these problems exist in every flight line we investigated. These measures of performance were used to reject bands with low signal-to-noise ratios.

Table 1. Data Used in This Work

| Flight Target | Date | Data Used |
|---|---|---|
| Moffett Field | 6/25/87 | Calib. only |
| Mountain Pass | 7/30/87 | Calib. only |
| Hebro | 8/01/87 | Calib. only |
| Sierra Foothills | 9/14/87 | Calib. only |
| Kelso Dunes | 9/14/87 | Calib. & image |
| Lake Powell | 9/18/87 | Calib. only |
| Grand Canyon | 9/18/87 | Calib. & image |
| San Francisco Bay | 10/13/87 | Calib. & image |

NOISE LEVEL ANALYSIS

Pre- and post-flight calibration files were processed and average and standard deviation values were obtained for each of the four separate internal intensity levels (Figure 1). Histograms of raw DN and of the absolute second difference of the raw DN were generated. Using linear interpolation of the corresponding cumulative histograms, the 1 and 99 percentile points of the raw DN, and the median and mean absolute second difference were computed. Similiar routines were run on the dark current and image files for Segment 4 of the Kelso Dunes flight. All analyses were done on raw AVIRIS data.

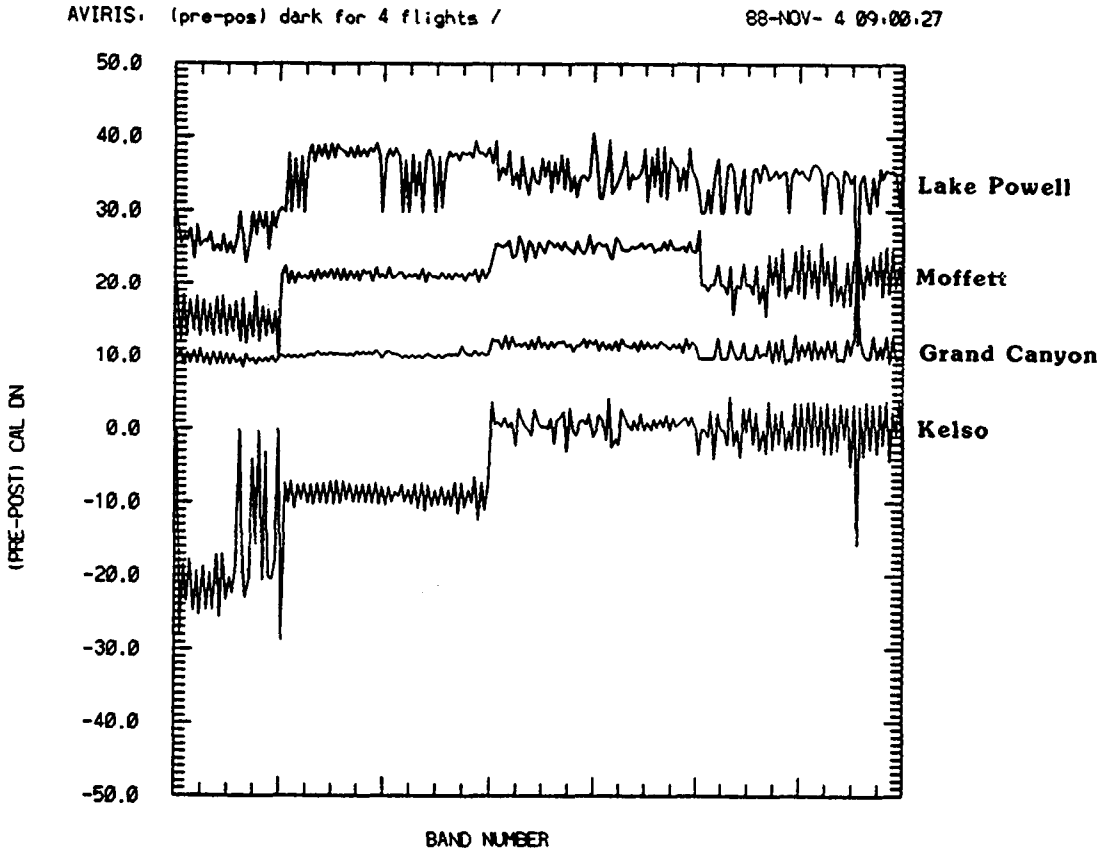


Figure 1. The difference between the pre- and post-calibration dark currents are compared for four AVIRIS flights. All four plots are actually centered on zero but each has been progressively offset vertically by 10 DN.

A simple measure of detector noise is one-half the median absolute value of the second difference (for Gaussian noise this is nearly identical to the standard deviation). This parameter varies strongly with detector, even within each of the four spectrometers. Typical values are 4.5, 2.5, 3.2, and 2.7 for spectrometers A, B, C and D, respectively. For the most responsive detectors in each spectrometer, the signal-to-noise ratio (SNR) for this measure of noise is approximately 150, 55, 100, and 60 for the four spectrometers. A revealing parameter is the "science-to-noise ratio", based on the variation of reflectivity within a scene,

ratioed to the noise level. This parameter is on the order of 20 to 30 for all four spectrometers.

There are several kinds of periodic noise within the AVIRIS data. In a wavelength "movie", waves with a period on the order of ten pixels flow across the image. In a uniform area (the ocean off the coast of Oregon) noise with the period of 14.16 pixels was shifted in phase by 10.5 samples between lines.

There are also several patterns of noise in the calibration data itself. The low-level pre-calibration data has an approximate square-wave pattern with amplitude of 4 to 6 DN with a period of 26 pixels. The dark level (1 pixel per line) shows high frequency noise, obvious, abrupt level shifts on the order of 5 pixels, and drifts on the order of a few DN per minute. In uniform scenes, some of the more obvious level shifts correspond to shifts in the dark current file.

## COHERENT NOISE

Coherent noise was modeled by Fourier transforms of a uniform AVIRIS subscene and on-board calibration data acquired during the Kelso Dunes flight. A subscene of the dune field provided a uniform flat-field target for study of coherent noise at brightness levels above dark current. The on-board calibration consisted of instrument data acquired with the fore-optics shutter closed and the internal calibration lamp either turned off providing dark current data, or at high and low intensity levels providing a flat-field at different instrument DN output levels.

A one-dimensional fast Fourier transform (FFT) was applied to 512 samples of a line for all 224 spectral channels. Because a uniform-radiance field was used, amplitudes of all the Fourier components can be attributed to either random or coherent Fourier noise (except zero frequency). Typical background-frequency amplitudes due to random noise for the four spectrometers fall within the range .5 to 1.0 DN for most detectors. Some of the detectors with a lower signal-to-noise ratio have noticably higher Fourier amplitudes at random frequencies. These include detectors 97, 113, 131 to 136, and 210.

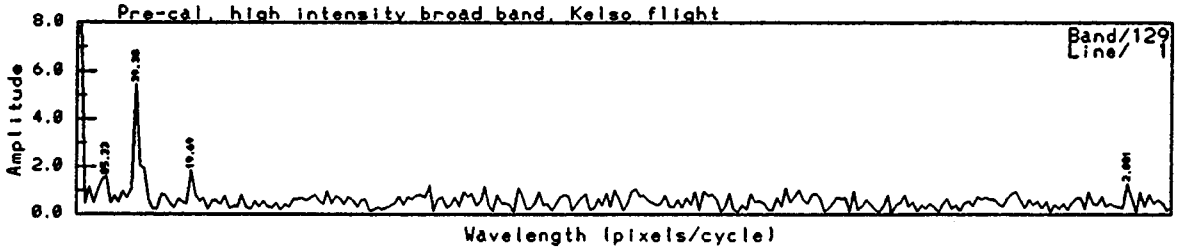


Figure 2. Fourier transform of the first 512 samples of a single scan line for detector C, band 129. The transform is of the Kelso Dunes flight pre-calibration data acquired with the fore-optics shutter closed and the internal calibration lamp at the high intensity level. Because a uniform-radiance field was used, the high-amplitude Fourier components can be attributed to coherent noise. The transform exhibits a sharp peak at 39.38 and 19.69 pixels/cycle and is typical of most of the detectors in spectrometer C.

The FFTs exhibited several sharp peaks well above background noise levels for the four spectrometers (see Table 2 and Figure 2). Because the coherent noise levels are approximately the same for the dark current calibration, low and high intensity lamp calibration, and image subscene, it is assumed to be an additive component to the signal and not a function of scene brightness.

In most cases all detectors of a spectrometer exhibited the same coherent noise frequency but with varying amplitude. Spectrometers A and B exhibited the lowest coherent noise levels of no larger than 2.0 DN amplitude. These noise patterns were not discernible above random noise levels when viewing a scene. Spectrometer D had slightly larger coherent noise levels of no larger than 4.0 DN amplitude. Visually, the 19.69 pixels/cycle coherent noise level was barely detectable above random noise levels in some detectors. Spectrometer C exhibited the greatest coherent noise levels and were visible well above the random noise levels. The 39.38 and 19.39 pixels/cycle coherent noise levels, having amplitudes as high as 8.0 and 4.0 DN respectively, were visible as oblique wave patterns.

TABLE 2. Summary of Fourier Transform Results

| Spectrometer | Noise Frequency (pixels/cycle) | Maximum Amplitude (Raw DN) | Comments |
|---|---|---|---|
| A | 19.69 | 1.8 | Greatest in detectors 13, 16, 19, 22, 24, 25, 28, 30. |
| | 2.12 | 2.0 | Present in all detectors but minimal in 10, 30, 31, 32. |
| B | 9.48 | 2.0 | Amplitude nearly uniform in all detectors. |
| | 5.70 | 1.8 | Amplitude nearly uniform in all detectors. |
| C | 39.38 | 8.0 | Greatest in detectors 126 to 146. Amplitude varies widely among detectors. |
| | 19.69 | 4.0 | Greatest in detectors 131,134, 139, 140, 145, 157. |
| D | 32.00 | 3.0 | Amplitude varies widely among detectors. |
| | 19.69 | 4.0 | Amplitude varies widely among detectors. |

WHITE-TARGET MODEL

An estimate of the expected response of AVIRIS to a uniform point target was computed based on the calibration file supplied by JPL, a nominal atmospheric transmission spectrum computed using LOWTRAN 7 (Alee, 1988), and the solar spectrum. This resulted in a "WHITE" spectrum that was used to convert AVIRIS data to surface reflectance (Kieffer, 1988). Although attempts to derive normalized calibrated spectra using the model gave poor results, the model was useful in estimating the quality of different spectral regions based on expected atmospheric transmission and instrument performance.

An estimate of the relative gain of each band was computed by developing a "reference" band composed of the sum of DN for a spectrally contiguous set of low-noise, high-gain bands. A comparision of the coefficient of a linear least-squares fit of the data from any band to this reference band with that predicted by the white-target model gives a direct indication of the change of response of each detector.

SOFTWARE DISPLAY TOOLS

Given the large quantity of data produced by the AVIRIS instrument, a new system of software was designed to handle cube-formatted data. The software runs on a DEC Microvax Graphics Workstation interfaced to an IVAS display system. The display program, QL3, allows the user to interactively examine a three-dimensional cube of image data. The cube is displayed in two adjacent segments. The left-hand segment is an image of the surface (x,y) at a particular wavelength band which is defined by the location of the cursor in the spectral (z) dimension. The right-hand side is a spectral image representing all y pixels and all z bands within an orthogonal plane whose x location is defined by the cursor. A graph of the full spectrum at the x,y pixel is displayed on the workstation. Band images can be displayed singly with numerous color-coded overlay planes, or as a three color composite. Various options include panning, pseudo-coloration, normalization, stretching and listings of current display values.

The cube display software is designed to run with a number of concurrent processes that share access to the data in memory. These concurrent processes enable one to interactively collect and manipulate spectral data and store the results of several such analyses in tabular form for later processing. For example, pixels that match a selected spectrum can be identified and used to produce a thematic map or mask. A series of these thematic images, which may be color coded, can be overlaid on the original image to delineate (or mask out) areas with specific spectral characteristics.

DATA ANALYSIS

An attempt to extract subtle spectral variations along surfaces within the scene by suppressing instrument gain and offset errors and spectral variation in atmospheric transmission was made using the linear fit coefficients of each band to the "reference" band mentioned above. For each band, the response at each pixel was adjusted by the deviation of the reference band, at that pixel,

from the reference band average and scaled by the slope of the linear correlation between this band and the reference band. This process removed the instrument dark level and atmospheric additive terms, and variation in instrumental gain, solar spectral radiance and atmospheric transmission. It does not amplify noise, but it does remove any correlation of spectral signature with the local incidence angle. To whatever extent the reference bands do not represent the spectrally averaged brightness of surface materials, this process has the unfortunate characteristic of magnifying the spectral signature of the reference bands.

A second technique was developed to remove the instrument and atmospheric effects without use of any absolute calibration and was applied to a portion of the Kelso Dunes data set (Soderblom et al., in preparation). This process deals separately with the additive and multiplicative errors inherent in the AVIRIS data so that psuedo-spectral signals are not created by the normalization of the additive component.

The white-target spectrum mentioned earlier was used to mask out spectral regions of low response. Next, bands with excessive noise or data clipping were identified and deleted. The next step involved a process to detect and delete noisy spectra, with any spectrum being deleted that had a mean-squared deviation from both its left and right neighbors greater than 10 DN. If two spectra compared within this tolerance, then their average was stored. This cleaned-up data set was then used to generate histograms of all remaining channels and to compute the first and third quartiles. Finally, a linear stretch was applied to each spectral channel, that scaled the widths and centroids of all histograms to coincide. The signatures in the resulting spectra are dominated by the spectral character of the surface, not the spectral nature of the instrument or atmosphere. This process considerably improves the ability to discern individual ground units. We are now in the process of comparing the normalized spectral features identified in this manner with absolute laboratory spectra.

REFERENCES

Alee, Ron, Feb. 2, 1988, Personal communication.

Kieffer, H. H., April 19, 1988, Memorandum to AVIRIS project scientist.

Soderblom, L. A. et al., in preparation, Data-Dependent Approaches For Correction and Analysis of AVIRIS Data

# ZONES OF INFORMATION IN THE AVIRIS SPECTRA

PAUL J. CURRAN, NASA/Ames Research Center, Moffett Field, CA 94035, USA; JENNIFER L. DUNGAN, TGS Technology Inc., NASA/Ames Research Center, Moffett Field, CA 94035, USA.

## ABSTRACT

To make the best use of Airborne Visible/Infrared Imaging Spectrometer (AVIRIS) data an investigator needs to know the ratio of signal to random variability or 'noise' (S/N ratio). The signal is land-cover dependent and decreases with both wavelength and atmospheric absorption and random noise comprises sensor noise and intra-pixel variability. The three existing methods for estimating the S/N ratio are inadequate as typical 'laboratory' methods inflate, while 'dark current' and 'image' methods deflate the S/N ratio.

We propose a new procedure called the 'geostatistical' method. It is based on the removal of periodic noise by 'notch filtering' in the frequency domain and the isolation of sensor noise and intra-pixel variability using the semi-variogram. This procedure was applied easily and successfully to five sets of AVIRIS data from the 1987 flying season.

## INTRODUCTION

To optimize the use of Airborne Visible/Infrared Imaging Spectrometer (AVIRIS) data there is a need to know the random variability or 'noise' associated with the sensor's signal. This information is required by the user community, as spectral zones of high and low noise will be common to each land-cover and by every investigator, as noise determines the accuracy with which absorption features can be distinguished in the spectra and objects can be detected on the ground. Noise alone is not a very useful measure, as a given level of noise will have a more deleterious effect on data quality if the signal is low. Therefore, the signal to noise, (S/N) ratio, which can be estimated by the ratio of the signal's mean ($\bar{x}$) to its standard deviation (s), will be used here.

The major part of the noise in the AVIRIS signal is additive to the signal and the signal decreases sharply with both an increase in wavelength and atmospheric absorption. Consequently, plots of S/N ratio versus wavelength will be similar in form to signal versus wavelength for each land-cover under investigation.

The aim of the work reported here was to develop a procedure for estimating the per-waveband S/N ratio of AVIRIS data.

ESTIMATING THE S/N RATIO OF AVIRIS DATA

AVIRIS data contain periodic (coherent) sensor noise, that can be removed and random noise that cannot. The noise of relevance to the investigator is random noise: the random sensor noise, which is image independent and intra-pixel variability, which is a result of spatially heterogeneous pixel contents and is image dependent. Unfortunately, methods commonly used to estimate the S/N ratio of remotely sensed imagery (termed for convenience 'laboratory,' 'dark current' and 'image') do not isolate this random noise for the investigator (Table 1).

Table 1. Existing methods for estimating the S/N ratio of AVIRIS data showing the level of signal and type of noise to be estimated. As an investigator's spectra can be free of periodic noise and inter-pixel variability a S/N ratio is required that contains only random sensor noise and intra-pixel variability. Therefore, these three methods either underestimate or overestimate the S/N ratio required by the investigator.

| Method | Signal level | Type of noise | | | | Estimated S/N ratio in relation to that required by investigator | Two examples from these proceedings |
|---|---|---|---|---|---|---|---|
| | | Periodic | Random | | | | |
| | | Sensor noise | Sensor noise | Intra-pixel variability | Inter-pixel variability | | |
| 'Laboratory' | Artificially high | x | x | | | Higher | Vane<br>Porter |
| 'Dark current' | Natural | x | x | x | | Lower | Abrams and Carerre<br>Vane and Green |
| 'Image' | Natural | x | x | x | x | Lower | Conel et al.<br>Clark |

A typical 'laboratory, method uses the $\bar{x}$ and s of a homogeneous surface with a high (e.g., 50%) albedo to estimate the S/N ratio for only a few wavebands. The presence of periodic noise will decrease the measured S/N ratio below that required by the investigator (see above) but this is more than compensated by the omission of intra-pixel variability and more importantly, by the use of an artificially high signal. A typical 'dark current' method uses variation (e.g., s) in the signal dark currents as a measure of noise. This value includes periodic noise which deflates the S/N ratio below that required by the investigator. A typical 'image' method uses the $\bar{x}$ and s of four, or more, visually homogeneous pixels as an estimate of the S/N ratio. The

resultant value is deflated below that required by the investigator, for it includes periodic noise (this could have been removed) and inter-pixel variability, which even on a visually homogeneous area can be around 2% of $\bar{x}$ (Conel et al., 1987).

To estimate the S/N ratio of the investigator's data a new procedure is proposed and this we have termed the 'geostatistical' method.

## THE 'GEOSTATISTICAL' METHOD FOR ESTIMATING THE S/N RATIO

Following the removal of periodic noise there is a need to estimate random noise, free of inter-pixel variability (Table 1). We therefore require an estimate of variability at a pixel and a tool to do this is the semi-variogram (Curran, 1988). This is produced from a transect of pixels where the radiance z, at pixel number x along the transect has been extracted at regular intervals and where x = 1, 2, ..., n. The relation between a pair of pixels, h intervals apart (the lag distance) can be given by the variance of the differences between all such pairs. This value, the semi-variance y(h), for pixels at distance h apart is given by half the expectation E of their squared difference,

$$y(h) = 1/2\ E[z(x_i)-z(x_i+h)]^2 . \qquad (1)$$

Within the transect there will be m pairs of observations separated by the same lag, this is estimated by,

$$\bar{S}^2 = 1/2m \sum_{i=1}^{m} [z(x_i)-z(x_i+h)]^2 . \qquad (2)$$

$\bar{S}^2$ is an unbiased estimate of the semi-variance, y(h), in the population (Webster, 1985) and is a useful measure of the difference between spatially separate pixels (Jupp et al., 1988). The larger $\bar{S}^2$ is and therefore y(h), the less similar the pixels will be. The semi-variogram is a plot of the function that relates semi-variance to lag (Fig. 1) and is described in Webster (1985) and Curran (1988). Three aspects of the semi-variogram are of interest here: (s) sill, the asymptotic upperbound value of y(h); (Co) nugget variance, the limit of y(h) when h approaches 0 and (C) spatially dependent structural variance, the sill minus nugget variance. By definition y(h)=0 when h=0 (Journal and Huijbregts, 1978), in practice however the limit of y(h) when h approaches 0 is positive because the nugget variance represents variability at scales smaller than a pixel.

The nugget variance is a sound estimate of spatially independent image noise at the scale of a pixel as it comprises random sensor noise and intra-pixel variability. The square root of this variance can be used to estimate the standard deviation of the random noise and thereby the S/N ratio of AVIRIS data,

$$\text{S/N ratio} \simeq \bar{x}/\sqrt{Co} . \qquad (3)$$

The assumptions underlying the use of nugget variance as an estimate of random noise are summarized in Table 2.

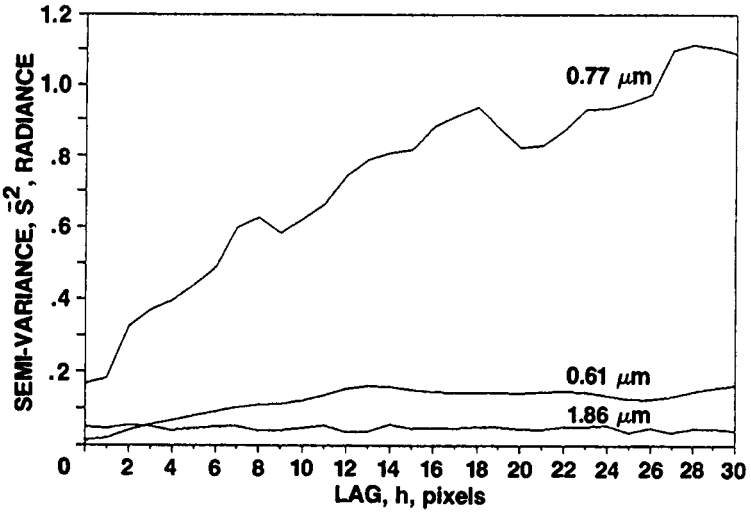


Fig. 1. Semi-variograms for three wavebands of AVIRIS data recorded for a plantation forest near Gainesville, Florida (Table 3).

Table 2. Assumptions in the use of nugget variance as an estimate of random noise (random sensor noise and intra-pixel variability) in AVIRIS data.

| Assumption | Explanation or reason | Comments on assumptions in relation to AVIRIS data |
|---|---|---|
| Stationarity | Spatial dependence of pixels is a function of lag and not location. | Generally true within a land cover. |
| Isotropy | Nugget variance is independent of transect direction. | Untrue, due to gain and offset variability therefore use row or column transects. |
| Fixed spatial resolution | Intra-pixel variability and therefore nugget variance is dependent upon spatial resolution. | True. |
| Scene does not contain random information. | Random features in scene increase nugget variance and could contain information. | Generally true but need to check. |
| Nugget variance is independent of spatially dependent structural variance. | Limit of y(h) when h approaches 0 has minor dependence upon the slope of the semi-variogram. | Untrue, but point-spread-function of sensor ensures that y(h) when h approaches 0 is similar to that at small lags and so the effect of this violation is minimal. |

THE 'GEOSTATISTICAL' METHOD FOR ESTIMATING THE S/N RATIO OF AVIRIS DATA

Application of the 'geostatistical' method involved two stages, first, data selection and preprocessing and second, estimation of the S/N ratio for each waveband of AVIRIS data.

Selection and preprocessing of AVIRIS data

Five AVIRIS data sets were selected (Table 3). They were recorded around solar noon, over a wide range of dates and land-covers. All data were converted from grey levels to radiance and radiometrically calibrated at JPL (Vane et al., 1987) and on receipt dropped scan lines were replaced with the means of adjacent lines.

Table 3. AVIRIS data for which the S/N ratio was estimated.

| Location | Land-cover of interest | Date of data acquisition (1987) | Time of data acquisition (start, hrs.) |
|---|---|---|---|
| Mountain View, California | Sediment-laden water | 25 June | 12:40 |
| Gainesville, Florida | Plantation forest | 4 July | 11:49 |
| Yuba City, California | Bare soil | 30 July | 12:49 |
| Metolius, Oregon | Semi-natural forest | 1 August | 11:14 |
| Cuprite, Nevada | Bare soil | 14 September | 11:14 |

The 1987 AVIRIS data contained considerable periodic noise, produced by the inadvertent coupling of the image signal with electrical and mechanical signals. This noise was dominated by frequencies around two pixels per cycle and increased in severity as the season progressed (Fig. 2). The major periodic noise frequencies were removed by 'notch filtering' in the frequency domain of the image (similar to Hlavka, 1986) (Table 4, for method). By comparison with prefiltered spectra this removal of major periodic noise made no difference to the relative radiometry and by comparison with prefiltered semi-variograms it reduced considerably the spatially dependent structural variance (C). The visual effects of such filtering are illustrated in Figs. 3 to 7 for the waveband centered at 1.018 μm. The success of this preprocessing was attributed to: (i) clarity of the noise, especially from 0.68 to 1.27μm (a result of low gain) and 1.84-2.40 μm (a result of low signal); (ii) clarity of the major periodic noise spikes in the vertical component of the frequency domain; (iii) spectrometer-independence of the major periodic noise frequencies and (iv) relatively homogeneous

sub-scenes with little chance of 'ringing' (crenulated tonal boundaries) in the filtered images (Moik, 1980).

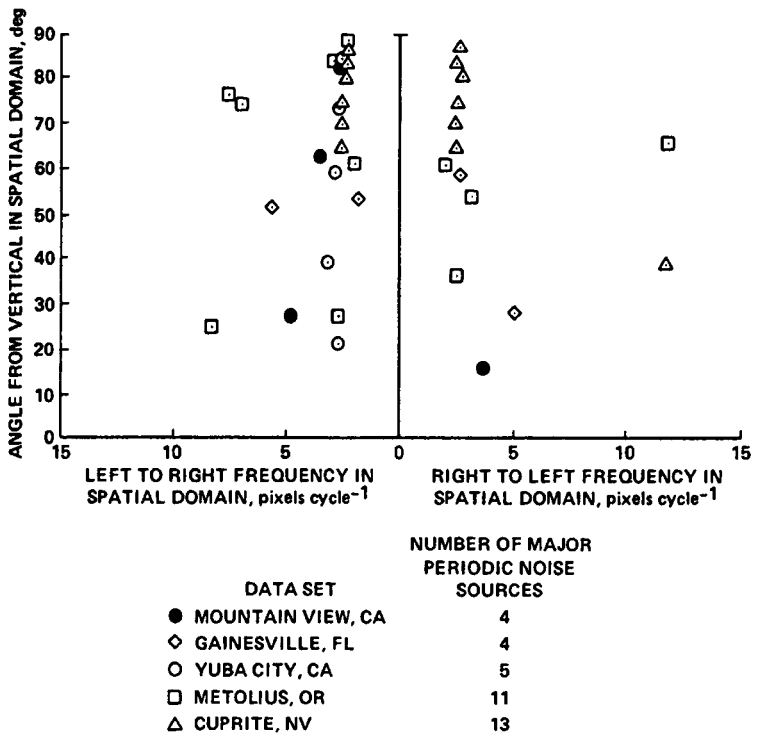


Fig. 2. The major types of periodic noise observed in five sets of AVIRIS data (Table 3). The noise characteristics were determined from the location of major periodic noise spikes in the frequency domain.

Table 4. Removing the major periodic noise in AVIRIS data.

| Stage | Procedure |
|---|---|
| 1 | Select 256 x 256 pixel sub-scene in one waveband. |
| 2 | Use fast Fourier transform to create a frequency domain image; major periodic noise appears as a series of spikes, each representing energy concentration at a specific frequency. |
| 3 | Design a 'notch filter', 0's represent the location of major periodic noise spikes and 1's represent the remainder; multiply by frequency domain image to create a new frequency domain image without major periodic noise spikes. |
| 4 | Invert filtered frequency domain image to create spatial domain image with no major periodic noise. |
| 5 | Repeat 4 on selected wavebands from each spectrometer. Define spectrometer-independent notch filter and use to filter all AVIRIS wavebands. |

## Estimating the S/N ratio for each waveband of AVIRIS data

The procedure for estimating the S/N ratio for each waveband of AVIRIS data is given in Table 5 and the results in Figs. 3 to 7. As was noted in the introduction, noise varies little with wavelength but the signal drops sharply with both an increase in wavelength and atmospheric absorption. As a result the first-order forms of the S/N ratio plots (Figs. 3 to 7) were signal dependent. The spectral zones of very high S/N ratio were green/red (0.50-0.70μm) for water and soil and near infrared (0.95-1.10μm) for vegetation. The spectral zones of high S/N ratio were blue for water and soil (0.40-0.50μm), green/red (0.50-0.70μm) for vegetation and near infrared (0.85-0.90, 0.95-1.10μm) for vegetation and soil respectively. The spectral zones of medium S/N ratio were blue (0.40-0.50μm) for vegetation and the near infrared regions (0.70-0.85μm) for water and vegetation, (0.85-0.95μm) for water and soil, (0.90-0.95μm) for vegetation and (0.95-1.10μm) for water. The regions of low and very low S/N ratio were near and middle infrared wavelengths in zones of low signal, either at long wavelengths or in atmospheric absorption bands. These spectral zones of S/N ratio are a useful summary of the utility of specific AVIRIS wavelengths from the 1987 flight season. Of more importance is the potential use of the 'geostatistical' method by individual investigators to plan for the restrictions that random noise places on the analysis of AVIRIS data.

Table 5. Estimating the S/N ratio in AVIRIS data.

| Stage | Procedure |
|---|---|
| 1 | Locate three row transects within a land-cover, each transect 75-100 pixels long to ensure that the statistically significant first fifth of the semi-variogram is at least 15 lags. |
| 2 | Calculate the mean signal ($\bar{x}$) and semi-variogram for each waveband. |
| 3 | Determine the nugget variance (Co) by extrapolating the slope of y(h)/h for each waveband. (Here the extrapolation was based on a linear fit over 8 lags, Fig. 1). |
| 4 | Plot $\bar{x}/\sqrt{Co}$ versus wavelength and $\bar{x}$ (with a $\sqrt{Co}$ envelope) versus wavelength as two representations of the S/N ratio (Figs. 3 to 7). |

## CONCLUSIONS

A new prodedure, that we have called the 'geostatistical' method, was used to estimate the S/N ratio of five sets of AVIRIS data. This method was designed around the needs of the AVIRIS investigator and has the following advantages: (i) it estimates only noise that is relevant to the investigator, unlike the existing 'laboratory,' 'dark current' and 'image' methods, (ii) it requires acceptable assumptions and (iii) is easy to apply.

Removal of major periodic noise

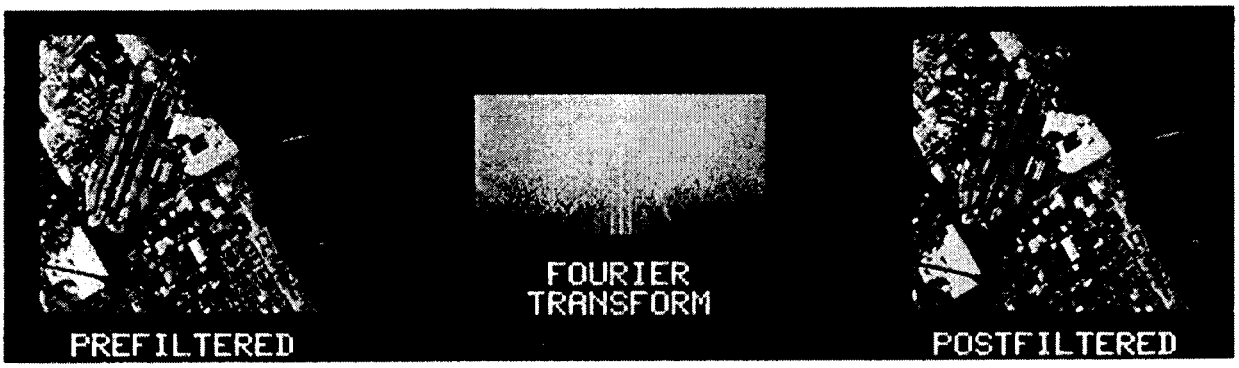


Representations of the S/N ratio

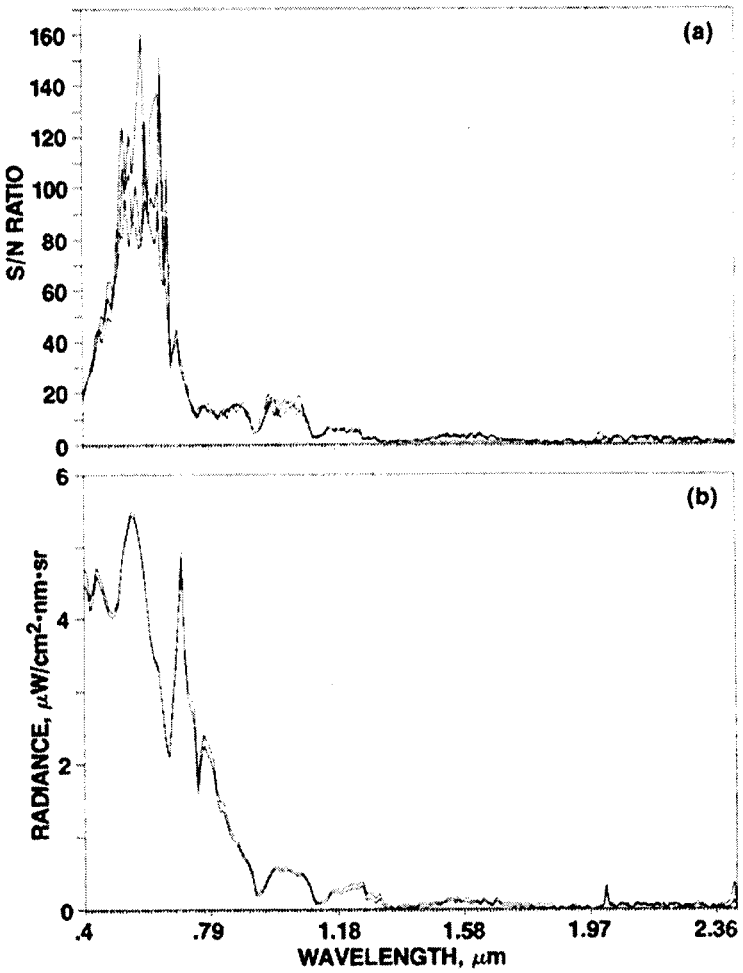


Fig. 3. Estimating the S/N ratio for sediment-laden water in the AVIRIS data of Mountain View, California (Table 3). Above: removal of major periodic noise by 'notch filtering' in the frequency domain. Below: (a) the S/N ratio versus wavelength and (b) the signal, with noise envelope, versus wavelength for three image transects.

Removal of major periodic noise

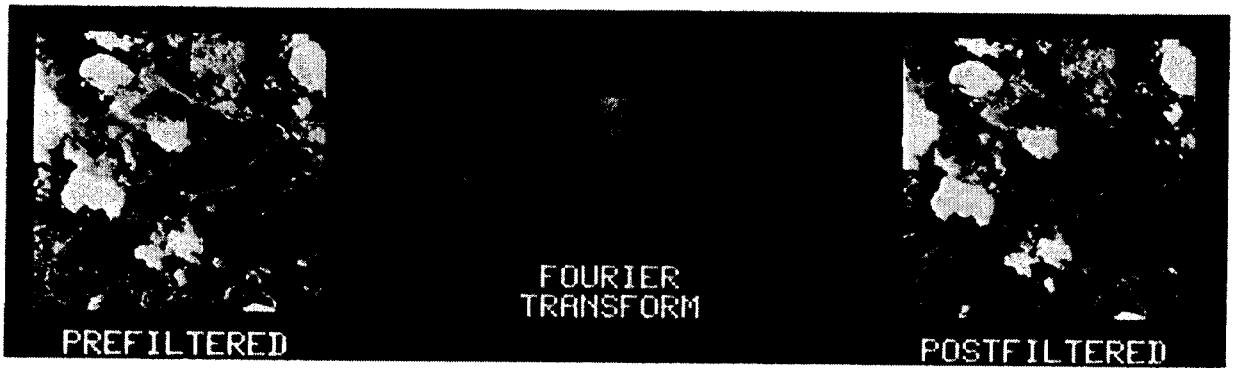


Representations of the S/N ratio

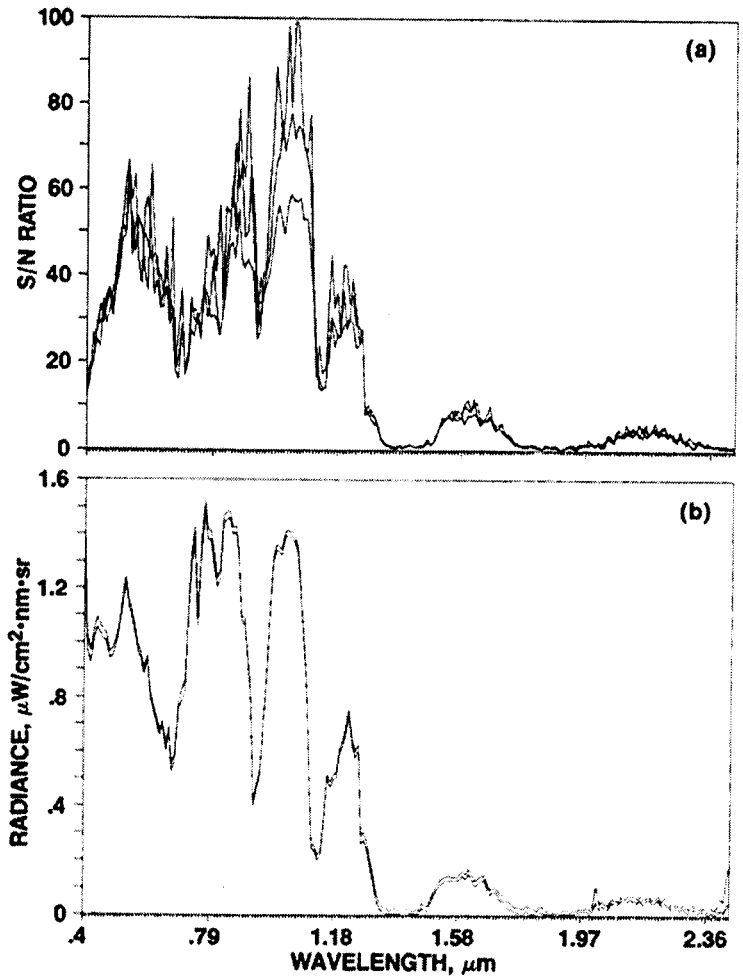


Fig. 4. Estimating the S/N ratio for a plantation forest in the AVIRIS data of Gainesville, Florida (Table 3). Above: removal of major periodic noise by 'notch filtering' in the frequency domain. Below: (a) the S/N ratio versus wavelength and (b) the signal, with noise envelope, versus wavelength for three image transects.

Removal of major periodic noise

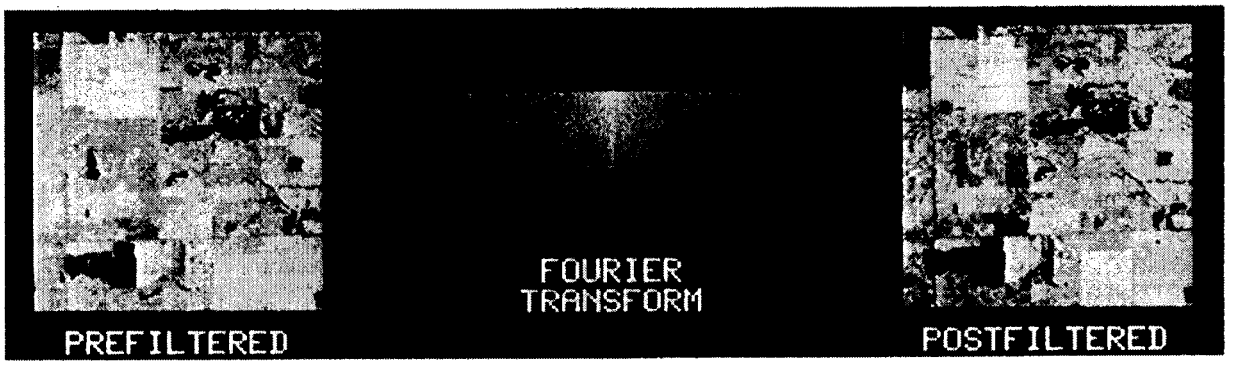


Representations of the S/N ratio

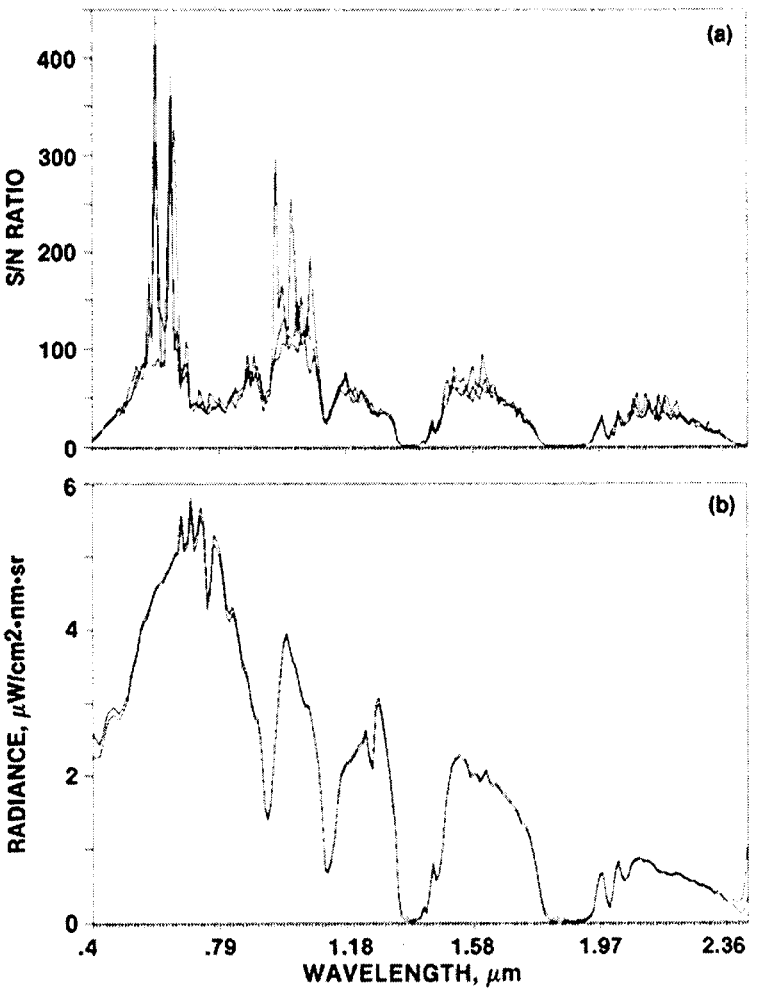


Fig. 5. Estimating the S/N ratio for bare soil in the AVIRIS data of Yuba City, California (Table 3). Above: removal of major periodic noise by 'notch filtering' in the frequency domain. Below: (a) the S/N ratio versus wavelength and (b) the signal, with noise envelope, versus wavelength for three image transects.

Removal of major periodic noise

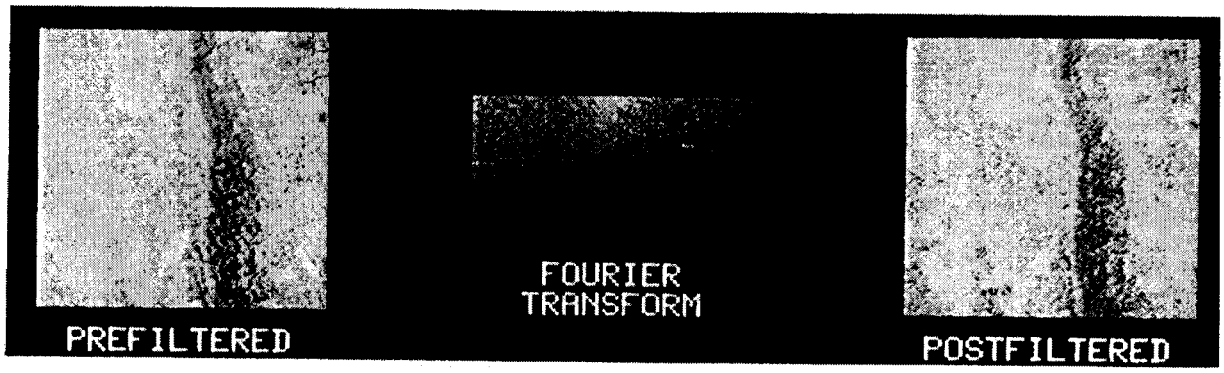


Representations of the S/N ratio

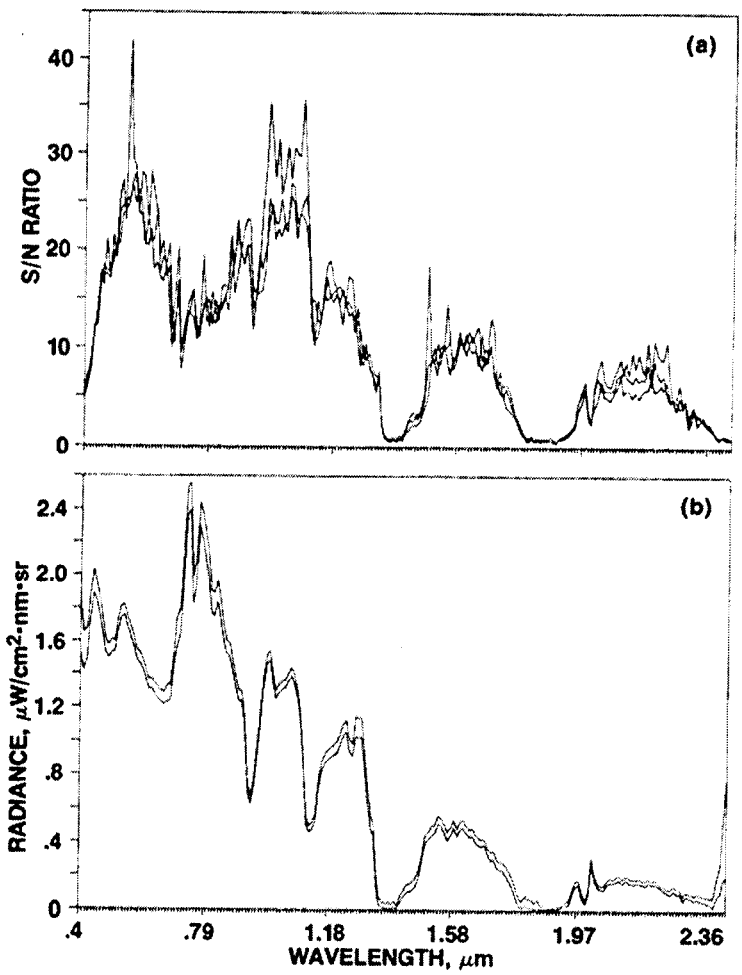


Fig. 6. Estimating the S/N ratio for semi-natural forest in the AVIRIS data of Metolius, Oregon (Table 3). Above: removal of major periodic noise by 'notch filtering' in the frequency domain. Below: (a) the S/N ratio versus wavelength and (b) the signal, with noise envelope versus wavelength for three image transects.

Removal of major periodic noise

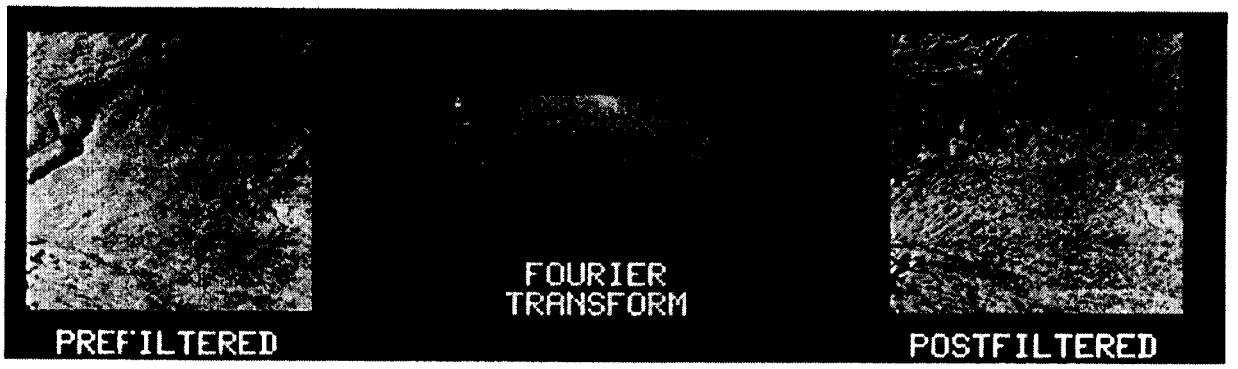


Representations of the S/N ratio

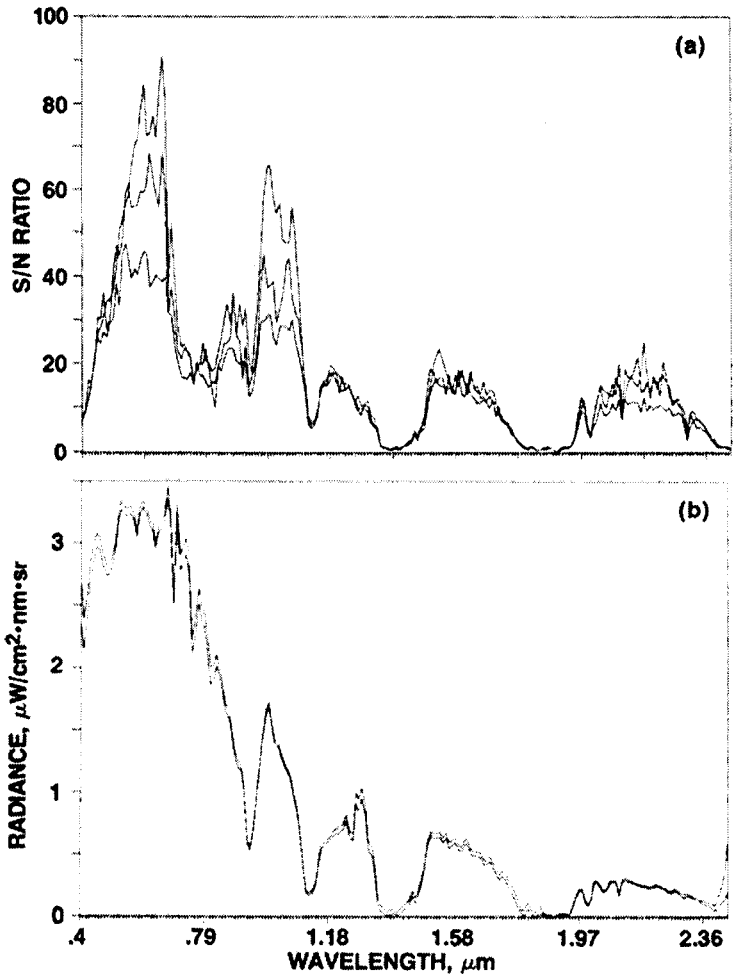


Fig. 7. Estimating the S/N ratio for bare soil in the AVIRIS data of Cuprite, Nevada (Table 3). Above: removal of major periodic noise by 'notch filtering' a fast Fourier transform. Below: (a) the S/N ratio versus wavelength and (b) the signal, with noise envelope, versus wavelength for three image transects.

ACKNOWLEDGEMENTS

This work was funded by NASA Earth Sciences and Applications Division under grant 677-21-35 and was conducted while PJC held a Senior NRC/NASA Research Associateship at NASA/Ames. The authors wish to thank Dave Peterson, Nancy Swanberg and Byron Wood (NASA/Ames) for access to their AVIRIS data and Sara Bzik, Don Card, Chris Hlavka, Dave Peterson and Vern Vanderbilt (NASA/Ames), Wally Porter and Gregg Vane (NASA/JPL), Alex Goetz (University of Colorado), Dave Myers (EROS Data Center), Peter Atkinson (Sheffield University) and Steve Briggs (NERC) for very helpful discussions.

REFERENCES

Conel, J.E., Green, R.O., Vane, G., Bruegge, C.J., Alley, R.E. and Curtiss, B.J. 1987. Airborne Imaging Spectrometer-2: radiometric spectral characteristics and comparison of ways to compensate for the atmosphere. In Imaging Spectrometry II (G. Vane ed.). SPIE Proceedings 834. Society of Photo-Optical Instrumentation Engineers, Bellingham, Washington: 140-157.

Curran, P.J. 1988. The semivariogram in remote sensing: an introduction. Remote Sensing of Environment, 24: 493-507.

Hlavka, C. 1986. Destriping AIS data using Fourier filtering techniques. In Proceedings of the Second Airborne Spectrometer Data Analysis Workshop (G. Vane and A.F.H. Goetz eds). JPL Publication 86-35. Jet Propulsion Laboratory, Pasadena: 74-80.

Journel, A.G. and Huijbregts, C.J. 1978. Mining Geostatistics. Academic Press, London.

Jupp, D.L.B., Strahler, A.H. and Woodcock, C.E. 1988. Autocorrelation and regularization in digital images. I Basic theory. IEEE Transactions on Geoscience and Remote Sensing, 26: 463-473.

Moik, J.G. 1980. Digital Processing of Remotely Sensed Images. NASA SP-431. National Aeronautics and Space Administration, Washington DC.

Vane, G., Chrien, T.G., Miller, E.A. and Reimer, J.H. 1987. Spectral and radiometric calibration of the Airborne Visible/Infrared Imaging Spectrometer. In Imaging Spectrometry II (G. Vane ed.). SPIE Proceedings 834. Society of Photo-Optical Instrumentation Engineers, Bellingham, Washington: 91-105.

Webster, R. 1985. Quantitative spatial analysis of soil in the field. Advances in Soil Science, 3: 1-70.

# CALIBRATION AND EVALUATION OF AVIRIS DATA: CRIPPLE CREEK IN OCTOBER 1987

ROGER N. CLARK,
BARRY J. MIDDLEBROOK, GREGG A. SWAYZE, K. ERIC LIVO,
DAN H. KNEPPER, TRUDE V.V. KING, and KEENAN LEE
U.S. Geological Survey, MS 964
Box 25046 Federal Center
Denver, CO 80225-0046
(303) 236-1332

## ABSTRACT

Airborne Visible/Infrared Imaging Spectrometer (AVIRIS) data were obtained over Cripple Creek and Canon City Colorado on October 19, 1987 at local noon. Multiple ground calibration sites were measured within both areas with a field spectrometer and samples were returned to the laboratory for more detailed spectral characterization. The data were used to calibrate the AVIRIS data to ground reflectance. Once calibrated, selected spectra in the image were extracted and examined, and the signal to noise performance was computed. Images of band depth selected to be diagnostic of the presence of certain minerals and vegetation were computed. The AVIRIS data were extremely noisy, but images showing the presence of goethite, kaolinite and lodgepole pine trees agree with ground checks of the area.

## INTRODUCTION

As part the NASA Airborne Visible/Infrared Imaging Spectrometer (AVIRIS) Investigators program, AVIRIS data were obtained over Cripple Creek and Canon City, Colorado, on October 19, 1987 at local noon. This paper describes analysis for Cripple Creek. The mineralogy of the Cripple Creek/Canon City area is varied and contains appropriate minerals for testing the spectral characteristics of AVIRIS. The region contains Tertiary volcanic rocks and Precambrian metamorphic and plutonic rocks, including areas of well-known alteration and mineralization. There are specific sites containing the minerals kaolinite, montmorillonite, gypsum, calcite, dolomite, jarosite, hematite, goethite, biotite, and muscovite that are large enough in extent to be resolved by AVIRIS. Exposures of rocks containing other OH-bearing minerals are also present.

The October 19th flight was the second to last of the AVIRIS flight season, and it was known that instrument performance had degraded somewhat (e.g. Vane and others, this volume). Our goal was to calibrate the AVIRIS data to ground reflectance (atmospheric absorptions and solar flux removed) and to use the calibrated data to evaluate mineral mapping capabilities. This initial investigation reports on 552 scan lines of AVIRIS data (614 pixels wide) centered on the towns of Cripple Creek and Victor, Colorado (Figure 1 and Slide No. 3).

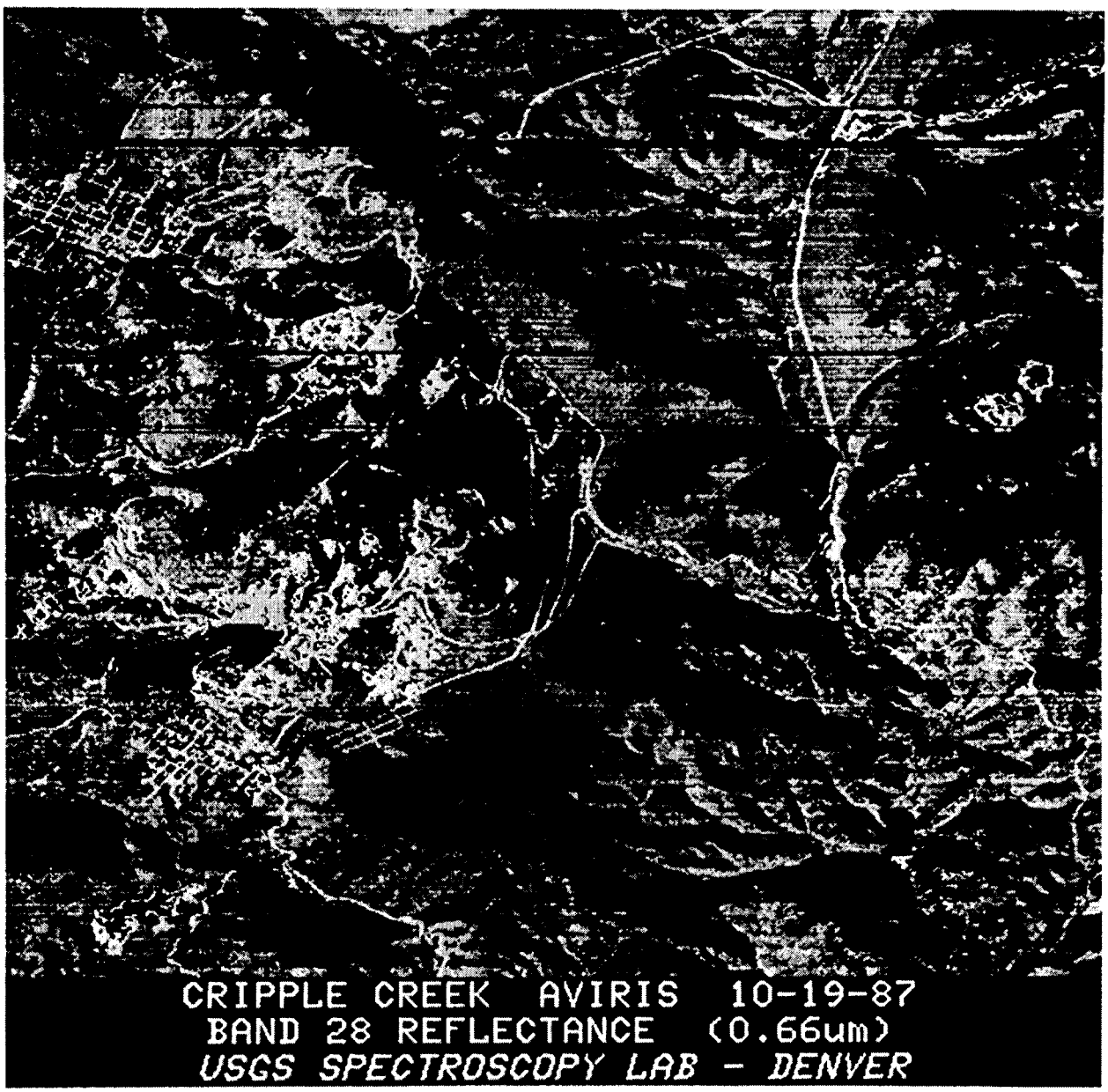


**Figure 1.** A visible reflectance image from channel 28 (0.66 $\mu$m) of the AVIRIS data over Cripple Creek, Colorado. The scene is 614 pixels wide by 552 lines long, covering an area of 11 by 10 km.

## CALIBRATION

Two concerns about the standard JPL processing of the AVIRIS data (Reimer *et al.*, 1987) were addressed. First and foremost was the spectral interpolation to a uniformly spaced wavelength set. Second was the smoothing of variations in the dark signal by averaging 101 scan lines of dark data.

Spectral interpolation can cause apparent shifts in band position of up to ½ channel. In practice, such shifts would only be significant for the sharpest absorption bands. More importantly, interpolation of data that includes a bad channel would result in two bad channels. AVIRIS does have noisy channels (e.g. see Vane and others, this volume). For these reasons, and because our software, the SPECtrum Processing Routines (SPECPR) (Clark, 1980), handles any wavelength set with any spacing, we were able to process noninterpolated data. Another advantage to using SPECPR is that our spectral library, which is in SPECPR format, has been measured at a spectral resolution higher than that for AVIRIS and then convolved to the AVIRIS resolution and sampling interval. SPECPR is not an imaging system, however, so that once the spectral analysis is complete, images are extracted and moved to our standard image processing system for further analysis and display.

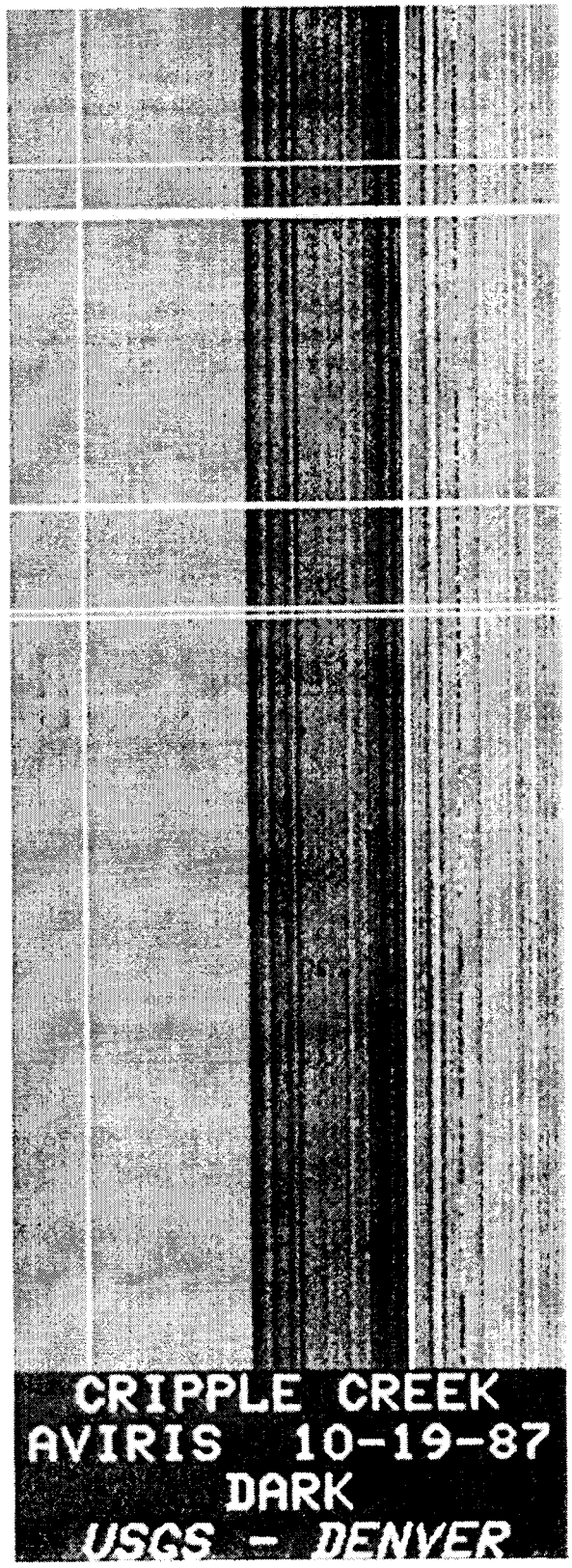


→

**Figure 2.** The image of the dark data from the scene in Figure 1. The image is 224 pixels across, corresponding to the 224 spectral channels and 552 lines long, corresponding to the 552 lines in Figure 1. The four vertical regions correspond to the four spectrometers in the AVIRIS instrument and wavelength increases from left to right. The white horizontal bands are dropped lines. The diagonal dark band in the center of the image is an artifact of photographic processing and is not in the dark data.

The raw Cripple Creek/Canon City data were first examined for general quality and for periodic noise. Other investigators (see other papers in this volume) had reported periodic noise in their data, but ours showed none (Figure 1). However, there appeared to be discontinuities in the raw image intensity level and scan line drop-outs. Upon further examination, it was discovered that the discontinuities also occur in the dark signal image (Figure 2). Therefore, it was decided to process the data from scratch because the standard JPL 101 scan line smoothing would have destroyed this information.

The dark image in Figure 2 appears to show some pattern, but Fourier analyses of each spectrometer show no clear frequency peaks; the bright and dark banding are random noise. A sample Fourier Transform of one channel is shown in Figure 3.

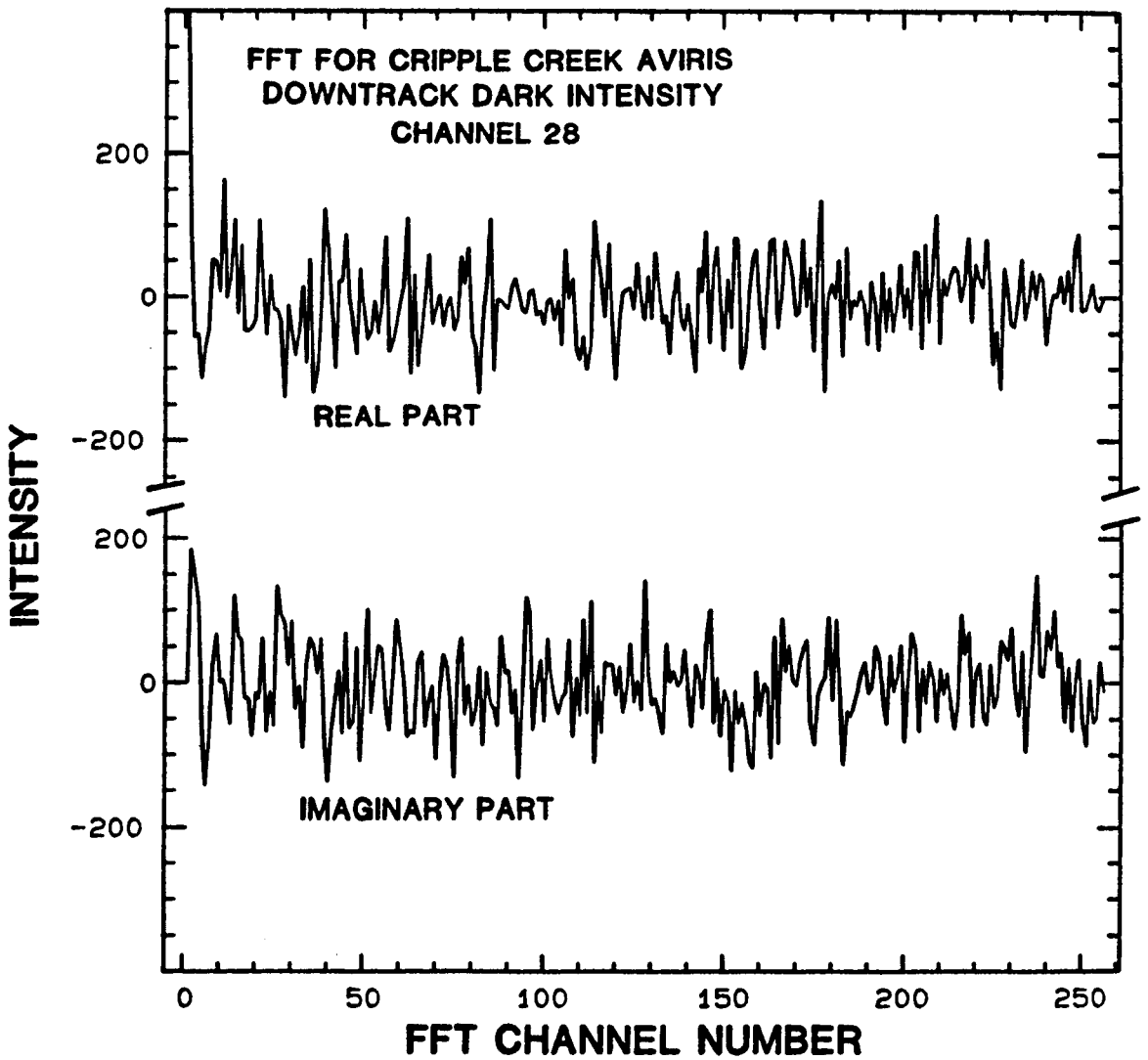


**Figure 3.** A Fourier Transform of channel 28 for 512 lines down the image in Figure 2. No periodic noise is evident.

Four ground calibration sites occur within the chosen 614 by 552 pixel data set. Samples were collected from each calibration site shortly after the flight for laboratory measurement. A field crew checked each site, verified pixel locations and identified uniform regions in the AVIRIS data within the calibration area. Laboratory reflectance spectra of samples collected within the calibration sites were convolved to AVIRIS raw data spectral resolution and sampling interval using SPECPR. Next, the corresponding AVIRIS raw spectral data, the JPL laboratory calibration data, and the dark spectra were extracted using SPECPR. The AVIRIS spectra were then dark corrected and calibration to ground reflectance, R, according to the following equation:

$$R = (DN - DK)\ CL\ CR, \qquad \text{eqn (1)}$$

where DN is the raw data number from the AVIRIS instrument at a given wavelength and pixel, DK is the dark measured once each scan line (one spectrum), CL is the JPL lab calibration (Vane *et al.*, 1987), and CR is the correction to convert the AVIRIS data to ground reflectance. Equation 1 is applied to each spectral channel in a pixel independently. The CL multiplier is necessary to correct the data for crosstrack vignetting (Vane *et al.*, 1987) and consists of 614 spectra, one for each crosstrack pixel. If there were no vignetting, the CL multiplier could be dropped from the equation. In practice, the CL correction amounts to only a few percent at the edges of the scan line relative to the center. The CR multiplier spectrum is an average of several pixels from each of the calibration sites. The laboratory calibration data are averages of two to four spectra from each calibration site.

Because of the use of ground calibration sites the calibration procedure in equation 1 corrects for any instrument response, solar irradiation function, and atmospheric transmission. The procedure is simplistic in that it ignores light contribution from atmospheric scattering, and the correction specifically applies to one elevation at a certain scan angle. In practice, the Cripple Creek area has significant topography, and while the atmospheric correction is only approximate, the small differential atmospheric paths can cause only minor inaccuracies. For the quality of this data set, no adverse effects could be detected.

Atmospheric scattering is negligible in this data set. Spectra of the lake in the lower right corner of the image have reflectance levels less than 1% at wavelengths greater than 1.3 $\mu$m, no more than about 2% from 0.7 to 1.3 $\mu$m, and a maximum of 8% at shorter wavelengths where there is likely scattering in the lake itself.

It is our intent in the future to use a digital elevation model to derive the correction factors as a function of elevation and scan angle, and to apply that function to each pixel so that all atmospheric features are properly removed. The problem is analogous to astronomical extinction corrections now commonly applied throughout the near infrared (e.g. McCord and Clark, 1979).

The calibrated reflectance image for channel 28 is shown in Figure 1. The image has a lot of scan line striping, at least in part due to no smoothing of the dark data. Discussions at the 1988 AVIRIS workshop at JPL showed considerable confusion about dark smoothing.

A dark spectrum is obtained by AVIRIS once each scan line. Thus if no smoothing is performed, the same dark spectrum is subtracted from 614 (crosstrack) spectra. If the dark data number for a particular channel was a little high (due to natural noise variations), then the dark subtracted channel for that whole scan line would tend to be low. A reasonable assumption from the way the AVIRIS instrument operates (e.g. Porter and Enmark, 1987) is that the noise level of the dark is equal to the noise level in an individual pixel. Examination of the Cripple Creek data shows that to be true. The following is a noise model of the system:

AVIRIS Pixel: $DN \pm \sigma_p$

AVIRIS Dark: $DK \pm \sigma_d$

AVIRIS Dark subtracted data: $A = DN - DK$

$$\text{Noise: } \sigma_a = (\sigma_p^2 + \sigma_d^2)^{1/2} \qquad \text{(eqn 2)}$$

If, as stated above, the noise in the dark equals the noise in the image data, then

$$\sigma = \sigma_p = \sigma_d, \text{ and}$$

$$\sigma_a = \sqrt{2}\,\sigma \qquad \text{(eqn 3)}$$

The dark subtracted image has a noise only 1.41 times greater than the original image. Dark averaging can reduce this noise increase according to the formula:

$$\sigma_a = (\sigma_p^2 + (\sigma_d^2)/n)^{1/2} \qquad \text{(eqn 4)}$$

Table 1 shows the specific improvements in the signal to noise as a function of n.

Table 1
**Noise of Dark Averaged and Subtracted Image Relative to the Noise in Original Image**

| Number of Darks Averaged | Noise |
|---|---|
| 1 (no smoothing) | 1.41 |
| 4 | 1.12 |
| 8 | 1.06 |
| 12 | 1.04 |
| 101 | 1.005 |

From Table 1, it is clear that there is little to be gained beyond smoothing a few spectra. Alternatively, if too many lines are smoothed and the instrument changes (e.g. the dark level drifts), then a larger error could result. If the dark is averaged over too many scan lines, any drifts and jumps in the dark level will be averaged out. Figure 4 shows such an effect.

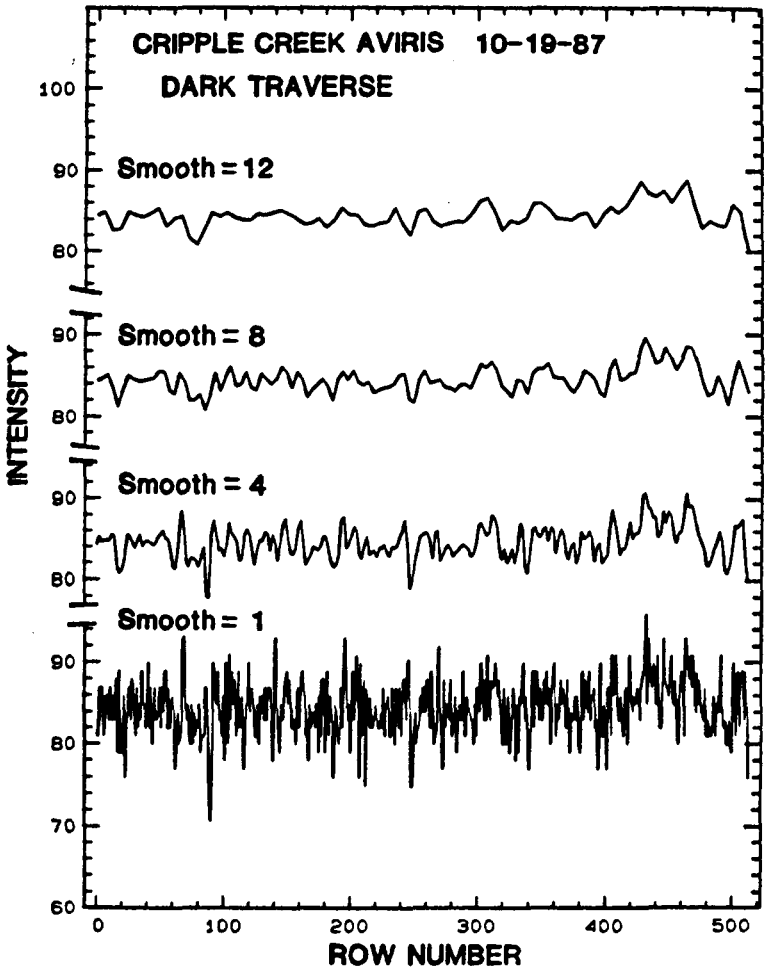


Figure 4. The dark value down the image for 512 lines is shown for channel 28 with different smoothing levels.

There is a rise in the dark level starting at about scan line 420. When the dark is smoothed by averaging adjacent lines, the boundary will become less of a step function, and significantly rounded at a smooth level of 12. The example shown is subtle, but the principles are clear. We recommend that the standard JPL processing be modified to so that the number of darks averaged is a variable that the user can specify in case the instrument is drifting.

In the process of calibrating the AVIRIS spectral data, it was decided to produce a data set whose channels were in increasing wavelength but sampled at the AVIRIS flight instrument wavelengths so no interpolation was done. In addition, each spectrometer has a small overlap region with adjacent spectrometers, and that overlap region was deleted. From the original 224 channel data, channels 31, 32, 33, 94, 95, 96, 97, 98, 160, 161, 162, and 163 were deleted so a 212 channel data set was produced. Finally, because the data are stored in 16-bit integers per pixel, the real data were scaled so that a reflectance of 1 is 20,000.

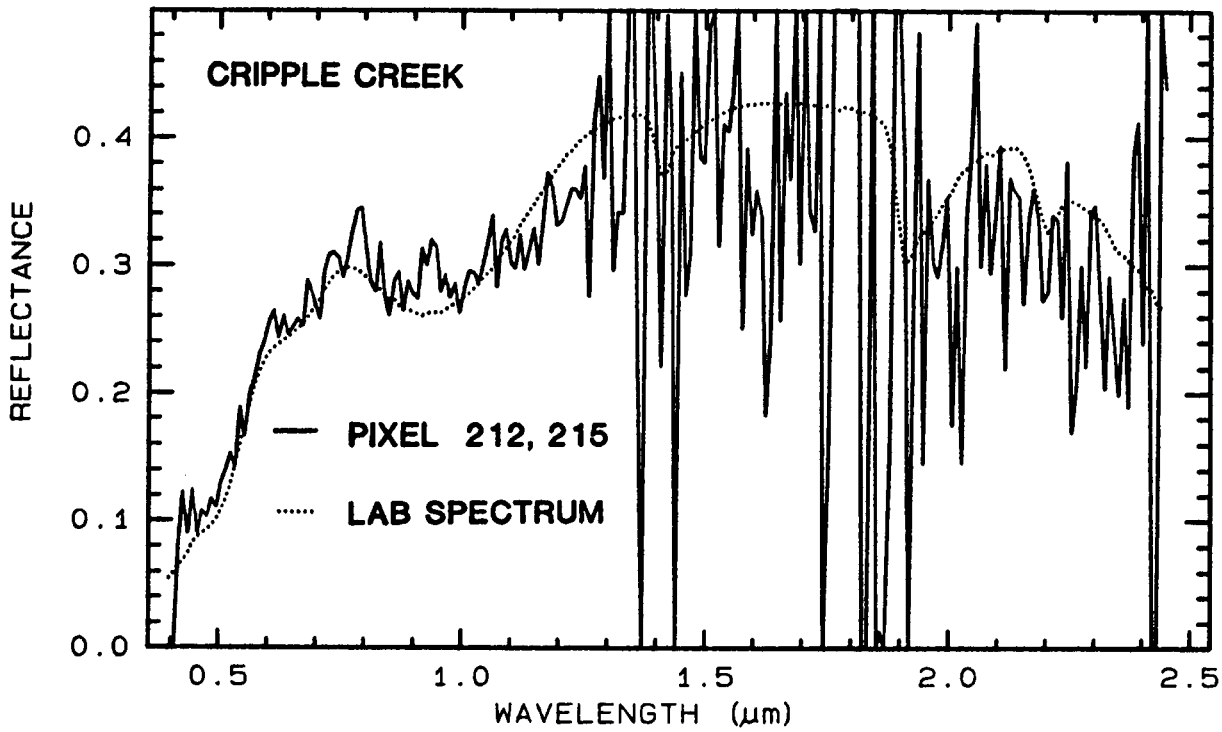


**Figure 5.** A sample AVIRIS spectrum (a single pixel at location scan line 212, pixel 215 in the image in Figure 1) is shown (solid line) compared to a laboratory spectrum convolved to the same spectral resolution and sampling interval (dotted line). The laboratory spectrum is of a representative soil sample from the area covered by the pixel. The general reflectance level and shape agrees well (within the noise). High noise is expected in the 1.4- and 1.9-$\mu$m regions because of absorption due to telluric water.

## SPECTRAL ANALYSIS

The calibrated AVIRIS data set can be used to extract reflectance spectra for direct analysis. Figure 5 shows a sample spectrum extracted and a laboratory spectrum of representative material from the pixel location. Within the noise, the AVIRIS data agree with the laboratory data.

The signal-to-noise-ratio spectrum was derived by computing the standard deviation of 36 pixels in a uniform region of the small lake seen in the lower right corner of the image in Figure 1. That standard deviation was inverted and scaled to indicate the signal to noise expected from an individual pixel (Figure 6). It can be seen that the signal to noise is very poor, especially from 1.25 to 2.45 $\mu$m. Again dark smoothing would improve the data by about a factor of 1.4. If the data were obtained in June rather than late October, the signal would have been nearly a factor of two higher, so the signal to noise could potentially be as high as about 25 in the 2.2-$\mu$m region instead of about 9.

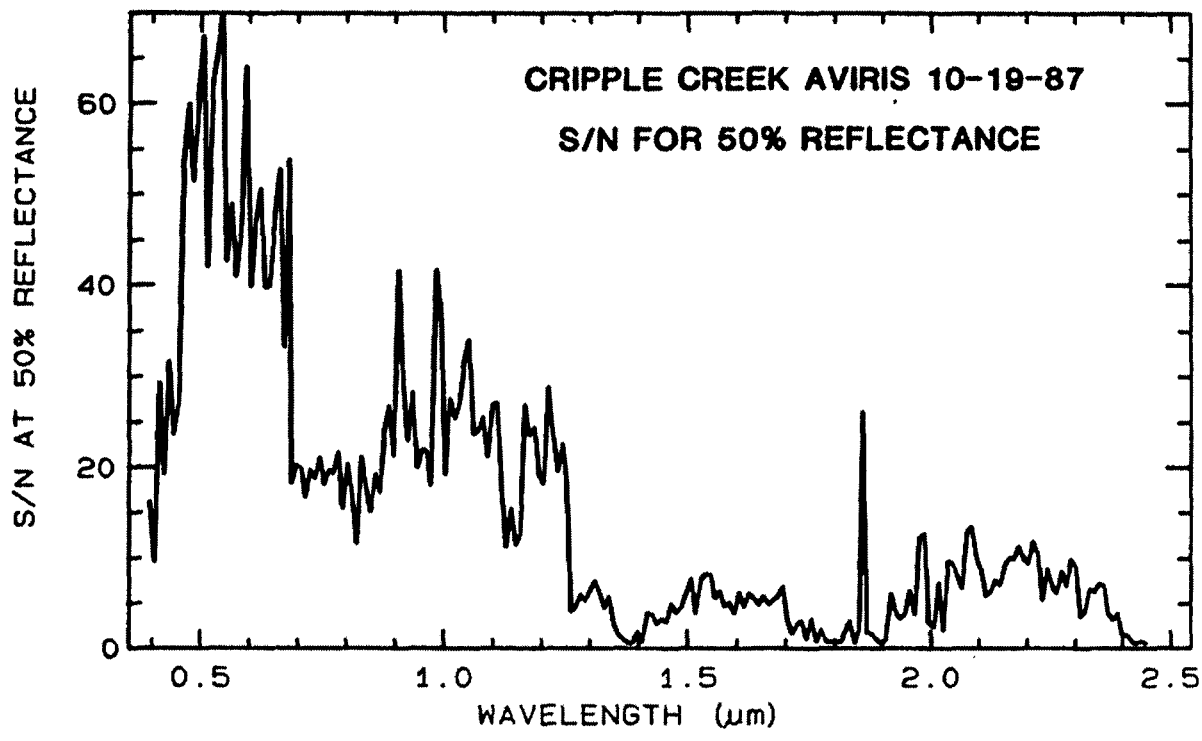


**Figure 6.** The signal to noise derived from the Cripple Creek AVIRIS data is shown relative to a constant reflectance of 50% at all wavelengths.

A simple spectral analysis was conducted to map specific absorption band depths in the image. Absorption bands were chosen for minerals and vegetation that are known or likely to be present in the Cripple Creek area. An absorption band was defined by two continuum channels and the channel closest to the absorption band center. The absorption band depth, D, is defined relative to its continuum, $R_c$ and the reflectance at the band center, $R_b$ (Clark and Roush, 1984):

$$D = 1 - R_b/R_c \qquad \text{(eqn 5)}$$

Band-depth images were computed for a number of minerals, including the 1.75-$\mu$m band of gypsum, the 1.27-$\mu$m band of biotite, the 2.34-$\mu$m band of calcite, the 2.32-$\mu$m band of dolomite, the 2.21-$\mu$m band of montmorillonite, the 2.20-$\mu$m band of kaolinite, the 0.45-$\mu$m and 0.93-$\mu$m bands of jarosite, the 0.85-$\mu$m band of hematite, and the 0.94-$\mu$m band of goethite. A band depth image for the 0.68-$\mu$m band of lodgepole pine was also computed. Because the visible data are much better than the near-IR, the band depths in the 1.25- to 2.45-$\mu$m spectral region show very little information (Figure 7). Absorptions in the visible show much more detail (Figure 8).

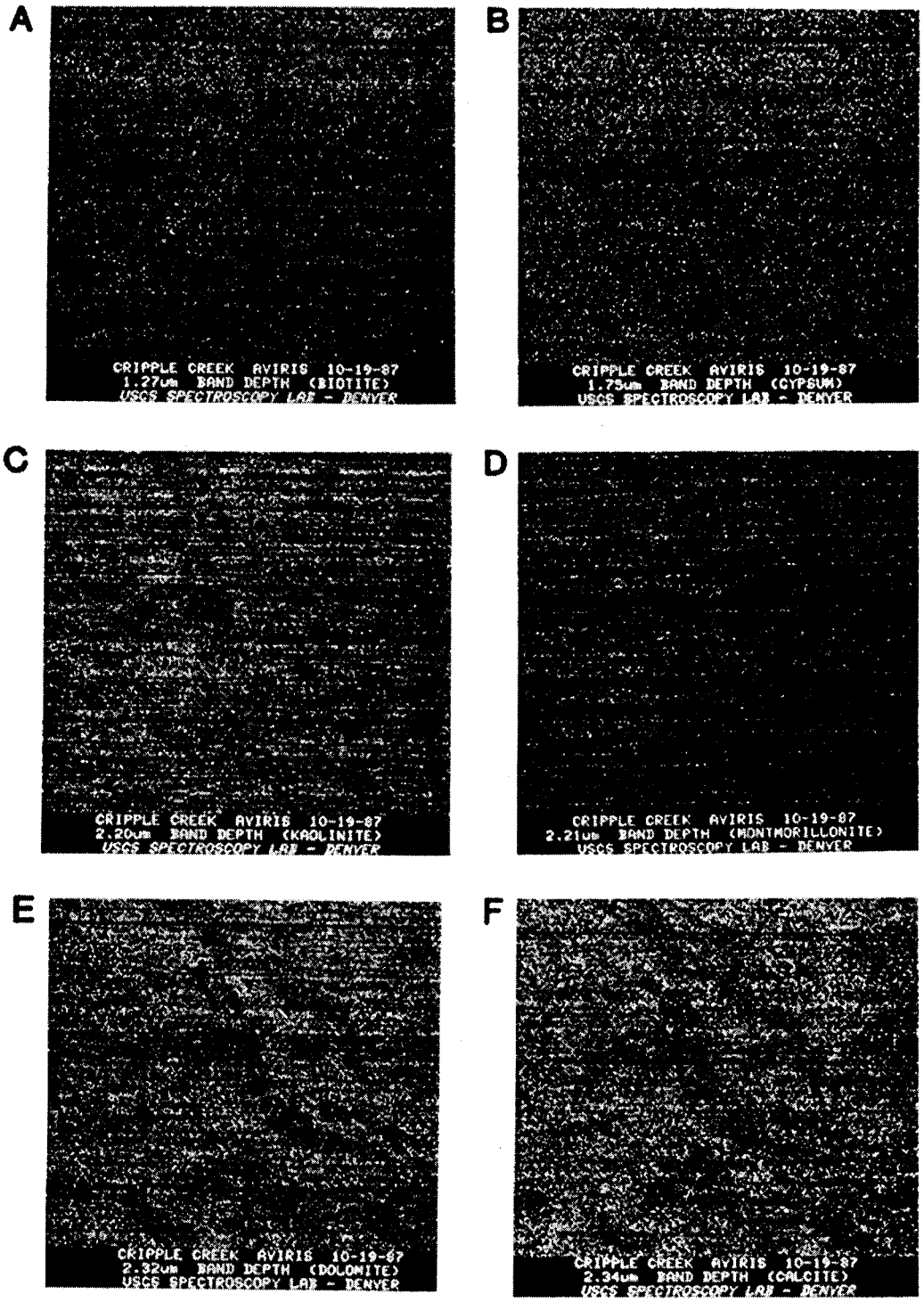


**Figure 7.** Band depth images of the Cripple Creek area: A) the 1.27-$\mu$m band of biotite, B) the 1.75-$\mu$m band of gypsum, C) the 2.20-$\mu$m band of kaolinite, D) the 2.21-$\mu$m band of montmorillonite, E) the 2.32-$\mu$m band of dolomite, and F) 2.34-$\mu$m band of calcite.

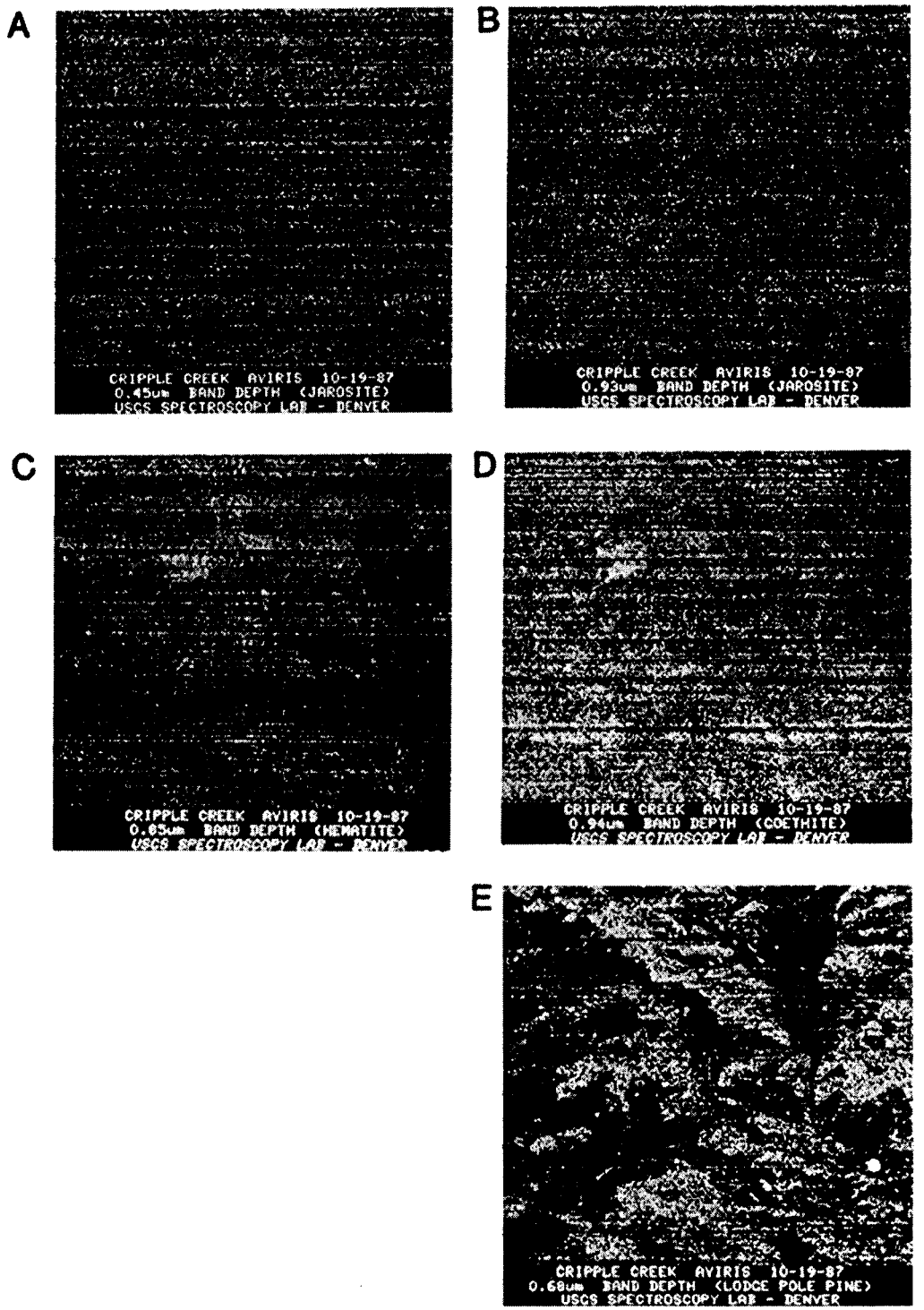


**Figure 8.** Band depth images of the Cripple Creek area: A) the 0.45-$\mu$m and B) 0.93-$\mu$m bands of jarosite, C) the 0.85-$\mu$m band of hematite, D) the 0.94-$\mu$m band of goethite, and E) the 0.68-$\mu$m band of lodgepole pine.

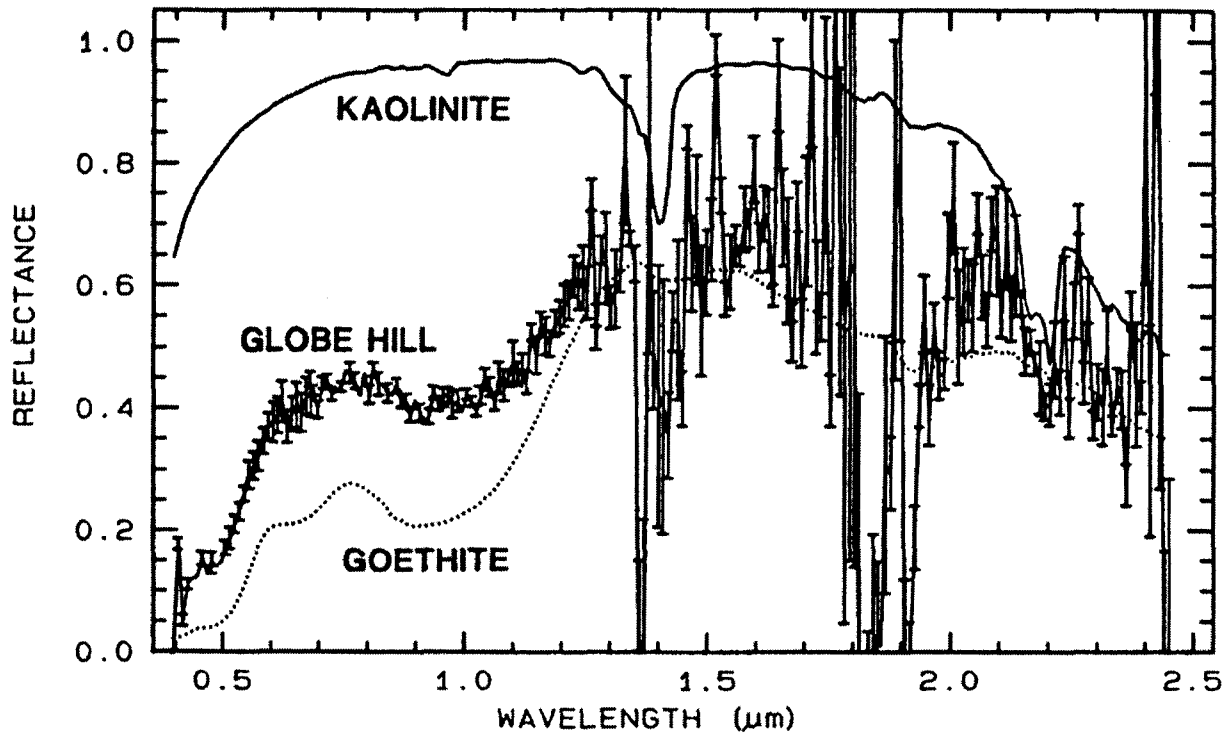


**Figure 9.** AVIRIS spectrum is shown for the Globe Hill area (average of 5 pixels: the spectrum with error bars) compared to spectrum library data convolved to the AVIRIS spectral resolution and sampling interval. The upper solid line is kaolinite and the lower dotted line is goethite.

Because of the 3-channel method of computing band depths, similar bands will show similar results. For example, the jarosite, hematite, and goethite 0.9-μm band images show similarities because the spectral features are broadly overlapping. Extracted spectra, however, show that the strongest absorption in the images (Globe Hill, to the upper left of center) is really goethite (Figure 9).

The kaolinite image also shows a weak signature indicating its presence in the Globe Hill area. A combination of the kaolinite, goethite, and lodgepole pine band depths were used to produce the Color-Composite-Band-Depth Image (CCBDI) shown in slide No. 4. The Globe Hill area shows a reddish-purple color indicating the presence of both kaolinite and goethite. Globe Hill is known to be a region of hydrothermal alteration and extracted spectra confirms this fact (Figure 9).

## CONCLUSIONS

The AVIRIS data for the 1987 flight season in October is very noisy, but it is still possible to calibrate the data to ground reflectance. The calibration to reflectance allows absorption bands from specific minerals to be mapped. Areas of goethite, kaolinite and lodgepole pine were clearly mapped in the Cripple Creek area. The signal to noise must be substantially improved, however, if mapping of minerals is to be done where the absorptions are weak due to low abundance or partial vegetation cover.

## REFERENCES


Clark, R.N., A Large Scale Interactive One Dimensional Array Processing System, *Pub. Astron. Soc. Pac.*, **92**, 221-224, (1980).

Clark, R.N. and T.L. Roush, Reflectance Spectroscopy: Quantitative Analysis Techniques for Remote Sensing Applications, *J. Geophys. Res.*, **89**, 6329-6340, (1984).

McCord, T.B., and R.N. Clark, Atmospheric Extinction 0.65-2.50 $\mu$m Above Mauna Kea, *Pub. Astron. Soc. Pac.*, **91**, 571-576, (1979).

Porter, W.M. and H.T. Enmark, A system overview of the Airborne Visible/Infrared Imaging Spectrometer (AVIRIS), in *Airborne Visible/Infrared Imaging Spectrometer (AVIRIS)* (G. Vane, ed.), JPL Publication 87-38, 3-12 (1987).

Reimer, J.H., J.R. Heyada, S.C. Carpenter, W.T. Deich, and M. Lee, AVIRIS ground data-processing system, in *Airborne Visible/Infrared Imaging Spectrometer (AVIRIS)* (G. Vane, ed.), JPL Publication 87-38, 61-72 (1987).

Vane, G., T.G. Chrien, E.A. Miller, and J.H. Reimer, Spectral and radiometric calibration of the Airborne Visible/Infrared Imaging Spectrometer, in *Airborne Visible/Infrared Imaging Spectrometer (AVIRIS)* (G. Vane, ed.), JPL Publication 87-38, 61-72 (1987).


## SLIDE CAPTIONS

Slide No. 3. A false-color-infrared composite of the Cripple Creek scene. The reflectance at 0.88 $\mu$m is red, the reflectance at 0.68 $\mu$m is green, and the reflectance at 0.54 $\mu$m is blue.

Slide No. 4. A Color-Composite-Band-Depth Image (CCBDI): the band depth for the 0.94-$\mu$m goethite band depth is assigned to red, the 0.68-$\mu$m lodgepole pine band depth is assigned to green, and the 2.20-$\mu$m kaolinite band depth is assigned to blue. A band depth of zero is black. The purplish area to the upper left of center is Globe Hill, a region of hydrothermal alteration.

# Automated extraction of absorption features from Airborne Visible/Infrared Imaging Spectrometer (AVIRIS) and Geophysical and Environmental Research Imaging Spectrometer (GERIS) data

Fred A. Kruse
Wendy M. Calvin[1]
and
Olivier Seznec[2]
Center for the Study of Earth from Space (CSES)
CIRES, University of Colorado
Boulder, Colorado 80309

## ABSTRACT

Automated techniques have been developed for the extraction and characterization of absorption features from reflectance spectra. The absorption feature extraction algorithms have been successfully tested on laboratory, field, and aircraft imaging spectrometer data. A suite of laboratory spectra of the most common minerals has been analyzed and absorption band characteristics tabulated. A prototype expert system has been designed, implemented, and successfully tested to allow identification of minerals based on the extracted absorption band characteristics. AVIRIS spectra for a site in the northern Grapevine Mountains, Nevada, have been characterized and the minerals sericite (fine grained muscovite) and dolomite have been identified. The minerals kaolinite, alunite, and buddingtonite have been directly identified and mapped for a site at Cuprite, Nevada, using the feature extraction algorithms on the new Geophysical and Environmental Research 64 channel imaging spectrometer (GERIS) data. The feature extraction routines (written in FORTRAN and C) have been interfaced to the expert system (written in PROLOG) to allow both efficient processing of numerical data and logical spectrum analysis.

## INTRODUCTION

Aircraft imaging spectrometers measure light reflected from the Earth's surface, utilizing many narrow contiguous spectral bands to construct detailed reflectance spectra for millions of discrete picture elements (pixels) (Goetz and others, 1985). One difficulty confronting researchers is that the immense volume of data collected by these systems prohibit detailed manual analysis. The objective of this work is to develop automated techniques for analysis of imaging spectrometer data that emulate the analytical processes used by a human observer. These techniques must

[1] Present address: U. S. Geological Survey, Box 25046, MS964, Denver, CO 80225
[2] Visiting scientist, Société Européenne de Propulsion (SEP)

efficiently use available computing power to complete the analysis in a reasonable period of time.

## FEATURE EXTRACTION

Techniques for extraction of spectral features from field and laboratory reflectance spectra have been in use for several years (Green and Craig, 1985; Kruse and others, 1986; Yamaguchi and Lyon, 1987; Clark and others, 1987). We are developing computer automated spectral feature extraction algorithms (implemented in FORTRAN and C) that allow extraction and subjective characterization of laboratory, field, and imaging spectrometer spectra (Kruse and others, 1986; Kruse, 1987, 1988a, 1988b). The absorption feature information is extracted from each spectrum using the following techniques. The computer rapidly identifies maxima in the spectrum and fits a continuum of straight line segments between these points. The continuum is removed from the data using division. The minima of the continuum-removed spectrum are determined and the 10 strongest features are extracted. The wavelength position, depth, full width at half the maximum depth (FWHM), and asymmetry for each of these 10 features are then determined and tabulated.

A fast, simple approach was chosen to fit the continuum. First, high points of the spectrum are determined using magnitude and slope criteria. The magnitude of the reflectance value of a high point must be larger than the average reflectance on either side. The exact number of points used in the average is determined by using a percentage of the total number of channels. The averaging procedure aids in the detection of band shoulders. In addition, the slope to the left of the high point must be positive and the slope on the right must be negative. Once the high points are located, straight line segments are drawn between them. Then for every point in the spectrum the actual reflectance and the line segment reflectance are compared. The reflectance value of the continuum at any given point is defined as the larger of these two values (Figure 1, Table 1). The advantage of this simple approach is that only a single pass through the spectrum is required to characterize the continuum.

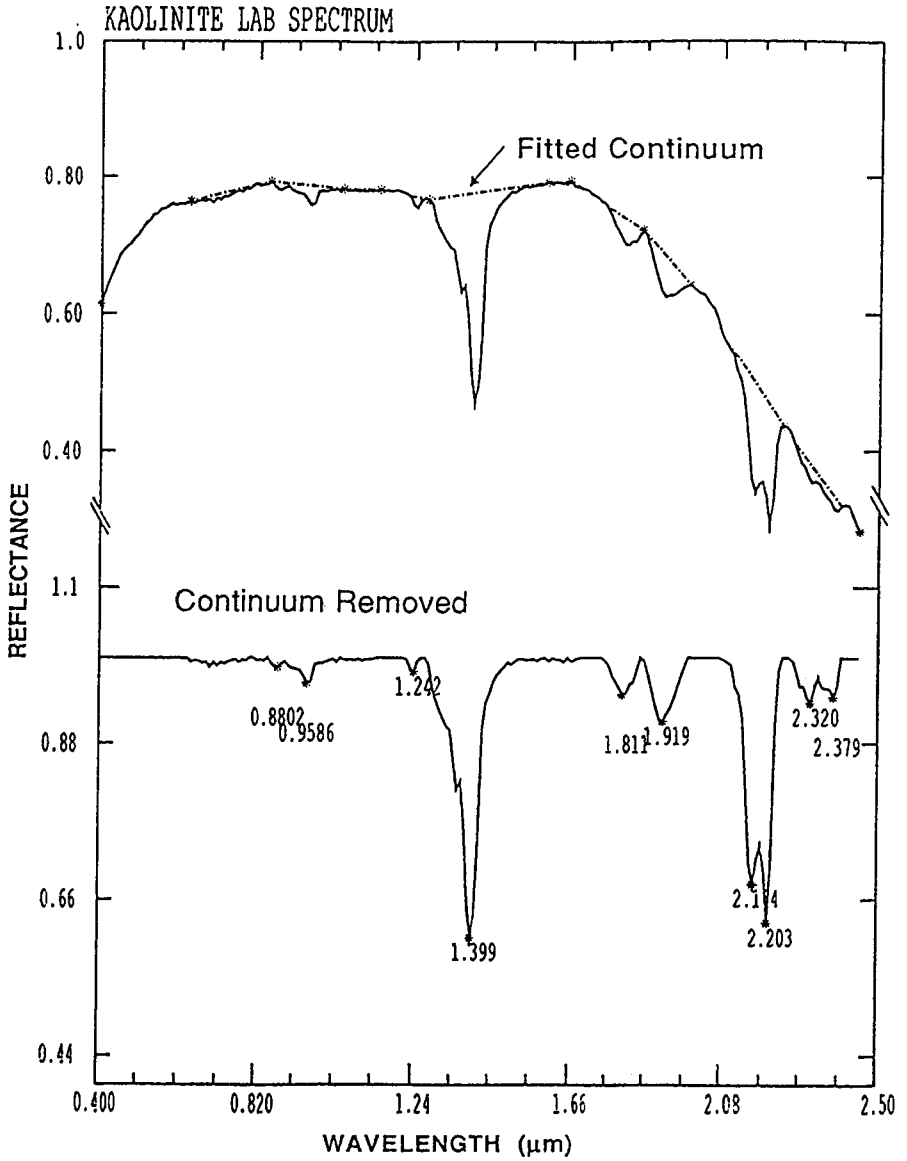


Figure 1. Laboratory spectrum of kaolinite showing fitted continuum, and continnuum removed spectrum. (Lab spectrum from the USGS, Denver spectral library).

ABSORPTION BAND ANALYSIS FOR KAOLINITE LAB SPECTRUM

| Band | Order | Wave | Depth | FWHM | Asym |
|---|---|---|---|---|---|
| 1 | 1/1 | 1.3996 | 0.3939 | 0.0588 | 0.6170 |
| 2 | 1/2 | 2.2032 | 0.3732 | 0.0784 | 0.2161 |
| 3 | 2/2 | 2.1640 | 0.3184 | 0.0000 | 0.0000 |
| 4 | 1/1 | 1.9190 | 0.0895 | 0.0686 | 1.2802 |
| 5 | 1/2 | 2.3208 | 0.0627 | 0.0588 | 1.8101 |
| 6 | 2/2 | 2.3796 | 0.0542 | 0.0000 | 0.0000 |
| 7 | 1/1 | 1.8112 | 0.0511 | 0.0686 | 1.1634 |
| 8 | 1/1 | 0.9586 | 0.0352 | 0.0392 | 0.5126 |
| 9 | 1/1 | 1.2428 | 0.0189 | 0.0294 | 0.2628 |
| 10 | 1/1 | 0.8802 | 0.0130 | 0.0490 | 10.3361 |

Table 1. Absorption band analysis for kaolinite lab spectrum.

Minima are located using the inverse of the criteria for determining maxima. Given a minimum depth threshold, the 10 features with the greatest depths are determined. For each of these 10 features, the wavelength position of the minimum is determined as well as the FWHM (Figure 2). If more than one minima lies between two high points then the band is defined as being a multiple band. Band "order" indicates the number of bands in the multiple band and the relative depth of the band compared with the other members of the multiple band. The asymmetry is defined as the sum of the reflectance values for feature channels to the right of the minimum divided by the sum of the reflectance values for feature channels to the left. Symmetrical bands have an asymmetry value of one. Bands that are asymmetrical towards shorter wavelengths have asymmetry less than one, while bands that are asymmetrical towards longer wavelengths have asymmetry greater than one.

## EXAMPLES FROM NEVADA AVIRIS AND GERIS

The continuum-removal and feature extraction procedures were used to analyze individual spectra from AVIRIS data for a site in the northern Grapevine Mountains, Nevada. Although these data have severe signal-to-noise problems, the feature extraction procedures successfully produced continuum-removed spectra that could be compared to laboratory spectra. Many of the features located in the AVIRIS data are noise, however, the strongest absorption bands correspond to bands in the laboratory spectra. Figures 3 and 4 show AVIRIS spectra for known areas of sericite (fine grained muscovite) and dolomite (Kruse, 1988a).

The feature extraction algorithms were also tested on Geophysical and Environmental Research Inc. 64 channel imaging spectrometer (GERIS) data from Cuprite, Nevada. This instrument is the first commercial imaging spectrometer. The GERIS collects data from 0.43 to 2.5 μm in 64 channels of varying width. The 24 visible and infrared bands between 0.43 and 0.972 are 23 nm wide, the 8 bands in the infrared between 1.08 and 1.8 μm are 120 nm wide, and the 31 bands from 1.99 to 2.5 μm are 16 nm wide (William Collins, written communication, 1988). Only the last 31 bands were used in this study. The feature extraction procedures were

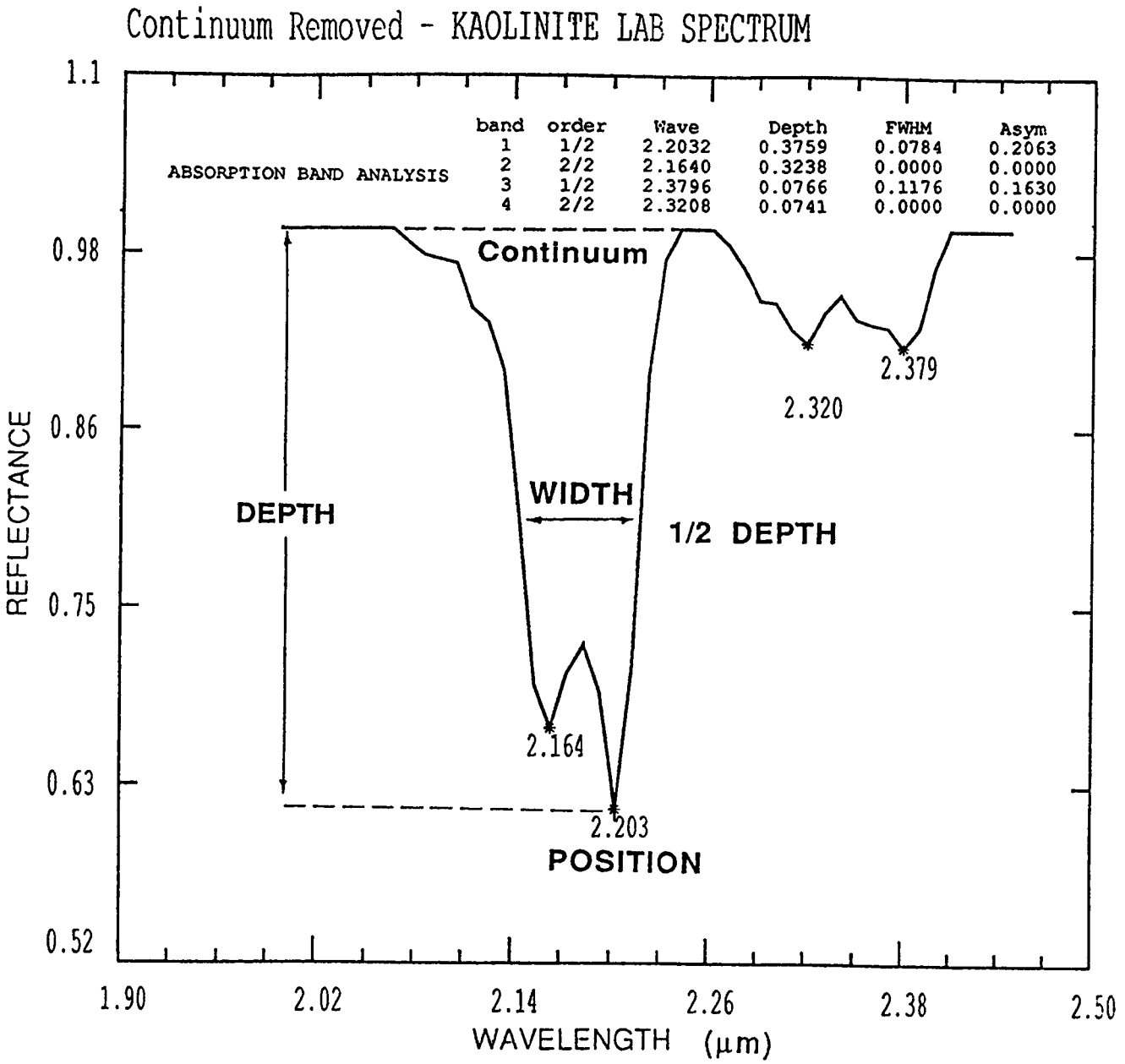


Figure 2 Laboratory spectrum of kaolinite showing the absorption band parameters position, depth, and width. (Laboratory spectrum is from the USGS, Denver spectral library.)

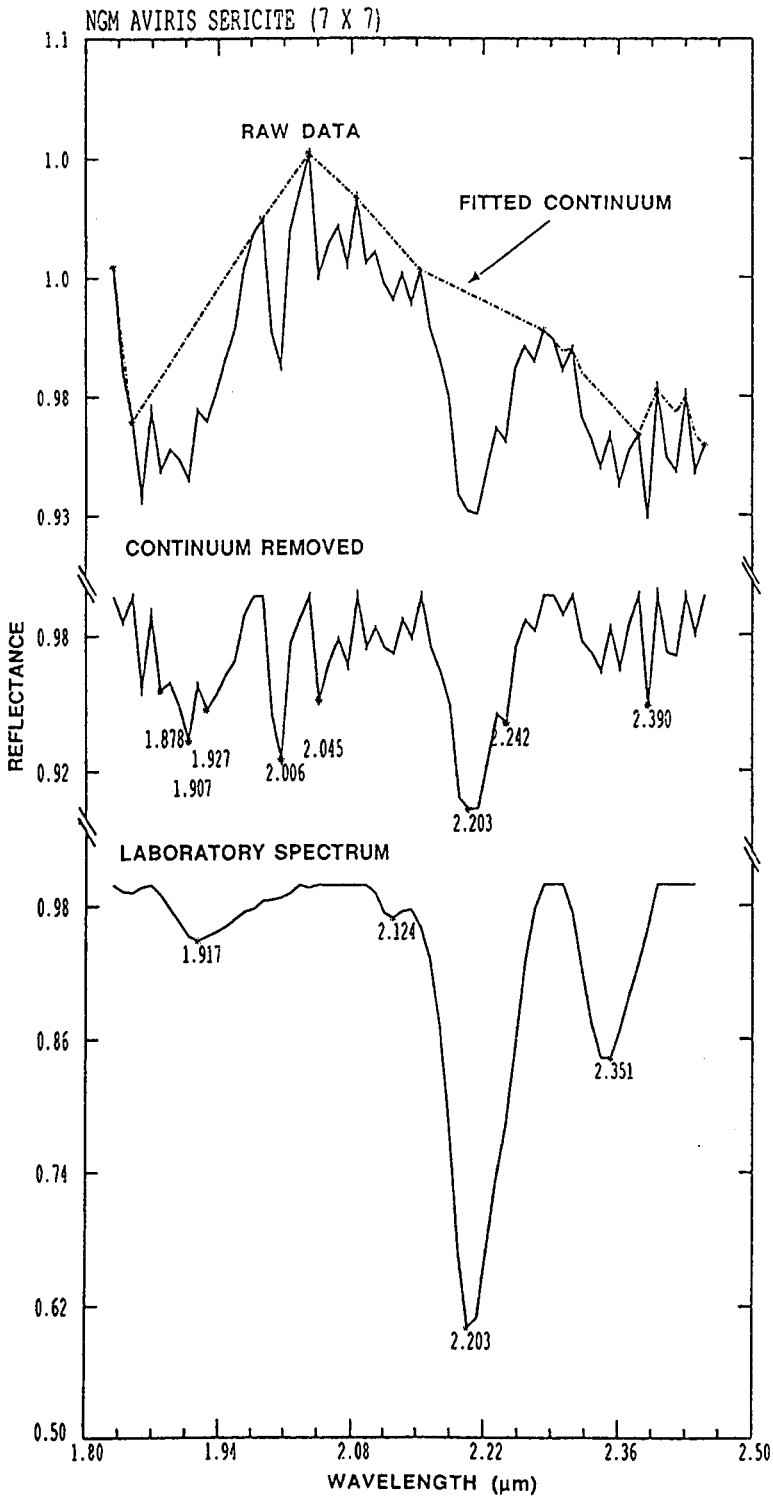


Figure 3. Raw and continuum-removed AVIRIS spectra for sericite (muscovite) from the northern Grapevine Mountains, Nevada, compared to a laboratory spectrum of muscovite. (Laboratory spectrum is from the USGS, Denver spectral library.)

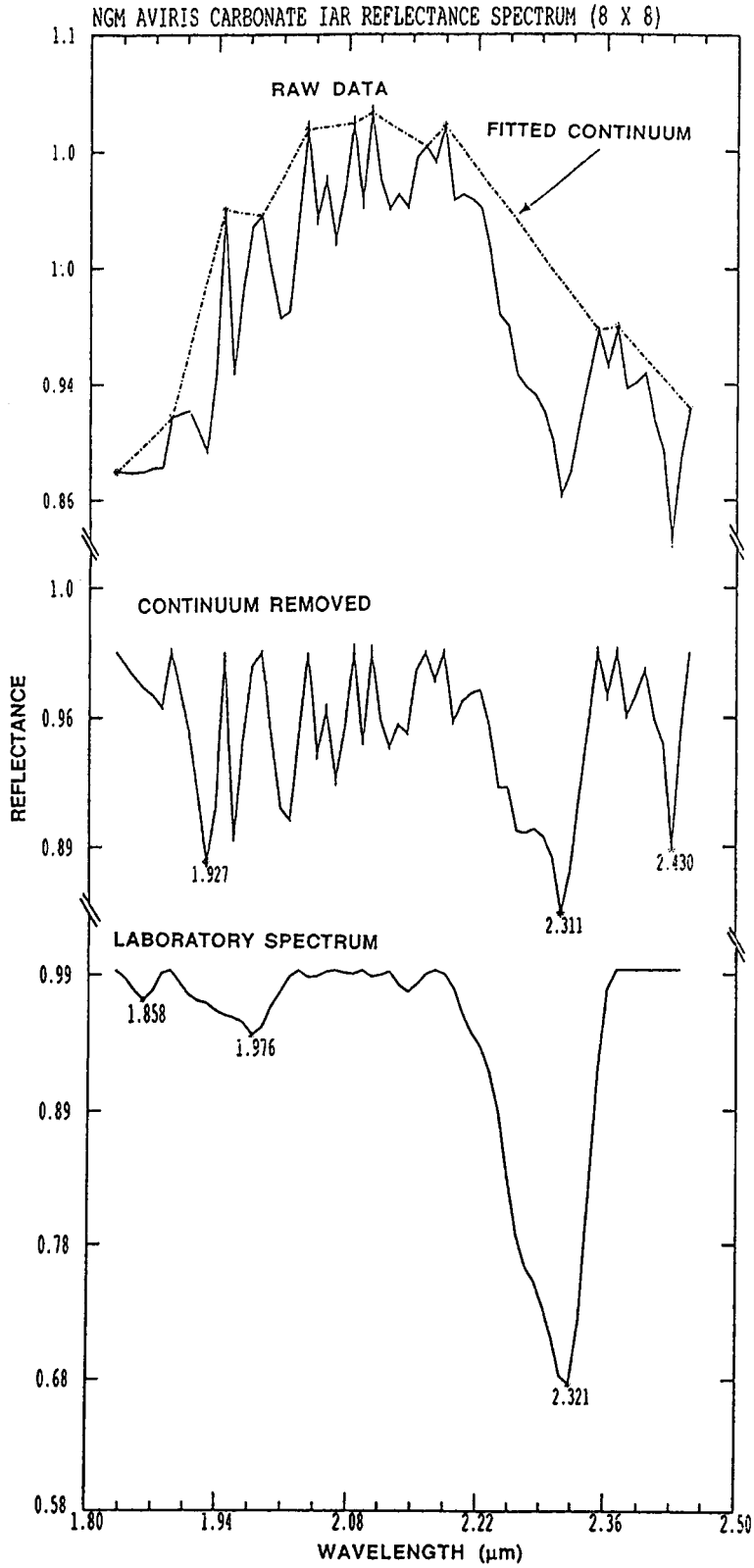


Figure 4. Raw and continuum-removed AVIRIS spectra for dolomite from the northern Grapevine Mountains, Nevada, compared to a laboratory spectrum of dolomite. (Laboratory spectrum is from the USGS, Denver spectral library.)

used to extract absorption band characteristics directly from the image data. Comparison of the continuum-removed GERIS spectra with laboratory spectra was used to identify kaolinite, alunite, and buddingtonite. An example of an alunite spectrum extracted from the GERIS data is shown in Figure 5 with a laboratory spectrum of alunite for comparison. Comparison of the tabulated absorption band characteristics are shown in Table 2.

## EXPERT SYSTEM

The second stage of this research uses facts and rules derived from the automated analysis of laboratory measurements of selected minerals to define a knowledge base that can be applied to analysis of reflectance spectra (Kruse, 1988b). The five parameters derived using the feature extraction procedure were used to derive the facts and rules utilized in the expert system. The knowledge base/expert system approach was chosen to minimize analysis time (Yamaguchi and Lyon, 1987; Goetting and Lyon, 1987). Other procedures under development (Clark and others, 1987) propose use of spectral library or feature library searching to determine a best match for a given spectrum. Analysis time required is proportional to the size of the library to be searched. The expert system approach reduces the analysis time by using a tree hierarchy (Figure 6). We are using the PROLOG programming language (Quintus Computer Systems, 1987) to implement the facts and rules in a logical fashion similar to the decision process followed by an experienced analyst. A decision is made at each level of the tree based on facts and rules derived through prior analysis of the spectral library. Critical absorption band characteristics for a given mineral are defined using the feature extraction procedure. Facts and rules are written for each mineral or group of minerals in the database. The spectral library itself is never accessed during the analysis of a spectrum.

The decision process followed by the computer is designed to emulate the logical steps followed by an experienced analyst. The strongest absorption feature for a given spectrum (or pixel) is determined, and the spectrum is broadly classified

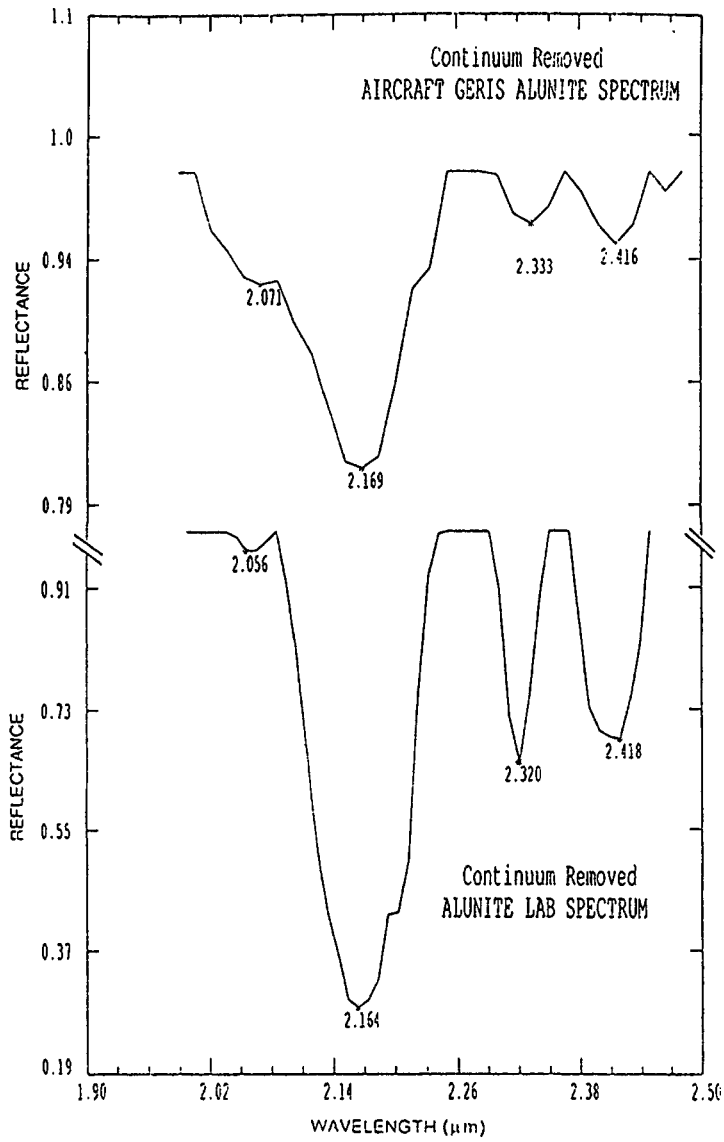


Figure 5. Comparison of GERIS and laboratory spectra of alunite.

ABSORPTION BAND ANALYSIS for
ALUNITE GERIS AIRCRAFT SPECTRUM

| Band | Order | Position | Depth | Width | Asymetry |
|---|---|---|---|---|---|
| 1 | 1/2 | 2.1697 | 0.1855 | 0.1314 | 0.5337 |
| 2 | 2/2 | 2.0711 | 0.0712 | 0.0000 | 0.0000 |
| 3 | 1/1 | 2.4161 | 0.0451 | 0.0657 | 0.7278 |
| 4 | 1/1 | 2.3340 | 0.0325 | 0.0657 | 0.7756 |

ABSORPTION BAND ANALYSIS for ALUNITE LAB SPECTRUM

| Band | Order | Position | Depth | Width | Asymetry |
|---|---|---|---|---|---|
| 1 | 1/1 | 2.1640 | 0.7057 | 0.1078 | 1.1114 |
| 2 | 1/1 | 2.3208 | 0.3422 | 0.0392 | 0.9432 |
| 3 | 1/1 | 2.4188 | 0.3074 | 0.0686 | 0.4155 |
| 4 | 1/1 | 2.0562 | 0.0278 | 0.0392 | 5.6839 |

Table 2. Comparison of absorption band parameters for GERIS and laboratory spectra of alunite.

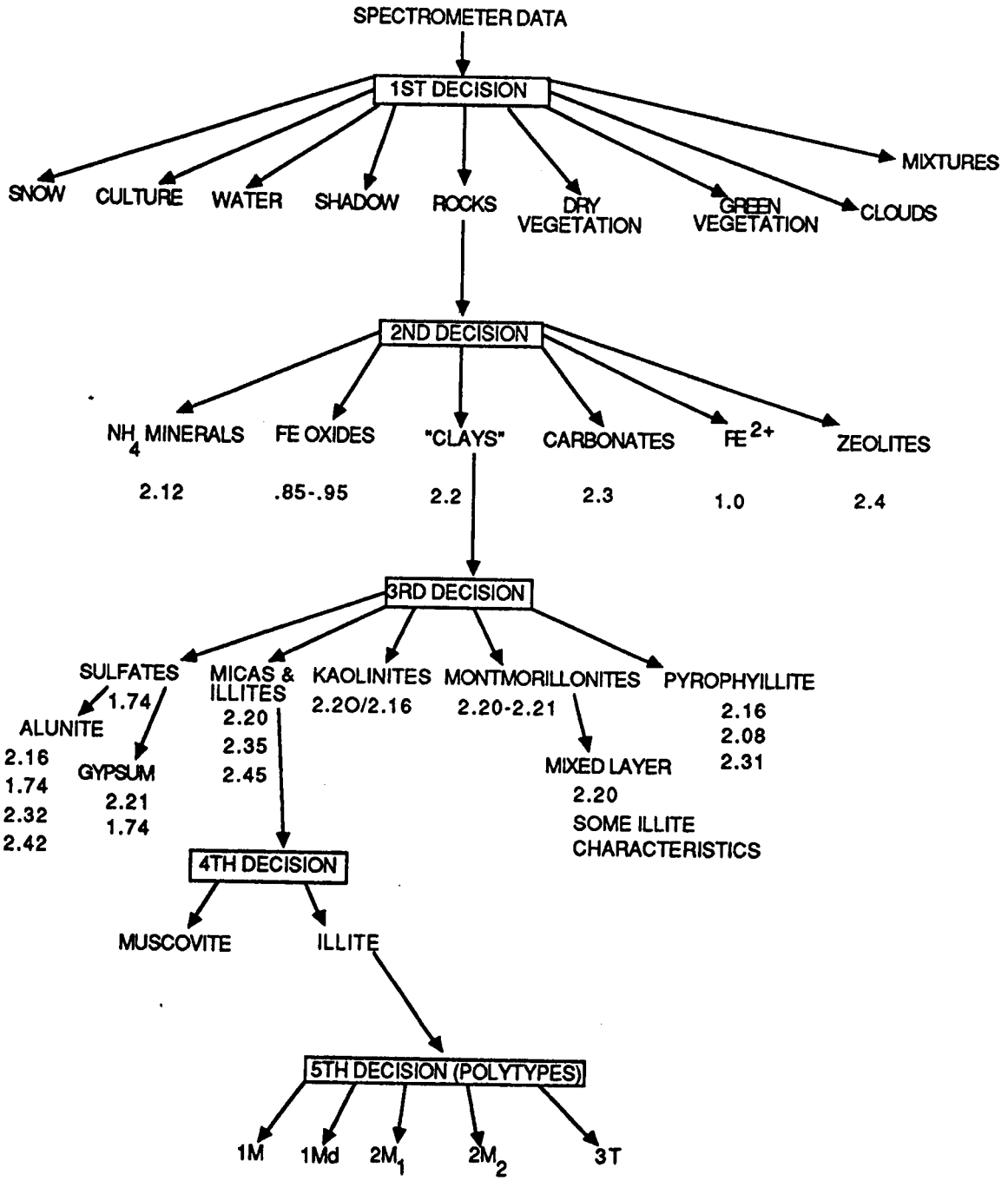


Figure 6. Prototype expert system decision tree.

(eg. clay, carbonate, iron oxide). Primary band characteristics (eg. doublet, triplet) and secondary/tertiary absorption bands are used to progress through the tree structure until an identification is made. If the decision process fails because there is insufficient information to identify a specific mineral, then the last classification is used to give the best answer possible. A comparison of two continuum-removed spectra and and example of the decision process is shown in Figures 7 and Table 3 and Figure 8.

## CONCLUSIONS

An absorption feature extraction procedure and prototype expert system have been developed that allow rapid analysis of reflectance spectra and identification of minerals. Numerical processing of the spectral data is optimized in FORTRAN and C. Logical decisions based on facts and rules derived from analysis of laboratory spectra are implemented in PROLOG. The combination of the numerical and logical processing routines takes advantage of the inherent strengths of the associated computer languages to efficiently analyze the data. The feature extraction techniques and expert system have been successfully tested on laboratory, field, and imaging spectrometer data. Additional minerals need to be added to the database, and facts and rules must be refined to fully utilize the expert system for mineral identification. Future efforts will concentrate on integrating the knowledge base into an image processing environment for analysis of entire AVIRIS and GERIS images.

## REFERENCES

Clark, R. N., King, T.V.V., and Gorelick, N. S., 1987, Automatic continuum analysis of reflectance spectra: *in* Proceedings of the 3rd Airborne Imaging Spectrometer Data Analysis Workshop, JPL Publication 87-30, Jet Propulsion Laboratory, Pasadena, p. 138-142.

Goetting, H. R., and Lyon, R. J. P., A knowledge-based software environment for the analysis of spectroradiometer data: in Proceedings, International Symposium on Remote Sensing of Environment, Fifth Thematic Conference, "Remote Sensing for Exploration Geology", Reno, Nevada, 29 September-2 October,

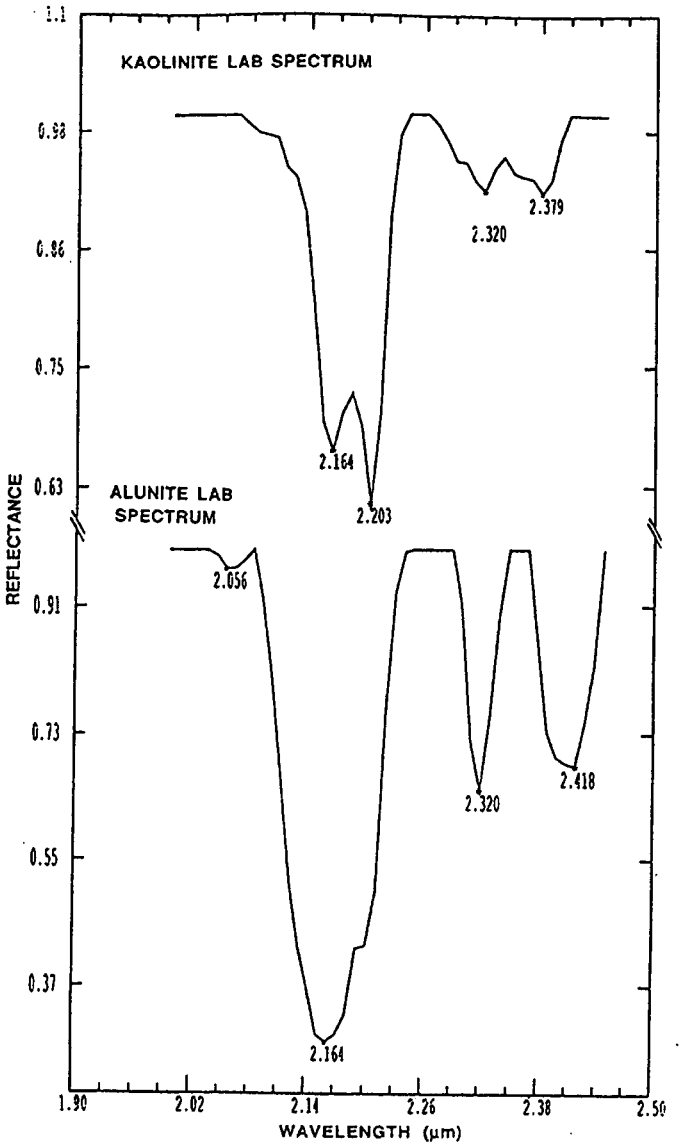


Figure 7. Comparison of kaolinite and alunite lab spectra.

ABSORPTION BAND ANALYSIS for KAOLINITE LAB SPECTRUM

| Band | Order | Position | Depth | Width | Asymetry |
|---|---|---|---|---|---|
| 1 | 1/2 | 2.2032 | 0.3759 | 0.0784 | 0.2063 |
| 2 | 2/2 | 2.1640 | 0.3238 | 0.0000 | 0.0000 |
| 3 | 1/2 | 2.3796 | 0.0766 | 0.1176 | 0.1630 |
| 4 | 2/2 | 2.3208 | 0.0741 | 0.0000 | 0.0000 |

ABSORPTION BAND ANALYSIS for ALUNITE LAB SPECTRUM

| Band | Order | Position | Depth | Width | Asymetry |
|---|---|---|---|---|---|
| 1 | 1/1 | 2.1640 | 0.7057 | 0.1078 | 1.1114 |
| 2 | 1/1 | 2.3208 | 0.3422 | 0.0392 | 0.9432 |
| 3 | 1/1 | 2.4188 | 0.3074 | 0.0686 | 0.4155 |
| 4 | 1/1 | 2.0562 | 0.0278 | 0.0392 | 5.6839 |

Table 3. Comparison of absorption band parameters for kaolinite and alunite lab spectra.

# Example : kaolinite vs. alunite.

1st Decision - predetermined to be "ROCK"

2nd Decision ( rock level )

**if** it has a deep band in 2.15-2.22 μm region
**then** look for in "clay" species.

3rd Decision ( "clay" species )

**if** it has a doublet near 2.2 μm
*and* strongest band of the doublet is 2.2 μm
*and* weakest band of the doublet is near 2.16
**then** it is **kaolinite.**

**if** it has a single band near 2.2 μm
*and* a weaker band near 2.32 μm
*and* a weaker band near 2.42 μm
**then** it is **alunite.**

Figure 8. Example of decision process for discriminating kaolinite from alunite.

1986, Environmental Research Institute of Michigan, Ann Arbor, p. 513-520.

Goetz, A. F. H., Vane, Gregg, Solomon, J. E., and Rock, B. N., 1985, Imaging spectrometry for earth remote sensing: Science, v. 228, p. 1147-1153.

Green, A. A., and Craig, M. D., 1985, Analysis of aircraft spectrometer data with logarithmic residuals: *in* Proceedings, AIS workshop, 8-10 April, 1985, JPL Publication 85-41, Jet Propulsion Laboratory, Pasadena, California, p. 111-119.

Kruse, F. A., 1988a, Use of Airborne Imaging Spectrometer data to map minerals associated with hydrothermally altered rocks in the northern Grapevine Mountains, Nevada and California: Remote Sensing of Environment, Special issue on imaging spectrometry, V. 24, No. 1, p. 31-51.

Kruse, F. A., 1988b, Automated extraction and analysis of spectral features from imaging spectrometer data (Abst.): *in* Program with Abstracts, Second Hidden Peak Symposium on Computer-Enhanced Analytical Spectroscopy 1-3 June 1988, Snowbird, Utah, p. 23.

Kruse, F. A., 1987, Extracting spectral information from imaging spectrometer data: A case history from the northern Grapevine Mountains, Nevada/California: *in* proceedings, 31st Annual International Technical Symposium, 16-21 August, 1987, Society of Photo-Optical Instrumentation Engineers, V. 834, p. 119-128.

Kruse, F. A., Knepper, D. H. Jr., and Clark, R. N., 1986, Use of digital Munsell color space to assist interpretation of imaging spectrometer data -- Geologic examples from the northern Grapevine Mountains, California and Nevada: *in* Proceedings, 2nd AIS Data Analysis Workshop, Pasadena, California 6-8 May, 1986, JPL Publication 86-35, Jet Propulsion Laboratory, Pasadena, California, p. 132-137.

Quintus Computer Systems, 1987, QUINTUS PROLOG Reference Manual, Version 10, Quintus Computer Systems, Mountain View, CA.

Yamaguchi, Yasushi, and Lyon, R. J. P., 1986, Identification of clay minerals by feature coding of near-infrared spectra: *in* Proceedings, International Symposium on Remote Sensing of Environment, Fifth Thematic Conference, "Remote Sensing for Exploration Geology", Reno, Nevada, 29 September- 2 October, 1986, Environmental Research Institute of Michigan, Ann Arbor, p. 627-636.

# Preliminary analysis of Airborne Visible/Infrared Imaging Spectrometer (AVIRIS) for mineralogic mapping at sites in Nevada and Colorado

Fred A. Kruse, Dan L. Taranik, and Kathryn S. Kierein-Young
Center for the Study of Earth from Space (CSES)
Cooperative Institute for Research in Environmental Sciences
University of Colorado, Boulder, Colorado 80309-0449

## ABSTRACT

Airborne Visible/Infrared Imaging Spectrometer (AVIRIS) data for sites in Nevada and Colorado were evaluated to determine their utility for mineralogical mapping in support of geologic investigations. Initially, the bad data lines were removed by replacing them with the average of adjacent lines. Bad spectral bands were replaced by the average of adjacent bands. The dark signal was subtracted from the data and the data were normalized using an equal energy normalization; a technique commonly used with imaging spectrometer data to reduce albedo effects. Techniques previously used with the Airborne Imaging Spectrometer (AIS) were utilized to reduce the AVIRIS data to internal average relative (IAR) reflectance by dividing the spectrum for each pixel of the image by the global average spectrum for the image. Spectra, profiles, and stacked, color-coded spectra were extracted from the AVIRIS data using an interactive analysis program (QLook) and these derivative data were compared to AIS results, field and laboratory spectra, and geologic maps. Images showing the spatial distribution of specific minerals were made using three band color-composites in the QLook environment. A feature extraction algorithm was used to extract and characterize absorption features from AVIRIS and laboratory spectra, allowing direct comparison of the position and shape of absorption features.

Both muscovite and carbonate spectra were identified in the Nevada AVIRIS data by comparison with laboratory and AIS spectra, and an image was made that showed the distribution of these minerals for the entire site. However, severe signal-to noise problems degraded the quality of all spectra extracted from the AVIRIS data and differentiation between calcite and limestone, and muscovite and montmorillonite, previously demonstrated with AIS data, was not possible using the AVIRIS spectra. Additional, distinctive spectra were located for an unknown mineral. This mineral was also located with AIS data and it is likely a zeolite mineral, however, this has not yet been verified with field or laboratory measurements. For the two Colorado sites, the signal-to-noise problem was significantly worse and attempts to extract meaningful spectra were unsuccessful. Problems with the Colorado AVIRIS data were accentuated by the IAR reflectance technique because of moderate vegetation cover. Improved signal-to-noise and alternative calibration procedures will be required to produce satisfactory reflectance spectra from these data. Although the AVIRIS data were useful for mapping strong mineral absorption features and producing mineral maps at the Nevada site, it is clear that significant improvements to the instrument performance are required before AVIRIS will be an operational instrument.

## INTRODUCTION

The Airborne Visible/Infrared Imaging Spectrometer (AVIRIS) is the first of a second generation of imaging spectrometers. It is a 224-channel instrument measuring surface radiance over the spectral range 0.41 to 2.45 μm in approximately 10 nm-wide bands (Porter and Enmark, 1987). The AVIRIS is flown aboard the NASA U-2 and ER-2 aircraft at an altitude of 20 km, with an instantaneous field of view of 20 m and a swath width of 10 km. It utilizes a linear array of discrete detectors and four individual spectrometers to collect data simultaneously for the 224 bands in a 614 pixel-wide swath perpendicular to the the aircraft direction. The forward motion of the aircraft moves the ground field of view across the terrain.

AVIRIS was flown for two well characterized sites during 1987, one in Nevada and one near Cripple Creek and Canon City, Colorado. The primary objective of this study was to assess the AVIRIS data characteristics and quality and the usefulness of the data for detailed mapping of subtle lithological variation. The AVIRIS data are being evaluated using image and spectrum processing techniques based on known physical properties of geologic materials. The investigation utilizes laboratory, field, and aircraft spectral measurements and geologic data to evaluate selected characteristics of the AVIRIS data. AVIRIS data are calibrated to reflectance and their capability to detect subtle mineralogical variations in the rocks and soils at both test sites is being tested.

## PREPROCESSING

Preprocessing of the AVIRIS data is required to obtain spectra that can be compared with laboratory spectra and to allow mineralogical mapping. The AVIRIS data for the sites used in this study were converted to internal average relative (IAR) reflectance (Kruse, 1988) using five preprocessing steps. This conversion has been successfully used with AIS data and does not require *a priori* knowledge of the site. One band of the raw AVIRIS data for each site was read from the tape to preview the data coverage. Because the AVIRIS data sets are very large, a 244 line by 192 sample subscene was selected from the raw band

previewed for each site. Sixty four of the AVIRIS raw data bands from the D spectrometer (1.83 to 2.45μm) were used in the study.

The first preprocessing step was to locate bad bands in the AVIRIS data and replace them with the average of adjacent bands. The positions of the bad bands were recorded so interpretations would not be made using those particular bands. The next step in the data processing was the removal of bad data lines. The bad lines were replaced with the average of adjacent lines. The positions of the bad lines were also recorded so as not to be used in the interpretation. Next the dark current file was subtracted from the AVIRIS data set. Because of the high noise level in the dark current file, a running 7 line by 1 band box was used to filter the data. This filtered dark current file was subtracted from the AVIRIS data set. An equal energy normalization was performed next on the AVIRIS data. The normalization was done by calculating a multiplier for each pixel that scales the data to a total image average (Dykstra and Segal, 1985; Kruse, 1987, 1988). This normalization removes albedo differences and topography effects by shifting the spectra to the same relative brightness. The normalized data were finally converted to internal average relative (IAR) reflectance (Kruse, 1988). This method converts the data to a quantity approximating reflectance by dividing the spectrum for each pixel by the overall average spectrum for the image. This technique also removes the major atmospheric features because the average spectrum contains atmospheric features which are divided out of the resulting spectra. Caution must be used when applying the IAR reflectance technique because spurious features can be introduced into the converted spectra if the average contains strong absorption features related to the surface composition. The average spectrum for the Nevada site did not show any of these absorption features. The Cripple Creek average data, however, had strong vegetation features which produced unusual spectra not characteristic of geologic materials.

## DATA ANALYSIS

A new software package called "QLook" developed by the United States Geological Survey in Flagstaff, Arizona and enhanced by CSES was used for the AVIRIS data analysis. QLook is a software

package that allows interactive analysis of imaging spectrometer data. This software runs under the Transportable Applications Executive (TAE) on MicroVAXII computers utilizing GKS graphics and an IVAS 1024 display device. QLook can handle up to three million pixels at one time and needs 12 megabytes of address space. Using a subscene containing 244 lines and 192 pixels allows 64 bands to be viewed at once.

The IVAS display device has a 1024 by 1024 monitor which shows the AVIRIS subscene zoomed by four. This allows individual pixels to be selected for the spectral analysis. Part of the IVAS display shows a spatial image and the rest of the display shows a stacked, gray-scaled or color-coded spectral image (Marsh and McKeon, 1983; Kruse, 1987, 1988). The stacked spectra correspond to a slice through the spatial image which can be interactively selected in real time using the mouse. The mouse also controls the spatial location, band, and stretch being viewed. A movie stepping through all the bands of the spatial image can be displayed. A three band color composite can be selected and displayed as the spatial image or the stacked spectra and black and white image can be psuedocolored with four different look-up-tables.

The GKS graphics software is used to plot the spectrum for the pixel at the current cursor position. A window with information about the currently viewed bands is displayed along with a window containing the stretch plot. Individual spectra can be selected and saved in another window for comparison. An average spectrum from a group of pixels can be calculated and saved in a table along with the standard deviation and minimum and maximum values. The data in this table is used as input into the feature extraction routines.

One difficulty confronting researchers is that the immense volume of data collected by imaging spectrometers prohibit detailed manual analysis. CSES is developing automated techniques for analysis of imaging spectrometer data that emulate the analytical processes used by a human observer. Automatic absorption feature extraction algorithms have been developed that allow subjective characterization of absorption bands. A continuum is defined by identifying high points in the spectrum

and fitting straight line segments between the high points. The continuum is removed from the data using division. The low points of the resulting spectrum are identified and the position, depth, and width of the absorption bands are determined (Kruse and Calvin, 1988). These results are input into an expert system which identifies the minerals based upon facts and rules derived from labatory spectra.

## Northern Grapevine Mountains, Nevada

The Nevada study area in the northern Grapevine Mountains has been studied in detail using conventional geologic mapping, geochemistry, field and laboratory reflectance spectroscopy, and imaging spectrometers (Raines and others, 1984; Wrucke and others, 1984; Kruse, 1987, 1988). Precambrian bedrock in the area consists of sedimentary (limestone, dolomite) and metasedimentary rocks (marble, hornfels, skarn). Mesozoic plutonic rocks include quartz syenite, a quartz monzonite porphyry stock, and quartz monzonite dikes. Tertiary volcanic rocks (primarily Timber Mountain Tuff, Wrucke and others, 1984) are abundant around the periphery of the study area. Quaternary deposits include Holocene and Pleistocene fanglomerates, pediment gravels, and alluvium.

The Mesozoic rocks are cut by narrow north-trending mineralized shear zones containing sericite (fine grained muscovite) and iron oxide minerals. Slightly broader zones of disseminated quartz, pyrite, sericite, chalcopyrite, and fluorite mineralization occur in the quartz monzonite porphyry. This type of alteration is spatially associated with fine-grained quartz monzonite dikes. There are several small areas of quartz stockwork exposed at the surface in the center of the area. Skarn, composed mainly of brown andradite garnet intergrown with calcite, epidote, and tremolite, occurs around the perimeter of the quartz monzonite stock in Precambrian rocks.

The Nevada site has been studied in detail using Airborne Imaging Spectrometer (AIS) data (Kruse, 1987, 1988). Figure 1 shows a mosaic of 7 AIS flightlines obtained between 1984 and 1986. AVIRIS data have obvious advantages over AIS because of the 10 km swath width and excellent image geometry. Figure 2 shows part of an AVIRIS image for the Nevada site. The AVIRIS data for

this site were reduced to IAR reflectance as described in the preprocessing section. The QLook program was used to extract spectra for areas of known mineralogy. Figure 3 shows an AVIRIS spectrum for sericite (fine grained muscovite) compared to a laboratory spectrum of muscovite. Figure 4 shows an AVIRIS carbonate spectrum compared to a laboratory spectrum of dolomite. Both AVIRIS spectra are very noisy, despite the fact that they are averages of several pixels. Sericite and dolomite have very strong absorption features and yet are only marginally identifiable using the AVIRIS data because of the noise. Additional spectra with a broad band near 2.4 μm were located in the AVIRIS data. Similar spectra for an unidentified mineral were also located with AIS data and the mineral is likely a zeolite, however, this has not yet been verified with field or laboratory measurements. Known occurrences of montmorillonite at this site were not identified using the AVIRIS data and it was not possible to distinguish between dolomite and calcite using the AVIRIS. These findings indicate that the AVIRIS data is not as useful as the AIS data for mapping subtle mineralogical variation, primarily because of signal-to-noise problems.

## Cripple Creek/Canon City, Colorado

The Cripple Creek mining district is located 21 miles southwest of Colorado springs (Figure 5). The district is hosted by a silica-undersaturated alkalic intrusive complex (Thompson, 1986). The most voluminous rock within the intrusive complex is a phonolitic breccia. This breccia has a bimodal size distribution and contains Precambrian and Tertiary rock fragments. The texture, structure and composition of the suggest a diatreme-like origin showing several root centers and episodes of activity (Wobus and others, 1976). The Pikes Peak Granite borders the Cripple Creek district to the north and is a medium to coarsely crystalline hornblende-biotite granite, locally grading to quartz monzonite. Lode gold mineralization is hosted by the upper Oligocene age phonolitic breccia pipes which have produced over 21 million ounces of gold since discovery in 1891. The objective of the work at Cripple Creek is to identify and map lithological

variation related to emplacement of the intrusive rocks and subtle lithological variation caused by hydrothermal alteration. It is expected that the AVIRIS data will contribute to a better understanding of the volcanic center and the processes that localized the gold deposits.

The Canon City Embayment lies 20 miles directly south of the Cripple Creek mining district. It is a large syncline which pitches to the southeast and contains long, continuous surface exposures of sedimentary rocks ranging from Ordovician to Tertiary age (Scott and others, 1978). The sedimentary units include limestones and dolomites, conglomerates, sandstones, siltstones, and shales. The embayment is bounded on the west side by Precambrian granites, gneisses and schists and to the north by Precambrian granodiorite. The Canon City oil field has produced over 14 million barrels of oil since its discovery in 1887. The objective of the work at Canon City is to identify and map lithological variation related to primary sedimentary deposition and subsequent changes produced by surface weathering. It is anticipated that the imaging spectrometer data will provide information about subtle lithological variation within mapped units that will lead to an improved understanding of the conditions of deposition of the sedimentary rock sequence.

The Cripple Creek/Canon City AVIRIS data were reduced to IAR reflectance using the procedures discussed in the preprocessing section. QLook was used to extract spectra from the data and to produce images and stacked, color-coded spectra. No meaningful spectra could be extracted from this data set because of severe signal-to-noise problems. Problems with the Colorado AVIRIS data were accentuated by the IAR reflectance technique because of moderate vegetation cover. Alternative calibration procedures will be required to produce satisfactory reflectance spectra even when the signal-to-noise problems are corrected.

## CONCLUSIONS

Software has been developed to correct AVIRIS data for bad lines and bad bands. Additional procedures have been developed for dark subtraction, normalization and reduction to IAR reflectance. IAR reflectance images have been produced, spectra

extracted, and minerals identified. Absorption features have been successfully extracted and characterized for AVIRIS spectra using automated feature extraction procedures. First results from the Nevada AVIRIS data for areas of known mineralogy show matches between extracted absorption features and laboratory measurements despite signal-to-noise problems. Initial evaluations of the Colorado AVIRIS data indicate that image geometry is excellent, however, severe signal-to-noise problems have hindered evaluation of spectral characteristics.

Evaluation of the 1987 data will continue, with additional laboratory analysis and field investigations planned for the remainder of 1988 and 1989. Analysis software will be refined and additional algorithms developed. Additional AVIRIS data has been requested for the 1988 flight season and if the improved signal-to-noise is adequate, the data will be re-evaluated for mapping subtle lithological variation.

## REFERENCES


Dykstra, J. D., and Segal, D. B., 1985, Analysis of AIS data of the Recluse Oil Field, Recluse, Wyoming: in Proceedings, AIS workshop, 8-10 April, 1985, JPL Publication 85-41, Jet Propulsion Laboratory, Pasadena, California, p. 86-91.

Kruse, F. A., 1987, Mapping hydrothermally altered rocks in the northern Grapevine Mountain, Nevada and California with the Airborne Imaging Spectrometer: in Proceedings, Third AIS workshop, 2-4 June, 1987, JPL Publication 87-30, Jet Propulsion Laboratory, Pasadena, California, p. 148-166.

Kruse, F. A., 1988, Use of Airborne Imaging Spectrometer data to map minerals associated with hydrothermally altered rocks in the northern Grapevine Mountains, Nevada and California: Remote Sensing of Environment, Special imaging spectrometer issue, V. 24, No. 1, p. 31-51.

Kruse, F. A., Calvin, W. M., and Seznec, Olivier, 1988, Automated extraction of absorption features from Airborne Visible/Infrared Imaging Spectrometer (AVIRIS) and Geophysical Environmental Research imaging spectrometer (GERIS) data: In Proceedings 1st AVIRIS performance evaluation workshop, JPL 6-8 June, 1988

Marsh, S. E., and McKeon, J. B., 1983, Integrated analysis of high-resolution field and airborne spectroradiometer data for alteration mapping: Econ. Geol., v. 78, no. 4, p. 618-632.

Porter, W. M., and Enmark, H. T., 1987, A system overview of the Airborne Visible/Infrared Imaging Spectrometer (AVIRIS): in Proceedings, 31st Annual International Technical Symposium, 16-21 August, 1987, Society of Photo-Optical Instrumentation Engineers, V. 834, p. 22-31.

Raines, G. L., Hoover, D. B., and Collins, W. E., 1984, Remote-sensing mineral discoveries in the Mojave Desert of California: in Proceedings, International Symposium on Remote Sensing of Environment, Third thematic conference, "Remote Sensing for Exploration Geology," Colorado Springs, Colorado, April, 1984, Environmental Research Institute of Michigan, Ann Arbor, p. 153-154.

Scott, G. R., Taylor, R. B., Epis, R. C., and Wobus, R. A. 1978, Geologic map of the Pueblo 1° x 2° quadrangle, south-central Colorado, U. S. Geological Survey, Miscellaneous Investigations Map I-1022, 2 sheets.

Thompson, T. B., "Cripple Creek Mining District-Fall Field Guidebook", Denver Region Exploration Geologists Society, 1986, 63 p.

Wobus,R.A., Epis,R.C., Scott,G.R., "Reconnaissance Geologic Map of the Cripple Creek - Pikes Peak Area, Teller, Fremont and El Paso Counties, Colorado", USGS Map MF 805, 1976.

Wrucke, C. T., Werschky, R. S., Raines, G. L., Blakely, R. J., Hoover, D. B., and Miller, M. S., 1984, Mineral resources and mineral resource potential of the Little Sand Spring Wilderness Study Area, Inyo County, California: U.S. Geological Survey Open File Report 84-557, 20 p.

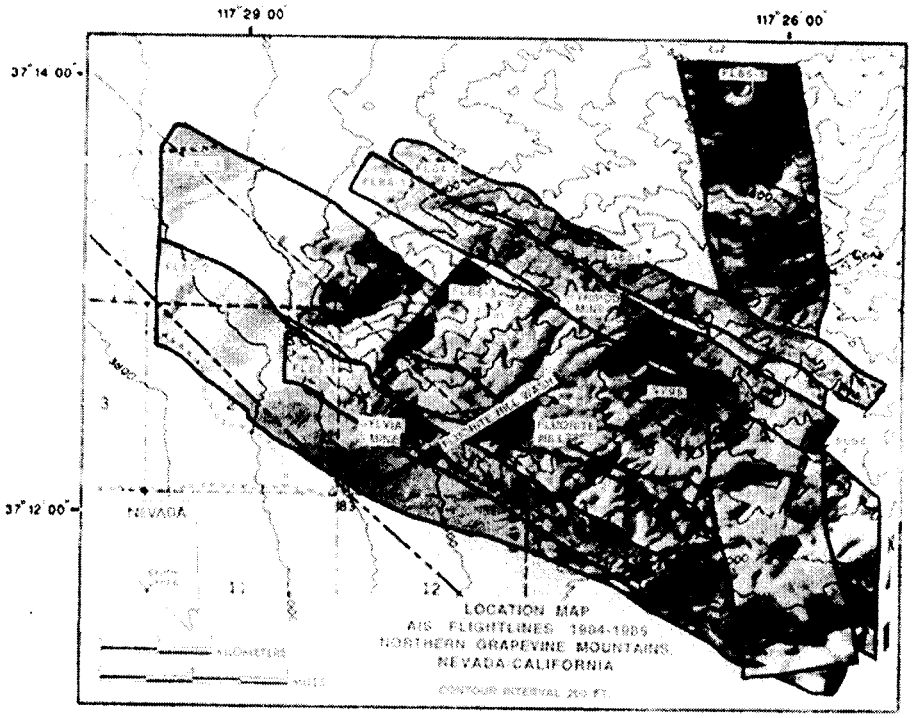


Figure 1 Nevada AIS single band mosaic, 2.0 μm.

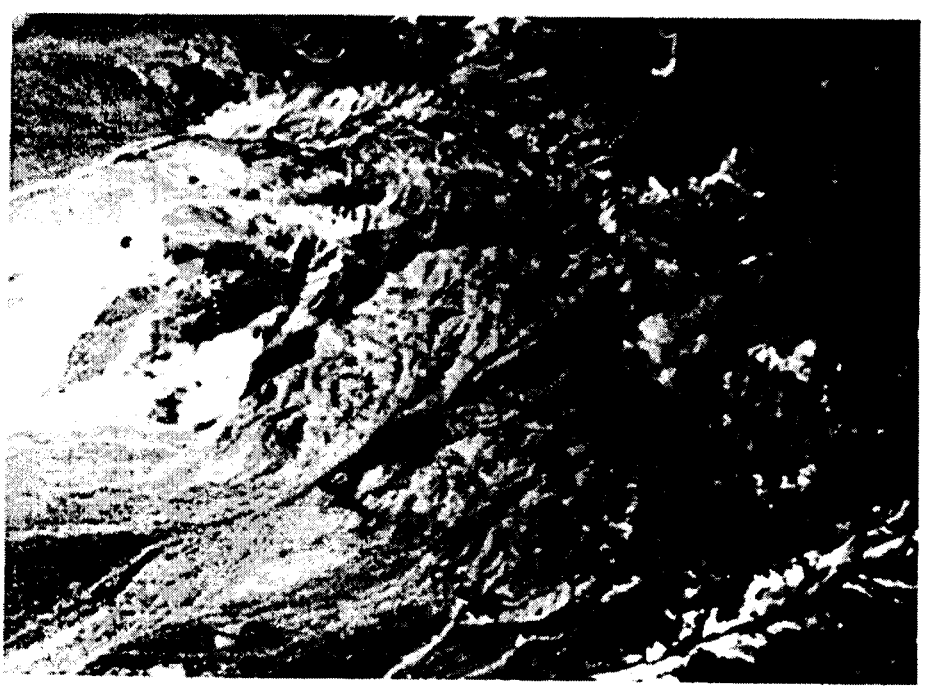

Figure 2 Nevada AVIRIS single band image, band 29, .67 μm.

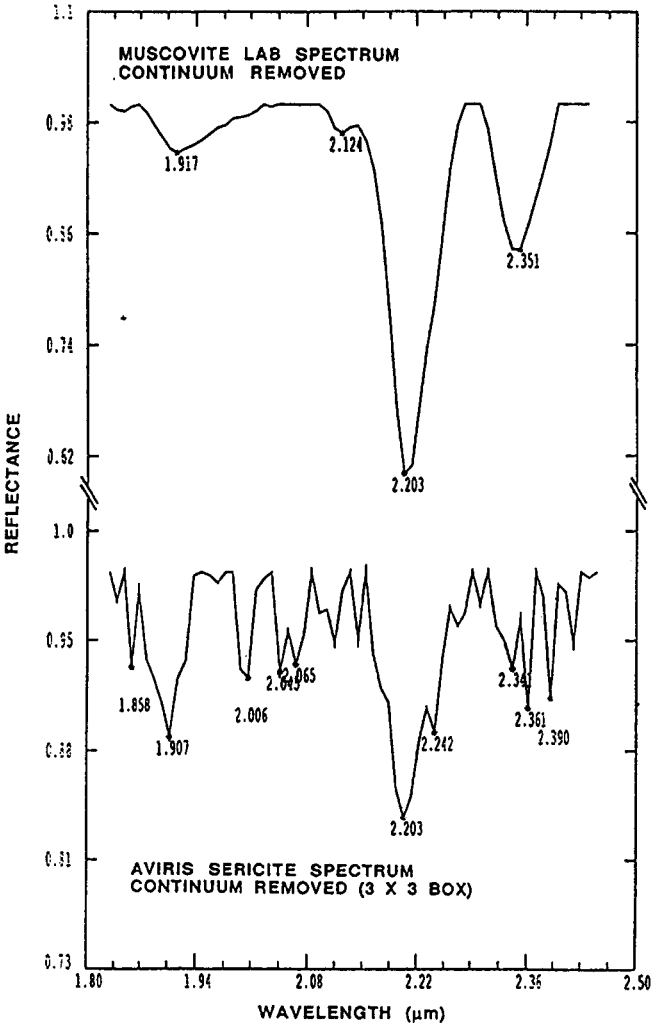


Figure 3. Nevada AVIRIS sericite compared to lab spectrum of muscovite.

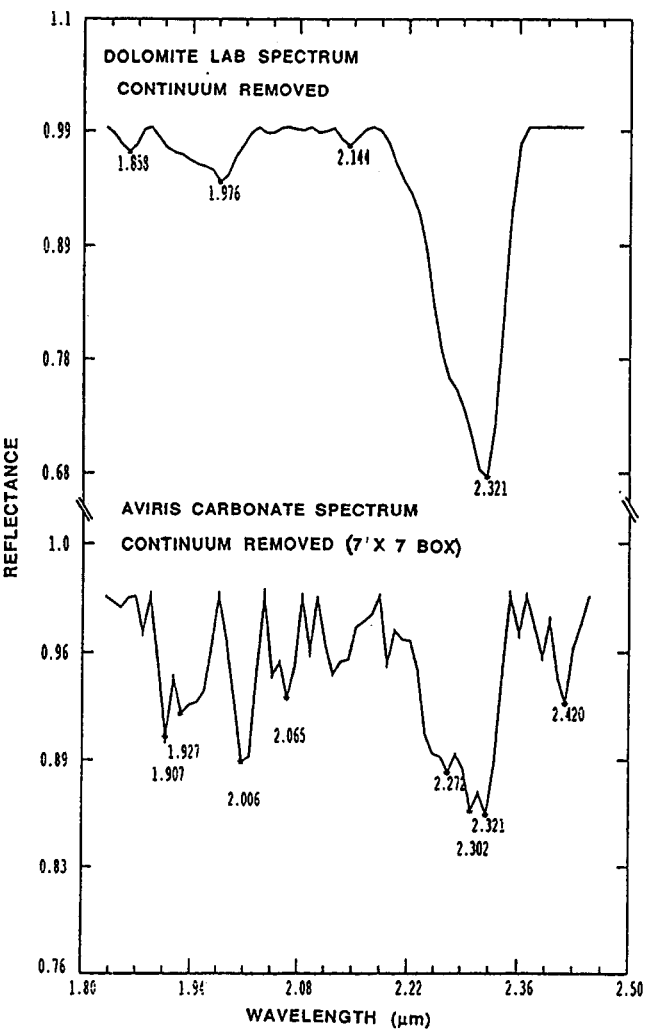


Figure 4. Nevada AVIRIS spectrum compared to lab spectrum of dolomite.

Figure 5. Location of Canon City and Cripple Creek AVIRIS study areas.

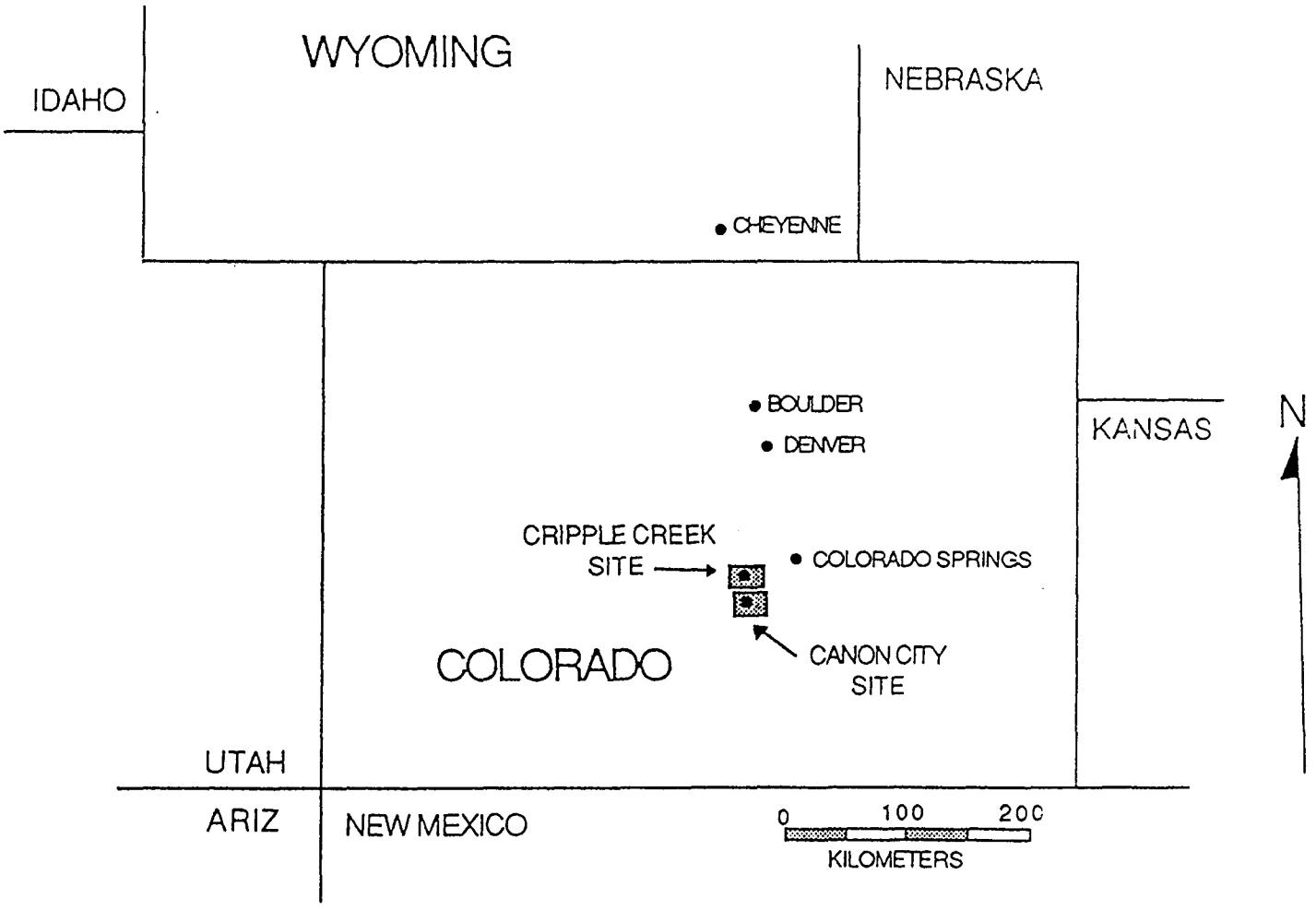

# ASSESSMENT OF AVIRIS DATA FROM VEGETATED SITES IN THE OWENS VALLEY, CALIFORNIA

ROCK, B. N., Complex Systems Research Center, University of New Hampshire, U. S. A.; ELVIDGE, C. D., Desert Research Institute, University of Nevada, U. S. A.; and DEFEO, N. J., Complex Systems Research Center, University of New Hampshire, U. S. A.

## ABSTRACT

Airborne Visible/Infrared Imaging Spectrometer (AVIRIS) data were acquired for the Bishop, CA area, located at the northern end of the Owens Valley, on July 30, 1987. Radiometrically-corrected AVIRIS data were flat-field corrected, and spectral curves produced and analyzed for pixels taken from both native and cultivated vegetation sites, using the JPL SPAM software program and PC-based spreadsheet programs. Analyses focussed on the chlorophyll well and red edge portions of the spectral curves. Results include the following: AVIRIS spectral data are acquired at sufficient spectral resolution to allow detection of "blue shifts" of both the chlorophyll well and red edge in moisture-stressed vegetation when compared with non-stressed vegetation; a normalization of selected parameters (chlorophyll well and near infrared shoulder) may be used to emphasize the shift in red edge position; and the presence of the red edge in AVIRIS spectral curves may be useful in detecting small amounts (20-30% cover) of semi-arid and arid vegetation ground cover. A discussion of possible causes of AVIRIS red edge shifts in response to stress is presented.

## INTRODUCTION

The detection of various types of stress in vegetation using in situ high-spectral resolution reflectance data has focussed on the red edge portion of the vegetation reflectance curve (Chang and Collins, 1983; Collins et al., 1983; Horler et al., 1980; Rock et al., 1986, 1988; Westman and Price, 1988). The shift of the red edge to shorter wavelengths (ie. toward the blue end of the visible spectrum) has been termed the "blue shift," and has been shown to occur in plants exposed to a variety of stress agents, including trace metals, airborne pollutants, and drying. A similar blue shift of the maximum absorption by chlorophyll pigments in the visible red, termed the chlorophyll well, has also been observed in vegetation exposed to these stress agents. These blue shifts are very subtle and range from 2-15 nm.

Datasets from airborne high-spectral resolution sensor systems have used blue shifts of red edge parameters (both red edge and chlorophyll wells) to detect and map areas of stressed vegetation (Collins et al., 1983; Milton et al., 1983; Rock et al., 1988). The airborne sensor systems used provided a large number of spectral bands, with spectral resolution on the order

of a few nanometers. Rock et al. (1988) used an airborne system known as the Fluorescence Line Imager (FLI), providing 288 spectral channels covering the spectral region from 0.4-0.8 um, each 2.3 nm wide, to detect and map areas of forest decline damage in Vermont (USA) thought to be due to air pollution. The present study was conducted in part, to determine if AVIRIS datasets acquired in 210 spectral channels (for radiometrically-corrected data) in the spectral region from 0.4-2.4 um, each 9.8 nm wide, would provide adequate spectral resolution to resolve red edge parameter blue shifts.

Although an attempt was made to acquire AVIRIS data for the forest decline damage sites in the northeastern United States, a lack of cloud-free weather conditions in the New England area during July, 1987 prevented such data acquisition. An AVIRIS overflight on July 30, 1987 did acquire excellent data for the northern end of the Owens Valley, CA, an area characterized as semi-arid, exhibiting extensive vegetation cover dominated by members of the Great Basin sagebrush community and saltbush community. Along river courses a number of tree species form dense canopies, and heavily irrigated areas support either agricultural crops such as alfalfa, or grass-dominated areas such as pastures, lawns, and a golf course. Based on a field visit, vegetated areas were selected from the flightline which represented three basic vegetation types: lush, green vegetation; dry, semi-arid vegetation; and cut, dried, vegetation which had been green prior to cutting. Preliminary analyses of AVIRIS data acquired for these vegetation types are presented.

## MATERIALS AND METHODS

AVIRIS data used in this study are from flight line #10, Run #009, Segment 03, and were acquired on July 30th, 1987 at approximately 11:36 AM Pacific Standard Time. The flight line was selected for study because of the diversity of vegetation types occurring near the town of Bishop, CA (37°22'N X 118°20'W) and the surrounding area. In addition, these data were selected because of their high quality. The AVIRIS data presented here are radiometrically corrected and have been flat-field corrected.

The radiometrically-corrected data were obtained from the Jet Propulsion Laboratory in Pasadena, CA. The radiometric correction was accomplished by subtracting the dark current values from the raw data, equalizing the response of the 224 individual detectors and resampling the wavelenghts to a uniform 9.8 nm sampling interval. The radiometrically-corrected data contain 210 spectral bands with band centers ranging from 0.4000 um (band 1) to 2.4482 um (band 210). The response of each detector is such that the same amount of reflected radiance in each of the bands would yield the same DN (digital number) value.

A flat-field correction was applied to the data to remove the effect of solar irradiance. A grus pit (consisting of the weathered products of granitic rocks) was used as the flat field. For each spectral band, pixel values from all vegetated sites

were divided by pixel values from the grus pit. Because the grus pit contains no vegetation, all the spectral data from the vegetation at the other sites was preserved while the component of solar irradiance was eliminated. A secondary effect of flat-field correction is the removal of atmospheric absorption features common to both the grus pit and vegetation datasets. The resulting spectral curves, produced by plotting brightness values of the 210 bands for each pixel or group of pixels were comparable to laboratory- or field-acquired spectra of vegetation. The resulting brightness values have not been converted to reflectance as yet, but this would be possible since ground reflectance data have been acquired for the grus pit calibration targets included within the AVIRIS flightline. The curves presented here were plotted on a Macintosh Plus using Cricket Graph software*. All plots are averages of several pixels from the areas cited.

It is difficult to compare red edge and chlorophyll well parameters from spectral curve plots because of variations in the height of the NIR (near infrared) plateau and the depth of the chlorophyll well characteristic of different vegetation types. If the data are normalized, differences in the position of the red edge and the extent of the blue shift can be more easily studied. Therefore, the data were normalized as follows. For each spectral curve, the value corresponding to the lowest spectral band in the chlorophyll well was subtracted from every spectral band in the curve. For all vegetated sites along the flight line, the lowest value occurred at either spectral band 29 (band center = 0.6744 um) or 30 (band center = 0.6842 um). The second step in the normalization involved scaling the curve so that channel 38 (band center = 0.7626 um) on the NIR plateau had a value of two. With these two points on each curve pinioned, the resulting curves clearly show relative red edge positions.

The native vegetation occurring in the Bishop, CA area include the following dominant types. In July, lush, green trees and large shrubs occur along stream banks and areas of damp soil, while semi-arid, non-green or partially green sagebrush/saltbush shrubs occupy drier sites. Common tree species are cottonwoods (Populus) and willows (Salix) and these occur in dense stands where there is enough soil moisture to support their growth. At drier sites, only low desert shrubs are found, consisting of either sagebrush (Artemisia tridentata) or rabbit brush (Chrysothamnus nauseosus). The rabbit brush characterizes disturbed areas (pasture lands) while the sagebrush is more typical of open range lands that are largely undisturbed. In drier sites characterized by soils high in salt levels, a small desert shrub known as saltbush (Atriplex spp.) is common. During the summer months, sagebrush retains its leaves, while rabbit brush and saltbush may lose their leaves.

Along portions of the AVIRIS flightline three major types of

* Reference to specific products is made for clarity, and does not constitute an endorsement of these products.

cultivated vegetation occurs: large areas of alfalfa (Medicago sativa) grown in rotation (some fields with green, actively growing plants, and other fields with cut, drying plants); a large golf course of green, well-watered grasses and trees (cottonwoods); and irrigated pastures of green grass. The alfalfa fields were of great interest in this study because they provided large, homogeneous areas of either green or dried plants of the same species. Because of their rectangular shape, they could be easily identified in the AVIRIS data. The harvesting of alfalfa results in rows of cut plants alternating with partly green stubble and exposed soil.

## RESULTS AND DISCUSSION

Radiometrically-corrected AVIRIS data are strongly influenced by both variation in solar illumination and by atmospheric absorption features. Figure 1 presents such AVIRIS spectral data acquired from the golf course. Note the decreasing brightness with increasing band numbers (wavelength) due to the drop in solar illumination intensity, as well as absorption by atmospheric water, centered at bands 57 (0.9488 um), 76 (1.1350 um), and 102 (1.3898 um). The absorption feature located at band 38 (0.7626 um) is likely due to atmospheric molecular oxygen, while the strong absorption centered at band 29 (0.6744 um) is due to chlorophyll in the vegetation. This feature is referred to herein as the chlorophyll well, and is followed by a sharp rise, the red edge, located between bands 30 and 37. The broad absorption in bands 1-12 (0.4000-0.5078 um) is due to both chlorophyll and carotenoid pigments.

Raw spectral data for the grus pits used for flat-field correction are presented in Figure 2. Many of the same absorption features seen in Figure 1 are also seen in Figure 2 (features at bands 38, 57, 76, and 102), indicating that they are common atmospheric components. A broad absorption seen centered at band 150 (1.8602 um) is due to atmosphereic water, while the strong feature at band 2 (0.4098 um) is likely due to iron oxide found in the grus. Causes of the absorption features at bands 89 (1.2624 um) and 165 (2.0072 um) have not yet been identified.

Flat-field corrected spectral curves are presented in Figure 3 for the golf course, green alfalfa, and an area of low rabbit brush and grass (approximately 20-30% cover). Note that the flat-field correction has removed the effects of variable intensity of solar illumination and of atmospheric absorptions. Artifacts introduced into these curves by the flat-field correction method include a shift of one band in the position of the chlorophyll absorption maximum and the apparent lack of absorption by chlorophylls and carotenoids in the visible blue (bands 1-11), due to the strong iron oxide absorption seen in the grus. The overall results are most encouraging however, since the flat-field corrected curves for the golf course and alfalfa look very much like typical vegetation curves acquired with field and laboratory spectrometers.

A more detailed presentation of flat-field corrected visible and near infrared AVIRIS data is seen in Figure 4. Spectral curves for cottonwoods and green alfalfa show maximum absorption due to chlorophyll (the chlorophyll well) at band 30 (0.6842 um) while the chlorophyll well for drying alfalfa is located at band 29 (0.6744 um). Rock et al. (1988) report a five nanometer blue shift in chlorophyll well position with increased damage in spruce (Picea) forests as measured by the airborne FLI, although a similar blue shift of only two nanometers was measured in situ. Westman and Price (1988) report a similar two nanometer blue shift in chlorophyll well position determined in situ for pines (Pinus) experimentally exposed to drying, acid misting, and ozone.

It is difficult to assess the true nature of the blue shift of the chlorophyll well reported here. Westman and Price (1988) attribute the blue shift seen in pine induced by drying to denaturing of chlorophylls. The blue shift seen in spruce has been correlated with decreases in the amount of chlorophyll b relative to chlorophyll a (Rock et al., 1988). The blue shift seen in Figure 4 may also be due to increased amounts of soil and stuble exposed by the cutting of alfalfa.

Note that the variations in amplitude of both red (bands 28-30) and NIR (bands 38-90) reflectance seen in the Figure 4 curves makes evaluation of the red edge position difficult. The red edge of green alfalfa appears shifted to shorter wavelengths when compared with the red edge of the cottonwoods. This apparent shift is due to the greater NIR reflectance seen for the green alfalfa, an effect which can be removed by normalizing the two curves. Figure 5 presents normalized red edge curves for the golf course, cottonwoods, and green alfalfa. This approach demonstrates that the red edge parameters for all three green vegetation types are very similar.

When the red edge data for the cut alfalfa are normalized to those of the green vegetation types (Figure 6) a distinct "shift" is seen such that the red edge curve for the drying vegetation is separated from the others. This blue shift of the red edge of cut alfalfa is very similar to that seen in normalized FLI data acquired from the forest decline sites (Rock et al., 1988). Regardless of the cause of the blue shift (alteration of plant pigments, increased reflectance from soil/stubble, etc.), it is clear that AVIRIS data have been acquired with sufficient spectral resolution to detect such spectral fine features associated with stress in vegetation.

The presence or absence of the red edge feature in spectral curve data may be useful in detecting trace amounts of vegetation in semi-arid regions. Although not presented in detail here, subtle changes in reflectance amplitude across the red edge region are seen in AVIRIS data for the sagebrush and rabbit brush areas of the flightline (see Figure 3). An investigation which relates the occurrence of such amplitude changes with percent ground cover and vegetation type will be needed to establish the

value of using red edge data for the purpose of trace vegetation detection and quantification.

ACKNOWLEDGEMENTS

The research reported here has been supported by the Earth Processes Branch of the National Aeronautics and Space Administration (NASA) and was carried out at the Jet Propulsion Laboratory (JPL), Pasadena, CA. Special thanks are given to Gregg Vane, Lisa Barge, and Alex Zak of JPL for their assistance in this effort.

REFERENCES

Chang, S.H., and Collins, W. 1983. Confirmation of the airborne biogeochemical mineral exploration technique using laboratory methods. Economic Geology 78:723-736.

Collins, W., Chang, S.H., Raines, G., Canney, F., and Ashley, F. 1983. Airborne biogeochemical mapping of hidden mineral deposits. Economic Geology 78:737-749.

Horler, D.N.H., Barber, J., and Barringer, A.R. 1980. Effects of heavy metals on the absorbance and reflectance spectra of plants. International Journal of Remote Sensing 1:121-136.

Milton, N.M., Collins, W., Chang, S.H., and Schmidt, R.G. 1983. Remote detection of metal anomalies on Pilot Mountain, Randolph County, North Carolina. Economic Geology 78:605-617.

Rock, B.N., Hoshizaki, T., and Miller, J.R. 1988. Comparison of in situ and airborne spectral measurements of the blue shift associated with forest decline. Remote Sensing of Environment 24:109-127.

Rock, B.N., Vogelmann, J.E., Williams, D.L., Vogelmann, A.F., and Hoshizaki, T. 1986. Remote detection of forest damage. BioScience 36:439-445.

Westman, W.E., and Price, C.V. 1988. Spectral changes in conifers subjected to air pollution and water stress: experimental studies. IEEE Transactions on Geoscience and Remote Sensing GE-26:11-21.

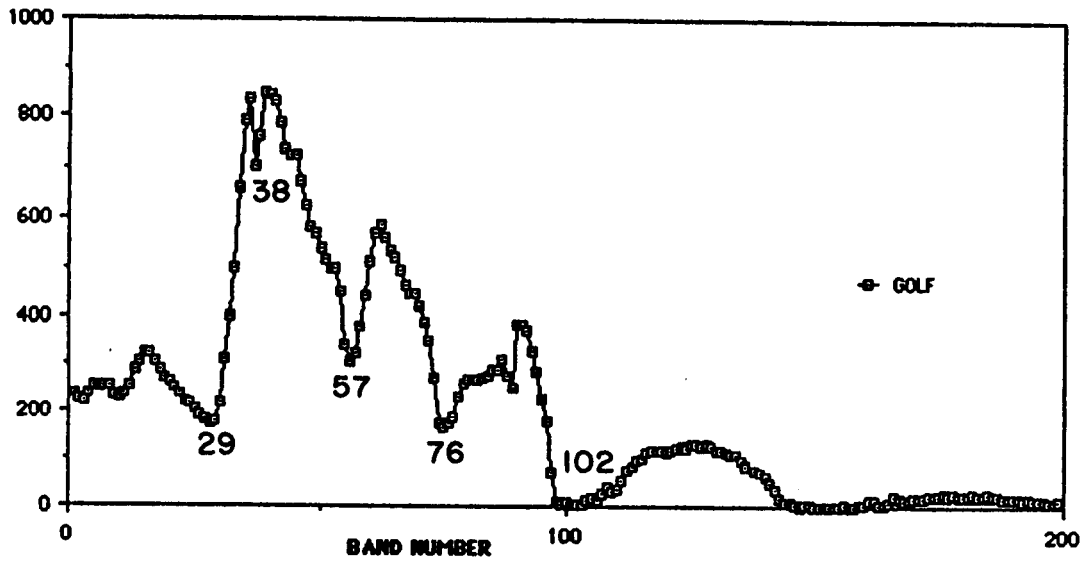


Figure 1. Radiometrically-corrected AVIRIS data plotted as DN vs. band numbers for pixels selected from the golf course. Band numbers discussed in text are labelled.

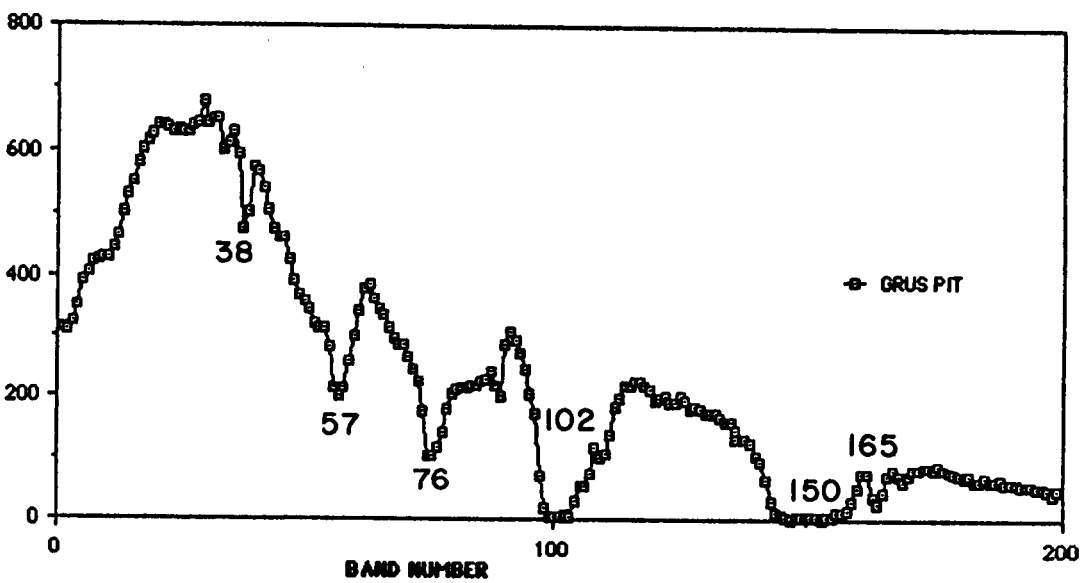


Figure 2. Radiometrically-corrected AVIRIS data plotted as DN vs. band numbers for pixels selected from the grus pits used as calibration targets. Band numbers discussed in text are labelled.

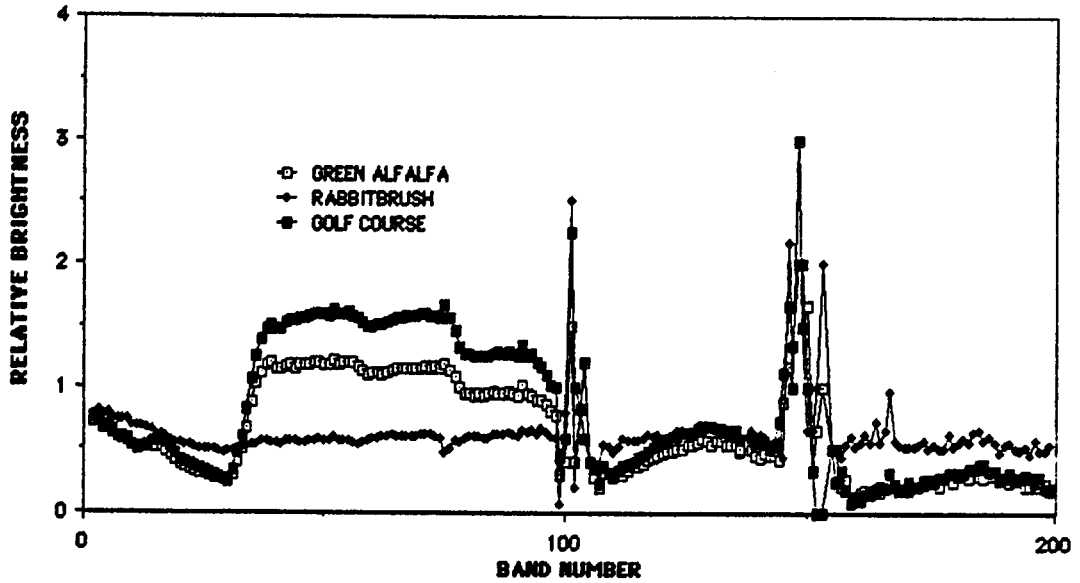


Figure 3. Flat-field corrected AVIRIS data plotted as relative brightness vs. band numbers for pixels selected from fields of green alfalfa, the golf course, and an area of low-density vegetation dominated by rabbit brush.

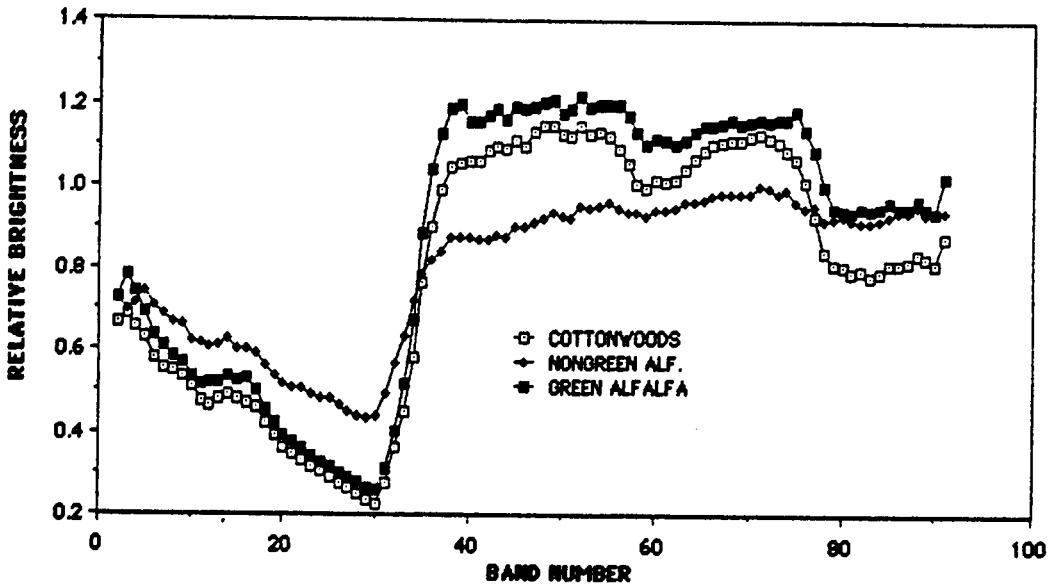


Figure 4. Flat-field corrected visible and near infrared AVIRIS data plotted as brightness values vs. band numbers for pixels selected from stands of cottonwoods and fields of green and cut alfalfa (labelled "nongreen alf."). Note the difference in both shape and position of the chlorophyll wells for green alfalfa and cottonwoods (centered at band 30) and drying alfalfa (centered at band 29).

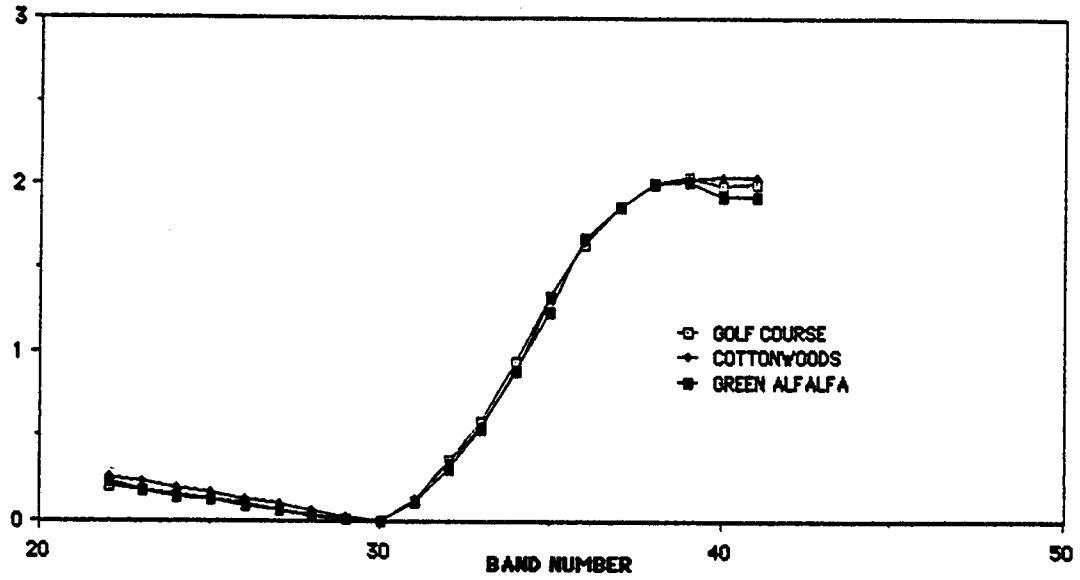


Figure 5. Normalized red edge AVIRIS data for three types of green vegetation: the golf course, cottonwoods, and alfalfa. Note the red edge position is very similar for all three types.

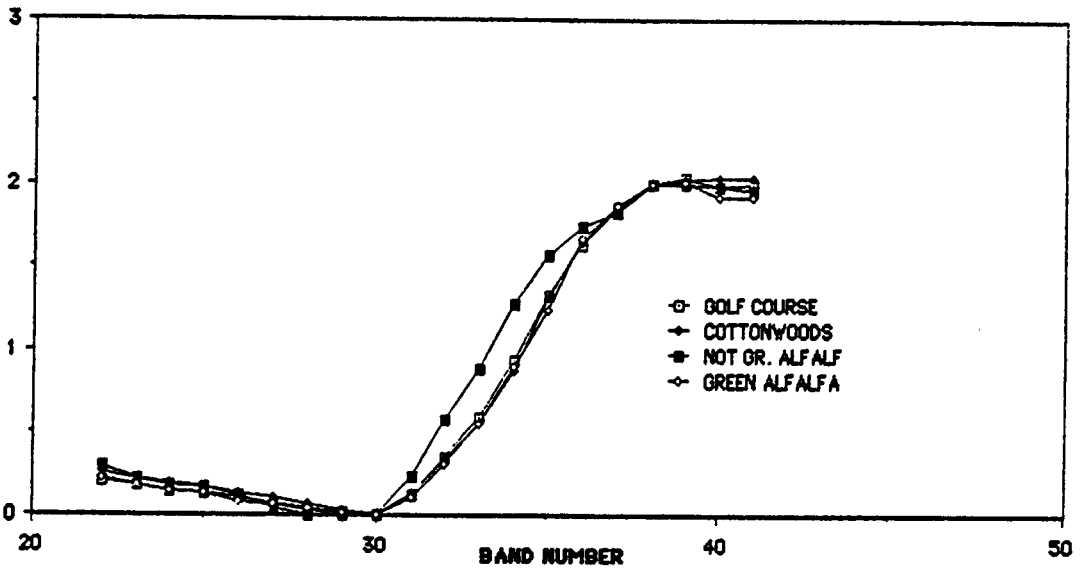


Figure 6. Normalized red edge AVIRIS data for three types of green vegetation (golf course, cottonwoods, and green alfalfa) and cut, drying alfalfa (labelled "not gr. alfalfa"). Note the change in position of the red edge of the cut alfalfa relative to the red edge of the green vegetation.

# EXAMINATION OF THE SPECTRAL FEATURES OF VEGETATION IN 1987 AVIRIS DATA

CHRISTOPHER D. ELVIDGE, Biological Sciences Center, Desert Research Institute, University of Nevada System, Reno, NV, U.S.A..

## ABSTRACT

Equations for converting AVIRIS digital numbers to percent reflectance were developed using a set of three calibration targets. AVIRIS reflectance spectra from five plant communities exhibit distinct spectral differences.

## 1. INTRODUCTION

A flight line of AVIRIS data covering Stanford University's 1200 acre Jasper Ridge Biological Preserve plus three calibration targets was acquire on July 24, 1987 at 12:56 PM Pacific Standard Time. Jasper Ridge is located directly west of the main campus, in the foothills of the Santa Cruz Mountains. The preserve contains examples of most of the major plant communities found along the Central California coast. A more detailed report on this study is provided by Elvidge (1988).

## 2. CALIBRATION OF AVIRIS DATA

The three calibration targets cover a wide range of reflectance values. At the bright end is the roof of the Pulgas Balancing Reservoir belonging to the San Francisco Water Department. This is a highly uniform buff-tan color surface with 35-45 % reflectance. A total of 84 AVIRIS pixels were extracted from the roof. An asphalt parking lot at Canada College was used as a target of intermediate brightness (10-25 % reflectance), providing 35 pixels. Bear Gulch Reservoir is used as the dark calibration target (0-5 % reflectance). A set of 64 lake water pixels were extracted from the reservoir.

Laboratory reflectance spectra were acquired of samples of the roof and asphalt surface using JPL's Beckman UV-5240 spectrophotometer. Due to a lack of access to Bear Gulch Reservoir, PFRS (JPL's Portable Field Reflectance Spectrometer) spectra from nearby Searsville Lake were used as surrogates for the reflectance of Bear Gulch Reservoir. The digital number value for each calibration target pixel has been paired to the average reflectance value for the target in all 209 bands of the radiometrically corrected data. These data sets were plotted and visually examined. Linear regression was used to develop equations of the form: Reflectance = A + B*DN. Highly linear relationships were found between digital numbers and reflectance for all three targets in the first two spectrometers (0.41 to 0.69 um and 0.69 to 1.27 um). Data from the third and fourth spectrometers exhibit in flight changes in the radiometric performance between the roof and the two darker targets plus Jasper Ridge. As a result, only the lake water and asphalt data was used to calibrate data from 1.28 to 2.45 um. There was no relationship between digital numbers and reflectance in the intense atmospheric water absorption bands

(e.g. at 1.40 um), signifying that the ground is not being seen with AVIRIS in these bands.

The results of the digital number to reflectance regressions for the 209 bands of radiometrically corrected AVIRIS data are summarized in Figure 1. The regression coefficients ($R^2$ values) versus wavelength are presented in the lower segment of Figure 1. Equations were formed only for bands yielding $R^2$ values of 0.7 or better. This excludes bands in three atmospheric water absorption regions (1.3506 to 1.4780 um, 1.7720 to 1.9852 um, and 2.3894 to 2.45 um). The middle segment of Figure 1 shows the slopes determined for the equation: Reflectance = A + B*DN. The upper segement of Figure 1 shows the "additive term" (digital number intercept for zero reflectance) versus wavelength. This curve, which is highest in the blue, depicts the radiance scattered in the atmosphere.

## 3. REFLECTANCE SPECTRA OF PLANT COMMUNITIES

Figure 2 shows the AVIRIS reflectance spectra derived from five plant communities. The spectra have been adjusted vertically to avoid overlap. The reflectance at 0.8 um is provided for each spectrum. The four plant communities containing green vegetation (golf course, swamp forest, broadleaf evergreen forest, and chaparral) all exhibit red edges, pigment absorptions in the visible, well developed NIR plateaus and leaf water absorption at longer wavelengths. Reflectance difference between plant communities in the pigment absorption region (0.4 to 0.7 um) are clearly visible in the reflectance spectra. The height of the NIR plateau above the pigment absorption and water absorption regions also varies between the plant communities.

The NIR plateau lobe between 1.0 and 1.2 um is normally coequal in height with the NIR lobe between 0.8 and 1.0 um in the reflectance spectra of green leaves. However, the lobe centered at 1.1 um has an abnormal height and shape in the golf course and swamp forest reflectance spectra. This may be due to a shattered blocking filter on the second spectrometer.

The reflectance spectrum of the dry annual grassland shows an absorption wing extending from the visible into the NIR. This is a typical spectral feature for dry yellow grass. Ligno-cellulose absorptions can be observed at 2.09, 2.26, and 2.33 um. A well developed absorption of probable ligno-cellulose origin can also be seen in the golf course spectrum from 2.30 to 2.38 um.

Figure 3 is an AVIRIS image of the Jasper Ridge area depicting the intensity of ligno-cellulose absorption. The image was formed by subtracting reflectance values for two composite bands centered at 2.20 and 2.35 um. Reflectance values in five AVIRIS bands (2.18 to 2.22 um) were averaged to form the first composite band, and eight bands (2.31 to 2.38 um) were averaged to form the second band. The ligno-cellulose vegetation index is of the form: reflectance at 2.20 um minus reflectance at 2.35 um. The strongest ligno-cellulose absorptions occur in dry grasslands, though measureable ligno-cellulose absorptions occurred in the chaparral and broadleaf evergreen forest.

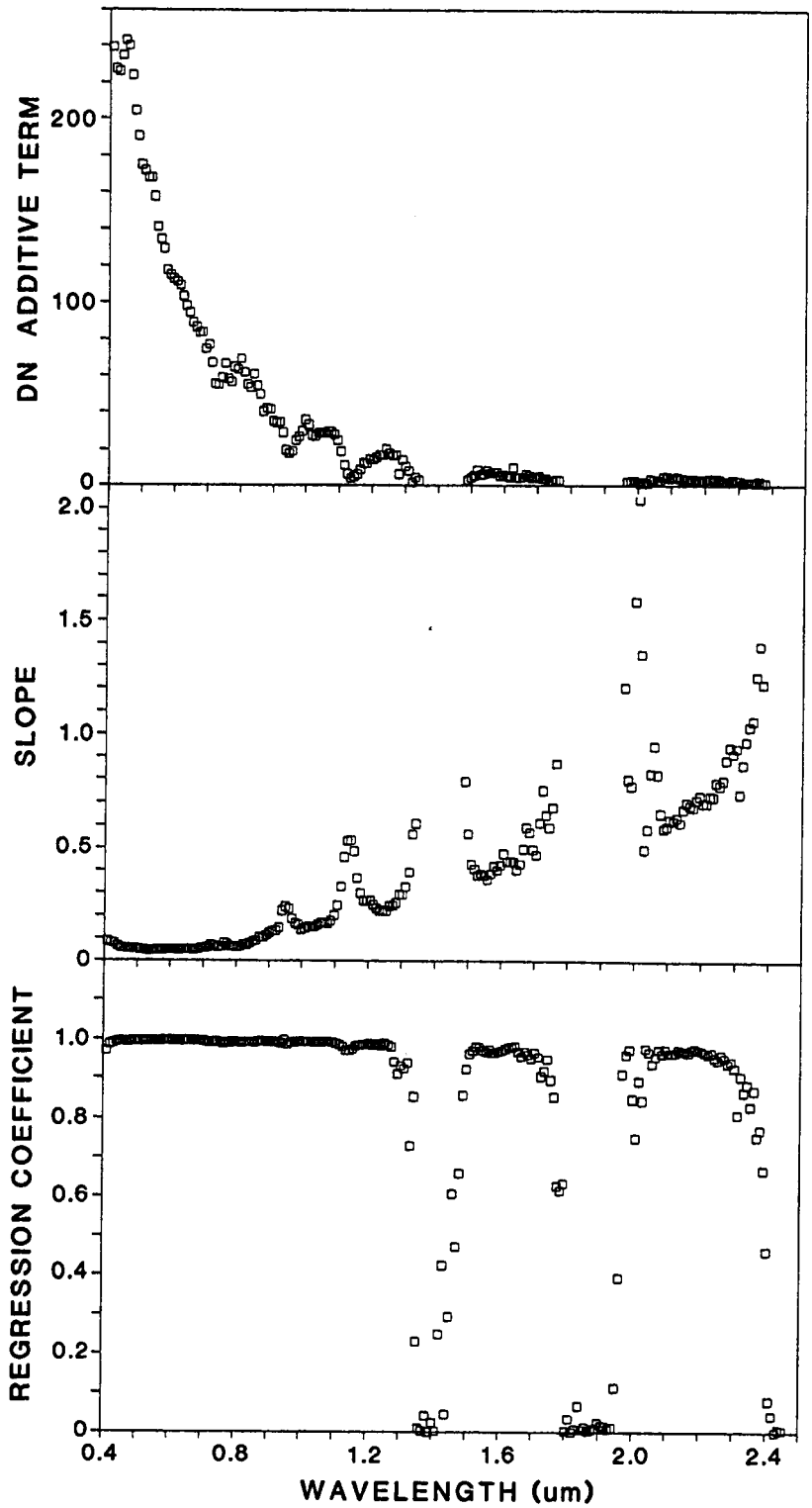


Figure 1. Results from the digital number to reflectance linear regressions.

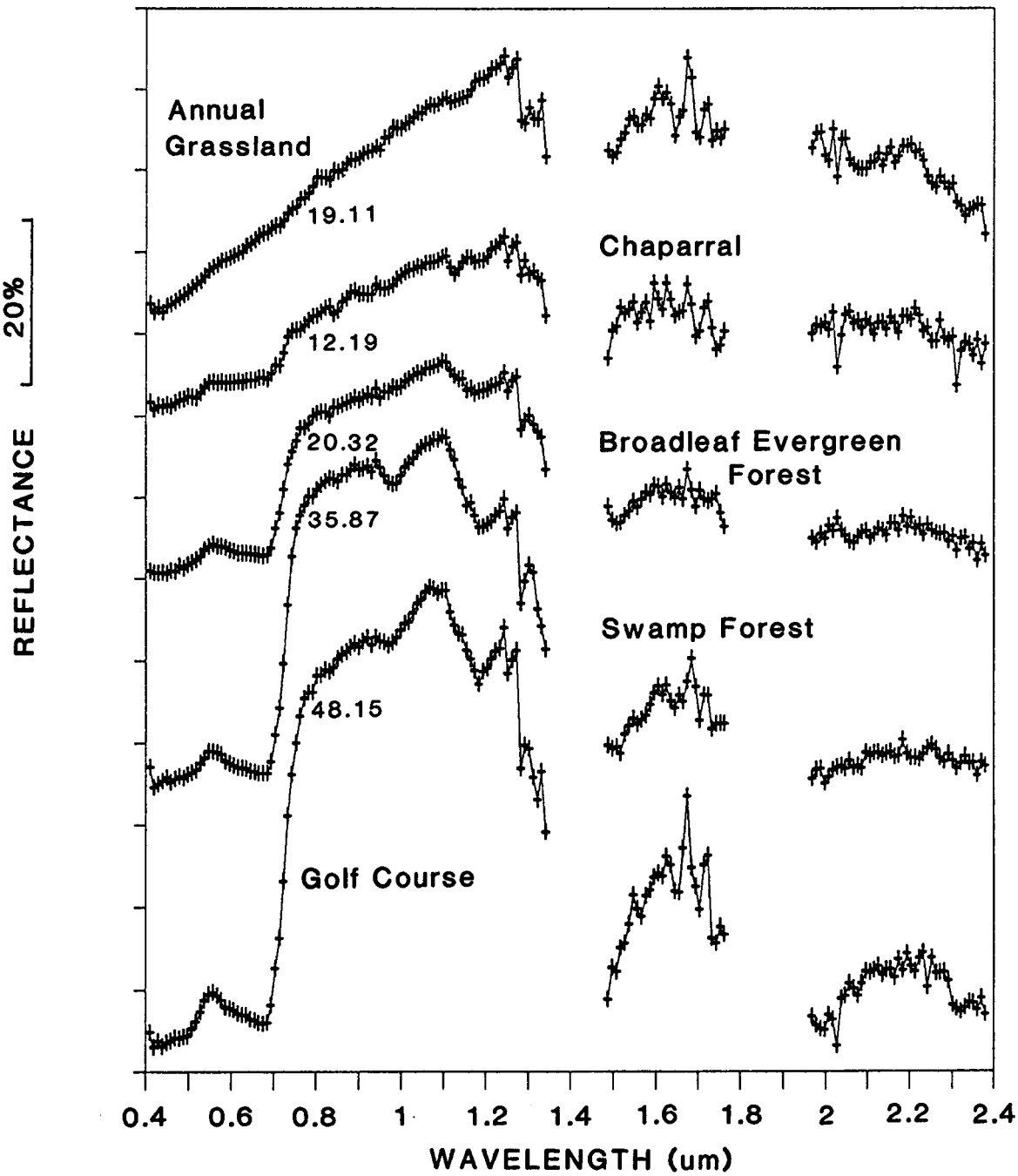


Figure 2. AVIRIS reflectance spectra averages for five plant communities: golf course (16 pixels), swamp forest (42 pixels), broadleaf evergreen forest (120 pixels), chaparral (49 pixels), and a senesced annual grassland (64 pixels).

## 4. CONCLUSION

AVIRIS data has been successfully employed to measure reflectance features of vegetation requiring high spectral resolution. Vegetation spectral features that have been observed in AVIRIS data include: details regarding pigment absorption in the visible, the red edge, leaf water absorptions at 0.97 and 1.19 um, and ligno-cellulose absorptions at 2.09, 2.26, and 2.33 um. The detail available in AVIRIS reflectance spectra is comparable to that obtained with laboratory spectrophotometers. Additional work will be required to develop techniques for measuring the spectral features of vegetation in AVIRIS data without the use of calibration targets.

## 5. REFERENCE

Elvidge, C.D., 1988, Vegetation reflectance features in AVIRIS data. Proceedings of the International Symposium on Remote Sensing of Environment, Sixth Thematic Conference, Remote Sensing for Exploration Geology, ERIM, Houston, TX, May 16-19, 14 p.

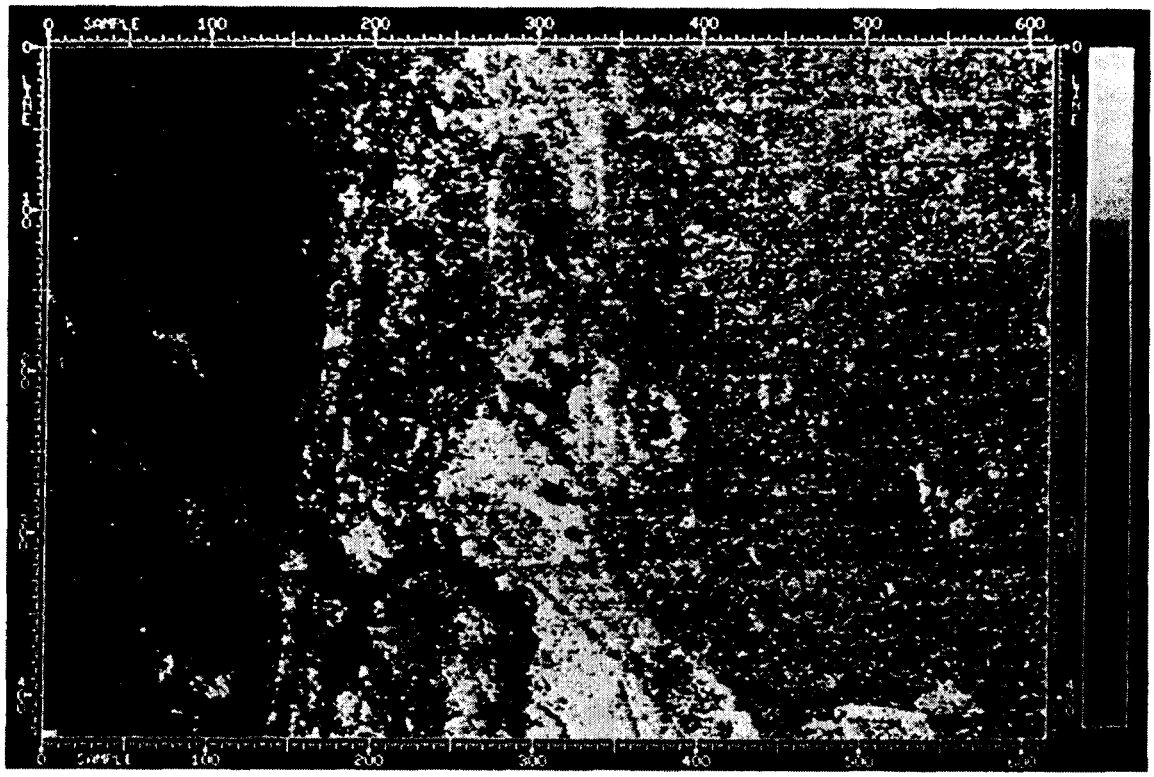


Figure 3. AVIRIS image of the Jasper Ridge area depicting the intensity of ligno-cellulose absorption. The ligno-cellulose vegetation index was formed by subtracting two composite bands of AVIRIS reflectance data: 2.20 um minus 2.35 um. The brightest areas on the image correspond to dry grasslands.

# AVIRIS DATA QUALITY FOR CONIFEROUS CANOPY CHEMISTRY

NANCY A. SWANBERG, TGS Technology Inc., NASA Ames Research Center, USA

## ABSTRACT

An assessment of AVIRIS data quality for studying coniferous canopy chemistry was made. Seven flightlines of AVIRIS data were acquired over a transect of coniferous forest sites in central Oregon. Both geometric and radiometric properties of the data were examined including: pixel size, swath width, spectral position and signal-to-noise ratio. A flat-field correction was applied to AVIRIS data from a coniferous forest site. Future work with this data set will exclude data from spectrometers C and D due to low signal-to-noise ratios. Data from spectrometers A and B will be used to examine the relationship between the canopy chemical composition of the forest sites and AVIRIS spectral response.

## INTRODUCTION

The objective of this study is to determine whether or not AVIRIS data can be used to study coniferous canopy chemistry. This involves two steps: (1) an evaluation of AVIRIS data quality and (2) if in step one the data proves good enough, an examination of the relationship between canopy chemical composition and AVIRIS spectral response. The first step is the subject of this paper.

## DATA COLLECTION

Seven flightlines of AVIRIS data were collected on August 1, 1988 over forest test sites in central Oregon. Together these zones form an east-west transect which exhibits a gradient of climate and fertility encompassing the western coast range, the interior coast range, the low elevation west cascades, the mid-elevation west cascades, the high cascade summit, the east slope cascades, and the interior high desert. AVIRIS data were acquired over 13 of the total 14 sites distributed troughout the transect where ground data had been collected in previous studies. The site missed was in the western coast range. Average spectra from three-by-three pixel windows over three forest

sites are shown in Figure 1.

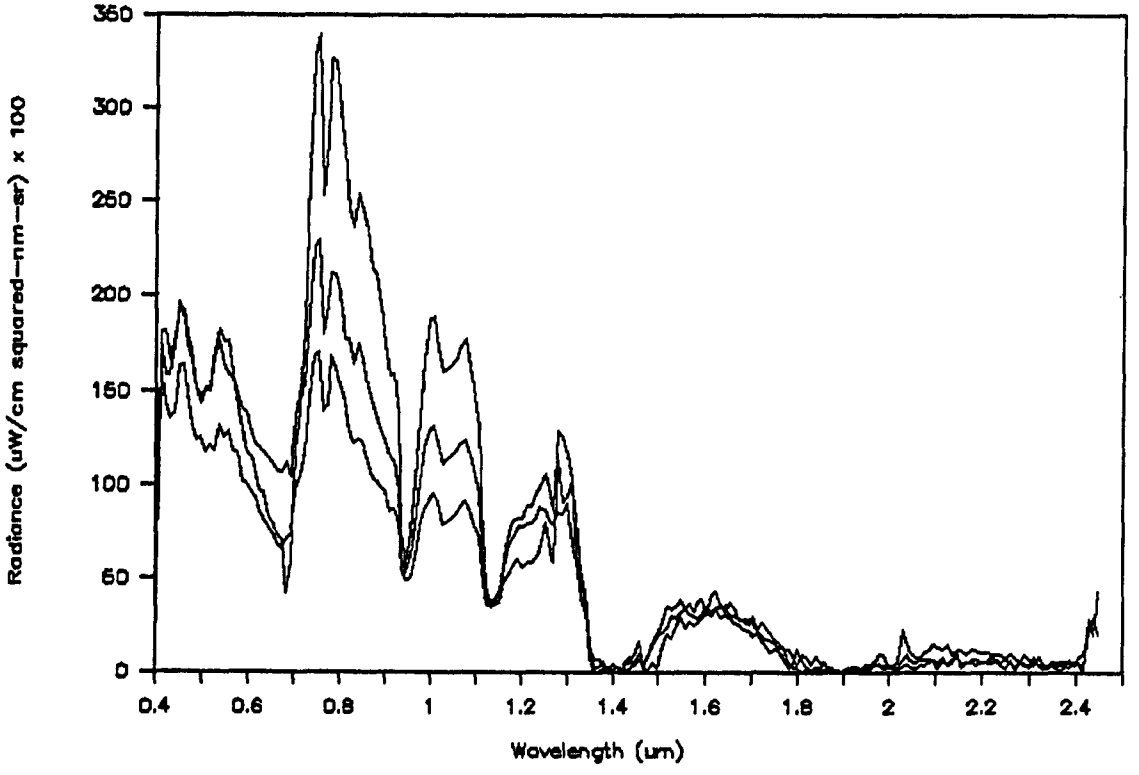


Fig. 1. Nine pixel mean AVIRIS spectra from three forest sites: Casacde Head (top), Metolius (middle), and Santiam Pass (bottom).

## METHODS AND RESULTS

Both geometric and radiometric properties of the radiometrically corrected AVIRIS data received from JPL were examined. Pixel size in the along-track and across-track directions were measured on three flightlines. United States Geological Survey orthophoto quadrangles were used as the basis for comparison. Swath width was calculated as the average across-track pixel size multiplied by the number of pixels per line (614). These measurements and calculations for each flightline are shown in Table 1.

Table 1. Mean pixel size and swath width of AVIRIS data

| Site Name | Across-Track Mean Pixel Size | Along-Track Mean Pixel Size | Swath Width |
|---|---|---|---|
| Cascade Head | 18.3 m | 18.9 m | 11,236 m |
| Trout Creek | 17.6 m | 17.5 m | 10,806 m |
| Metolius | 17.8 m | 16.7 m | 10,929 m |

The average across-track pixel size ranged from 17.6 to 18.3 m while in the along track direction it ranged from 16.7 to 19.1. The swath width ranged from 10,806 to 11,236 m. This variation is most likely due to differences in topographic relief between these flightlines.

An atmospheric model, LOWTRAN 6 (Kniezys et al., 1983), was used to evaluate AVIRIS spectral position. Known atmospheric absorption features were compared to those from a flat-field AVIRIS spectrum. This comparison is shown in Figure 2. where a fifty pixel average spectrum from a beach and LOWTRAN 6 output from the mid-lattitude summer model of solar spectral irradiance reflected by a hypothetical fifty percent reflector are plotted.

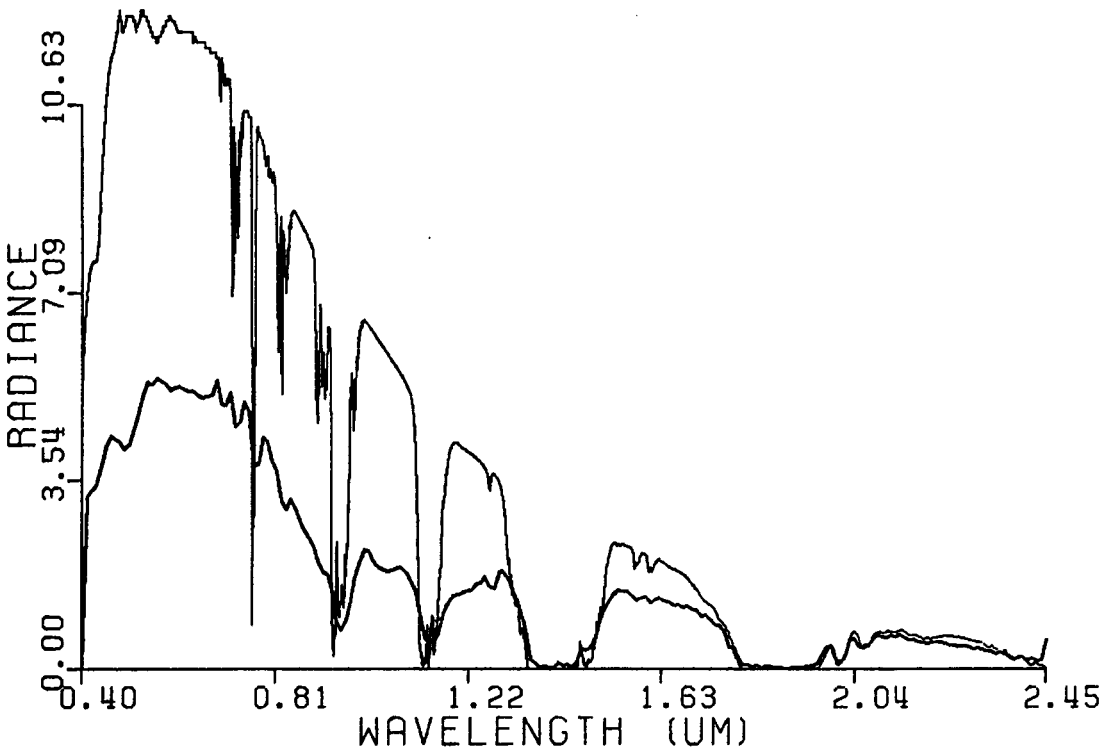


Fig. 2. Solar spectral radiance (uW/cm squared-nm-sr) from LOWTRAN (top) and an AVIRIS flat-field (bottom) showing the relative positions of atmospheric water and carbon dioxide absorption features.

As can be seen in Figure 2. the atmospheric water absorbtion features at 0.942, 1.135, 1.389 and 1.876 micrometers (Coulson, 1975) as well as atmospheric carbon dioxide features at 1.4, 1.6 and 2.0 micrometers (Liou, 1980) are properly located within the appropriate 10 nanometer AVIRIS spectral band.

Visual inspection of the data revealed a noise pattern, present in all channels and especially noticable in homogeneous areas, that made the image look like

corrugated cardboard. This periodic noise was evident in the Fourier domain as noise spikes, but was not filtered out prior to the following analysis of the signal-to-noise ratio. Sudden shifts in scene brightness were also evident in several flightlines, but did not occur between imaging of the forest study site and the beach site used in this analysis.

The ratio of mean radiance to standard deviation of the radiance over a homogeneous surface was used to estimate the ratio of signal-to-noise for each AVIRIS spectral band. Assuming the beach was a relatively homomgeneous surface an estimate of the signal-to-noise ratio for each AVIRIS spectral band was obtained by computing the mean radiance of the fifty beach pixels and dividing it by the standard deviation of those fifty pixels. This is a "best case" estimate of the signal-to-noise ratio for this flightline since beach sand is a highly reflective target as compared to the rest of the scene, but it does provide an upper bound.

To obtain a signal-to-noise estimate for forested sites of interest in this study a similar method was employed. Nine adjacent pixels were extracted over the forest test site from the same flightline as the beach and for each channel the mean was divided by the standard deviation. In this case the assumption of homogeneity is not as good as for the beach and will lower the estimate of signal-to-noise. To minimize this effect a dense stand with a high leaf area index was chosen to provide as homogeneous a target as possible. This estimate served as a lower bound on the signal-to-noise ratio for forest targets on this flightline. Estimates of signal-to-noise ratios for both targets in all bands are shown in Figure 3.

The signal-to-noise ratio is lower in nearly all channels for data taken over the forest test site than for data from the beach (as would be expected from their different albedos). Excluding the atmospheric water absorption bands centered at 1.38 and 1.87 micrometers, the greatest difference between the two estimates is in spectrometers C and D. In spectrometer C between 1.55 and 1.68 micrometers the mean signal-to-noise ratio as calculated from the beach AVIRIS data is 20.8 while the mean signal-to-noise ratio for the forest data is 7.7. In spectrometer D between 2.08 and 2.26 micrometers the estimates for the signal-to-noise ratio are 14.6 and 2.3 for the beach data and the forest data, respectively.

A flat-field approach (Roberts et al., 1986) was used to correct for atmospheric effects in data from the forest site. The spectrum from the beach was divided into the forest spectrum to produce the spectrum shown in Figure 4. This spectrum looks like a typical vegetation spectrum with some exceptions: the flat region centered at approximately 1.2 micrometers, the noisy portion between approximately 2.0 -2.4 micrometers, and the decending values between 0.4

- 0.55 micrometers.

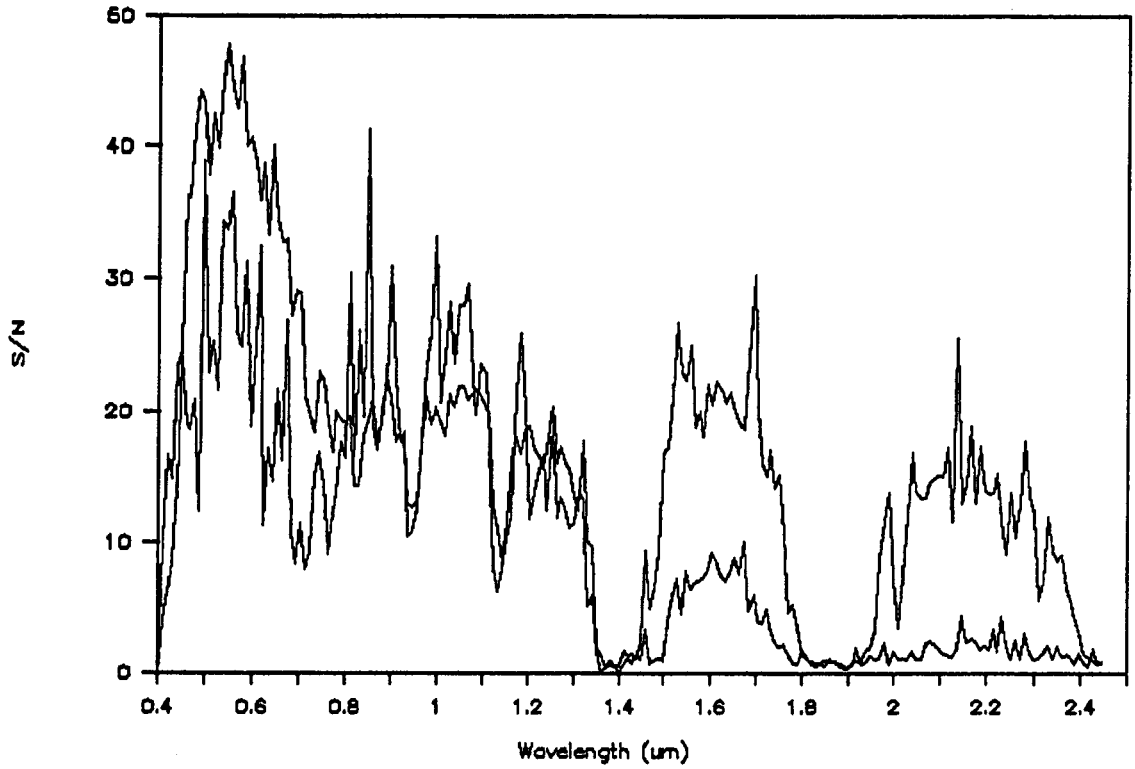


Fig. 3 AVIRIS signal-to-noise (S/N) estimates for a flat-field (top) and forest site (bottom)

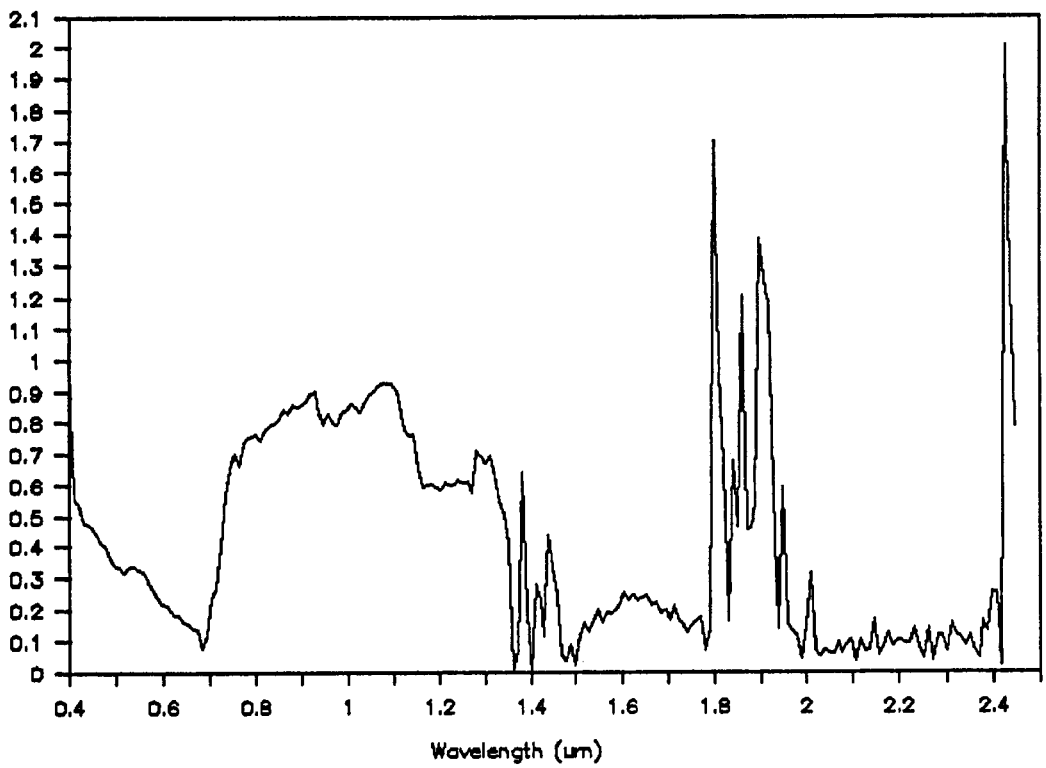


Fig. 4. Ratio of an AVIRIS forest spectrum to a flat-field spectrum

## DISCUSSION AND CONCLUSIONS

Site coverage of 13 out of 14 sites, spatial resolution of better than 20 m, and spectral position of within one AVIRIS bandwidth are all expcted to be sufficient for this study of coniferous canopy chemistry. Excluding the atmospheric water absorption bands the signal-to-noise ratio in spectrometer A and B as bounded by even the low estimate in Figure 3. is above ten for nearly all bands and should be adequate for this work. AIS data of similar spectral resolution for this same forest site exhibited signal-to-noise ratios greater than ten in all channels and correlated well to canopy chemistry in a previous study (Swanberg and Peterson, 1987).

The mean signal-to-noise ratio in spectrometers C and D, however, fall somewhere in the range 7.7 - 20.8, and 2.3 - 14.6, respectively. If one believed that the true signal-to-noise ratio for the forest site were actually closer to the upper bound the data could be considered useable; however, it is probably closer to the lower bound. The lower bound, calculated from data of the forest site, is an underestimate, but all efforts were made to use as homogeneous a forest target as possible and any lack of homogenity probably accounts for only a small percentage of the noise in this estimate.

Although the results of flat-field correction were encouraging they exhibit a number of problems. The flat region at 1.2 micrometers can be explained by the discrepancy in that spectral region between the beach spectrum and the LOWTRAN model output. The noisy region between 2.0 - 2.4 micrometers can be attributed to the AVIRIS signal-to-noise ratio in spectrometer D. The decending values between 0.4 - 0.55 micrometers can not easily be explained. This technique and additional methods of atmospheric corection will need to be examined before data from several flightlines can be compared.

## FUTURE WORK

Since the signal-to-noise ratios in spectrometers C and D are unacceptabely low, future work with these data will be restricted to data from spectrometers A and B. Fourier filters will be constructed for each flightline to reduce periodic noise and methods to normalize data from different flightlines with respect to the dark current offsets will be investigated. Atmospheric corrections will be invesigated to corect for differences in elevation as well as possible differences in atmospheric composition between sites. Finally, the relationship between canopy chemical composition, as characterized in previous studies, and AVIRIS spectral response at each site will be examined.

ACKNOWLEDGEMENTS

The author thanks J. Leipner at NASA Ames Research Center for her help running the LOWTRAN model and making plots for this paper. The author also thanks J. Dungan and P. Curran at NASA Ames Research Center for their helpful discussions. Funding for this research was provided by the Earth Science and Applications Division, Land Processes Branch, Terrestrial Ecosystems Program, NASA Headquarters.

REFERENCES

Coulson, K.L. 1975. Solar and Terrestrial Radiation. Academic Press, New York, New York, pp. 265-267.

F.X., E.P. Shettle, W.O. Gallery, J.H. Chetwynd, Jr., L.W. Abreu, J.E.A. Selby, S.A. Clough, R.W. Fenn 1983. Atmospheric Transmittance/Radiance:Computer Code LOWTRAN 6. Air Force Geophysics Laboratory, Environmental Research Paper, No. 846, 200 pp.

Liou, K. 1980. An Introduction to Atmospheric Radiation. Academic Press, New York, New York, pp 60-63.

Roberts, D.A., Y. Yamaguchi, and R.J.P. Lyon 1986. Comparisons of Various Techniques for Calibration of AIS Data, Proceedings of the Second Airborne Imaging Spectrometer Data Analysis Workshop, JPL 86-35, pp.21-30.

Swanberg, N.A. and D.L. Peterson 1987. Using the the Airbone Imaging Spectrometer to Determine Nitrogen Content in Coniferous Forest Canopies, Proceedings of the International Geoscience and Remote Sensing Symposium, p. 981.

# AVIRIS DATA CHARACTERISTICS AND THEIR EFFECTS ON SPECTRAL DISCRIMINATION OF ROCKS EXPOSED IN THE DRUM MOUNTAINS, UTAH: RESULTS OF A PRELIMINARY STUDY

G. B. BAILEY, U.S. Geological Survey, EROS Data Center, Sioux Falls, South Dakota, U.S.A.; J. L. DWYER, TGS Technology, Inc.*, EROS Data Center, Sioux Falls, South Dakota, U.S.A.; and D. J. MEYER, TGS Technology, Inc.*, EROS Data Center, Sioux Falls, South Dakota, U.S.A.

## ABSTRACT

Airborne Visible and Infrared Imaging Spectrometer (AVIRIS) data collected over a geologically diverse field site and over a nearby calibration site were analyzed and interpreted in efforts to document radiometric and geometric characteristics of AVIRIS, quantify and correct for detrimental sensor phenomena, and evaluate the utility of AVIRIS data for discriminating rock types and identifying their constituent mineralogy. AVIRIS data acquired for these studies exhibit a variety of detrimental artifacts and have lower signal-to-noise ratios than expected in the longer wavelength bands. Artifacts are both inherent in the image data and introduced during ground processing, but most may be corrected by appropriate processing techniques. Poor signal-to-noise characteristics of this AVIRIS data set limited the usefulness of the data for lithologic discrimination and mineral identification. Various data calibration techniques, based on field-acquired spectral measurements, were applied to the AVIRIS data. Major absorption features of hydroxyl-bearing minerals were resolved in the spectra of the calibrated AVIRIS data, and the presence of hydroxyl-bearing minerals at the corresponding ground locations was confirmed by field data.

## INTRODUCTION

The Airborne Visible and Infrared Imaging Spectrometer (AVIRIS) is potentially a powerful earth remote sensing tool, and it may provide geologists with their most effective capability yet to map

---

Publication authorized by the Director, U.S. Geological Survey.



* Work performed under U.S. Geological Survey contract 14-08-0001-22521.

lithologic variation and determine rock composition from remotely sensed data. However, in order for AVIRIS data to be applied most successfully in the solution of geologic and other interdisciplinary scientific problems, a variety of instrument and data characteristics must first be determined and evaluated. The radiometry and geometry of AVIRIS data must be characterized, and the information content of the data relative to specific interdisciplinary measurement requirements must be determined.

## OBJECTIVES

The overall goal of these studies was to use the attributes of the selected field sites to determine and evaluate as many characteristics and capabilities of AVIRIS as possible, particularly as relate to geologic applications of AVIRIS data. Specific objectives identified at the outset were to:

- evaluate radiometric fidelity and spectral resolution
- document geometric characteristics
- quantify detrimental sensor phenomena
- evaluate capabilities to identify constituent mineralogy of diverse rock types
- evaluate effects of vegetation on such capabilities
- develop improved data products for interpretation

## FIELD SITE CHARACTERISTICS

The Drum Mountains in west-central Utah were selected as the primary field site for these studies because good exposures of many diverse rock and alteration types present in an area of about 25 square km make the site particularly well suited for geologic evaluation of AVIRIS data. Furthermore, the detailed geology of the area is well documented (Bailey, 1974; Lindsay, 1979), and there exists a variety of other remotely sensed and ground-based data that also contribute to a comprehensive evaluation of AVIRIS data (Bailey and others, 1985).

Rocks exposed in the field area include a thick sequence of west-dipping Cambrian limestones, dolomites, and shales that overlies an even thicker, heterogeneous sequence of Cambrian and pre-Cambrian quartzite and argillite. Intermediate to silicic Tertiary volcanic rocks occur in fault contact with the sedimentary rocks in the northern part of the area, and older intermediate to mafic Tertiary volcanic rocks overlie the sediments on the west and south. The volcanic rocks have been hydrothermally altered in places, and some carbonate rocks adjacent to the volcanics have been bleached and recrystallized. A contact metamorphic aureole, which is characterized by development of calcsilicate mineralization in limestone and shale units, occurs in the central part of the area. The aureole is associated with the intrusion of two small stocks. One of the intrusives is a diorite and is essentially unaltered where exposed. The other was probably a monzonite, but it has undergone such intense hydrothermal alteration that the original lithology is uncertain.

A second field site, located near Pavant Butte and approximately 50 km south of the primary site, was used for data calibration purposes. It is characterized by rather large, uniform, and topographically flat occurrences of black volcanic soils, light buff-colored dry lake sediments, and white salt crusts.

## APPROACH TO DATA ANALYSIS AND INTERPRETATION

### Data Acquisition

AVIRIS data were acquired over the two field sites near solar noon on September 18, 1987, under cloud-free, low-haze atmospheric conditions. The data swath collected over the calibration site was almost precisely that which was requested, but a deviation of approximately 3 km over the primary site resulted in the exclusion of geologic targets in the thick basal quartzite and argillite units.

Concurrent with the AVIRIS flyover, ground spectral measurements of the light, intermediate, and dark targets at the Pavant Butte calibration site were collected using a Geophysical Environmental Research, Inc. (GER) Infra-Red Intelligent Spectroradiometer (IRIS). Field spectra of various rock and soil targets in the primary Drum Mountains field site were collected using an IRIS on the two days prior to the AVIRIS flyover. In addition, an extensive set of ground spectral data, including nearly all rock and alteration units in the primary field site, was acquired during the first week in August 1988 using an IRIS and the Portable Instantaneous Display and Analysis Spectrometer (PIDAS). Selected field stations flagged in August were reacquired in September as a mechanism for relating data collected during the two different collection efforts. Surface soil moisture conditions appeared to be uniformly dry with the possible exception of a small number of sites measured the day after a thunderstorm that occurred during the August field effort. However, effects of this possible variation are not evident in the data.

### Image Quality Analysis and Artifact Correction

Preliminary analysis of this AVIRIS data set revealed a variety of detrimental data artifacts and noise, as well as a lower signal-to-noise ratio than expected in some of the data. Consequently, initial efforts were devoted to identifying and correcting artifacts that would hamper data analysis and interpretation. These artifacts are of two types: those that are inherent in the AVIRIS flight data, and those that are introduced during subsequent processing of the flight data. The inherent artifacts are line drops, low output signal for individual bands, and coherent (periodic) noises. Processing artifacts originate from noises in dark current data used during calibration and from spectral resampling that is performed to produce contiguous and evenly incremented wavelength bands from the original bands that overlap and have varying bandwidths.

The line drops and low output bands in the image data were corrected by straightforward means. Bad line segments were replaced by averaging adjacent lines, and low output bands were replaced by averaging adjacent bands. Table 1 lists the AVIRIS bands with low output, as determined by observing dark current levels.

Coherent noise patterns were the most apparent artifacts in the image data. Initially, one band from each spectrometer (fig. 1) was analyzed to determine the frequency and magnitude of these noises. Due to the prominence of noise in spectrometers B and D, detailed Fourier analysis then was performed on 32 bands from both the B and D spectrometers. Each band was transformed individually, and the resulting magnitudes were averaged for each 32-band subset and used to locate noise frequencies (figs. 2a and 2b). The following observations were made:

(1) All components of the coherent noises occur at very specific horizontal frequencies.

(2) Many noise patterns appear to be invariant with respect to spectrometer, and with respect to channel within a spectrometer.

(3) The frequency components of the noise can be categorized as belonging to one of two groups. The first group is invariant with respect to vertical frequency, appearing as a modulation between horizontally adjacent pixels. Components of the second noise group exhibit well-defined horizontal harmonic relationships and a weak time-dependent preference for certain vertical frequencies. These components interact to produce the "herringbone" pattern seen in the image data.

Table 1. Low output AVIRIS bands.

| Raw channel # | Spectrometer | Raw channel # | Spectrometer |
|---|---|---|---|
| 20 | A | 162 * | D |
| 24 | A | 163 * | D |
| 26 | A | 165 * | D |
| 28 | A | 168 | D |
| 32 * | A | 169 | D |
| 34 * | B | 173 | D |
| 40 | B | 176 | D |
| 64 | B | 189 | D |
| 72 | B | 205 | D |
| 80 | B | | |

* Indicates redundant channel due to spectrometer overlap.

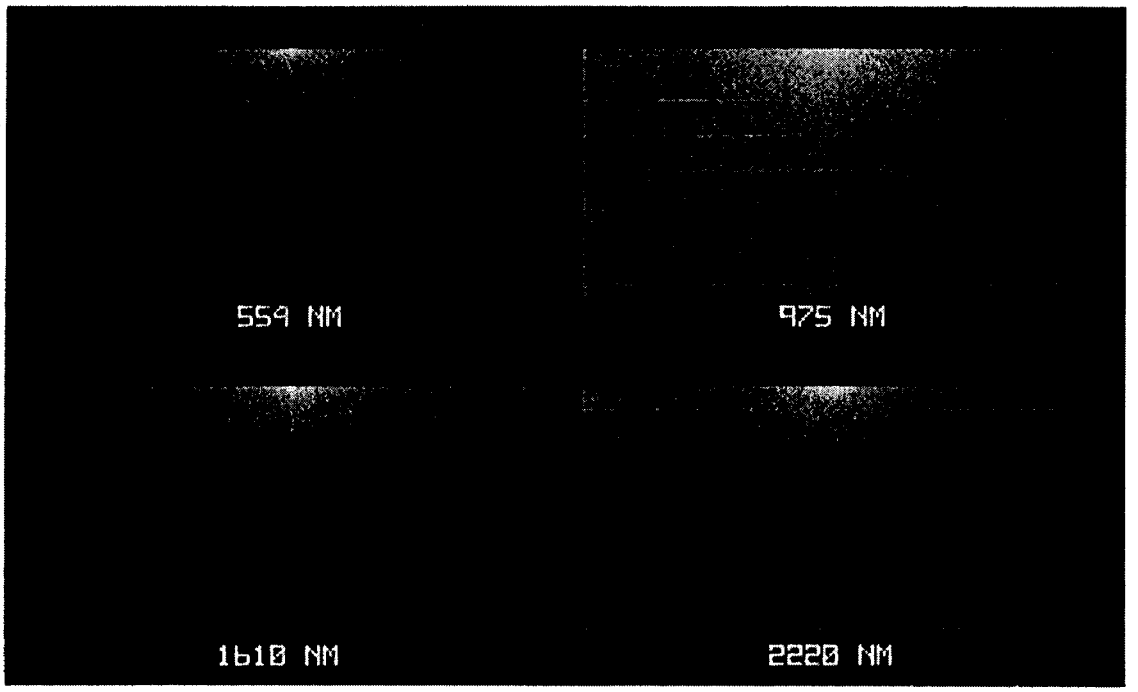


Fig. 1. $Log_{10}$ magnitudes of sample bands from each of the four AVIRIS spectrometers. DC is centered at the top. Vertical axes correspond to horizontal frequencies (0 to 0.5 cycles/sample), and horizontal axes correspond to vertical frequencies (-0.5 to 0.5 cycles/line).

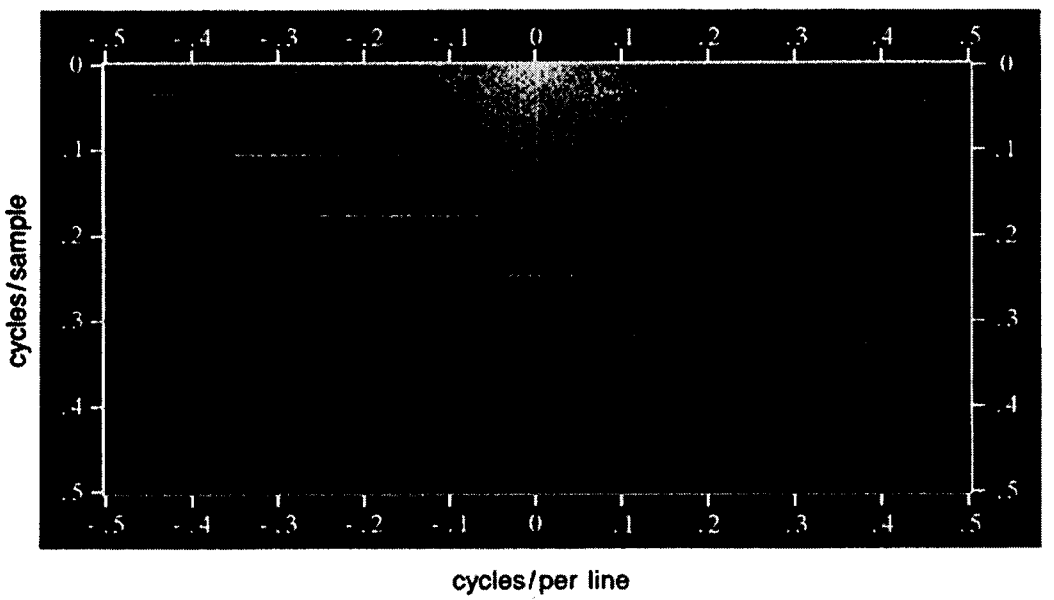


Fig. 2a. $Log_{10}$ of the average magnitude of 32 consecutive bands from spectrometer B (0.71 to 1.00 micrometers). Horizontal frequencies are plotted vertically, and vertical frequencies are plotted horizontally.

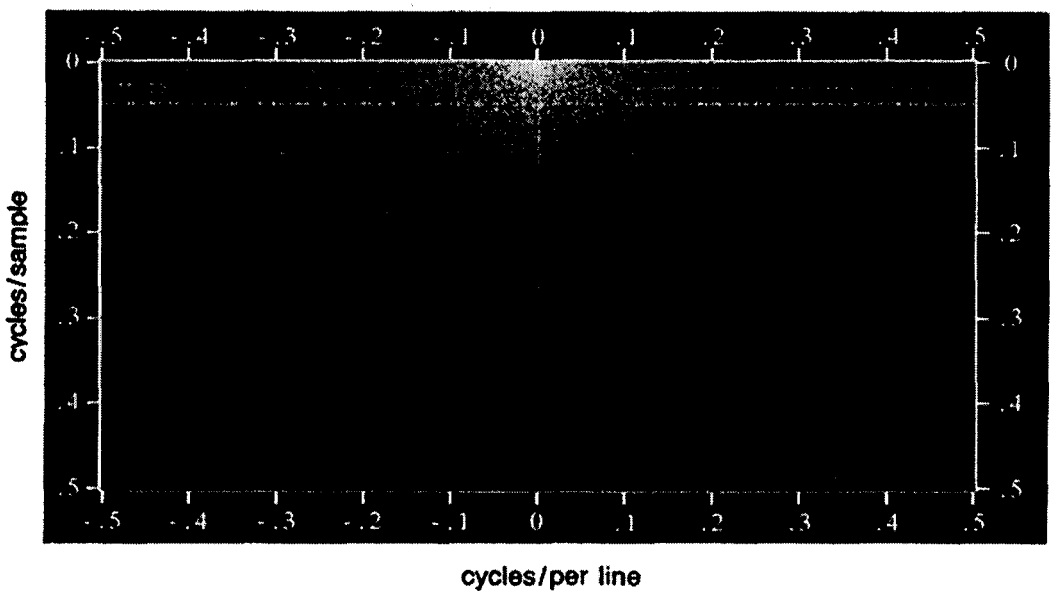


Fig. 2b. $Log_{10}$ of the average magnitude of 32 consecutive bands from spectrometer D (2.11 to 2.41 micrometers). Horizontal frequencies are plotted vertically, and vertical frequencies are plotted horizontally.

Some of the major noise components were removed from the data by using "Gaussian notch" frequency filters (Moik, 1980). Table 2 is a list of noise frequencies having the characteristics of the first noise group, and table 3 lists those belonging to the second group.

Spectral resampling of AVIRIS images introduces a "smearing" of information between adjacent bands. This is particularly troublesome when low output bands are present in the data, because the resampling process causes these bands to corrupt immediately adjacent bands. To avoid this source of data degradation, raw AVIRIS data used in data analysis were processed without spectral resampling.

A final source of degradation is the subtraction of dark current data from the image data. The dark current data themselves were quite noisy, and the dark current noise from spectrometer B exhibited a pronounced periodicity with components at 0.11, 0.29, 0.31 and 0.42 cycles/line. Consequently, these data were smoothed by a moving 101-element averaging filter (Reimer and others, 1987). This smoothing did not, however, take into account offset discontinuities (Vane, 1987a). For the Drum Mountains data, the locations of these discontinuities were visually identified, and the dark current data were smoothed between these locations only.

The characteristics of "total noise" (not attempting to differentiate between systematic and random noises) were determined by measuring the standard deviation of the image over a uniformly bright and topographically flat hardpan target and over a nearby lake.

Figure 3 plots these measurements for both targets. Three points can be made about this figure. First, the major influences (assumed to be system noise) on the standard deviation appear to be purely additive; no significant dependence on target brightness is evident.

Table 2. Periodic noise components that are invariant with vertical frequency.

| Horizontal frequency (cyc/samp) | Spectrometer | Horizontal frequency (cyc/samp) | Spectrometer |
|---|---|---|---|
| 0.010 * | B,D | 0.361 | B |
| .030 * | B,D | .369 | D |
| .043 | B | .383 | B |
| .049 * | B,D | .387 | B,D |
| .064 | B | .402 | B |
| .148 | D | .408 | D |
| .168 | D | .412 | B,D |
| .201 | B | .430 | D |
| .209 | D | .457 | D |
| .214 | B,D | .468 | B,D |
| .250 | B | .477 * | A,B,C,D + |
| .289 | B | .480 * | D |
| .305 | B | .484 | B |
| .320 | B | .486 * | B,D |

* Indicates prominant noise feature.

\+ Figures for A and C spectrometers were determined from bands at 0.554 and 1.61 micrometers, respectively.

Table 3. Periodic noise components exhibiting vertical frequency dependence.

| Horizontal frequency (cyc/samp) | Vertical peak frequency (spec. B) (cyc/line) | Vertical peak frequency (spec. D) (cyc/line) |
|---|---|---|
| 0.004 | 0.094 | ---- |
| .016 | .277 | ---- |
| .018 | .461 | ---- |
| .025 | .469 | -0.457 |
| .035 * | .434 | - .429 |
| .105 * | .295 | - .295 |
| .176 * | .164 | - .174 |
| .246 * | .029 | - .033 |
| .316 * | .113 | .113 |
| .326 + | .459 | |

* Indicates element of harmonic sequence (all spectrometers).

\+ Possible aliased element of harmonic sequence.

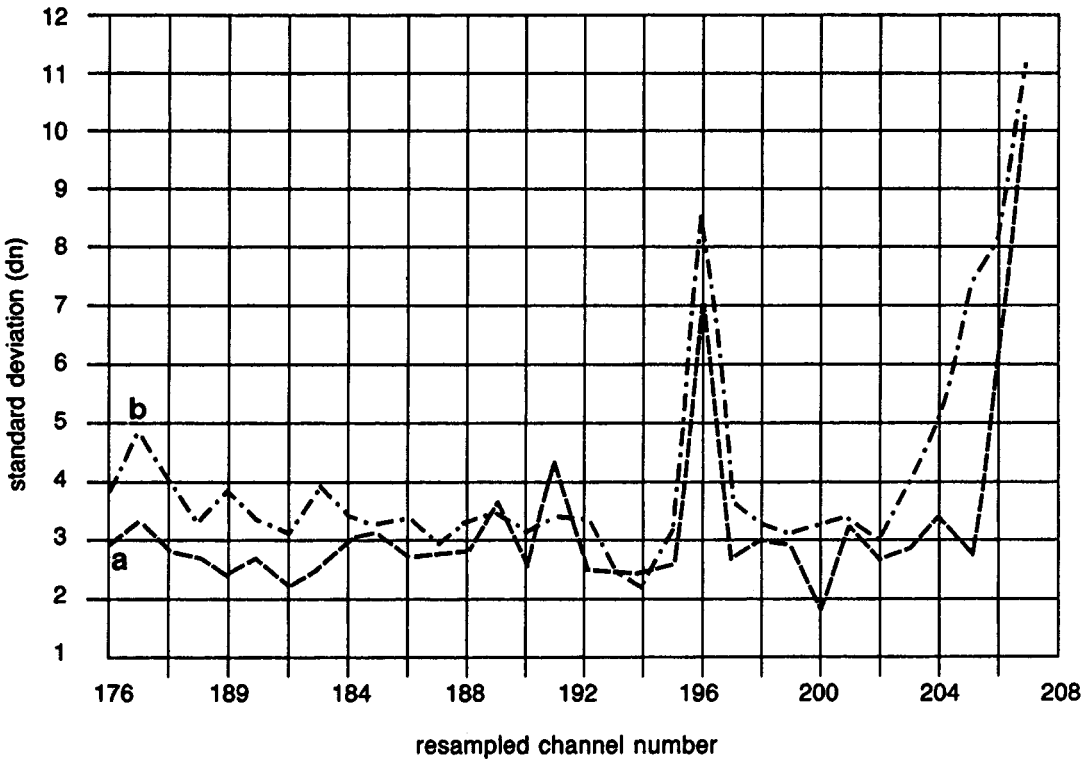


Fig. 3. Standard deviation of reflectance for spectrometer D for bright (a) and dark (b) calibration targets.

Second, the "noisy" channel (196) at 2.31 micrometers stands out clearly. Third, noise levels increase rapidly at the longer wavelengths in this range.

Signal-to-noise figures were computed based on "coefficients-of-variance" (Simpson and others, 1960) measurements of the hardpan target. Figure 4 plots the reflectance of the hardpan over relevant wavelengths as acquired by an IRIS, and these data show that the hardpan approximates a 50-percent albedo target over this spectral range. The curve reflects a fall-off in solar irradiance from 2.1 to 2.4 micrometers. Figure 5 depicts signal-to-noise estimates based on the coefficients-of-variance method. The numbers given in this plot are generally lower than published figures (Vane, 1987b), particularly at the longer wavelengths.

## Data Analysis

Two approaches were used to evaluate the analytical utility of AVIRIS data. The first involved the use of standard image processing and enhancement techniques, such as band ratioing, principal components analysis, and band averaging, to generate products for visual interpretation. The second approach took advantage of spectrometric properties of the AVIRIS system using the SPectral Analysis Manager (SPAM) software (Mazer and others, 1987) to interrelate image spectra to ground measurements.

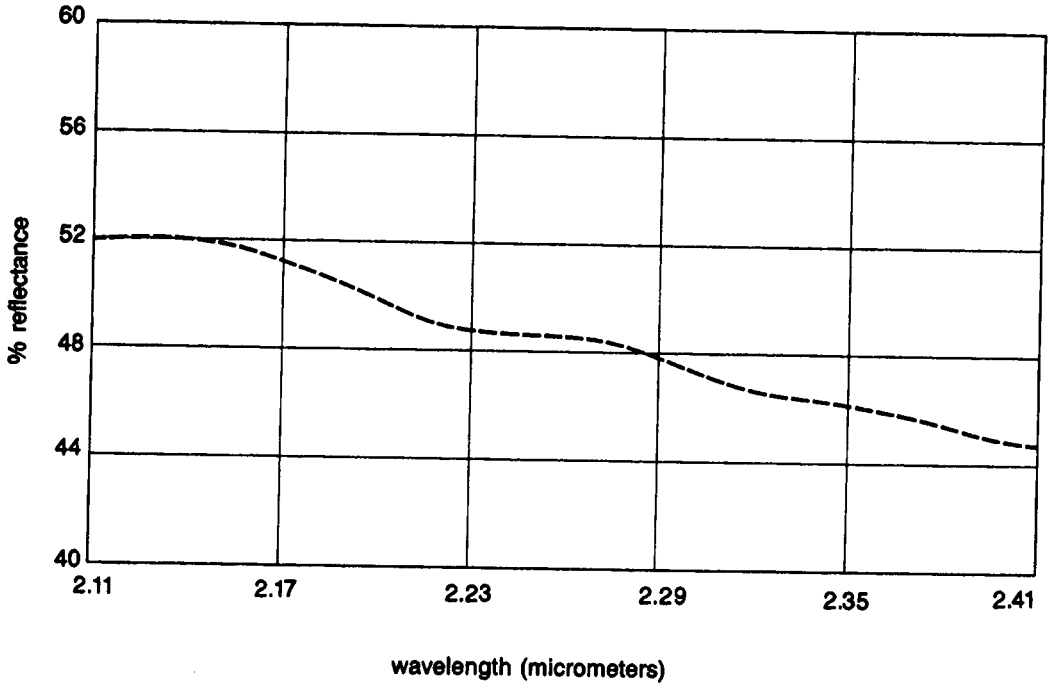


Fig. 4. Percent reflectance for a bright calibration target as measured with a field spectrometer.

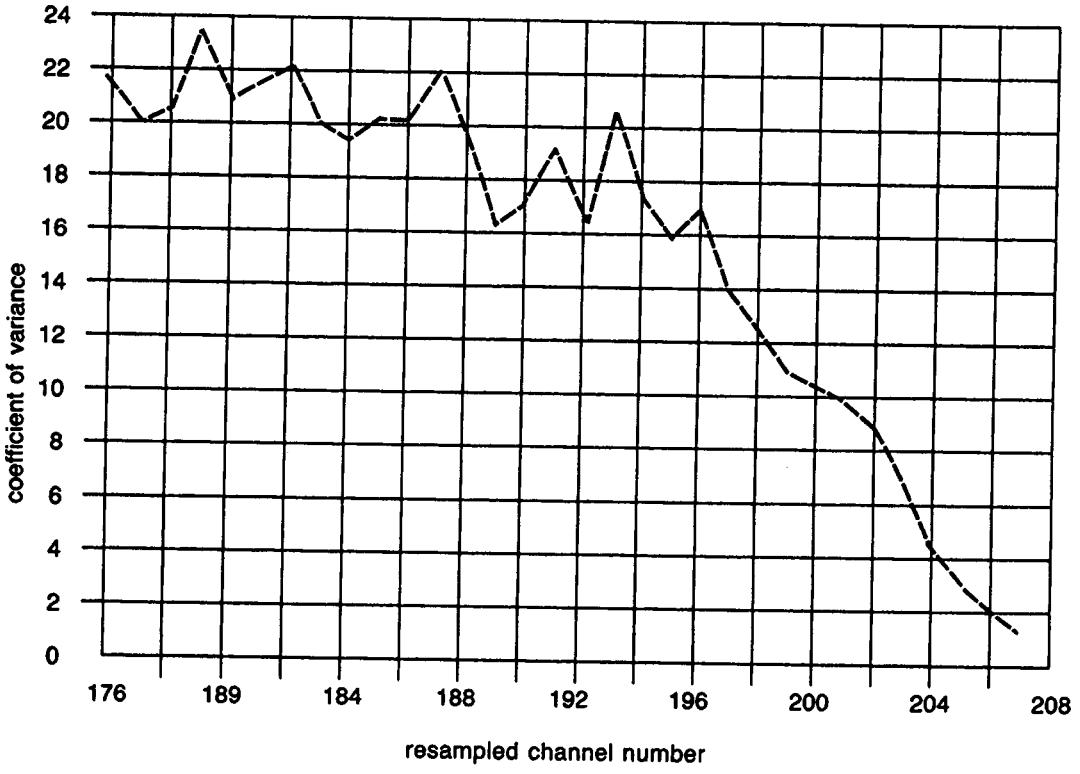


Fig. 5. Signal-to-noise ratio for 50-percent reflectance calibration target.

Criteria for determining the spectral performance of AVIRIS included the ability to discriminate iron oxide, hydroxyl-bearing, and carbonate mineral absorption features from image spectra. Thus, the analysis addressed the 0.41-0.71 (spectrometer A), 1.59-1.62 (spectometer C), and 2.11-2.41 (spectrometer D) micrometer regions. In spite of the poor signal-to-noise characteristics of spectrometer D data, information extraction efforts focused on data from that spectrometer because of hydroxyl-bearing and carbonate mineral absorption features of interest in that region of the spectrum and because of interest in determining what effects the poor signal-to-noise characteristics had on information extraction.

Image products generated from digital processing and enhancement techniques applied to AVIRIS data were generally disappointing. In no case was an image produced that displayed the distribution of iron oxide, hydroxyl-bearing, and carbonate minerals with as good clarity and detail as displayed in similarly processed Landsat thematic mapper data of the area. These results were not surprising, however, given the measured signal-to-noise ratios of spectrometer D data. Attempts to improve the signal-to-noise by computing multiple-band averages for certain hydroxyl features in the 2.2 micrometers region met with little apparent success, and they were likewise unsuccessful for carbonate features in the 2.31-2.35 micrometers range. The latter problem likely was due to the presence of a noisy detector at 2.31 micrometers and to the generally low-albedo nature of the carbonate rocks in the Drums Mountains. Due primarily to higher signal-to-noise in the A spectrometer, good results were achieved in displaying iron oxide distribution using approximations of TM band ratio 3/1.

Results of studies to relate AVIRIS image spectra to ground and laboratory spectral measurements using SPAM software met with varying success. Matching techniques implemented within SPAM and used for data calibration in this approach included: (1) flat field corrections, (2) regression ("empirical line"), and (3) "equal energy" normalization (Conel and others, 1987). The flat field correction used the hard-pan target for reference, whereas the empirical line method used all three Pavant Butte calibration targets as points on a ground reflectance versus image digital counts regression line. The third method does not require use of an independent calibration site, but rather involves normalization of primary site target albedos to determine empirical "air-to-ground" relationships.

Several factors must be considered when analyzing data calibrated by these techniques. First, the poor signal-to-noise characteristics of the D spectrometer dictated use of spectral filtering. Figure 6 illustrates the use of the SPAM function FILTER with and without weighted averaging. Note the spectral shifts which can occur as a result of this operation. Second, the reference areas in the Pavant Butte scenes are 300 to 600 meters lower in elevation than the target areas in the Drum Mountains, which possibly affected the results from the first two methods due to different atmospheric pathlengths. Third, AVIRIS data were truncated to 8 bits for SPAM processing, although this probably had no impact on the degraded data from

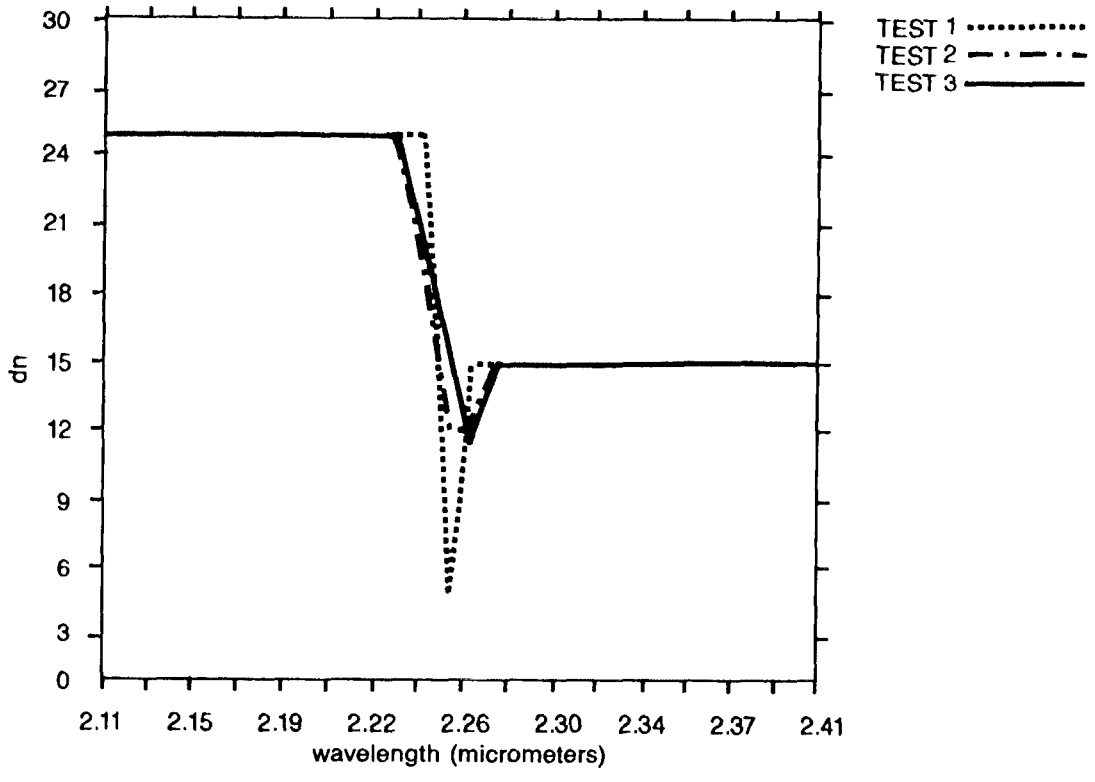


Fig. 6. Test plots of an asymmetrical spectral feature and subsequent results of the SPAM function FILTER. TEST 1 is the raw data; TEST 2 is the result from the box filter; TEST 3 is the result from the weighted filter. Filter size is 3 in both cases.

spectrometer D. Finally the empirical line technique discussed above was implemented in SPAM using several intermediate byte variables that introduced a substantial quantization error into the process.

After the data were calibrated, targets in the Drum Mountains were used to assess the instrument's ability to provide data that would resolve both hydroxyl-bearing and carbonate mineral absorption features. The altered intrusive was used as the primary hydroxyl-bearing target for analysis.

All three calibration techniques produced image spectra that resolved the major ground-measured hydroxyl features, although the width and depth of the features varied between the different techniques (fig. 7). The empirical line method did not perform as well as the other methods, probably due to the quantization error and elevation differences. In general, absorption features in the AVIRIS spectra appeared to be shifted about 10 nm toward shorter wavelengths compared to both IRIS and PIDAS spectra. Once again, due to poor signal-to-noise characteristics, different carbonate features in the 2.31-2.35 micrometer region could not be resolved.

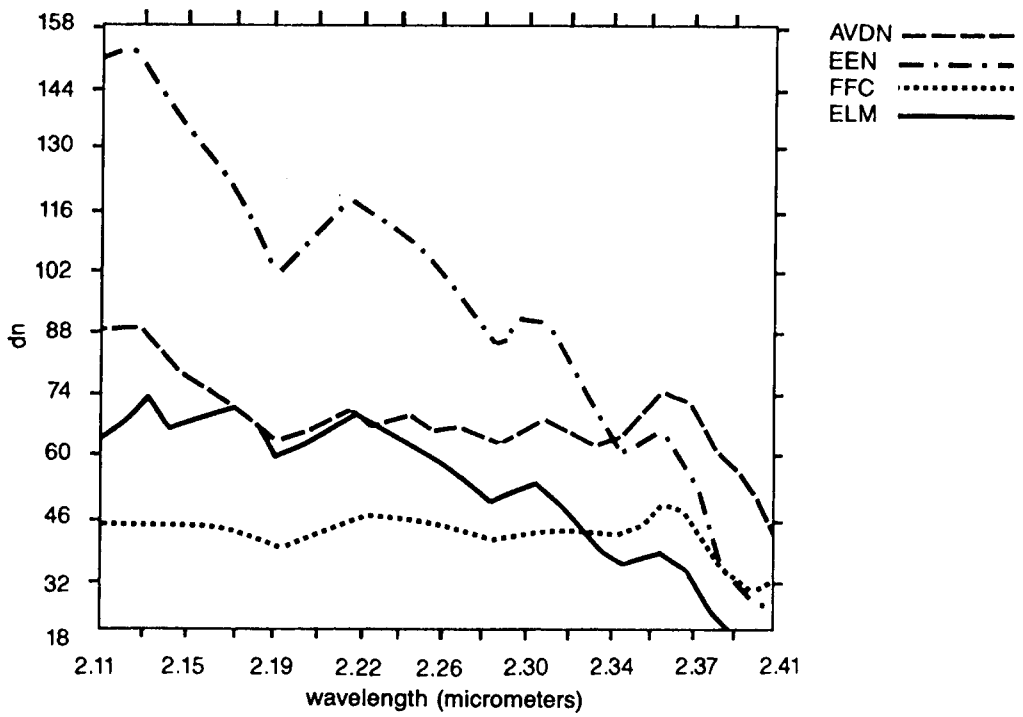


Fig. 7. AVIRIS spectral curves for altered intrusive. AVIRIS data were radiometrically corrected without spectral resampling; bad data channels were replaced; and data were spectrally smoothed in SPAM using a 3-point weighted filter. ADVN is a plot of AVIRIS DN's; EEN is derived from equal energy normalization; FFC was extracted after flat-field correction; and ELM is a preliminary result from AVIRIS data calibrated using the empirical line method.

## SUMMARY AND CONCLUSIONS

These studies accomplished some, but not all, of their original objectives. The radiometric characteristics of AVIRIS data acquired over the Drum Mountains and Pavant Butte sites have been documented, and procedures used to correct detrimental artifacts in the data have been described. However, objectives related to geometric characteristics of AVIRIS are yet to be addressed.

In general, data acquired by the A and C spectrometers were of sufficiently good quality to identify iron-oxide-bearing rocks. However, poor signal-to-noise characteristics in spectrometer D limited the ability to discriminate and identify hydroxyl-bearing rocks and minerals and precluded differentiation of carbonate minerals, particularly in images of AVIRIS data. Major absorption features of hydroxyl-bearing minerals were resolved in spectra of raw,

normalized, and ground-calibrated AVIRIS data. Conclusive evaluations of AVIRIS data capabilities for lithologic discrimination and mineral identification were not possible from the data set acquired. Such evaluations should be possible following recent improvements in the signal-to-noise characteristics of spectrometer D and other repairs made to the AVIRIS system, and they will be made if a second data set is acquired over the study sites.

REFERENCES


Bailey, G. Bryan. 1974. The occurrence, origin, and economic significance of gold-bearing jasperoids in the central Drum Mountains, Utah. Stanford University Ph.D. Dissertation, 300 pp.

Bailey, G. B., Dywer, J. L., and Podwysocki, M. H. 1985. Evaluation of Landsat Thematic Mapper data for geologic mapping in semi-arid terrains (abs.). In International Symposium on Remote Sensing of Environment-Remote Sensing for Exploration Geology, Fourth Thematic Conference, San Francisco, California, 1985, Proceedings (Ann Arbor, Michigan: Environmental Research Institute of Michigan), v. I, pp. 325-326.

Conel, J. E., Green, R. O., Vane, G., Bruegge, C. J., and Alley, R. E. 1987. Airborne imaging spectrometer-2: radiometry and a comparison of methods for the recovery of ground reflectance. In Airborne Imaging Spectrometer Data Analysis Workshop, Third, Proceedings (Pasadena, California: Jet Propulsion Laboratory 87-30, August 1987), pp. 18-47.

Lindsey, D. L. 1979. Geologic map and cross-sections of Tertiary rocks in the Thomas Range and northern Drum Mountains, Juab County, Utah. (Washington, D.C.: U.S. Geological Survey), map I-1176.

Mazer, A. S., Martin, M., Lee, M., and Solomon, J. E. 1987. Image processing software for imaging spectrometry. In Imaging Spectroscopy II, San Diego, California, August 1987, Proceedings, ed. Gregg Vane (Bellingham, Washington: SPIE), v. 834, pp. 136-139.

Moik, Johannes G. 1980. Digital processing of remotely sensed images. NASA SP-431, pp. 25-26.

Reimer, J. H., Heyada, J. R., Carpenter, S. C., Deich, W. T. S., and Lee, M. 1987. AVIRIS ground data-processing system. In Imaging Spectroscopy II, San Diego, California, August 1987, Proceedings, ed. Gregg Vane (Bellingham, Washington: SPIE), v. 834, pp. 79-90.

Simpson, G. G., Roe, A., and Lewontin, R. C. 1960. Quantitative zoology (New York: Harcourt Brace), pp. 90-143.

Vane, Gregg. 1987a. Personal communication, January 1987.

Vane, Gregg. 1987b. First results from the Airborne Visible/ Infrared Imaging Spectrometer (AVIRIS). In Imaging Spectroscopy II, San Diego, California, August 1987, Proceedings, ed. Gregg Vane (Bellingham, Washington: SPIE), v. 834, pp. 166-174.

# APPLICATION OF IMAGING SPECTROMETER DATA TO THE KINGS-KAWEAH OPHIOLITE MELANGE

JOHN F. MUSTARD and CARLE M. PIETERS, Department of Geological Sciences, Box 1846, Brown University, Providence, RI 02912

## Abstract

The Kings-Kaweah ophiolite melange in east-central California is thought to be an obducted oceanic fracture zone and provides the rare opportunity to examine in detail the complex nature of this type of terrain. It is anticipated that the distribution and abundance of components in the melange can be used to determine the relative importance of geologic processes responsible for the formation of fracture zone crust. Laboratory reflectance spectra of field samples indicate that the melange components have distinct, diagnostic absorptions at visible to near-infrared wavelengths. The spatial and spectral resolution of AVIRIS is ideally suited for addressing important scientific questions concerning the Kings-Kaweah ophiolite melange and fracture zones in general.

## Introduction

The development of imaging spectrometers as accurate and reliable tools for the examination of geologic terrain (Goetz et al, 1986) has opened up a whole new range of scientific problems that can be addressed. The application of imaging spectrometer data is advanced even further by the development of powerful analytical tools which can reduce the enormous volume of data obtained by such instruments to basic information about the surface (i.e Kruse, 1988; Mustard and Pieters, 1987; Adams et al, 1986). However, not all geologic problems are amenable to this type of analysis and careful merging of scientific goals, the specific geology and nature of the terrain, and capabilitites of the instrument are necessary in order to exploit the unique perspectives provided by imaging spectrometer data.

The Kings-Kaweah ophiolite melange poses scientific questions which are best addressed with imaging spectrometer data. The overall composition and nature of deformation in this ophiolitic terrain led Saleeby (1978, 1979) to conclude that it is an obducted oceanic fracture zone. There are few well documented fracture zone assemblages exposed sub-aerially and the Kings-Kaweah ophiolite melange is particularly interesting because of the range of fracture zone processes exposed. It provides a rare opportunity to examine the net result of the deformation of oceanic crust to form fracture zone crust. Fundamental questions remain regarding the development of the melange matrix and the relative importance of various processes thought to be active in fracture zones. We propose to map the distribution and abundance of important mineral components in the matrix of the melange with imaging spectrometer data and relate regional geochemical variations to the tectonic development of fracture zone crust.

## Background

Fracture zones, which are common and well recognized features in oceanic crust, are typically hundreds to thousands of kilometers long and 5-50 kilometers in width. The crust within the boundaries of a fracture zone is commonly refered to as fracture zone crust. In regions where oceanic crust is being formed at a rapid rate (i.e the East Pacific Rise) fracture zone crust comprises about 10-15% of the ocean floor while in areas of extremely slow spreading (i.e. Southwest Indian Ridge) fracture zone crust may reach 50% of the ocean floor (Abott, 1987). Although some basic characteristics of fracture zone crust have been deduced from geophysical investigations and examination of material dredged from fracture zones (Fox and Gallo, 1984; Forsythe and Wilson, 1984) the exact nature of the processes responsible for its formation as well as the details of the interactions between active processes in fracture zones are still not well understood.

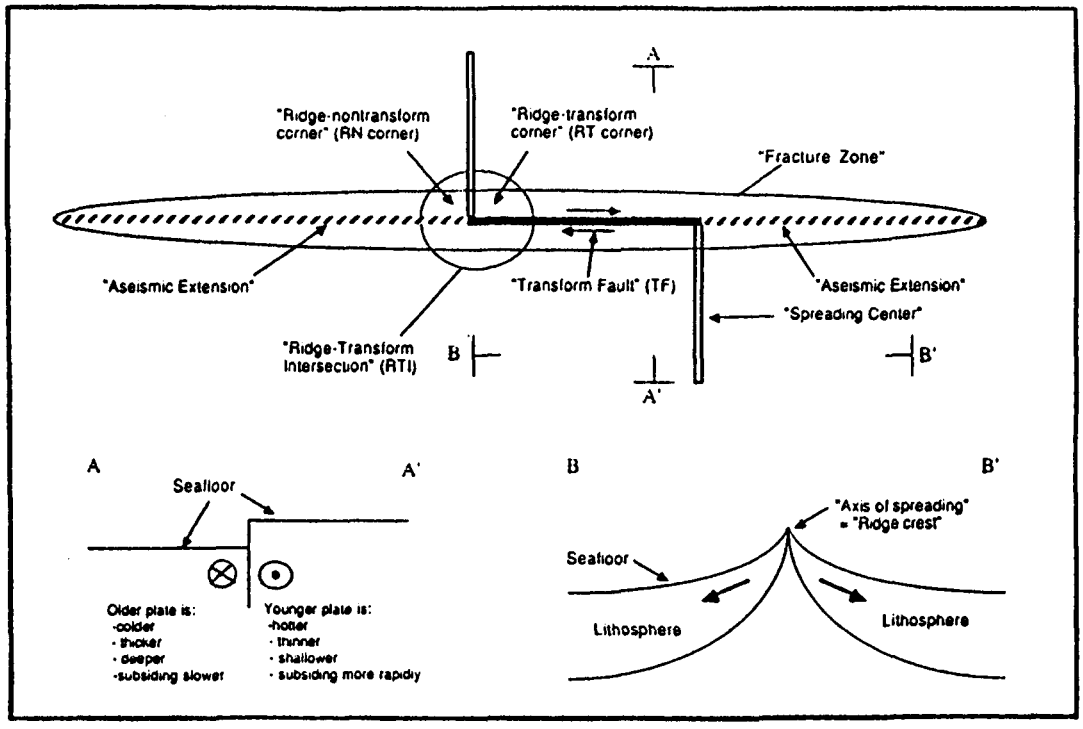


Figure 1. General terminology and spatial relationships of components associated with fracture zones (from Kastens, 1987).

In general a fracture zone consists of two primary segments (Fig. 1); the transform domain which occurs in the region between offset spreading centers and the non-transform or aseismic extension which can extend for many hundreds of kilometers beyond the ridge-transform intersections. Deformation processes within these domains are variable, complex, and polyphase. The active processes can be summarized as consisting of strike-slip and dip-slip faulting, hydrothermal alteration and metamorphism, ridge crest magmatism, diapiric intrusion of serpentinized ultramafics, and sedimentation. These processes are active with variable intensity throughout both segments of a fracture zone, but generally have localized zones of maximum intensity (i.e. the principal region of strike-slip deformation occurs in the transform domain while ridge crest magmatism is localized at the ridge-transform intersection (Karson and Dewey, 1978). The principal driving forces are spreading at the ridge crests and the offset thermal decay histories of the oceanic segments on either side of the fracture zone.

Serpentinization and protrusion of ultramafic mantle material is thought to be a common, and perhaps dominant process in fracture zones (MacDonald and Fyfe, 1985). The serpentinization of mantle rocks is facilitated by the highly fractured crust in fracture zones, availability of abundant water, and the discontinuity of thermal profiles across the fracture zone which can drive vigorous hydrothermal cells. Under these conditions serpentinite bodies are very mobile. Diapiric emplacement of serpentine is facilitated by the density contrast between the serpentine bodies and the surrounding country rock as well as the weak shear strength of serpentine. A consequence of these processes is that abundant fine-grained sheared serpentined is created which is then available to form the matrix. In addition, vertical mixing of ophiolitic components is enhanced by diapiric activity (Saleeby, 1984).

The net result of these processes is that the standard three layer stratigraphy of oceanic crust is disrupted and blocks and fragments of typical ophiolite crust are distributed in a fine-grained mobile matrix creating fracture zone crust. Although the matrix is predominantly ser-

pentine, contributions from the mafic components and the effects of the mechanical and geochemical processes operating in fracture zones can alter the overal bulk chemistry. Therefore, the distribution and abundance of mineral components within the melange matrix contains important information for understanding these complex geologic zones. Most of the previous work on sub-aerially exposed fracture zones have focused on the structural relationships between components and chemical analysis of the protoliths (Saleeby, 1977; Karson and Dewey, 1978). Analysis of regional geochemical variations in the matrix has not been pursued becaused of the diffuculty in obtaining unbiased samples for analysis (due to the extreme, small-scale heterogeneity of the matrix components). However a tool such as AVIRIS is ideally suited for examining the nature of regional geochemical variations in this type of terrain. The pixel size (20 m) averages the small scale heterogeneity and allows large scale processes to be recognized. Also, characteristic minerals in the melange have diagnostic features throughout the AVIRIS wavelength range.

## General Geology and Spectroscopic Character

The Kings-Kaweah ophiolite melange is located in the eastern foothills of the Sierra Nevada near Fresno, California (Fig. 1). In constrast to the classical interpretation that ophiolite-melange associations are indicative of a convergent margin emplacement (i.e. Coleman, 1971), the primary tectonic mixing and melange development for the Kings-

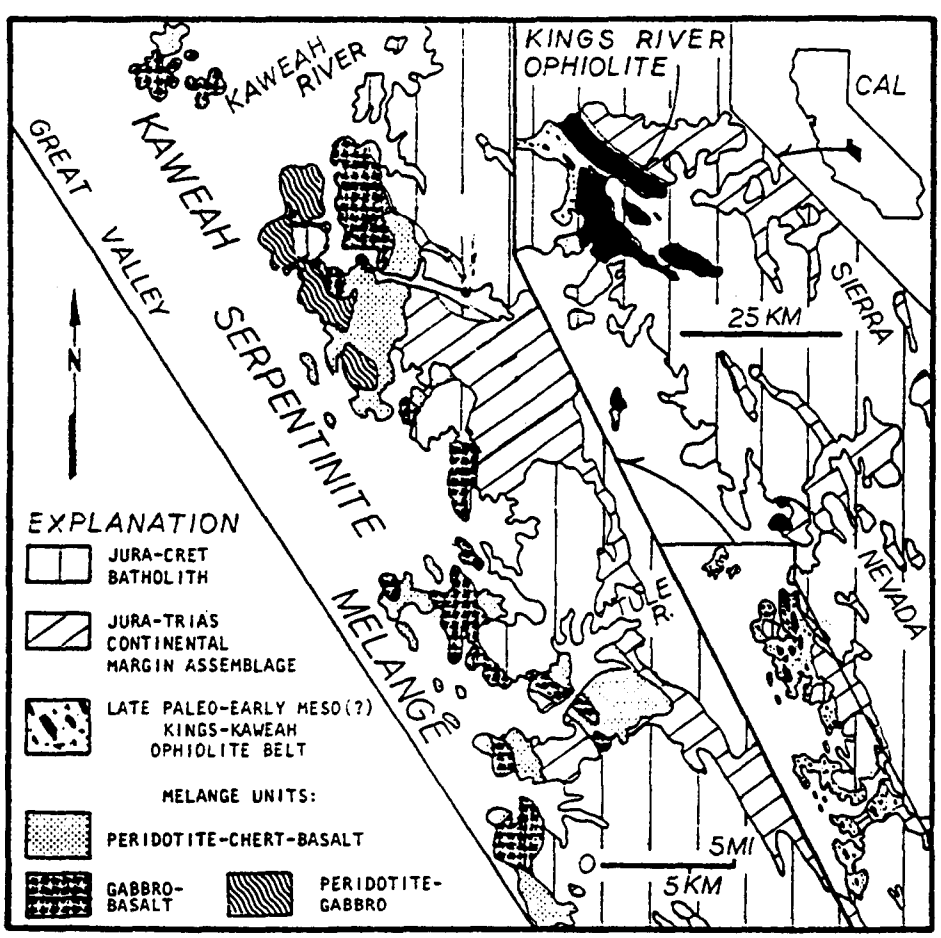


Figure 2. Location map for the Kings-Kaweah ophiolite melange showing the distribution of tectonic slabs and blocks. Also shown is the melange unit map of the Kaweah serpentinite melange (from Saleeby, 1979).

Kaweah ophiolite melange occured on the ocean floor in a fracture zone environment (Saleeby, 1977). This interpretation is based on the observations that no continental or arc rocks and sediments are found in the melange, no minerals typical of subduction emplacement are found, continental margin rocks are deposited unconformably over the melange, and the range and nature of the polyphase deformation is most consistent with an oceanic fracture zone. The Kings–Kaweah ophiolite belt was emplaced against the truncated margin of North America in Triassic to Middle Jurassic time and was contact metamorphosed to the hornblende–hornfels facies during the intrusion of the Sierra Nevada plutons between 125 and 102 my ago (Saleeby, 1977).

The Kings–Kaweah ophiolite melange is composed of two primary segments (Fig. 1): the Kings River ophiolite in the northern part of the belt and the Kaweah serpentinite melange in the southern part of the belt. The Kings River ophiolite contains large slabs of basalt, peridotite, and gabbro seperated by thin zones of serpentine melange. In contrast the Kaweah serpentinite melange contains no tectonic slabs and the serpentine matrix is very well developed (Saleeby, 1978; 1979). We have chosen to focus on the Kaweah serpentinite melange because the fracture zone assemblage is more highly developed and therefore the complex interactions between the processes responsible for the overall character of fracture zone crust should be better represented.

The Kaweah serpentinite melange consists of coherent to semi–coherent blocks distributed in a pervasively deformed matrix. The blocks range in size from millimeter sized particles to fragments tens to hundreds of meters in length. The blocks consist of harzburgite, peridotite, serpentinized ultramafics, gabbro, basalt, silica–carbonate rocks, and chert. They commonly show a tectonic fabric which parallels the schistosity of the matrix and the general southeast–northwest trend of the belt (Saleeby, 1979). Bidirectional reflectance spectra of a few representative handsamples collected from the field are shown in Fig. 3a. All spectra were measured from naturally weathered surfaces. $Fe^{2+}$ and $Fe^{3+}$ absorptions dominate in the visible and near–infrared portions of the spectra while overtones and combination overtones of fundamental $OH^-$ absorptions are primarily responsible for the narrow features in the infrared portions of the spectra.

The matrix primarily consists of schistose serpentine, ophicalcite, and silica–carbonate rocks, although talc and tremolite are locally abundant. Variations in matrix composition reflect shifts in the bulk chemistry (i.e. the presence of talc over serpentine represents a siliceous shift in the bulk chemistry) (Saleeby, 1979). This variation is of fundamental importance for addressing questions related to the character and developement of fracture zone crust. Some examples of reflectance spectra from exposed matrix surfaces are shown in Fig. 3b. Like the spectra shown for the block lithologies, the visible to near–infrared portion of the spectra are dominated by $Fe^{2+}$ and $Fe^{3+}$ absorptions while the infrared portions of the spectra are dominated by absorptions related to $OH^-$.

Much of the field area has a variable cover of soils and grass. It will be necessary to remove the spectral signatures of the grasses using an appropriate mixing model (Mustard and Pieters, 1987; Adams et al, 1986) while the soils may provide clues as to the nature of geochemical variation within the subsurface. We have collected an extensive series of grass and soil samples and some examples of reflectance spectra from these are shown in Fig. 3c. Field spectra of rocks, soils, and grasses have also been acquired with PIDAS (Goetz, 1987) to characterize the actual ground reflectance of these surface types as well as potential calibration targets. A PIDAS spectrum of typical grass cover is shown in Fig 3d. This type of data is an essential link between laboratory and remotely acquired reflectance data.

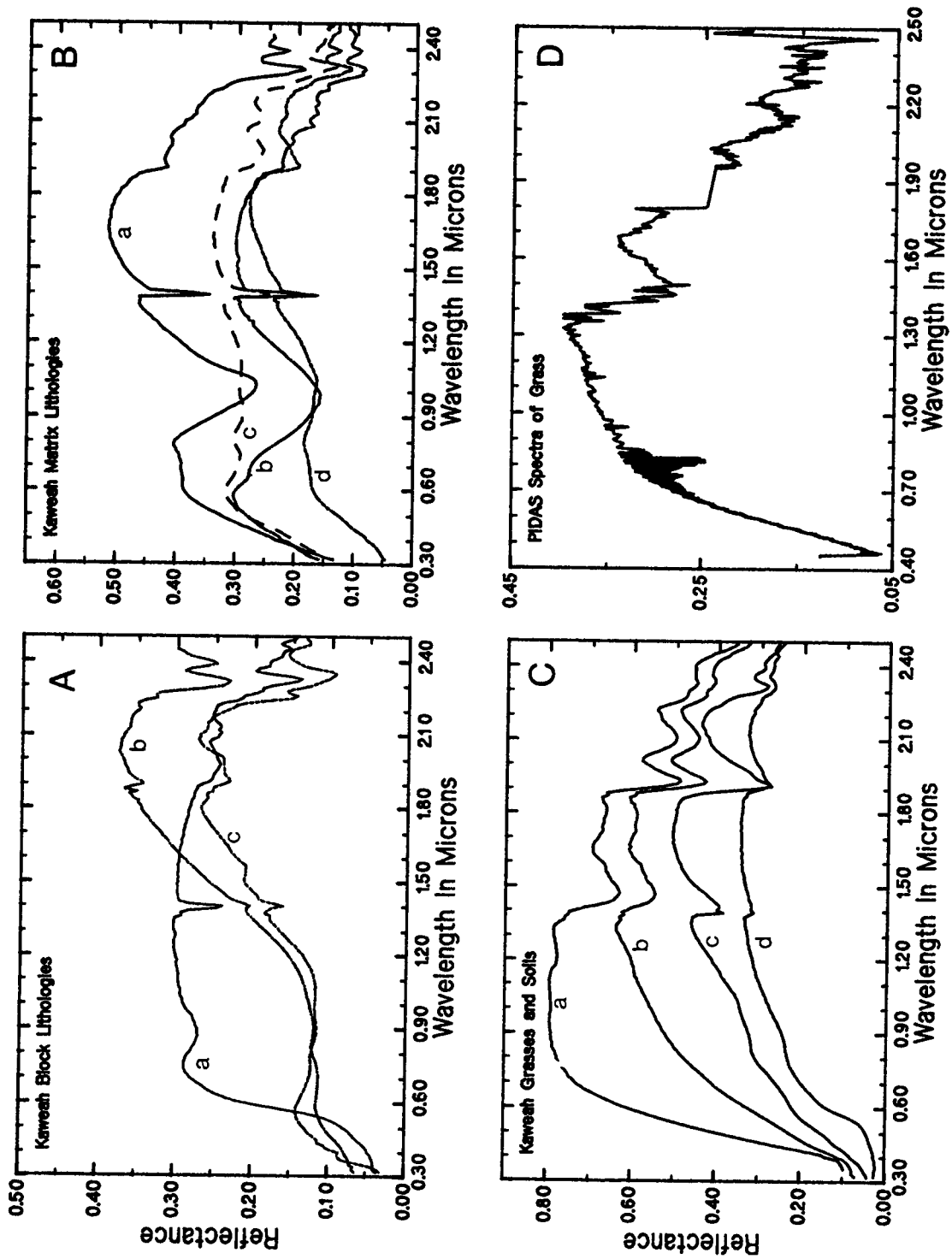


Figure 3. RELAB reflectance spectra of some components in the Kaweah serpentinite melange. A) Some typical block lithology spectra where (a) is a serpentinized peridotite, (b) is a gabbro, and (c) is a pillow basalt. B) Examples of matrix lithology spectra where (a) is predominantly talc bearing, (b) has both talc and tremolite, (c) is from a serpentine rich region, and (d) is an ophicalcite. C) Examples of grass and soil spectra where (a) is dry, brown grass, (b) is partially decayed grass, (c) is a talc rich soil, and (d) is a soil containing Fe-oxide. D) Field spectrum of a grassy area. The spectra of the components grass, decayed grass, soil, and shade are all contribute to this average spectrum.

## Imaging Spectrometer Analysis

Imaging spectrometer data were acquired over the field site on September 14, 1987 with AVIRIS. Although the principal science target was not covered by the AVIRIS overflight, some secondary targets were imaged as well as a calibration target. Examination of these data indicate that the spatial resolution of the instrument is very good for addressing the scientific goals outlined above. However, the complexity of the field site and nature of the extraneous ground cover (grasses) requires that the instrument perform at optimum precision and accuracy. Due to the low signal to noise during this flight, and other problems outlined by others in this volume, it is not possible to address our scientific goals with these data.

In summary, the Kaweah serpentinite melange provides the opportunity to address fundamental scientific questions concerning the formation and development of oceanic fracture zones and the general behavior of oceanic crust during intense disruption. An imaging spectrometer such as AVIRIS permitts the mapping of the distribution and abundance of diagnostic minerals in the highly deformed and complex matrix, and this information, which is not readily obtained by other methods and techniques, allows one to begin to unravel the complexity of such terrain. We look forward to analyzing high quality AVIRIS data over the principal science target in the near future.

## References


Abbott, D., Statistics of fracture zones, subduction of ridges, and the composition of ophiolites, *EOS Trans. Am. Geophys. Union, 68*, p. 408, 1987.

Adams, J. B., M. O. Smith, and P. E. Johnson, Spectral mixture modeling: A new analysis of rock and soil types at the Viking Lander 1, *J. Geophys. Res., 91*, 8098-8112, 1986.

Bonatti, E., Vertical tectonism in oceanic fracture zones, *Earth Planet. Sci. Letters, 37*, 369-379, 1978.

Bonatti, E., and J. Honnorez, Sections of the Earth's crust in the equatorial Atlantic, *J. Geophys. Res., 81*, 4104-4116, 1976.

Coleman, R. G., Plate tectonic emplacement of upper mantle peridotites along continental edges. *J. Geophys. Res., v. 76*, p. 1212-1222, 1971.

Dewey, J. F., and J. M. Bird, Origin and emplacement of the ophiolite suite: Applachian ophiolites in Newfoundland. *J. Geophys. Res. v. 76*, 3179-3266, 1971.

Fox, P. J., and D. G. Gallo, A tectonic model for ridge-transform-ridge plate boundaries: Implications for the structure of oceanic lithosphere, *Tectonophysics, 104*, 205-242, 1984.

Forsyth, D, W, and B. Wilson, Three dimensional structure of a ridge-transform-ridge system, *Earth Planet. Sci. Lett., 70*, 355-362, 1984.

Goetz, A. F. H., The Portable Instant Display and Analysis Spectrometer (PIDAS), *Proc. Third Airborne Imaging Spectrometer Data Analysis Workshop (G. Vane ed.), JPL Publication 87-30*, 8-17, 1987.

Goetz, A. F. H., G. Vane, J. E. Solomon, and B. N. Rock, Imaging spectrometry for earth remote sensing, *Science, 288*, 1147-1153, 1986

Karson, J, and J. F. Dewey, Coastal complex in western Newfoundland: An early Ordivician oceanic fracture zone: *G.S.A. Bull., 89*, 1037-1049, 1978.

Kastens, K. A., A compendium of causes and effects of processes at transform faults and fracture zones, *Rev. Geophys., 25*, 1554-1560, 1987.

Kruse, F. A., Use of Airborne Imaging Spectrometer data to map hydrothermal alteration in the northern Grapevine Mountains, Nevada and California, *Remote Sens. Environ*, 31-52, 1988.

MacDonald, A. M., and W. S. Fyfe, Rate of serpentinization in seafloor environments, *Tectonophysics, 116*, 123-135, 1985.

Mustard, J. F., and C. M. Pieters, Quantitative abundance estimates from bidirectional reflectance measurements, *Proc. 17th Lunar Planet. Sci. Conf., J. Geophys. Res., 92*, E617-E626, 1987.

Saleeby, J. B., Fracture zone tectonics, continental margin fragmentation, and emplacement of the Kings-Kaweah ophiolite belt, southwestern Sierra Nevada, California, *in* Coleman, R. G., and Irwin, W. P., eds., North American ophiolites, *Oregon Dept. Geol. Min. Ind. Bull. v.91*, p. 141-160, 1977.

——Kings River Ophiolite, Southwest Sierra Nevada Foothills, California. *Geol. Soc. Am. Bull. v. 89*, p. 617-636, 1978

——Kaweah Serpentinite Melange, Southwest Sierra Nevada Foothills, California. *Geol. Soc. Am. Bull. v. 90*, p. 24-46, 1979.

——Tectonic significance of serpentinite mobility and ophiolite melange, *in* Raymond, L. A., ed., Melanges; Their nature, origin, and significance, *Geol. Soc. Am. Special Paper 198*, 153-168, 1984.

# AVIRIS SPECTRA OF CALIFORNIA WETLANDS

MICHAEL F. GROSS, College of Marine Studies, University of Delaware, Newark, DE 19716, USA; SUSAN L. USTIN, Department of Botany, University of California, Davis, CA 95616, and Space Sciences Laboratory, University of California, Berkeley, CA 94720; and VYTAUTAS KLEMAS, College of Marine Studies, University of Delaware, Newark, DE 19716.

## ABSTRACT

Spectral data gathered by the AVIRIS from wetlands in the Suisun Bay area of California on 13 October 1987 were analyzed. Spectra representing stands of numerous vegetation types (including Sesuvium verrucosum, Scirpus acutus and Scirpus californicus, Xanthium strumarium, Cynadon dactylon, and Distichlis spicata) and soil were isolated. Despite some defects in the data, it was possible to detect vegetation features such as differences in the location of the chlorophyll red absorption maximum. Also, differences in cover type spectra were evident in other spectral regions. It was not possible to determine if the observed features represent noise, variability in canopy architecture, or chemical constituents of leaves.

## INTRODUCTION

Gross et al. (1987) analyzed 0.8-1.6μm (11 September 1986) AIS-2 data of Suisun Bay, CA, wetlands vegetation and could not identify any narrow-waveband differences between vegetation types, although there were broad-band differences in brightness. The objective of this study is to compare AVIRIS spectra of various wetland vegetation types from the same area to determine how they differ and how these features relate to other land cover types such as soil. Ultimately, we hope to use imaging spectrometry to distinguish vegetation by species (or type) and to measure key chemical constituents, such as chlorophyll, cellulose, lignin, and nitrogen.

## DATA ACQUISITION AND ANALYSIS

One flightline of AVIRIS data was acquired over wetland portions of Grizzly Island and Joice Island in Suisun Marsh (Figure 1) on 13 October 1987. The flightline was about 10.5km wide, composed of 614 20m pixels (17% overlap). The area within the flightline is dominated by leveed wetlands that are managed to optimize waterfowl habitat, such that tidal flooding and salinity are controlled, thus causing vegetation distribution and condition to differ between ponds. At the time of data acquisition, lack of rainfall had resulted in senescence of most of the vegetation. In comparison with site conditions at the time of AIS-2 data acquisition, more vegetation was in a senescent condition, and more areas had been recently flooded (starting in September).

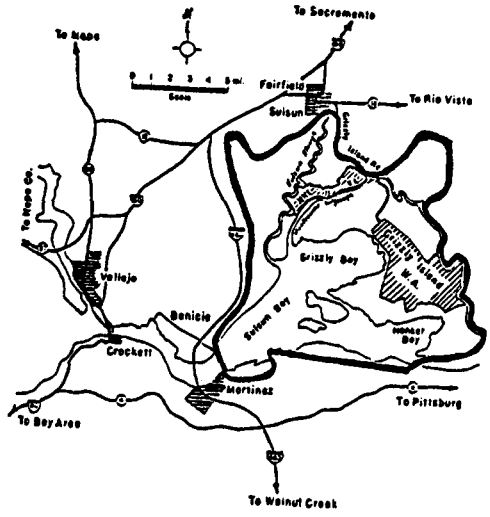


Figure 1. Location of Suisun Marsh
(area within thick solid line)

The data were radiometrically corrected and line drop-outs were removed by averaging at JPL. Data were analyzed using the AVIRIS version of SPAM (Spectral Analysis Manager) software at JPL. Information on land cover types/uses and vegetation distribution was provided by low altitude aircraft photography and high altitude photographs flown at the time of AIS-2 data acquisition. Because the dominant species of vegetation are perennials and often grow in monotypic stands, vegetation distribution does not change substantially over a one year period.

## RESULTS

Data quality was generally better than that of AIS-1 and AIS-2 data. Data defects with easily detectable effects included numerous line drop-outs, sudden changes in apparent scene brightness, low signal/noise ratio in Spectrometer D, and fixed pattern noise (particularly evident in Spectrometers A and B). In addition, some horizontal striping was evident (i.e., adjacent rows differed in brightness). Figure 2 shows band 68, or 1.06μm (following radiometric rectification). Water and flooded areas appear dark, and dense vegetation appears bright. The fixed pattern noise is evident at the top of the figure as wavy bands oriented diagonally. A sudden change in apparent scene brightness is evident near the bottom of the image.

To derive spectra of various cover types in the image, the mean spectrum of 1x1 to 5x5 pixel samples (N=4-10) of distinct vegetation types or soil was computed and considered to represent the spectral response of the cover type. Distinct cover types identified included green Sesuvium verrucosum (purslane), senescing Xanthium strumarium (cocklebur), senescing Cynadon dactylon (bermudagrass), senescing Distichlis spicata (saltgrass), (saltgrass),senescing Scirpus acutus and S. californicus (tules), a senescing mixture of the above vegetation types plus a few others,senescent

Figure 2. Band 68 (1.06μm) after radiometric rectification.

mowed tules, senescent unmowed tules and Typha (cattails), a flooded area of senescing Scirpus paludosus (alkali bulrush), a sparsely vegetated area, two soil areas, and water. These spectra were stored in a library. To better distinguish vegetation spectral features from atmospheric features, all vegetation spectra and one of the soil spectra were multiplied by 50 and then divided by the other soil spectrum using the FUNCTION program (the spectral response of the soil was assumed to approximate that of a flat field).

Spectra were displayed in both normalization modes (area and amplitude). Spectra were compared within five groups of wavebands separated by atmospheric absorption features: 0.45-0.90μm, 0.98-1.11μm, 1.15-1.35μm, 1.49-1.72μm, and 1.97-2.35μm. Because of the poor signal/noise ratio for Spectrometer D, and possible loss of features for those wavebands resulting from data compression (to achieve a range of 0 to 255 DN), we chose not to analyze the region between 1.97 and 2.35μm.

As expected, the vegetation spectra were distinct from the soil spectrum by having higher reflectance in the near-infrared relative to the visible region. In addition, there were some other differences between vegetation and soil spectra (for example, vegetation had absorption features at 0.80, 0.82, 0.84μm, a steeper slope between 1.01μm and 1.02μm, a reflectance peak at 1.18μm relative to soil, and absorption features at 1.31μm, 1.51μm, 1.55μm, and 1.62μm).

Green vegetation exhibited an absorption maximum at 0.68μm, whereas the absorption maximum occurred at 0.67μm for senescing vegetation. Comparison of vegetation spectra with each other revealed several other wavelengths at which there was considerable variability in either slope or amplitude of signal. These included 0.76-0.77μm, 0.80-0.84μm, 1.04-1.09μm, 1.29-1.33μm, 1.50-1.52μm, and 1.57-1.65μm. The Xanthium spectrum differed the most from the other spectra. Its notable features included absorption maxima at 0.81, 1.32, and 1.51μm, where other vegetation spectra showed increased reflectance, smaller peaks at 1.29 and 1.56μm than the other spectra, and the lack of an absorption feature at 1.62μm that was present in other vegetation spectra. The features of various vegetation spectra are evident in Figure 3.

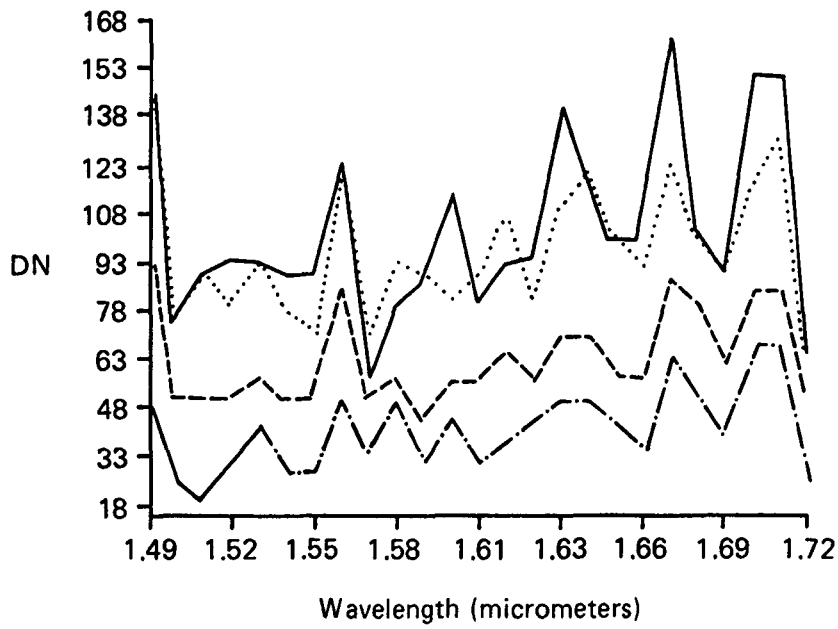


Figure 3. Spectra of four vegetation types, shown between 1.49-1.72μm. ····· = Cynadon, ——— = Xanthium, – – – – = Sesuvium, and – · – · – · = mixture of wetland vegetation types.

Numerous unsupervised classifications of the image were performed using the CLUSTER algorithm for various portions of the spectral region sampled by the AVIRIS. Results were generally not satisfactory. Most images were "salt and pepper"-like in appearance. Manual and automatic merging of classes did not result in substantial improvement.

Somewhat better results were obtained using MIXTURE, a program that, when used in the "area" mode, assigns pixels to classes based on user-specified spectra (somewhat analogous to a supervised classification). The distribution of cover types assigned by the algorithm corresponded reasonably well to the actual distribution when based solely on spectral characteristics in narrow regions of the spectrum. Tested separately, these included 0.67-0.72μm (Figure 4), 0.74-0.88μm, 1.49-1.72μm, 1.57-1.61μm, and 1.58-1.64μm. In Figure 4, the sudden apparent change in scene brightness is evident in columns 2-6, and the fixed pattern noise, in column 6.

Another program that created accurate output was FIND. This program locates all pixels matching a user-defined spectrum within user-supplied allowable deviations in slope and amplitude. The procedure can be repeated for several spectra in one image. In contrast to MIXTURE, FIND works on only one spectrum at a time (i.e., it does not compare all spectral classes with each other and assign pixels to the most likely class). FIND accurately located all Sesuvium and other lush green pixels based on the 0.67-0.72μm spectral values. When spectra from several cover types were supplied, reasonably accurate results for this spectral region were obtained, after some manipulation of allowable spectral deviations. Likewise, results were satisfactory when spectra from four spectral regions (0.67-0.68, 0.74-0.76, 1.50-1.52, and 1.56-1.58μm) of six cover types were used as input. Other spectral regions were not tested.

Figure 4. Results of MIXTURE analysis, using four spectra (senescent vegetation [column 2], flooded senescing S. paludosus [column 3], green S. verrucosum [column 4], and sparse senescent vegetation [column 5]). Column 1 is the raw image (0.67μm), and column 6 is the residual, or pixels whose spectra do not match any of the four spectra. In this case, the residual pixels correspond to water.

## DISCUSSION

Our results suggest that, despite considerable noise in the data, the spectral resolution is sufficient to detect differences in the position of chlorophyll absorption maxima.

Also, there may be narrow spectral regions between 0.4-1.72μm for which the amplitude and slope of the spectral response of various vegetation types are sufficiently different to enable them to be

distinguished. These include the 0.76-0.77, 0.80-0.84, 1.04-1.09, 1.29-1.33, 1.50-1.52, and 1.57-1.65μm areas. Recent attention has been focused on the ability to remotely sense canopy chemical constituents based on their absorption features. Peterson et al. (1988), Norris et al. (1976), and Burdick et al. (1981) report significant correlations between the concentration of chemical constituents and reflectance at various wavelengths, principally between 1.55-1.75μm and between 1.95-2.35μm. The specific wavelengths useful for detecting these constituents seem to vary from study to study and to depend on whether the raw spectra, first derivative, second derivative, or some other transformation is being used. Our results indicating the presence of some species-dependent differences in spectra may reflect variations in canopy architecture (including the influence of soil), the concentration of major chemical constituents, or some combination of these factors. We did not have the resources to chemically analyze vegetation samples, so we can only speculate about the significance of these spectral features. Because of the data quality problems mentioned above and our division of vegetation spectra by a soil spectrum, it is likely that some apparent spectral features were not real. However, we tried to minimize this possibility by sampling, for each spectrum, a large number of pixels scattered throughout the image.

Future research efforts should be directed towards obtaining spectral measurements of the vegetation on the ground, and measuring the concentration of chemical constituents in the vegetation to understand the features in the spectra sensed by the AVIRIS. Initial studies could focus on determining what constituents influence reflectance at 0.76-0.77μm, 0.80-0.84μm, 1.04-1.09μm, 1.29-1.33μm, 1.50-1.52μm, and 1.57-1.65μm.

## ACKNOWLEDGEMENTS

This research was supported by the NASA Earth Science and Applications Division Land Processes Program under Grant No. NAGW-950, and the Universities of Delaware and California. The authors are indebted to Lorena Hobart for secretarial expertise, and the staff at JPL for processing the raw data and allowing us to use their image analysis facility (special thanks go to Lisa Barge for help with SPAM).

## LITERATURE CITED

Burdick, D., F. E. Barton, II, and B. D. Nelson. 1981. Prediction of bermudagrass composition and digestibility with a near-infrared multiple filter spectrophotometer. Agron. J. 73:399-403.

Gross, M. F., S. L. Ustin, and V. Klemas. 1987. AIS-2 spectra of California wetland vegetation, pp. 83-90 in Proc. Third AIS Data Anal. Workshop, JPL Publ. 87-30, Jet Propulsion Lab, Pasadena, CA.

Norris, K. H., R. F. Barnes, J. E. Moore, and J. S. Shenk. 1976. Predicting forage quality by infrared reflectance spectroscopy. J. Animal Sci., 43:889-897.

Peterson, D. L., J. D. Aber, P. A. Matson, D. H. Card, N. Swanberg, C. Wessman, and M. Spanner. 1988. Remote sensing of forest canopy and leaf biochemical contents. Remote Sens. Environ., 24:85-108.

# AN ASSESSMENT OF AVIRIS DATA FOR HYDROTHERMAL ALTERATION MAPPING IN THE GOLDFIELD MINING DISTRICT, NEVADA

VERONIQUE CARRERE and MICHAEL J. ABRAMS, Jet Propulsion Laboratory, California Institute of Technology, Pasadena, CA 91109

## ABSTRACT

Airborne Visible and Infrared Imaging Spectrometer (AVIRIS) data were acquired over the Goldfield Mining District, Nevada, in September 1987. Goldfield is one of the group of large epithermal precious metal deposits in Tertiary volcanic rocks, associated with silicic volcanism and caldera formation. Hydrothermal alteration consists of silicification along fractures, advanced argillic and argillic zones further away from veins and more widespread propylitic zones. Alteration minerals include alunite, kaolinite, adularia and opal, montmorillonite and chlorite. An evaluation of AVIRIS data quality (spectral accuracy, signal to noise performance, signal variations,...) was performed. Faults in the data, related to engineering problems and a different behaviour of the instrument while on-board the U2, were encountered. Consequently, a decision was made to use raw data and correct them only for dark current variations and detector read-out-delays. New software was written to that effect. Atmospheric correction was performed using the "flat field" correction technique. Analysis of the data was then performed to extract spectral information, mainly concentrating on the 2-2.45 micron window, as the alteration minerals of interest have their distinctive spectral reflectance features in this region. Principally kaolinite and alunite spectra were clearly obtained. Mapping of the different minerals and alteration zones was attempted using ratios and clustering techniques. Poor signal-to-noise performance of the instrument and the lack of appropriate software prevented us from producing an alteration map of the area. Spectra extracted locally from the AVIRIS data were checked in the field by collecting representative samples of the outcrops. In all cases, lab PIDAS (Portable Instant Display and Analysis Spectrometer) and Beckman UV5240 measurements verified the identifications obtained from AVIRIS data. Despite the rather poor quality of the data and the lack of appropriate software, this test demonstrates the potential of high resolution imaging spectrometers for alteration mapping and identification of mineralogy.

## I. INTRODUCTION

This paper describes some preliminary results arising from the analysis and interpretation of data from the September 1987 Airborne Visible and Infrared Imaging Spectrometer (AVIRIS) flight over Goldfield Mining District, Nevada.

AVIRIS acquires simultaneously 224 channels (distributed over 4 spectrometers) of data in the 0.4 to 2.45 micron region, with an average spectral resolution of about 10 nm. Operating from NASA's U2 at an altitude of 20 km, the IFOV is 20m with a swath width of 12 km. This is the first instrument of its kind to obtain complete high spectral resolution reflectance data with a wide swath width.

The Goldfield Mining district was selected as a test area because it is one of a group of large epithermal precious-metal deposits in Tertiary volcanic rocks found in the western part of the Great Basin. The area covered by the AVIRIS flight includes the eastern part of the Goldfield Hills (Figure 1). Study of the data focused on the main alteration area. Formations represented in the test-area are mainly Miocene in age. They are composed of pyroclastic tuffs and welded ash flow tuffs of early Miocene age (about 22-20.5 M.Y old, Ashley and Silbermann, 1976; Cornwall, 1972), ranging in composition from dacitic to quartz latitic and rhyolitic. Lava flows and intusives of similar composition and some andesites and basalts are also common.

The oldest most widespread and most voluminous of these units is the Milltown Andesite, which consists of trachyandesite and rhyodacite tuffs and flows with minor basalts and quartz latite. A K-Ar age of 21.5 M.Y makes the formation Miocene in age (Silbermann and MacKee, 1972).

A porphyritic rhyodacite (unnamed dacite of Ransome, 1909) intrudes and overlies the Milltown Andesite, forming a group of flow dome complexes. These rocks are particularly prominent in the test area. The sequence includes localized units of quartz latite, andesite and basalt.

The Milltown Andesite and porphyritic rhyodacite are overlain by the Tuff of Chispa Hills (unnamed dacite vitrophyre of Ransome, 1909) and the Chispa andesite, a trachyandesite flow, on the south side of the area, and by the andesite-rhyodacite breccia on the eastern side. The andesite-rhyodacite breccia is a locally very coarse breccia sheet, composed of debris from the Milltown Andesite and porphyritic rhyodacite.

The Spreadhead Member of the Thirsty Canyon Tuff flanks the Goldfield Hills on the south side of the area. It consists of a sequence of rhyolitic to pantelleritic ash flow and minor ash-fall tuffs that were erupted from the Blackcap Mountain caldera area. The Thirsty Canyon Tuff and associated lavas are Pliocene in age (Noble and others, 1964).

Three major structural events happened in this area. Ashley (1972) suggested that the oldest tertiary structure in the district is a ring fracture. Faulting occurred during the period of early Miocene volcanism. The faulting and mineralization were probably both produced by a pluton that intruded the area to shallow levels but did not reach the surface. The test-area is mainly affected by

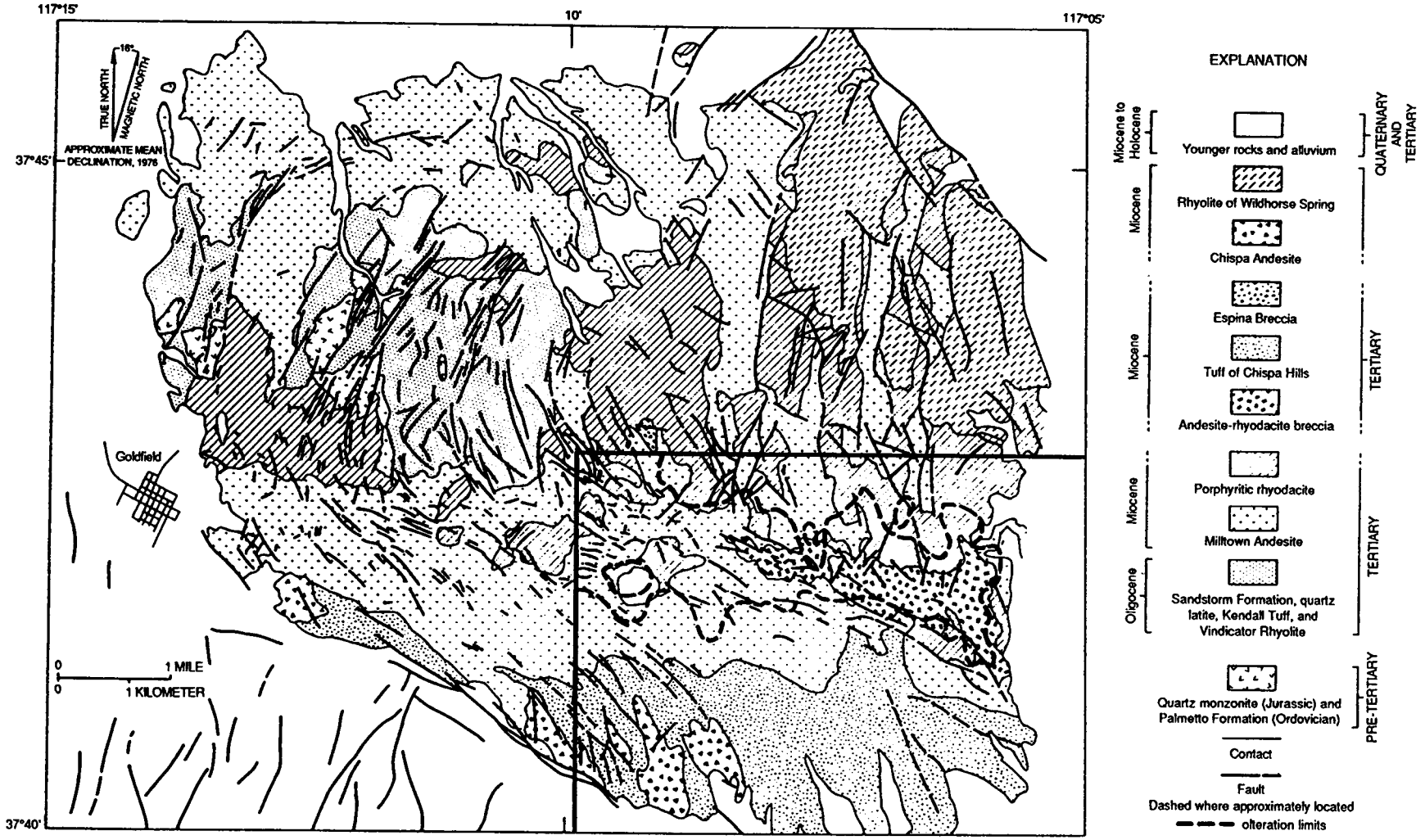


**FIGURE 1. Generalized geologic and alteration map of the Goldfield Mining District (after Ashley, 1976) Location of the study area.**

late Tertiary faults (Basin and Range faults), mostly northerly trend and NW trending post-Siebert faults.

Hydrothermal alteration and ore deposition at Goldfield occured within the episode of andesitic-dacitic volcanism beginning with the Milltown Andesite and ending with the Chispa Andesite. Although the Milltown Andesite, porphyritic rhyodacite, andesite-rhyodacite breccia and Tuff of Chispa Hills are hydrothermally altered, the Chispa Andesite is not.

Direct dating of hydrothermal minerals (alunite and sericite) yield an age range of 21-20 MY for the hydrothermal alteration (Ashley and Silbermann, 1976). Alteration zones (Table 1) include silicified zones along fractures, many alunite-bearing, surrounded by advanced argillic, argillic and more widespread propylitic zones (Harvey and Vitaliana, 1964; Ashley and Albers, 1975; Ashley, 1974). Some montmorillonite-bearing argillic areas also occur.

Table 1

| ALTERATION TYPE | MAJOR MINERALS |
|---|---|
| Silicified | Q+Al+K+Pp+D+Km |
| Advanced Argillic | Q+Al+Pp+K+D+Op+Km |
| Argillic | Q+K+Km+mixed layers |
| Montmoril.-bearing Argillic | M+K+Q+mixed layers+Ca+Chl |
| Propylitic | Ep+Chl+Ab+Ca+minor K-mica and Pyrite |

| ABBREVIATIONS: | | | | |
|---|---|---|---|---|
| | Ab | Albite | K | Kaolinite |
| | Al | Alunite | Km | K-mica |
| | Ca | Calcite | M | Montmorillonite |
| | Chl | Chlorite | Op | Opal |
| | D | Diaspore | Pp | Pyrophyllite |
| | Ep | Epidote | Q | Quartz |

The basic objective of this study was to determine the efficiency of AVIRIS data for hydrothermal alteration mapping. An evaluation of the intrinsic properties of the instrument during its September 14th overflight of Goldfield was also performed.

After being corrected for dark current variations, detector read-out delays and atmospheric effects, various techniques were applied to identify minerals using spectral information, and map alteration zones using mineral assemblage and distribution. Since most of the minerals involved in the alteration process present features in the near-infrared, the study focused on the 2.0-2.45 micron region (see table 2).

Results were checked by collecting samples in the field and getting lab PIDAS (Portable Instant Display and Analysis Spectrometer) and Beckman UV5240 spectra. Mainly kaolinite and alunite were identified but the quality of the data and the lack of appropriate software prevented us from mapping alteration zones.

Table 2

| MINERAL | ABSORPTION FEATURES (microns) |
|---|---|
| Alunite | 1.77; 2.17; 2.20; 2.317 |
| Calcite | 2.34 |
| Chlorite | 2.26; 2.355 |
| Kaolinite | 2.16; 2.21 |
| K-mica | 2.205; 2.3; 2.4 |
| Montmorillonite | 2.2 |
| Pyrophyllite | 2.166; 2.314 |

## II. DATA QUALITY

Some problems, related to AVIRIS data acquisition have been brought to our attention while evaluating our data set.

### 1. Drift in the offset

The most serious is that the instrument offset, particularly in spectrometer D, is subject to long term drift. This results in a lower or higher than optimum offset and, in the worst case, data clipping. It shows up in the data as detector elements having apparent outputs of zero (Figure 2). This drift was related to:
-the poor quality of the potentiometers used in the pre-amplifier circuits to adjust offset magnitude (Vane, personal communication);
-changes in temperature; it has been noticed that small changes in the detector temperature could give rise to offset signals equal to the predicted full scale image signal (Steinkraus and Hickok, 1987). This can be explained by the fact that the spectrometer heater configuration designed to athermalize the spectrometers and thereby maintain alignment of the optical elements was not adequate for the U2 flight environment (Vane, personal communication);
-nonsystematic vibration introducing fluctuation in instrument output level.

### 2. Offset in brightness

An offset in brightness occurs in the middle of the scene. This is also the result of a vibrationally induced change in the potentiometer setting in a pre-amplifier circuit which caused a step change in the offset applied to the data during onboard processing.

### 3. Noise characterization

Several types of noise are present in the data. First, an estimation of the signal-to-noise performances of the instrument for this data set was done. Two methods were used. The first one (Figure 3) consists in calculating the mean spectral response of an homogeneous area and its standard deviation (Conel et al., 1987).

The mean value of the average response is considered to be the signal and the noise estimate is provided by the standard deviation. The ratio mean/standard deviation gives a first estimation of the signal-to-noise response for each wavelength. The only homogeneous area big enough to be used in the scene was the Chispa Andesite which happens to be dark. But using a 9x9 area increases the signal-to-noise and partly compensates for this problem. According to this method, the signal-to-noise in the various spectrometers is (Figure 4):

A 30/1
B 10/1
C 10/1
D 8/1

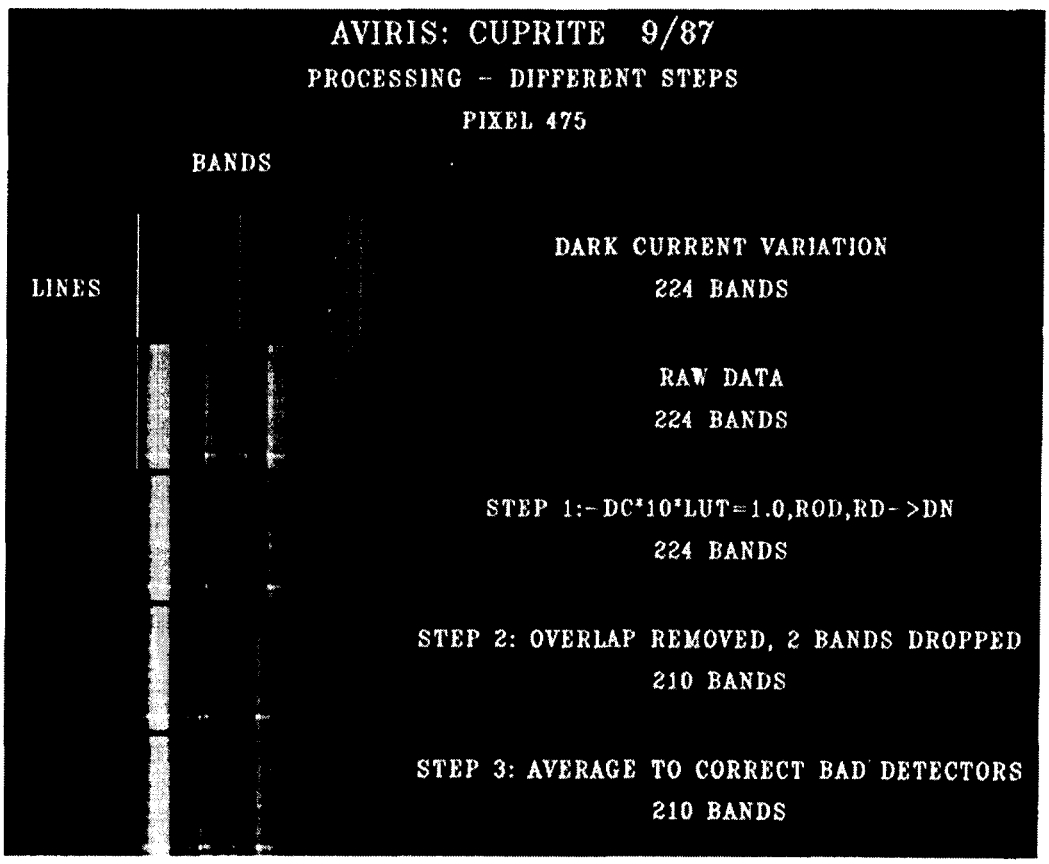


Figure 2. Different steps used to pre-process the AVIRIS data

A second way to estimate the quantity of noise in the data coming from the instrument itself and allowing us to get rid of any inhomogeneity in the data is to look at the standard deviation of the dark current (Figure 5). By dividing the signal coming from one single pixel by the standard deviation of the average dark current, we get another estimation of the signal-to-noise. This has been done for a bright sample and a dark sample to give an idea of the range.

The results are (Figure 6):

| | |
|---|---|
| A | 30:1 to 70:1 |
| B | 10:1 to 30:1 |
| C | 10:1 to 25:1 |
| D | 8:1 to 18:1 |

Both methods give consistent results. The second one presents the advantage of characterizing the instrument itself and should be more accurate.

A quick comparison (Table 3) with the performances published before the flight season shows that, even in the best case (bright sample), the noise level increased drastically.

The image data also contain periodic noise and, at least, three distinct spatially recognizable patterns are present. The most prominent of these has a period of about 10.3 lines per cycle (0.097 line-1) normal to the banding, which trends at an angle of about 18 degrees to the scan direction. A second band set has a period of 12.8 lines per cycle (0.78 line-1) at an angle of about 65 degrees; the third periodic variation is manifested within the second set with a period of one line per cycle (1 line-1) along the flight direction.

**Table 3**

| SPECTROMETER | 1st METHOD | 2nd METHOD | LAB (pre-flight) |
|---|---|---|---|
| A | 30:1 | 30:1-70:1 | 151:1 |
| B | 10:1 | 10:1-30:1 | 140:1 |
| C | 10:1 | 10:1-25:1 | 70:1 |
| D | 8:1 | 6:1-18:1 | 30:1 |

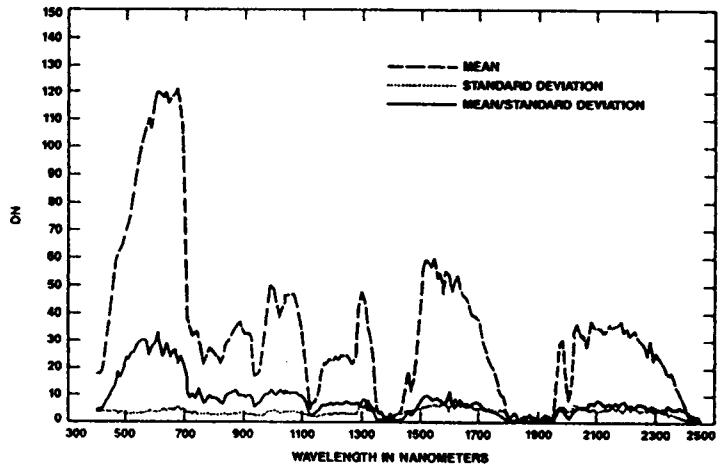


FIGURE 3. Estimation of signal-to-noise (method n°1)

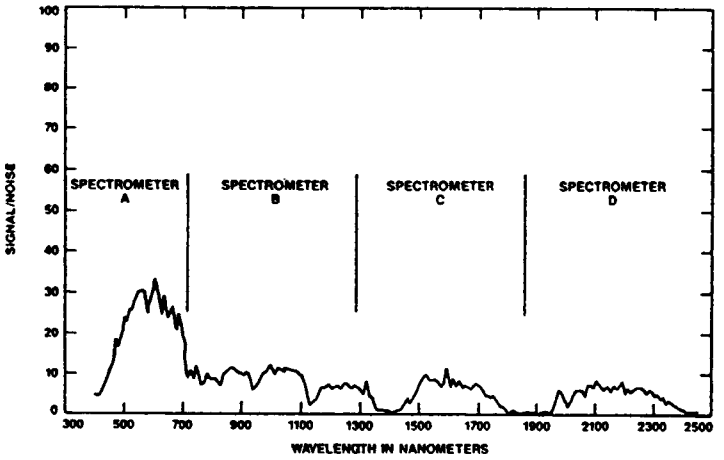


FIGURE 4. Signal-to-noise results from method n°1

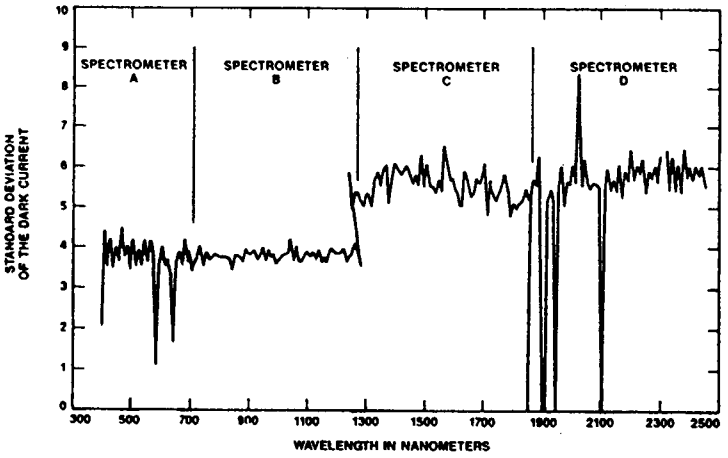


FIGURE 5. Estimation of the noise (method n°2)

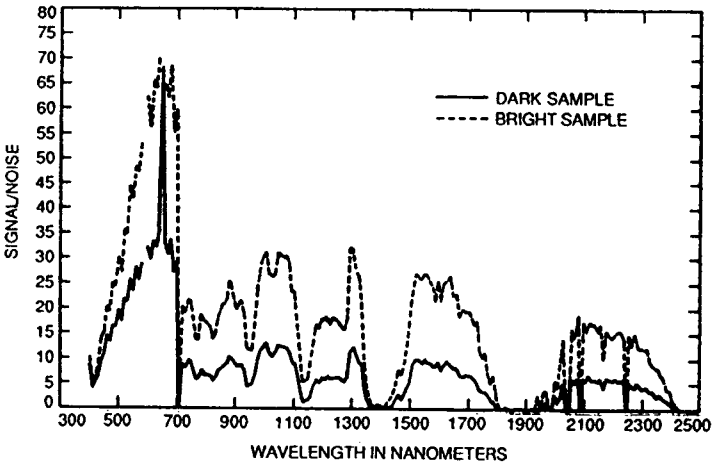


FIGURE 6. Signal-to-noise range (method n°2)

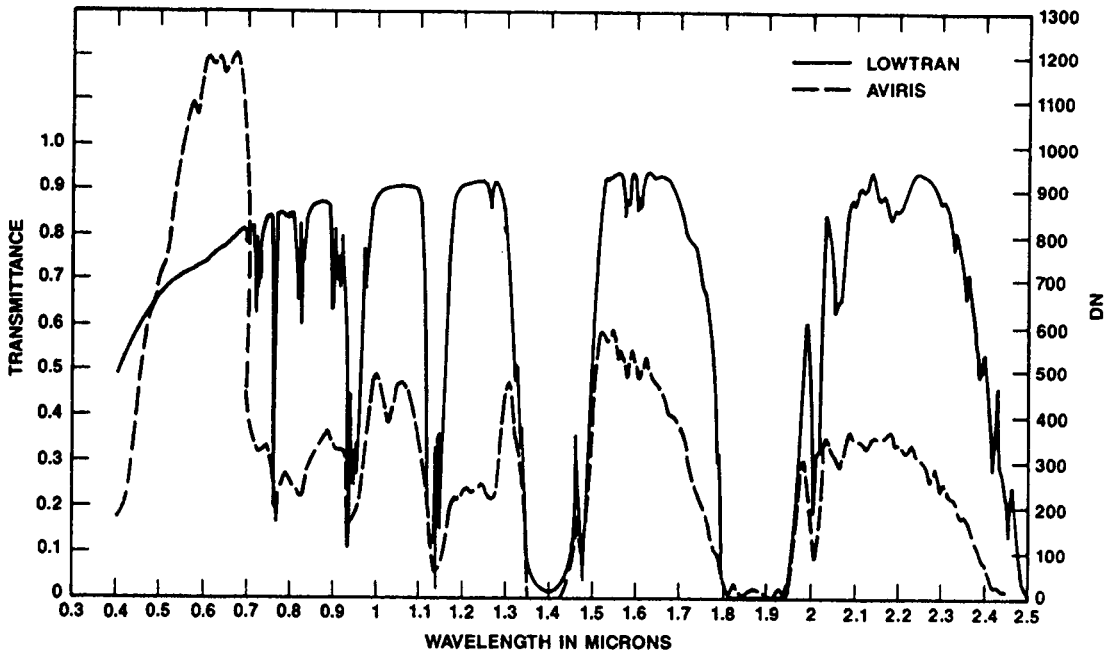


Figure 7. Estimation of the Effective Spectral Resolution

The precision oscillator has been identified as one possible part of the problem of increase of the level of random noise by a factor of two in spectrometer D. Mechanical vibrations of the circuit boards and their components seem to be responsible for the rise of fixed pattern noise in spectrometer D.

After termination of the flight season, inspection revealed that the optical fibers connecting spectrometer A and B to the foreoptics had come loose from their mountings. This can explain the loss of 50% signal caused by the resulting defocusing.

## 4. Estimation of effective inflight spectral resolution

A quick estimation of the inflight spectral resolution was performed. By spectral resolution, we mean the detection of separate radiance minima associated with neighboring absorption bands. We chose to compare the AVIRIS raw spectrum of the same homogeneous area and the model for the atmospheric transmittance provided by LOWTRAN 7. Figure 7 shows a perfect match between the atmospheric absorption bands displayed by AVIRIS and those from LOWTRAN. This means that the sampling interval is correct and that sharp features can be resolved by AVIRIS. For example, the pair of CO2 bands at 2050nm (in spectrometer D) are clearly resolved. A more detailed study of these characteristics can be found in Green and Vane (1988). It shows that the spectral resolution (or sampling interval) is of about 10nm in spectrometers C and D and about 20 nm in spectrometers A and B.

## 5. Summary

Data characteristics can be summarized as follows:

1. As a consequence of a drift in the offset, several detector elements have an apparent response of zero, particularly in spectrometer D.

2. The signal-to-noise performances are by far lower than those announced before the flight season, mainly because of engineering problems and a different behaviour of the instrument while on board the U2.

3. The spectral resolution seems to be as good as expected.

# III. DATA CORRECTION

Trying to map alteration using mineral spectral absorption features generally implies using calibrated data and radiance to be able to compare them easily with lab or field spectral measurements. The standard procedure used at JPL to calibrate AVIRIS data (see, Reimer, 1988) includes:

- dark current subtraction,
- conversion to radiance using a calibration file obtained on lab (see, Chrien, 1988),
- detector read-out delays correction (spatial resampling),
- spectral resampling using interpolation, ending up with 210 bands and a sampling interval of 9.8nm.

Considering the problems presented previously, it did not seem appropriate:

1. to transform the data into radiance using a calibration file that does not reflect the state of the instrument on board the U2. As the calibration file is a multiplicative factor, it will disappear anyway when correcting the data for atmospheric effects using flat field correction or normalization technique.
2. to proceed with a spectral resampling which would include detector elements showing an apparent output of zero and spread those wrong values.

So the procedure was modified to perform only dark current subtraction and detector read-out delays correction. The "clipped" detectors were replaced by the average value of the previous and next element. The overlap between spectrometers was removed and two bands were dropped in spectrometer B (as no specific absorption features for interesting minerals occur in that portion of the spectrum) to end up with the 210 bands. No spectral resampling was performed as the sampling intervals for each spectrometer are close enough (9.56 to 10nm)(see Figure 3).

The offset in brightness was corrected by subtracting the dark current separately from each part.

## Retrieval of ground reflectance

Easy to apply methods of compensating for the atmosphere, not requiring radiometric calibrated data, are available. The most common one is the "flat spectral field reduction". This correction procedure involves formation of ratio of the radiance from an unknown target to the radiance of a standard target whose spectral reflectance is known or independant of wavelength.

To implement the flat-field procedure, we used the Chispa Andesite as the reference as it is the only spectrally flat formation available in the scene. It is dark, homogeneous and unaltered. A 9x9 area was used to compensate for the waste of signal-to-noise due to the use of a dark area. The entire scene was divided by this average spectrum.

The only inconvenience of this method is that it does not compensate for path radiance, which can be a problem in the visible, resulting in shift in wavelength for some features. LOWTRAN model can be used to make an approximate correction (Conel et al., 1987), but as we were focussing on the 2.0-2.45 portion of the spectrum, we decided not to do it.

The normalization technique was also used, that is to say dividing the entire scene by the average spectrum of the entire flight line. This procedure did not give results as good as the flat-field correction technique, presumably because of too-important spectral variations and elevation changes in the scene.

# IV. DATA ANALYSIS

## 1. Local analysis

Spectra were first extracted locally to check if, despite the low signal-to-noise, minerals could be identified and discriminated. Areas were picked refering to an AVIRIS color composite of the test-site (Figure 8) and geologic maps.

Several spectra, corresponding to an average of 9 to 15 samples (Figures 9 and 10), mainly showing kaolinite and alunite absorption features, were obtained using VICAR and CSIRO software. It seemed at that point that minerals involved in hydrothermal alteration, as they generally display deep absorption bands, could be identified.

## 2. Hydrothermal alteration mapping

The next step was to determine the spatial distribution of those minerals to end up with a map of the alteration zones. Different techniques were used: ratios, SPAM software, clustering.

### a. Ratios

We first tried the classic method of ratioing, using the absorption features observed in the spectra extracted locally from the AVIRIS data themselves and theoretical values for the specific minerals we were looking for. Several combinations were

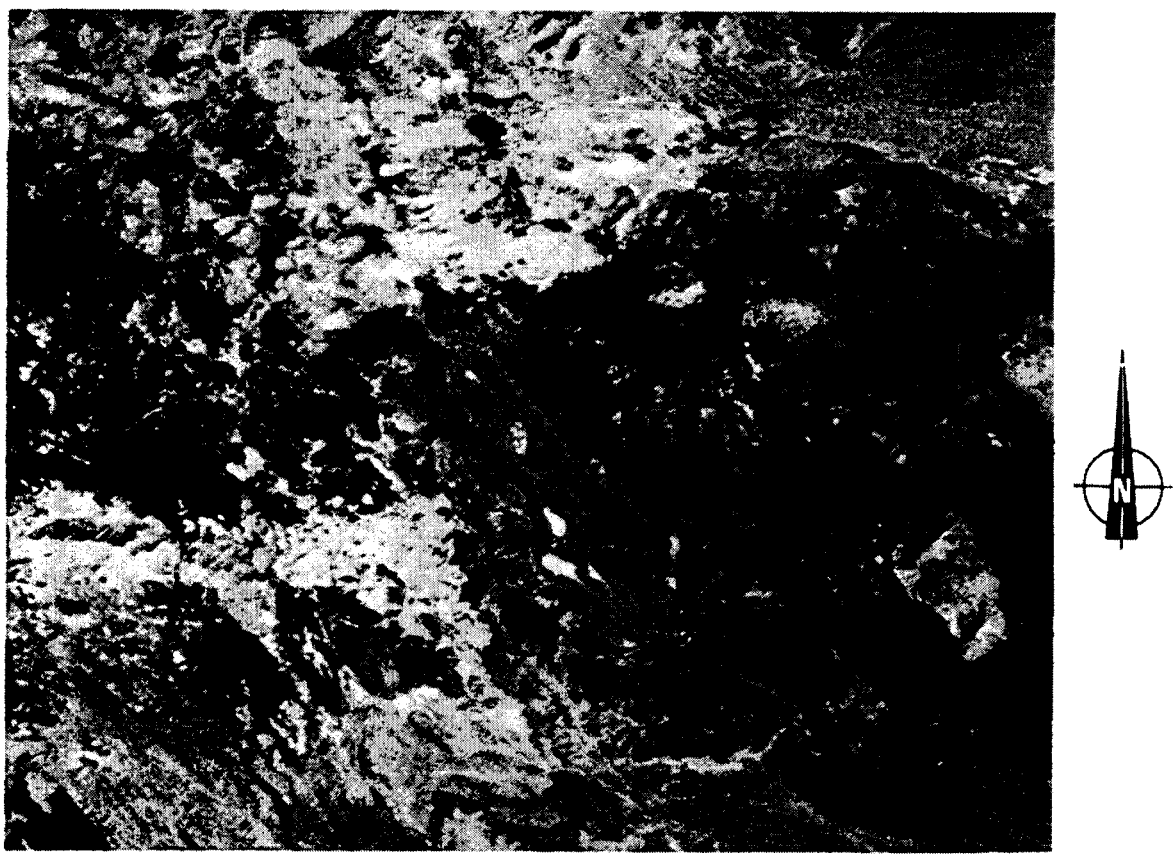


FIGURE 8. AVIRIS false-color composite of the test area (refer to slide No. 5). Red: b200 (2.21 $\mu$m); Green: b130 (1.56 $\mu$m); Blue: b50 (0.8 $\mu$m) (The bands are only corrected for dark current variations and detector read-out delays).

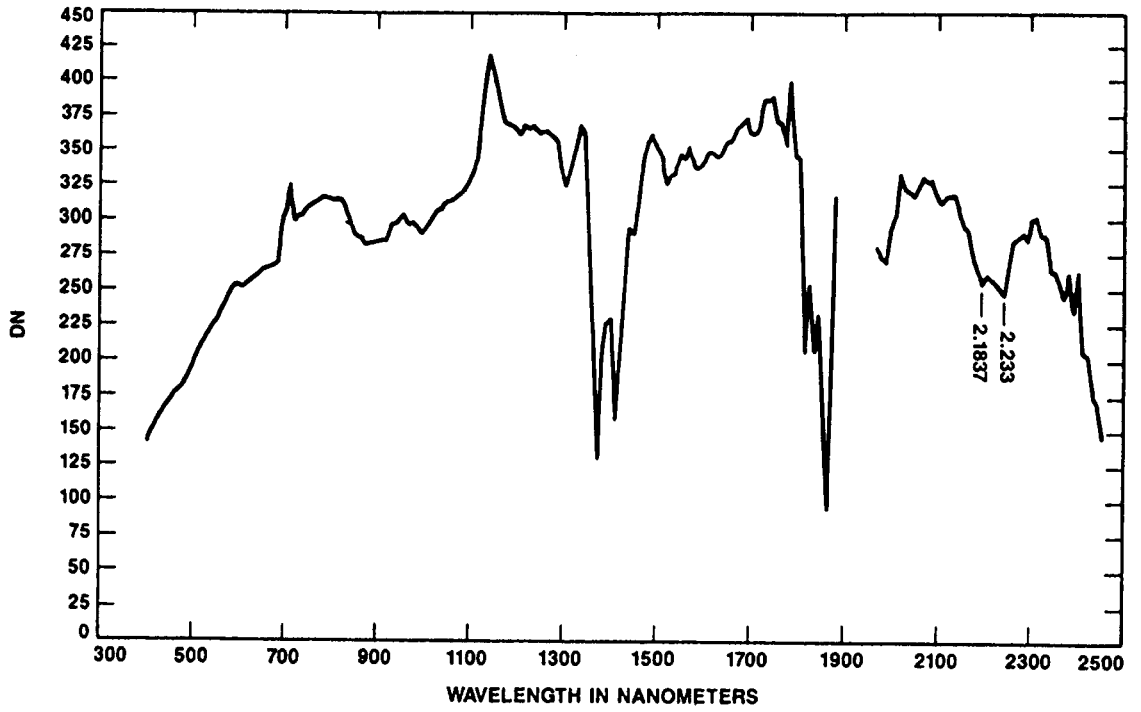


Figure 9: Example of spectrum extracted after flat-field correction (I)

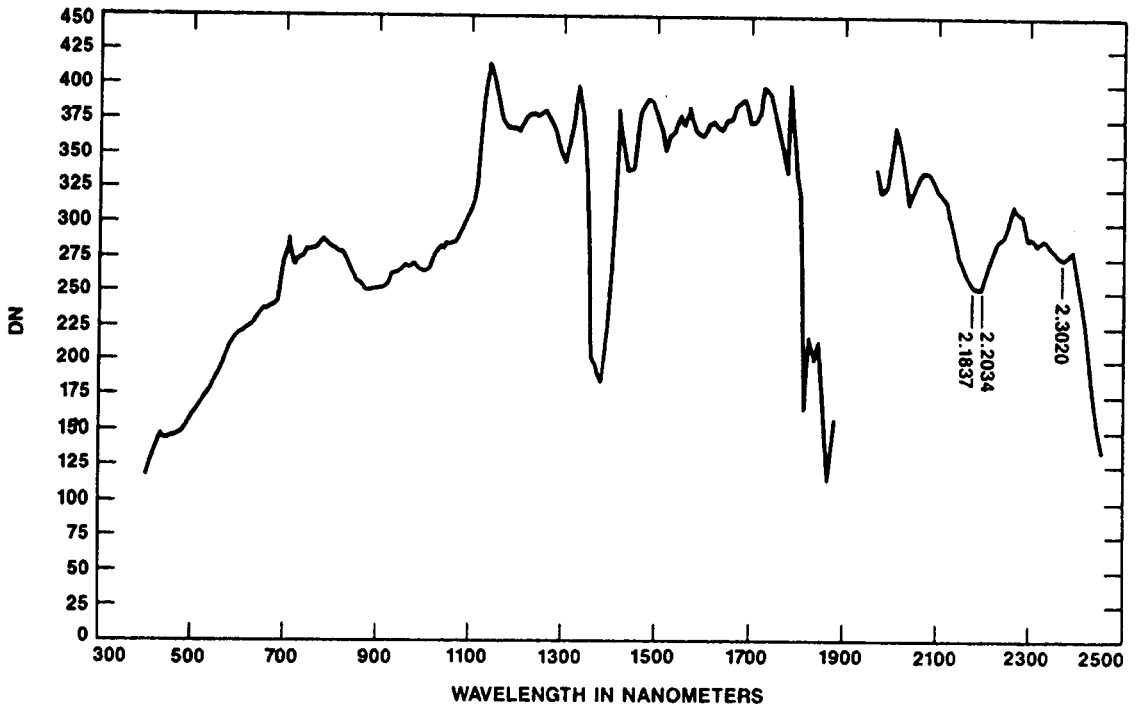


Figure 10: Example of spectrum extracted after flat-field correction (II)

tried. Results appeared noisy but showed color variations (Figure 11). The meaning of those different colors was checked by going back to the flat field corrected data and extracting the spectra corresponding to those areas. No clear relationship was found between specific colors and types of spectrum that could allow identification and mapping of minerals. This confirmed that the signal-to-noise performances of the instrument were not high enough to allow discrimination using this simple technique.

We tried to estimate roughly what were the chances to obtain a good ratio for kaolinite (Figure 12). The uncertainty on the continuum is given by:

$$\Delta c = \frac{\Delta noise}{c} = 6/63 = 9.5\%$$

The uncertainty on the feature is given by:

$$\Delta f = \frac{\Delta noise}{c} = 6/58 = 10.3\%$$

So, the uncertainty on the ratio is given by:

$$\Delta R = \sqrt{(\Delta c)^2 + (\Delta f)^2} = 14.06$$

According to this formula, there are 67% chances for the ratio to be in a range of ± 14.06%.

b. SPAM (Spectral Analysis Manager)

Knowing there was some information available at least locally, we tried to use a partly modified version of SPAM. We focused on the 2.0-2.35 portion of the spectrum and a 100x100 subarea as SPAM could not handle a complete AVIRIS data set at that time.

The spectra locally extracted during the first step were checked by comparing them to the spectra from the SPAM library. A good match was found in most of the cases (Figure 13).

We then tried to use the program "Cluster" to have an idea of which classes were present in the image and to what mineral or combination of minerals they could be related. It happened that this program was not working at that time so we tried next the program "Find", using our knowledge of the minerals that should be present in the area. It was impossible to get consistent results from this program. A decision was made to wait until the entire package has been checked and fixed.

As our goal was to get a map of the area, we tried to modify a clustering program already existing in TAE/VICAR2 so it can handle AVIRIS data.

C. Clustering

The program "CLUSAN" was modified to handle BIL data and 64 bands. This clustering algorithm uses the "simulated annealing"

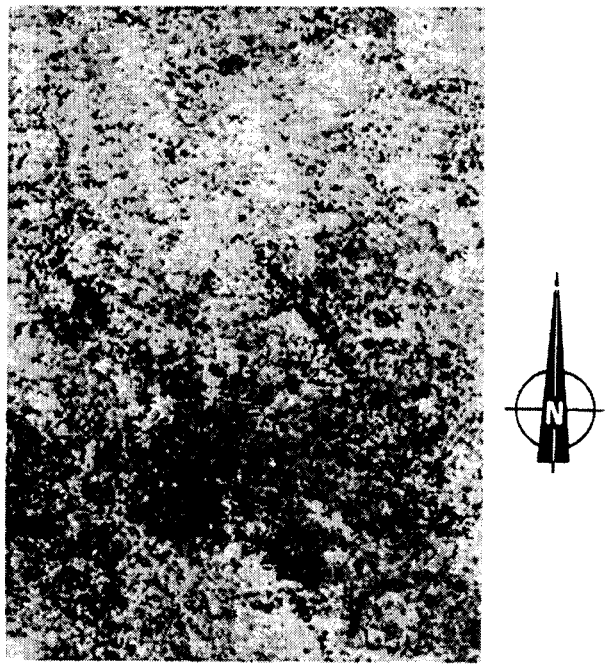


Figure 11: Example of color composite combining different ratios (refer to slide No. 6). Red: Kaolinite (b179/b172); Green: Jarosite (b5/b20); Blue: Alunite (b134/b131)

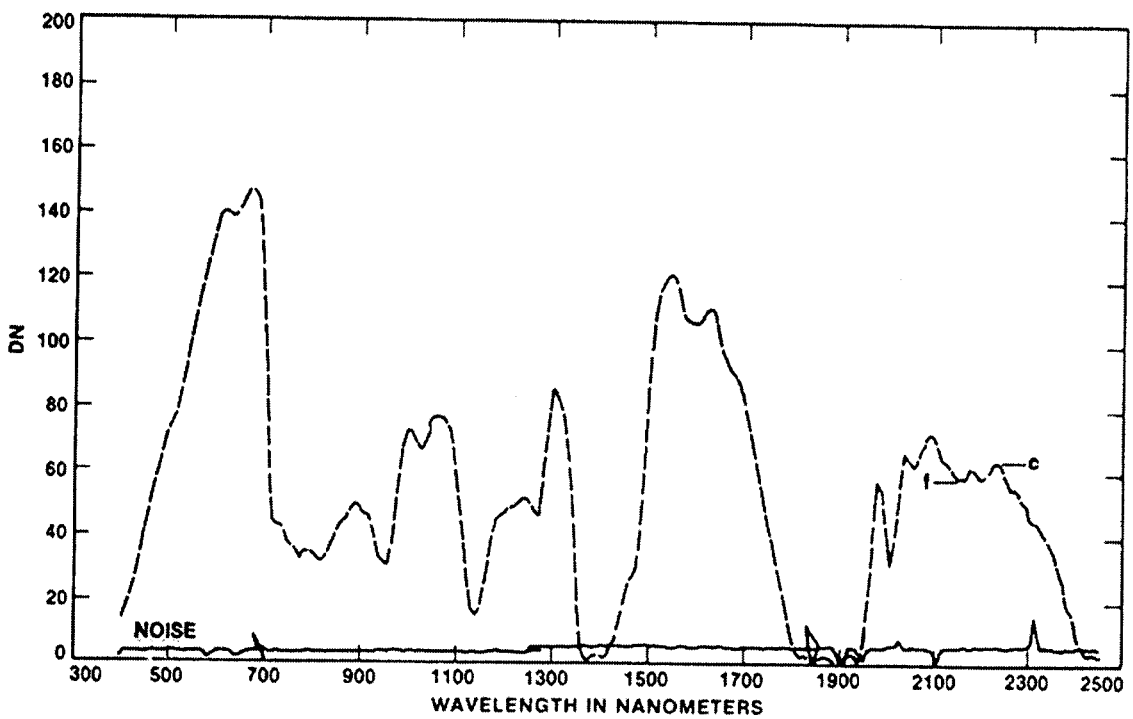


Figure 12: Estimation of ratioing efficiency-c: continuum; f: feature

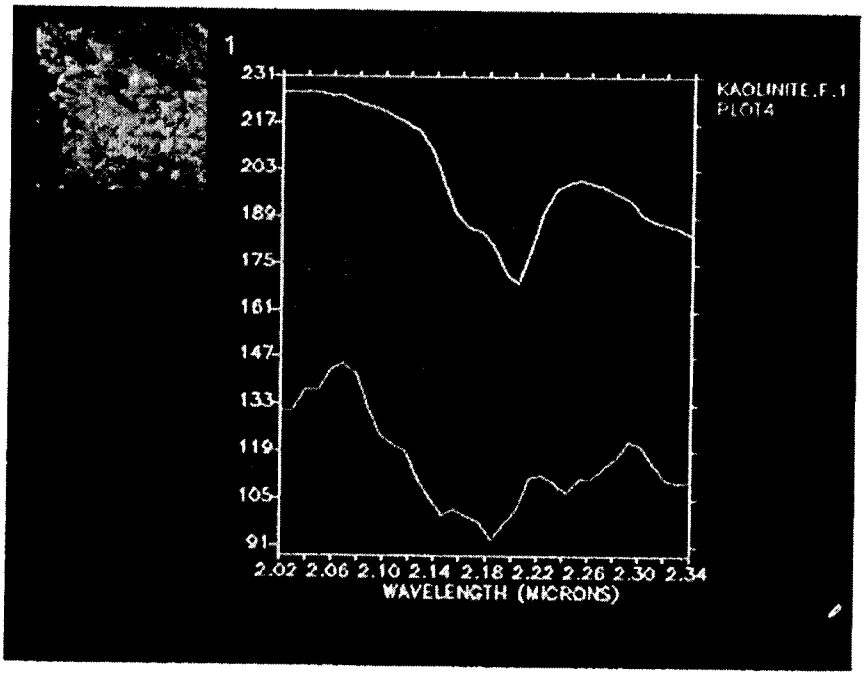


A

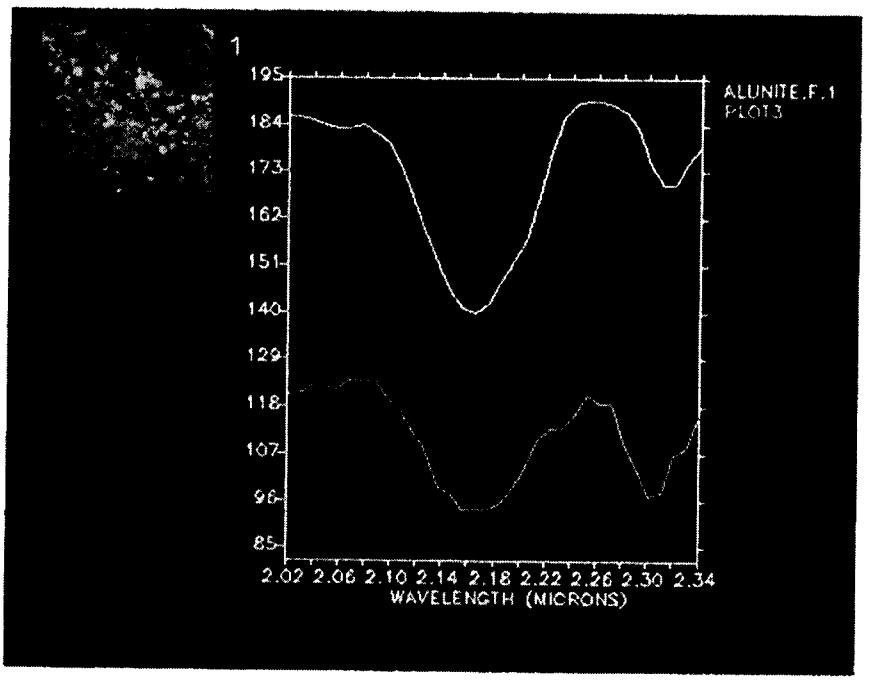


B

Figure 13: Comparison of AVIRIS spectra and library spectra using SPAM. A: Example of Kaolinite (refer to slide No. 7); B: Example of Alunite (refer to slide No. 8).

optimization technique to find the best cluster partition. The program has to be run several times until it converges.

It was first applied to flat field corrected data, 34 bands from 2.0 to 2.34. The classes obtained were seen to be separated according to brightness (Figure 14). For example class 3 is composed of samples having a low DN value in every band. Class 3 and 4 or 2 and 5 would be considered the same by a spectroanalyst.

Several other tries were attempted using data preprocessed to enhance absorption features: ratios, combination of ratios, residuals, normalized data, etc.

No improvement appeared, meaning that the algorithm is not appropriate for "pattern recognition" of absorption features.

## V. FIELD CHECKING

Spectra obtained locally were checked by collecting representative samples in the field. Each sample was analysed in lab using:

- PIDAS under artificial vertical illumination;
- the Beckman UV5240;
- XRD technique to get a precise mineralogic composition of non-obvious samples.

A representative spectrum for each outcrop was obtained by averaging the spectra of its samples; it was then compared to the AVIRIS spectrum of the same region. Some problems can be noticed on PIDAS spectra. They are mainly related to grating position and the fact that the samples were not covering the entire field of view of the instrument. Some of the black velvet background is included, causing the jump between the visible and the NIR for example.

In most cases, a good correlation was found as shown on Figure 15. Analysis of mixed area was attempted using Beckman and XRD information. One simple example is shown on Figure 16 where mainly Alunite, Kaolinite and iron oxides are combined. A more detailed study will be published later.

## VI. CONCLUSIONS

In conclusion, we can say that despite the engineering problems, some spectral information is present in this data set. Field checking showed a good correlation between spectra obtained on lab from samples and AVIRIS spectra.

No mapping of hydrothermal alteration could be done despite significant efforts mainly because of signal-to-noise performances not good enough and the lack of appropriate software at that time.

An increase in signal-to-noise performances of the instrument, specially in spectrometer D and modification of the SPAM software should allow mapping of alteration areas. This test demonstrates however the potential of high resolution imaging spectrometers for alteration mapping and identification of mineralogy.

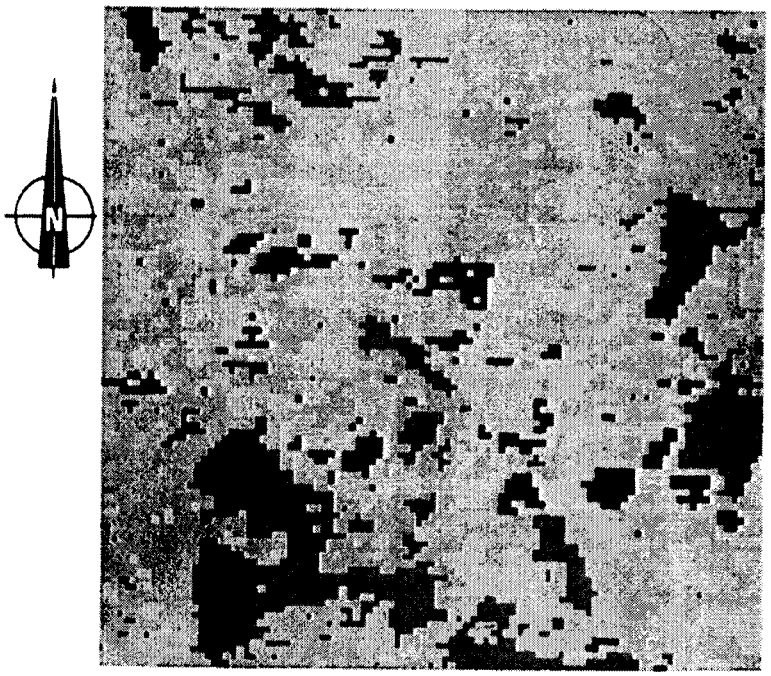


A

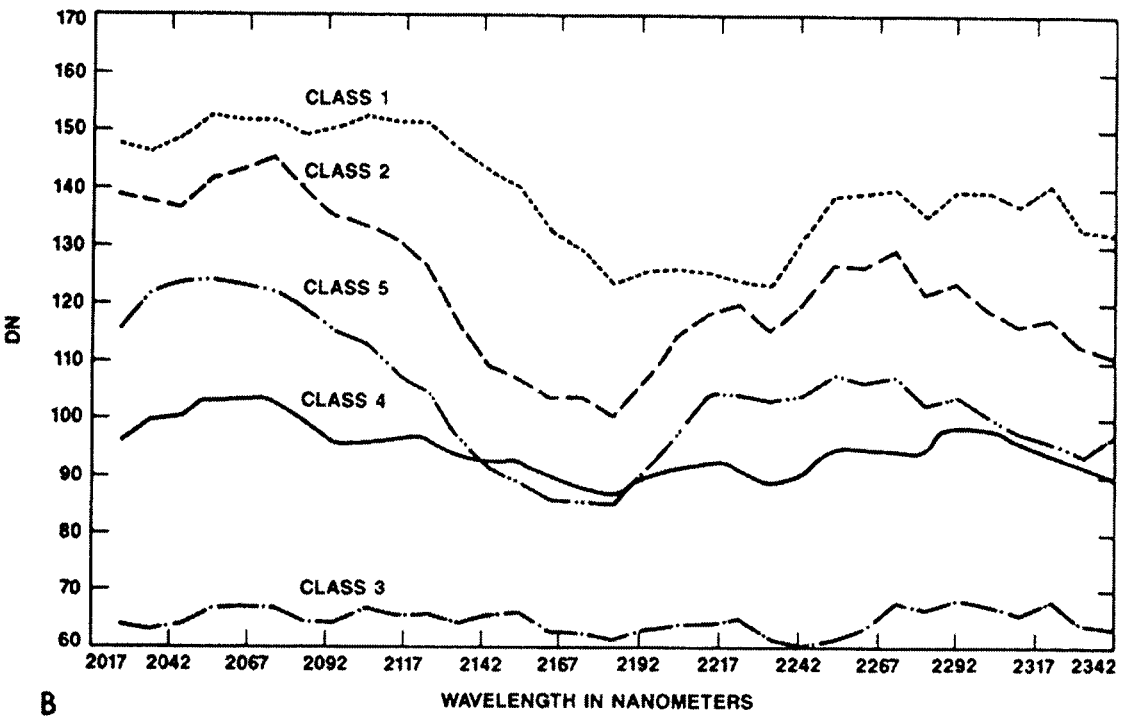


B

Figure 14: A: Classified image obtained using the clustering program CLUSAN (refer to slide No. 9); B: Examples of classes as determined by CLUSAN

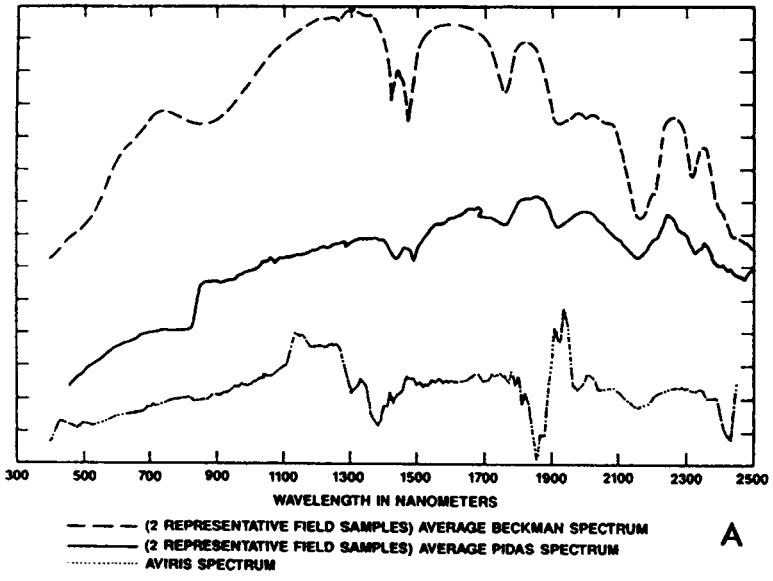


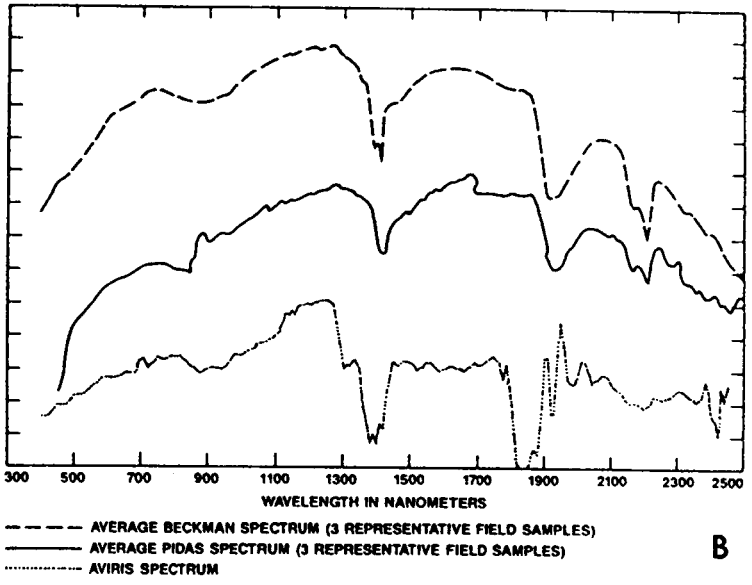


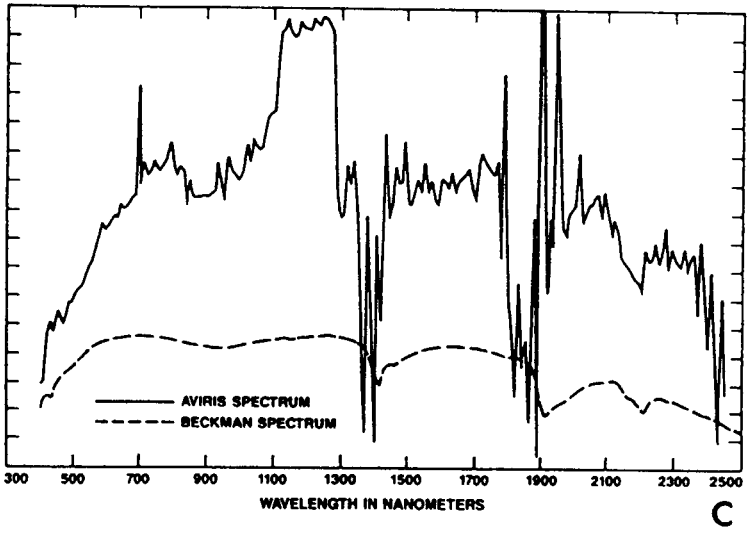


FIGURE 15. Examples of AVIRIS, PIDAS and Beckman spectra for 3 outcrops.

A: outcrop 9 (mainly Alunite)
B: outcrop 13 (mainly Kaolinite)
C: outcrop 15 (mainly Jarosite)

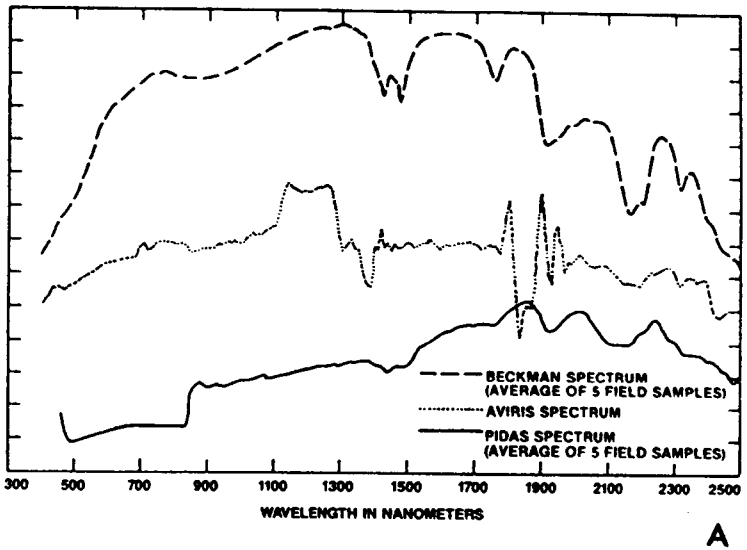


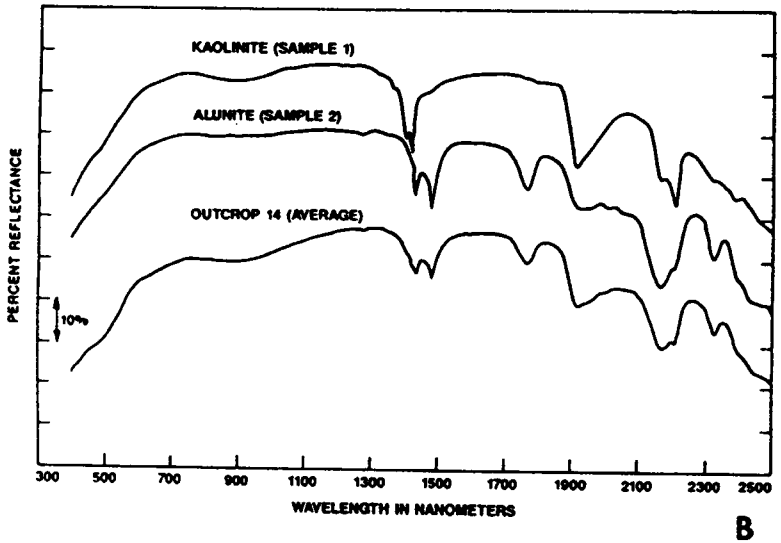


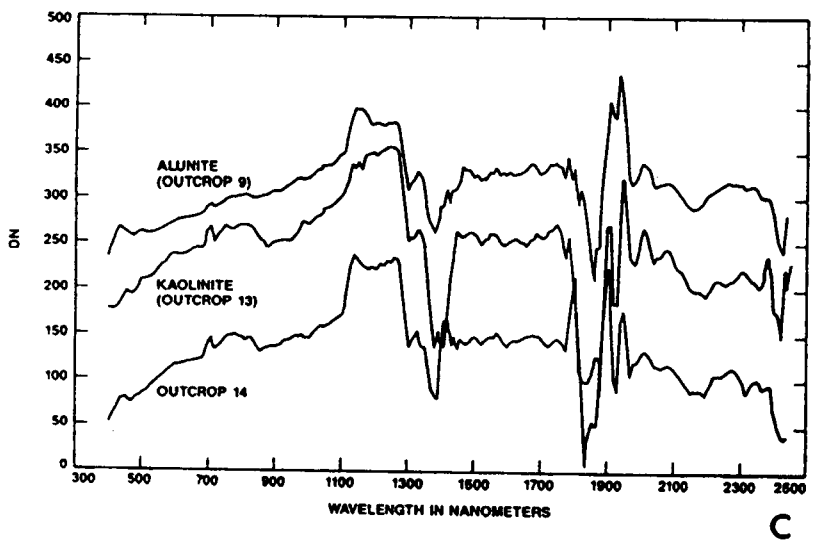


FIGURE 16: Example of mixed area.
A: outcrop 14 - Beckman, PIDAS and AVIRIS spectra;
B: Combination of Kaolinite and Alunite (Beckman spectra from field samples of outcrop 14):
C: Combination of Kaolinite and Alunite (AVIRIS spectra).

## REFERENCES


Ashley, R. P. 1972. Premineralization structural history of the Goldfield volcanic center, Nevada. Econ. Geology, v.67, p.1002.

Ashley, R. P. 1974. Goldfield Mining District. In Guidebook to the Geology of four tertiary volcanic centers in central Nevada, Nevada Bur. Mines and Geology Rept 19, p49-66.

Ashley, R. P. and Albers, J. P. 1975. Distribution of gold and other ore-related elements near ore-bodies in the oxidized zone at Goldfield, Nevada. U.S. Geol. Survey Prof. Paper 843-A, 48p.

Ashley, R. P. and Silbermann, M. L. 1976. Direct dating of mineralization of Goldfield, Nevada, by Potassium-Argon and fission-track methods. Econ. Geology, vol. 71, p904-924.

Chrien, T. 1988. AVIRIS laboratory calibration status. Proceedings of the AVIRIS performance evaluation Workshop, this publication.

Conel, J. E., Green, R. O., Vane, G., Bruegge, C. J., Alley, R. E. and Curtiss, B. J. 1987. Airborne Imaging Spectrometer 2, Radiometric and spectral characteristics, and comparison of ways to compensate for the atmosphere. SPIE 834, Imaging Spectroscopy II, 140-157.

Cornwall, H. H. 1972. Geology and mineral deposits of southern Nye County, Nevada. Nevada Bureau of Mines and Geology, Bull. 77, Mackay School of Mines, University of Nevada, Reno.

Green, R.O. and Vane, G. 1988. Inflight determination of AVIRIS spectral calibration using atmospheric gas and surface neodynium absorptions in the vicinity of Mountain Pass, California. Proceedings of the AVIRIS performance evaluation Workshop, this publication.

Harvey, R. D. and Vitiliano, C. J. 1964. Wall-rock alteration in the Goldfield District, Nevada. Jour. Geology, v. 72, p564-579.

Noble, D. C., Anderson, R. E., Ekren, E. B. and O'Connor J. T. 1964. Thirsty Canyon Tuff of Nye and Esmeralda Counties, Nevada. In Geological Survey Research, USGS Prof. Paper 475-D, pD24-D27.

Ransome, F. L. 1909. Geology and ore deposits of Goldfield, Nevada. USGS Prof. Paper 66, 258p.

Reimer, J. 1988. AVIRIS ground data processing. Proceedings of the AVIRIS performance evaluation Workshop, this publication.

Steinkraus, R. E. and Hickok, R. 1987. AVIRIS on-board data handling and control. In Airborne Visible/Infrared Imaging spectrometer (AVIRIS). A description of the sendor, ground data processing facility, laboratory calibration and first results, JPL pub-87-38, Gregg Vane Ed., p.52-60.

Silbermann, M. L. and Mac Kee, E. H. 1972. Summary of radiometric age determinations on Tertiary volcanic rocks from Nevada and eastern California: part. II, western Nevada, Isochron/West n. 4, p7-28.

# EVALUATION OF AIRBORNE VISIBLE/INFRARED IMAGING SPECTROMETER DATA OF THE MOUNTAIN PASS, CALIFORNIA CARBONATITE COMPLEX

JAMES CROWLEY, LAWRENCE ROWAN, and MELVIN PODWYSOCKI, U.S. Geological Survey, MS 927, Reston, Virginia 22092, U.S.A.; DAVID MEYER, Eros Data Center, Sioux Falls, South Dakota 57198, U.S.A.

## ABSTRACT

Airborne visible/infrared imaging spectrometer (AVIRIS) data of the Mountain Pass, California carbonatite complex have been examined to evaluate the AVIRIS instrument performance and to explore alternative methods of data calibration. Although signal to noise estimates derived from the data indicated that the A, B, and C spectrometers generally met the original instrument design objectives, the S/N performance of the D spectrometer was below expectations. Signal to noise values of 20 to 1 or lower were typical of the D spectrometer and several detectors in the D spectrometer array were shown to have poor electronic stability. The AVIRIS data also exhibited periodic noise, and were occasionally subject to abrupt dark current offsets. Despite these limitations, a number of mineral absorption bands, including $CO_3$, Al-OH, and unusual rare earth element bands, were observed for mine areas near the main carbonatite body. To discern these bands, two different calibration procedures were applied to remove atmospheric and solar components from the remote sensing data. The two procedures, referred to as the "single spectrum" and the "flat field" calibration methods gave distinctly different results. In principle, the single spectrum method should be more accurate; however, additional fieldwork is needed to rigorously determine the degree of calibration success.

## INTRODUCTION

This report summarizes the initial evaluation of Airborne Visible/Infrared Imaging Spectrometer (AVIRIS) data acquired in 1987 over the Mountain Pass, California alkalic igneous rock-carbonatite complex (Fig. 1). A detailed discussion of the Mountain Pass area geologic setting and a description of the carbonatite complex itself may be found in Olson et al., 1954. The carbonatite complex is noted for its extremely high rare earth element (REE) concentrations, and samples of the main carbonatite body have been shown to exhibit numerous REE absorption features in the 0.4 to 2.5 μm wavelength range (Fig. 2; Rowan et al., 1986). Because of the REE and other mineral absorption features, the complex provides an especially useful test area for assessing AVIRIS's spectral measurement capabilities. AVIRIS data have also been requested, but not obtained, for two additional carbonatite complexes, Iron Hill, Colorado, and Oka, Quebec, which contain lower rare earth concentrations and represent different exposure and weathering conditions. Emphasis in this evaluation is placed on characterizing the AVIRIS instrument behavior during the Mountain Pass overflight, and on describing various spectral observations and data calibration techniques.

## DATA ACQUISITION

Three flightlines of AVIRIS data (Fig. 1) were acquired by the NASA ER-2 aircraft under clear sky conditions at approximately 11:00 A.M., July 28, 1987. Digital tapes of the raw data and the radiometrically corrected, spectrally resampled data with related calibration files were received from the Jet Propulsion Laboratory (JPL) during November, 1987. All of the data analysis discussed in this report was conducted for flight line 2, which covered five areas selected as ground calibration targets. The targets included: (1) an asphalt parking area approximately 1 km southwest of Mountain Pass, (2 & 3) an area of alluvium and a playground at the Mountain Pass school, (4) the Ivanpah playa located 20 km east of Mountain Pass, and (5) a plowed field near Valley Wells station located 15 km west of Mountain Pass (fig. 1). The JPL Portable Instant Display and Analysis Spectrometer (PIDAS) and the U.S. Geological Survey's IRIS spectrometer manufactured by Geophysical Environmental Research, Inc.,* were used to record in situ reflectance spectra for each of the calibration targets during the overflight. In addition, spectra for 27 field samples were remeasured in the laboratory using a Beckman UV 5240 spectrophotometer equipped with an integrating sphere. The AVIRIS image data were analyzed using the JPL Spectral Analysis Manager software package in conjunction with other image enhancement and statistical software programs developed at the U.S. Geological Survey.

## RESULTS

### Signal to Noise Analyses

Signal to noise estimates for the line 2 radiometrically corrected and spectrally resampled data were made by selecting a target area of 35 pixels within the Ivanpah playa, which provided a relatively bright target that was known from field and laboratory measurements to be very uniform spectrally. The average playa reflectance from 0.7 to 2.4 μm is 40 percent $\pm$ 6 percent. At shorter wavelengths the playa reflectance diminishes sharply due to iron oxide absorption. Using the block of 35 pixels, the mean digital number (DN) and the standard deviation were calculated for each of the 210 spectral channels. The mean DN divided by the standard deviation, a value known as the coefficient of variation, provides an empirical measure of signal to noise. Figure 3 plots coefficients of variation versus channel number for 84 representative AVIRIS channels.

The dark current (DC) data recorded after each image scanline were also analyzed statistically to help characterize the in-flight instrument behavior. Such an approach isolates the detectors and the related signal chain electronics from the complicating influences of atmospheric and ground target variations. Coefficients of variation were determined by summing 100 dark current values for each of the 224 detectors. This analysis showed that the detectors in all four AVIRIS spectrometers generally exhibited similar dark current behavior, with three exceptions. Three detectors in the D spectrometer array (raw channel nos.

---

* Brand names are for descriptive purposes only and do not represent an endorsement by the U.S. Geological Survey.

173, 181, and 210) gave anomalous coefficients of variation that were much lower than those calculated for other channels. Two of these channels (181 and 210) were known from previous reports to involve bad detector elements. However, channel 173 was not previously identified as having degraded performance.

To characterize periodic noise in the AVIRIS data, Fourier analysis of the Mountain Pass and Ivanpah image segments was done by forward transforming 64 bands for each segment (32 apiece from the B and D spectrometers), averaging the 32 transformed bands from each spectrometer, and then taking the logarithm of each average to identify noise peaks (Gonzalez and Wintz, 1979). The analysis identified two primary types of periodic noise common to both the B and D spectrometers. The first type exhibits strong horizontal frequency dependence, but only weak vertical frequency dependence (Table 1a). The frequencies in this noise group are related harmonically, characterized by a fundamental period of 28.4 pixels/cycle and missing even-numbered terms. This noise sequence is manifest as the "herringbone" pattern seen in some AVIRIS imagery. Although the Mountain Pass and Ivanpah images generally had similar noise characteristics, the Ivanpah vertical frequencies were somewhat shifted from those observed for the Mountain pass image (Table 1a). The second type of noise is localized horizontally but has no apparent vertical dependence (Table 1b). The highest frequency members of this noise class are responsible for an "odd-even" intensity modulation observed in some image data. This modulation intensifies and fades within each line of data, apparently due to constructive and destructive interference of these frequencies with each other and with the sampling frequency.

## Calibration of AVIRIS Data

Despite the noise limitations described above, the AVIRIS data did permit the detection of a variety of spectral absorption features, including REE absorption bands, as well as bands caused by carbonate- and hydroxyl-bearing minerals. To make these observations, it was first necessary to remove atmospheric and solar irradiance effects from the AVIRIS data. Three methods to remove these effects were evaluated: (1) the flat field method, (2) the single spectrum method, and (3) the empirical line method. This report focuses on a comparison between the flat field and single spectrum methods. The empirical line method is discussed in a companion paper by Vane and Green elsewhere in this volume.

The flat field method of calibration has been widely applied in studies involving imaging spectrometer data. In this technique a small area within an image is used to normalize the entire image, i.e. the spectrum for the small area is divided into the spectrum for every other pixel in the scene. The method assumes that the small area contains no absorbing minerals or vegetation, in which case the shape of its remotely sensed spectrum is entirely determined by atmospheric transmission, scattering, and solar irradiance. If this assumption is true, then the normalization procedure will remove the atmospheric transmission, and solar irradiance components from the image data.

Unfortunately, few areas on the earth are spectrally featureless, and the effect of having a weak spectral feature in the normalization area is to remove an equivalent feature throughout the image, thereby changing the intensity and/or distorting other spectral bands of

interest (Clark and King, 1987). The single spectrum method of calibration eliminates this major drawback of the flat field technique. The method requires a single spectrally well-characterized ground target, situated at about the average scene elevation. The spectrum for this ground target is divided by the radiometrically corrected, but otherwise uncalibrated, image DN's for the same area. The resulting quotients for each wavelength channel provide a set of scalars for calibrating the image data.

In this study, the flat field and the single spectrum methods were compared by using an area of alluvium as the calibration target for both procedures. Slide no. 10 depicts three curves including (1) an average IRIS spectrum for alluvium, shown in magenta, (2) the uncalibrated image spectrum for the alluvium calibration target, shown in red, and (3) the residual curve formed by dividing (1) into (2), shown in cyan. The subtle differences between curves (2) and (3) in the slide represent the differences between the flat field and the single spectrum calibration methods using the alluvium calibration target. Although these calibration curve differences appear at first to be minor, they produce substantial differences in the appearance of final image spectra. Two pairs of spectra that depict such calibration-related differences are shown in slide 11. The upper two spectra represent a 4 by 4 pixel area within a unit of mica-rich metamorphic rock; the lower two spectra were extracted from a 4 by 4 pixel area in a sedimentary carbonate unit. The top spectrum in each pair was calibrated using the flat field curve, the bottom spectrum using the single spectrum residual curve (refer back to slide 10). Notice the dissimilar shapes of the 2.2 $\mu$m absorption feature in the upper two spectra. In the lower two spectra notice the small relative displacement of the 2.3 $\mu$m carbonate absorption features. Although it is not presently known which curve in each pair gives the most accurate spectral representation, this calibration exercise does serve to emphasize the need for well-constrained calibration assumptions.

## DISCUSSION AND CONCLUSIONS

Signal to noise estimates reported in this initial study of the Mountain Pass, California AVIRIS data generally agree with the pre-flight season estimates determined at JPL (Greg Vane memorandum dated 5/31/88). However, the anomalous behavior of the detector corresponding to raw channel 173 in the spectrometer D detector array apparently was not previously recognized. Although this detector is currently positioned at 1.947 $\mu$m, i.e. within an atmospheric water band, the detector behavior might present a problem if the array is swapped into a different spectrometer. One such possibility that has been suggested by others would involve trading detector arrays between spectrometers C and D in order to relocate the bad detectors corresponding to raw channels 181 and 210. This swap would place the questionable channel 173 detector within the water band at 1.36 $\mu$m and, therefore, should not raise any data quality concerns.

Our preliminary study of data calibration procedures indicates that the single spectrum calibration method shows considerable promise as an improvement over the flat field procedure. Remaining problems include the need to better characterize the field calibration targets and to define test areas for verifying the calibration results. Additional work is also needed to devise techniques for removing additive

calibration terms, such as those related to detector to detector offsets, and atmospheric path irradiance variations with wavelength (R. Green, personal communication). In principle, additive terms can be removed as an initial step in the single spectrum calibration method, i.e., prior to applying the calibration scale factors. The difficulty lies in determining the proper shape of the scattering curve to subtract from the image data. Although atmospheric path irradiance due to Raleigh scattering is a relatively simple function for AVIRIS scenes, irradiance contributions from aerosols and dust are likely to be more complex. In the coming field season we plan to obtain additional field spectra of rock and soil units of the Mountain Pass study area. Using these spectra we will develop techniques for the removal of additive terms from AVIRIS data, and continue to test the single spectrum calibration method.

REFERENCES


Clark, R. N., and King, T. V. V. 1987. Causes of spurious features in spectral reflectance data: in Proceedings of the Third Airborne Imaging Spectrometer Data Analysis Workshop, June 2-4, 1987, Jet Propulsion Laboratory Publication 87-30.

Gonzalez, R. C., and Wintz, P. 1979. Digital Image Processing, Addison-Wesley Pub. Co., Reading, Mass.

Heinrich, E. W. 1980. The Geology of Carbonatites: Robert E. Krieger Pub. Co., Huntington, New York, 585 p.

Olson, J. C., Shawe, D. R., Pray, L. C., and Sharp, W. N. 1954. Rare-earth mineral deposits of the Mountain Pass District, San Bernardino County, California: U.S. Geological Survey Professional Paper 261, DC, 75 p.

Rowan, Lawrence C., Kingston, Marguerite J., and Crowley, James K. 1986. Spectral reflectance of carbonatites and related alkalic igneous rocks: Selected samples from four North American localities: Economic Geology, Vol. 81, p. 857-871.


Table 1a. AVIRIS periodic noises having strong horizontal and weak vertical frequency dependence.

| Mountain Pass | | Ivanpah |
|---|---|---|
| Horizontal norm. freq. (cycles/sample) | Vertical norm. freq. (cycles/line) | Vertical norm. freq. (cycles/line) |
| .035 | .433 | .437 |
| .105 | .297 | .316 |
| .175 | .164 | .213 |
| .246 | .017 | .074 |
| .316 | .125 | .062 |
| .332 | .209 | .271 |
| .402 | .299 | .293 |

Table 1b. AVIRIS periodic noises having horizontal frequency dependence only.

| Horizontal norm. freq. (cycles/sample) | |
|---|---|
| .009 | (cont.) |
| .017 | .289 |
| .027 | .451 |
| .045 | .471 |
| .084 | .486 |
| .201 | .494 |

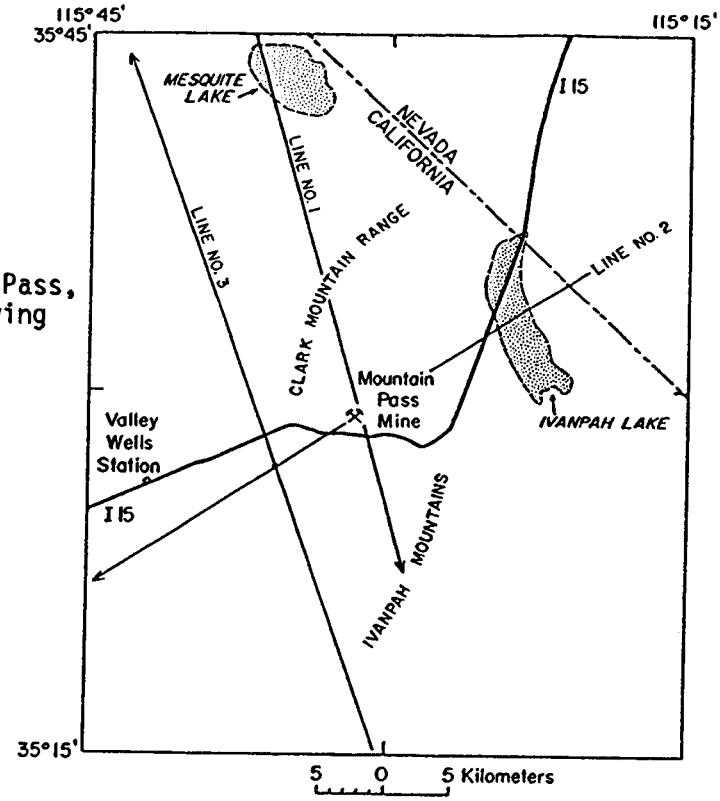


Figure 1. Map of Mountain Pass, California, study area showing locations of the AVIRIS flightlines.

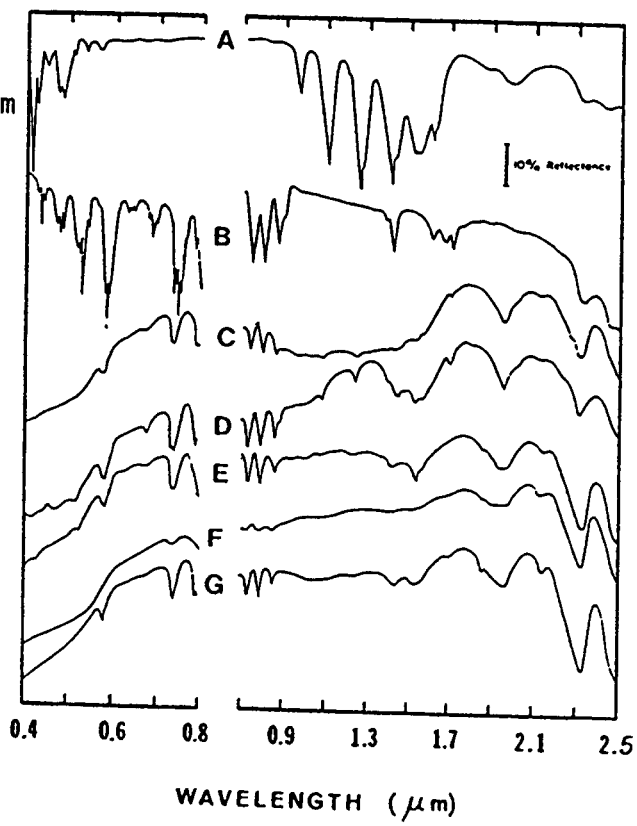


Figure 2. Reflectance spectra of sovite (D, E, F, G) and rauhaugite (C) rock samples from the Sulphide Queen mine and adjacent areas at the Mountain Pass carbonatite complex. Also shown for comparison purposes are spectra for reagent grade $Nd_2O_3$ (B) and $Sm_2O_3$ (A) standards. "Sovite" and "rauhaugite" are rock names applied to calcitic and dolomitic carbonatite materials, respectively (Heinrich, 1980). Figure adapted from Rowan et al., 1986.

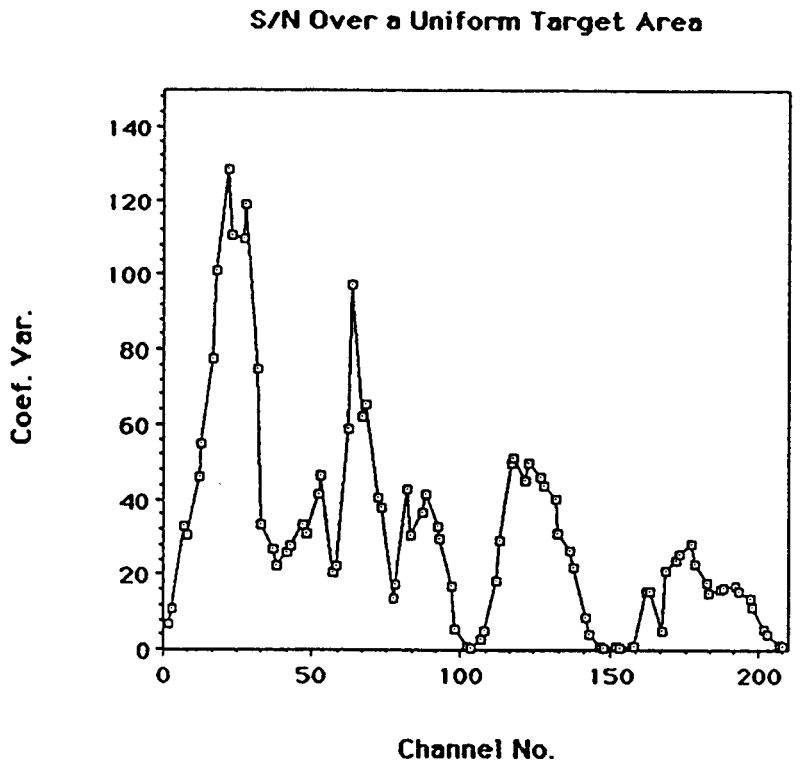


Figure 3. [Above] Signal to noise estimates for resampled AVIRIS data determined by the coefficient of variation method. A uniform area of the Ivanpah playa (35 pixels) was used to determine the coefficient values for each channel. Refer to text for details.

Slide 10 Single spectrum residual compared with original atmospheric curve for alluvium calibration target. Slide located in pocket at end of volume. Refer to text for discussion

Slide 11 Comparison between flat field corrected and single spectrum corrected data. Slide located in pocket at end of volume. Refer to text for discussion.

# DETERMINATION OF IN-FLIGHT AVIRIS SPECTRAL, RADIOMETRIC, SPATIAL AND SIGNAL-TO-NOISE CHARACTERISTICS USING ATMOSPHERIC AND SURFACE MEASUREMENTS FROM THE VICINITY OF THE RARE-EARTH-BEARING CARBONATITE AT MOUNTAIN PASS, CALIFORNIA

ROBERT O. GREEN, GREGG VANE and JAMES E. CONEL, Jet Propulsion Laboratory, 4800 Oak Grove Drive, Pasadena, CA 91109

## ABSTRACT

An assessment of the Airborne Visible/Infrared Imaging Spectrometer (AVIRIS) performance was made for a flight over Mountain Pass, California, July 30, 1987. The flight data were reduced to reflectance using an empirical algorithm which compensates for solar, atmospheric and instrument factors. AVIRIS data in conjunction with surface and atmospheric measurements acquired concurrently were used to develop an improved spectral calibration. We also performed an accurate in-flight radiometric calibration using the LOWTRAN 7 radiative transfer code together with measured surface reflectance and atmospheric optical depths. A direct comparison with coincident Thematic Mapper imagery of Mountain Pass was used to demonstrate the high spatial resolution and good geometric performance of AVIRIS. The in-flight instrument noise was independently determined with two methods which showed good agreement. A signal-to-noise ratio was calculated using data from a uniform playa. This ratio was scaled to the AVIRIS reference radiance model, which provided a basis for comparison with laboratory and other in-flight signal-to-noise determinations.

## 1.0 INTRODUCTION

The performance characteristics of AVIRIS in the laboratory environment have been measured through a series of calibrations over the past year of instrument development (Vane et al., 1987, 1988). The objectives of this experiment were to develop and apply methods for assessing the in-flight spectral, radiometric, spatial and signal-to-noise performance of the instrument and to provide an in-flight spectral and radiometric calibration.

AVIRIS data were acquired over the Mountain Pass region on the 30th of July, 1987, 10:15 AM PST, under clear sky conditions. Concurrent surface reflectance measurements were collected at the playa, asphalt and graded soil targets. These areas were selected for surface homogeneity, for contrast in albedo and for aerial extent significantly greater than an AVIRIS resolution element. A spectrum of the mineral bastnaesite, which occurs at Mountain Pass (Olson et al., 1954) was independently measured with a laboratory spectrometer. Bastnaesite contains narrow spectral absorption features in the visible and near infrared which are suitable for assessing AVIRIS spectral performance. Atmospheric optical depth measurements were acquired contemporaneously with the over-flight. The coverage of the flight data and the location of the surface targets are shown in Figure 1. Thematic Mapper (TM) satellite data were obtained with coverage encompassing the Mountain Pass experiment region.

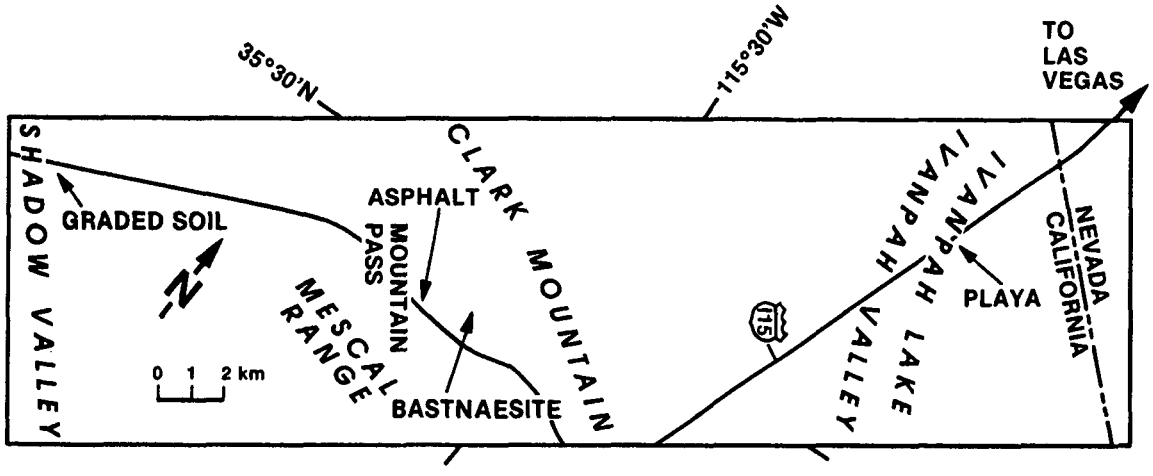


Figure 1. Location of AVIRIS flight data over the Clark Mountains on July 30th, 1987 at 10:15 AM PST. The positions of the playa, bastnaesite, asphalt and graded soil target areas are indicated.

With these data the in-flight performance of AVIRIS was determined. Additionally, a spectral and radiometrical calibration was generated for these imaging spectrometer data. We describe in the paper the data used, the methods of analysis, and results obtained.

## 2.0 DATA USED IN THE STUDY

### 2.1 AVIRIS Image Data.

AVIRIS data of 2048 image lines by 614 cross-track samples and 224 spectral channels were acquired on an east to west flight line from the Ivanpah Playa across Clark Mountain to Shadow Valley. The data were corrected through subtraction of the end-of-line dark current and spatial resampling to correct for detector readout delay (Vane et al, 1987). These corrections generated data that were proportional to total radiance and spatially registered between spectral channels. Corrected AVIRIS spectra from the playa, the bastnaesite locality, the asphalt and the graded soil targets are plotted in Figure 2. The playa data were taken from a 200 by 200 meter homogeneous area of Ivanpah Playa and represent an average of 100 AVIRIS spatial elements. The bastnaesite spectrum was extracted from 4 contiguous resolution elements. The asphalt target is a large recently surfaced parking lot from which 12 spatial elements were extracted and averaged. The soil target was derived from an average of 12 resolution elements selected from a large area of recently graded soil.

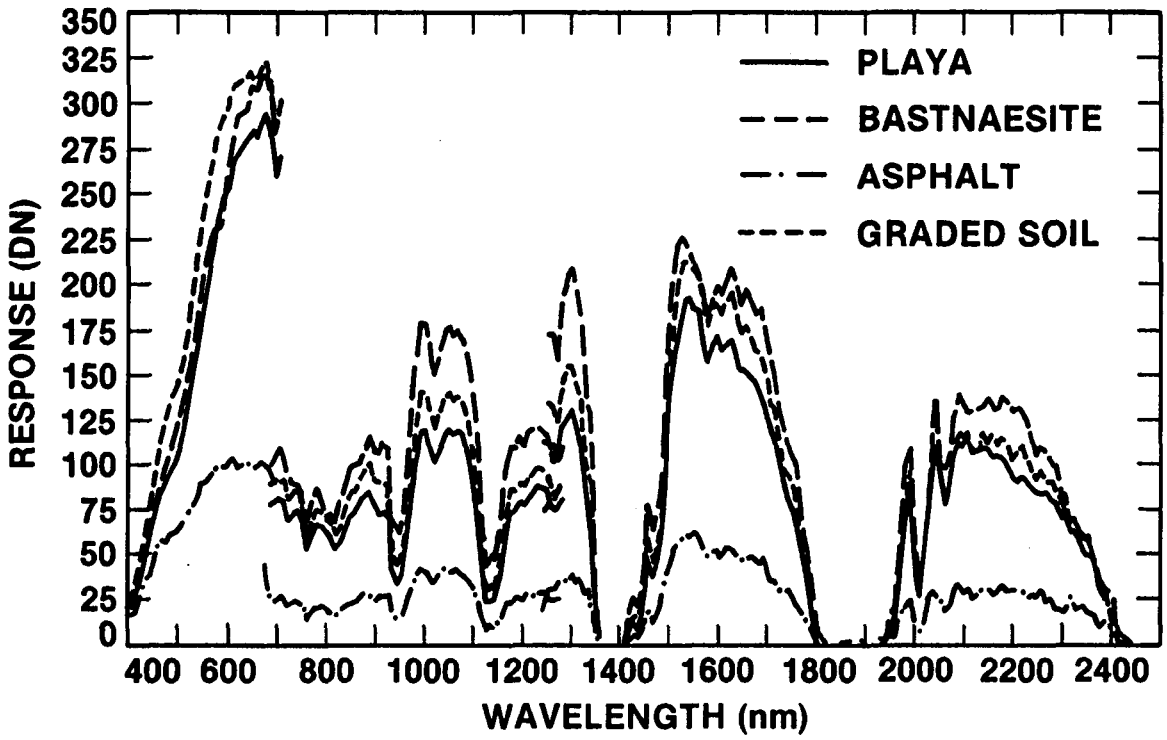


Figure 2. AVIRIS spectra of the playa, bastnaesite, asphalt and graded soil targets with compensated dark current and detector readout delay. These data represent averages of 100, 4, 12 and 12 pixels respectively.

## 2.2 Surface Reflectance Data.

The Portable Instantaneous Display and Analysis Spectrometer (PIDAS) (Goetz, 1987) was used to acquire in situ surface reflectance spectra for the playa, asphalt and graded soil targets. The eight second spectral acquisition time of the instrument allowed the collection of 102, 93 and 35 spectra for the playa, asphalt and soil targets respectively in the period between 10:00 AM and noon. These data have a spectral sampling interval of better than 5 nm in the wavelength region from 450 to 2450 nm, and were reduced to reflectance using spectra of a pressed halon reference target. For comparisons and calculations using these reflectance spectra and the AVIRIS data, the PIDAS spectra were convolved with the AVIRIS channel response functions. The resulting reflectance spectra, reduced to AVIRIS spectral resolution, are plotted in Figure 3. Standard deviations of 1, 1 and 2 percent reflectance were calculated for the playa, asphalt and soil respectively, confirming the nearly homogeneous surface reflectance of these targets. A

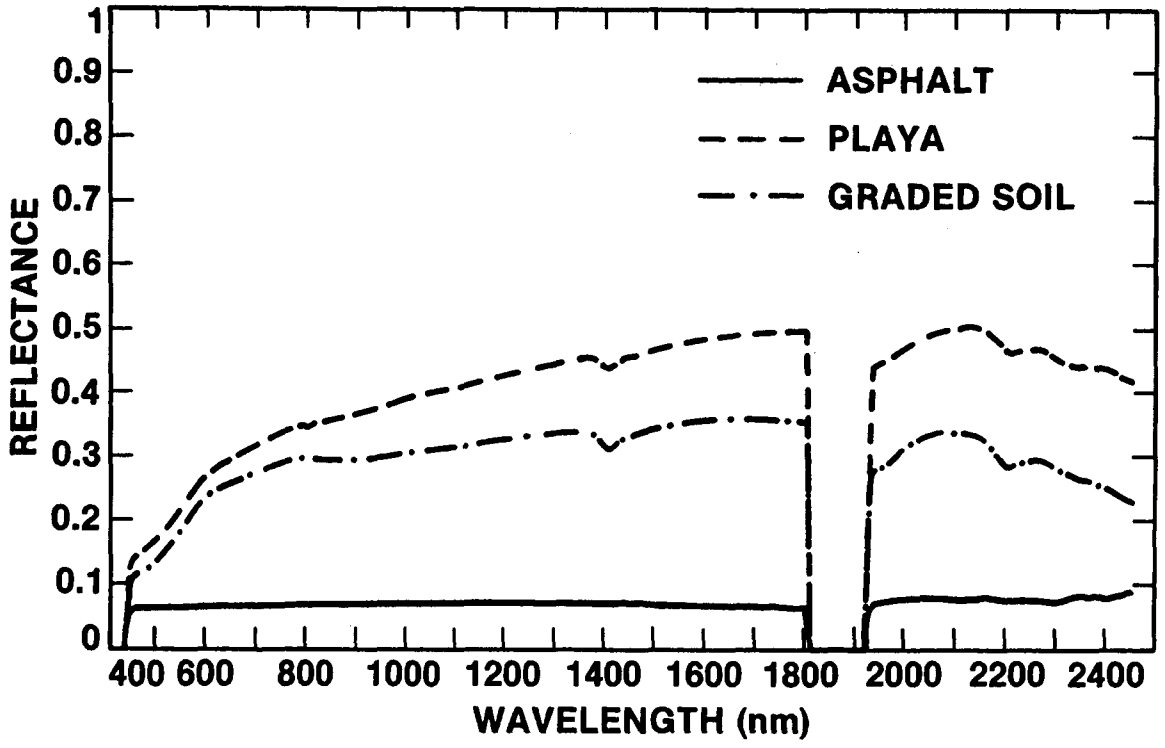


Figure 3. PIDAS reflectance spectra of the asphalt, playa and graded soil target acquired contemporaneously with the AVIRIS flight data. The data are averages of 102, 93 and 35 spectra and have been convolved with the AVIRIS channel spectral response functions.

laboratory reflectance spectrum of the mineral bastnaesite, acquired independently with a Beckman UV5240 spectrometer, is plotted in Figure 4.

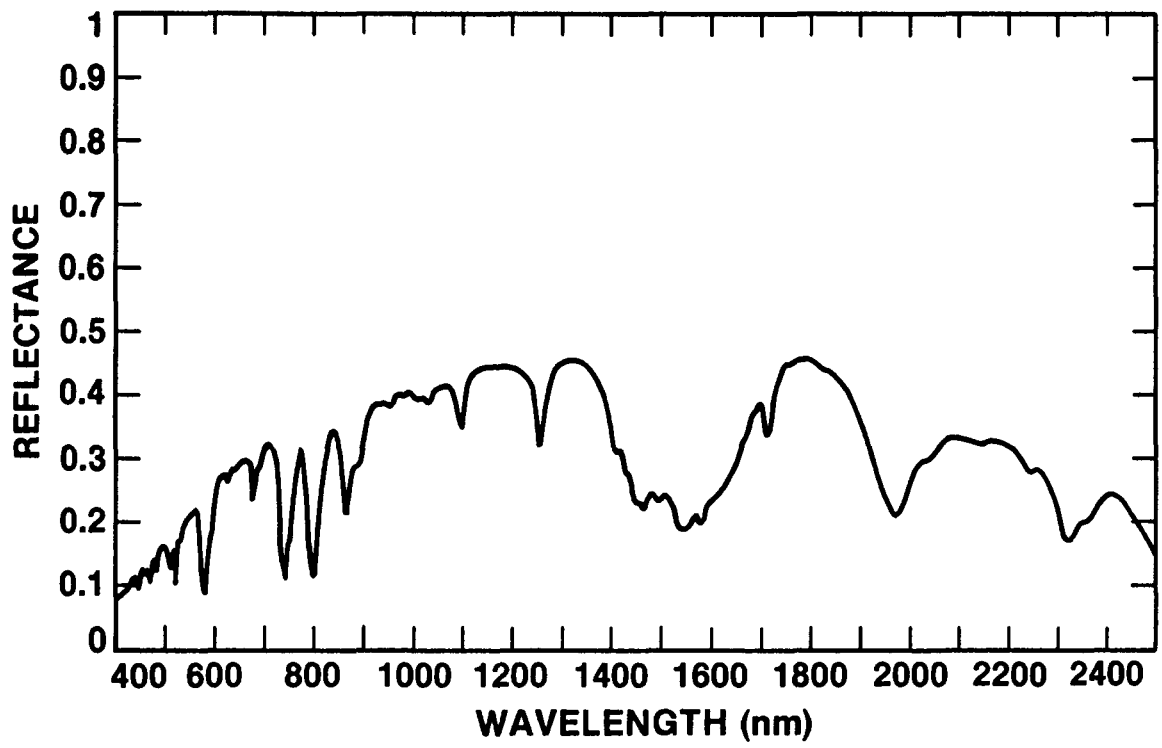


Figure 4. A reflectance spectrum of the mineral bastnaesite acquired with a Beckman UV5240 laboratory spectroradiometer showing the narrow absorption features in the visible and near infrared region of the spectrum caused by trivalent rare earth elements (Adams, 1965)

## 2.3 Atmospheric Measurements.

Solar illumination measurements were acquired with a Reagan-type radiometer (Shaw et al, 1973) from 7:32 am to 11:55 am at ten minute intervals from an elevated site at the asphalt target on the day of the overflight. Atmospheric optical depths were determined from standard Langley plots, as described in Herman et al, (1978). The optical depths for the ten wavelength positions with 10 nm filter bandwidths are given in Table 1.

Table 1. Optical depth measurements at Mountain Pass, CA.

| Center Wavelength (nm) | Calculated Optical Depth |
|---|---|
| 370 | 0.551 |
| 400 | 0.417 |
| 440 | 0.305 |
| 520 | 0.197 |
| 610 | 0.154 |
| 670 | 0.105 |
| 780 | 0.069 |
| 870 | 0.056 |
| 940 | 0.398 |
| 1003 | 0.047 |

## 3.0 DATA REDUCTION

### 3.1 Empirical Line Reflectance Recovery.

The empirical line algorithm, described for example in Conel et al, (1987), recovers surface reflectance from instrument response data. The method compensates for multiplicative components of solar illumination, atmospheric attenuation and instrument response. Additionally, the additive factors of atmospheric path radiance and instrument dark current are removed.

The algorithm requires two targets of contrasting albedo and equivalent spectral resolution for which both surface reflectance and AVIRIS instrument response are known. Two first order linear equations are developed of the form

$$DN = A * R + B$$

where DN is the instrument response, R is the surface reflectance, A accounts for the solar, atmospheric and instrument multiplicative factors and B for the instrument and atmospheric additive components. These equations are solved for A and B for each AVIRIS spectral channel. The resulting equation

$$R = ( DN - B ) / A$$

is formed with the determined multiplicative and additive factors, which transform instrument DN to reflectance for the entire imaging

spectrometer data set. Primary assumptions of the algorithm are a constant instrument performance and a uniform atmosphere over the region to which it is applied.

The algorithm was implemented with the reflectance spectra measured with PIDAS at the asphalt and graded soil targets and the corresponding instrument response (Figures 2 and 3). An empirical line spectrum derived from AVIRIS data over the bastnaesite target after the application of the algorithm resolves the narrow neodynium absorption features between 700 and 940 nm (Figure 5).

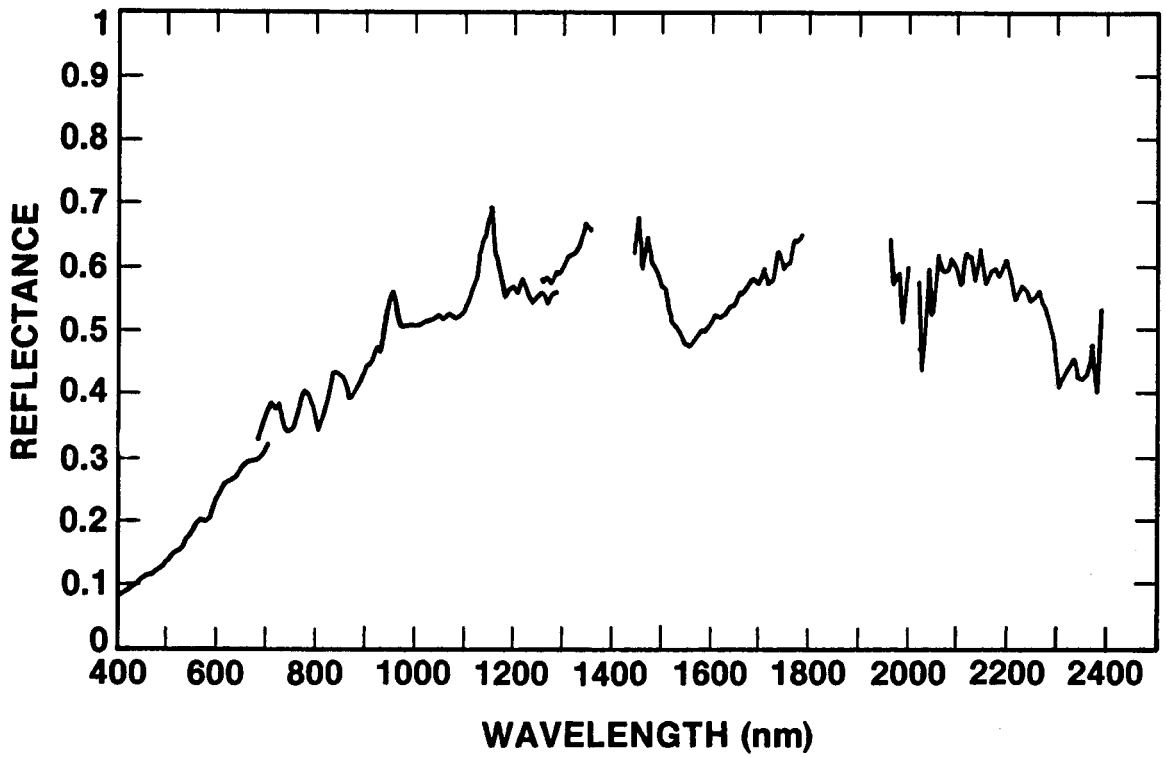


Figure 5. Spectra derived from AVIRIS data using the empirical line reflectance retrieval algorithm. The three strong neodynium absorption features between 700 and 900 nm are well resolved. Other features in the spectrum are discussed in the text.

The anomalous reflectance peaks at 940 and 1125 nm are due to the difference in atmospheric water vapor content between the bastnaesite and empirical line targets. This demonstrates that the assumption of uniform atmosphere is not true in regions of atmospheric water absorption. We (Conel, et al, 1988a) have subsequently mapped the variations in atmospheric water vapor with elevation using the AVIRIS channel responses in the 940 and 1125 nm water bands. The offsets in the reflectance curves at approximately 700 and 1280 nm are due to changes in the response functions of spectrometers A and B over the course of the flight line (Vane et al., 1988). The gaps at about 1400 and 1900 nm are due to

the strong atmospheric water bands, and the gap at about 2000 nm is due to a noisy detector element in spectrometer D. These features can be seen in most of the full spectrum plots in this paper.

## 3.2 LOWTRAN 7 Radiance Model.

In situ measurements of surface reflectance and atmospheric optical depth were used in conjunction with the radiative transfer code LOWTRAN 7 (Kneizys et al, 1988) to calculate the total radiance at AVIRIS for the Mountain Pass overflight. The atmospheric path and surface reflected as well as the total radiance for the Ivanpah Playa target are plotted in Figure 6. An extensive discussion of this methodology for modeling radiance with radiative transfer codes and surface and atmospheric measurements is given in Conel et al, (1988b). The high resolution atmospheric gas absorptions provide features suitable for assessment of the in-flight spectral performance, while modeled total radiance allows evaluation of the radiometric calibration.

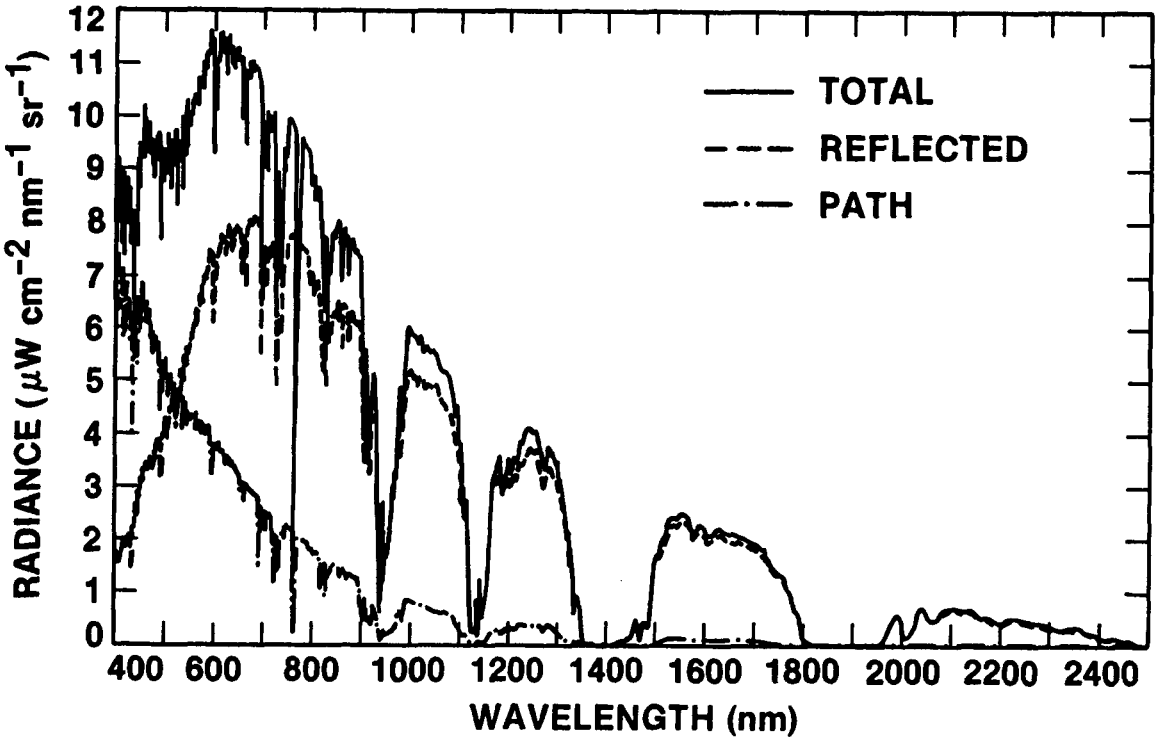


Figure 6. A LOWTRAN 7 model radiance for Ivanpah Playa constrained by the conditions of the AVIRIS overflight. The atmospheric path, surface reflected and total radiances are plotted. The path radiance is a significant contributor, ranging from 80 to 10 percent of the total from 400 to 1300 nm.

# 4.0 ANALYSES AND RESULTS

## 4.1 Spectral Performance and calibration.

In-flight spectral performance was assessed using the neodymium absorption features between 700 and 940 nm and various atmospheric gaseous absorption features that occur throughout the spectral region of AVIRIS.

To provide a common basis for comparison the laboratory bastnaesite spectrum was convolved with the preflight season channel wavelength positions and spectral response functions. Figure 7 shows the Gaussian approximation for the spectral response function for AVIRIS channel 98 with the wavelength position determined as the wavelength of maximum amplitude and spectral response characterized as the full width at half maximum amplitude (FWHM). The correspondence of AVIRIS spectral response to a Gaussian function is consistent with the instrument design and

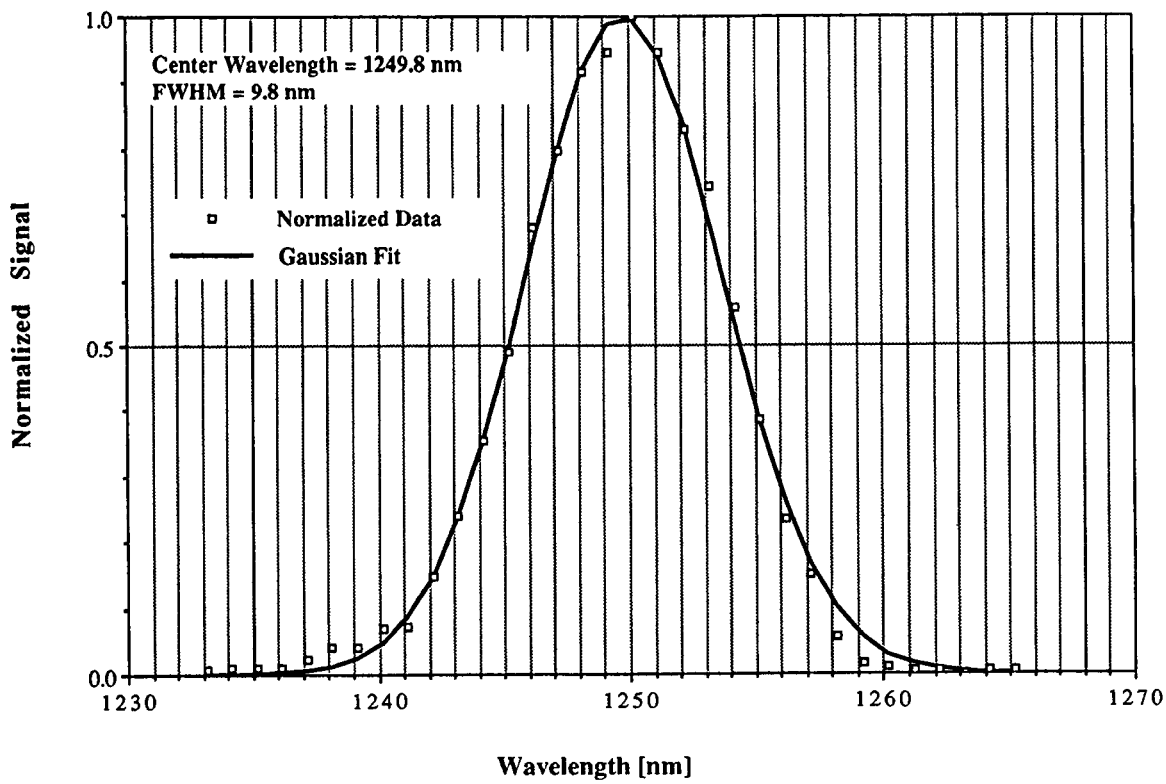


Figure 7. A typical normalized AVIRIS spectral response function for channel 98, spectrometer C, compared to a Gaussian representation which closely approximates the measured function.

laboratory determination (Macenka and Chrisp 1987, and Vane et al, 1988). In Table 2 the pre-season spectral calibration is presented (Vane et al, 1987) such that the spectral position of an AVIRIS detector is determined by the product of the detector number and the sampling interval summed with the starting wavelength position of the spectrometer. Both the convolved laboratory measured bastnaesite spectrum and the AVIRIS empirical line spectrum are plotted in Figure 8 for the wavelength region between 700 and 940 nm. A spectral shift of several nanometers of the AVIRIS spectrum

Table 2. Pre-season laboratory spectral calibration

| Spectrometer | Sampling Int. (nm) | Starting Pos. (nm) | Detector Number | Response Width (nm) |
|---|---|---|---|---|
| A | 9.858 | 396.5 | 0 - 31 | 9.7 |
| B | 9.579 | 678.2 | 0 - 63 | 9.7 |
| C | 9.849 | 1241.7 | 0 - 63 | 9.0 |
| D | 9.859 | 1828.8 | 0 - 63 | 11.6 |

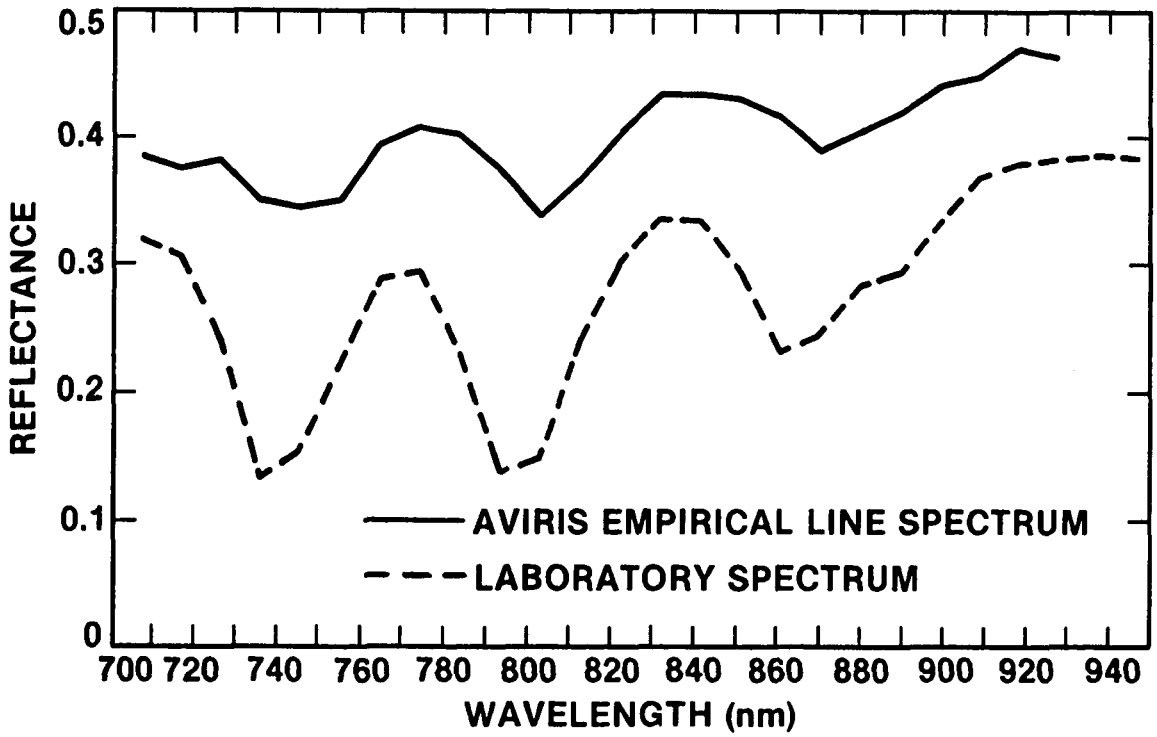


Figure 8. An empirical line derived bastnaesite spectrum compared to a Beckman spectrum of bastnaesite showing a shift of AVIRIS in-flight spectral position to shorter wavelengths.

to longer wavelengths is observed. This indicates the spectral channel positions for spectrometer B are shifted to shorter wavelengths for these flight data as compared to the laboratory measured bastnaesite spectrum.

To utilize the atmospheric absorption features in an independent assessment of in-flight spectral performance, the LOWTRAN 7 total radiance was convolved with the preflight season AVIRIS channel spectral positions and response functions and compared with the AVIRIS in-flight radiance over Ivanpah Playa. Figure 9 shows the results for each of the four AVIRIS spectrometers. Spectrometer B exhibits a shift in spectral alignment to longer wavelengths, which is consistent with the determination derived from the bastnaesite spectrum. Spectrometer D likewise shows a shift to shorter wavelengths, while spectrometers A and C show good agreement between in-flight and laboratory spectral alignment. The predicted total radiance at AVIRIS allows evaluation of the in-flight spectral response. For

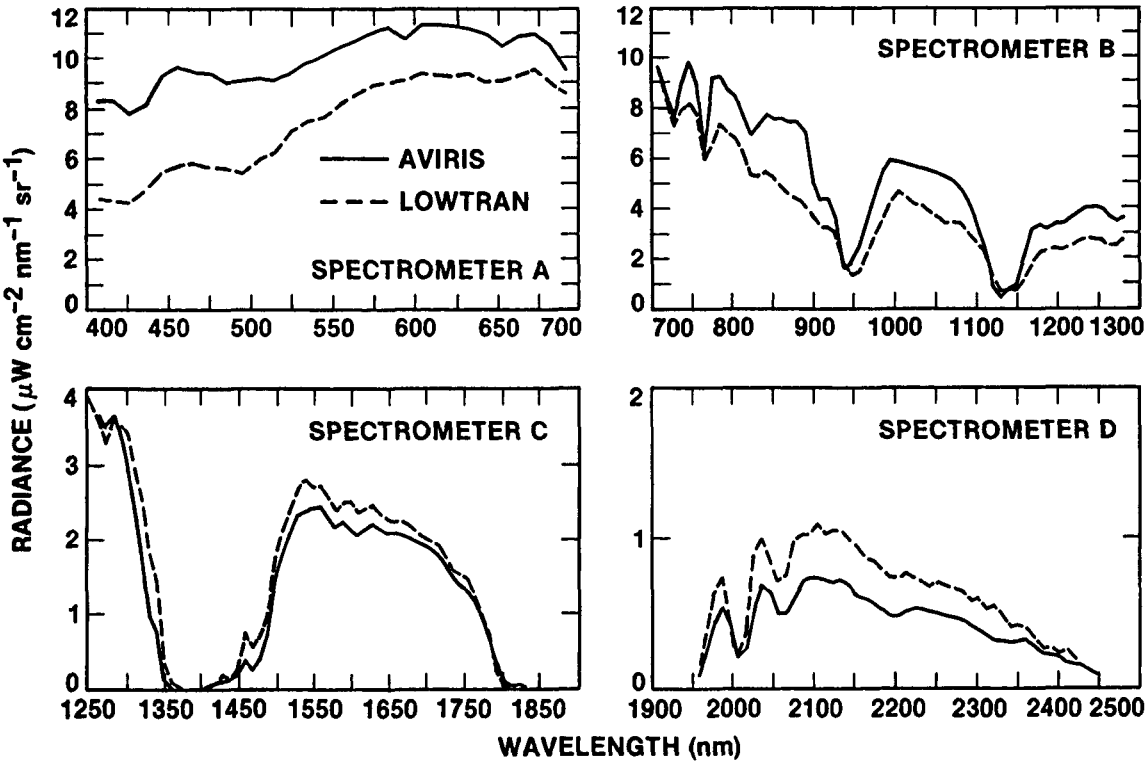


Figure 9. A comparison of AVIRIS radiance to LOWTRAN 7 modeled radiance for spectrometers A through D. Spectrometer B exhibits a broadened spectral response function and a shift to shorter wavelengths relative to the predicted LOWTRAN 7. Spectrometer D has also shifted several nanometers to shorter wavelengths, while spectrometers A and C show good agreement with the LOWTRAN 7 model.

spectrometer B , the atmospheric oxygen feature at 760 nm is more completely resolved in the LOWTRAN 7 modeled data than the in-flight data indicating a broadening of spectral response at the time of flight data acquisition. This broadening of the spectral response function is evident in the water bands at 735, 840, 940 and 1125 nm as well.

Using the LOWTRAN 7 model, an algorithm was developed to optimize for the Gaussian function which best describes the in-flight AVIRIS channel wavelength position and spectral response function. This algorithm minimizes the mean squared radiance difference between the AVIRIS retrieved radiance and modeled radiance while varying the response width and position of the Gaussian function convolved with the LOWTRAN 7 model. The algorithm was applied to sharp atmospheric absorption features where a change in position and response strongly affects the returned radiance. The spectral characteristics for spectrometer A were determined using the the water absorption band near 675 nm. The absorptions between 700 and 850 nm were used to fit the spectral characteristics for spectrometer B, while the carbon dioxide doublets centered at 1600 and 2050 nm were used for spectrometers C and D respectively. An example of the results for this minimizing algorithm for spectrometer C is given in Figure 10a and b. The spectral position is optimized for 1 nm to shorter wavelengths than the pre-season calibration (Figure 10a), while the spectral response is characterized by 1 nm less than the nominal 10 nm FWHM response function (Figure 10b). Table 3 describes the resulting in-flight spectral calibration derived using this error

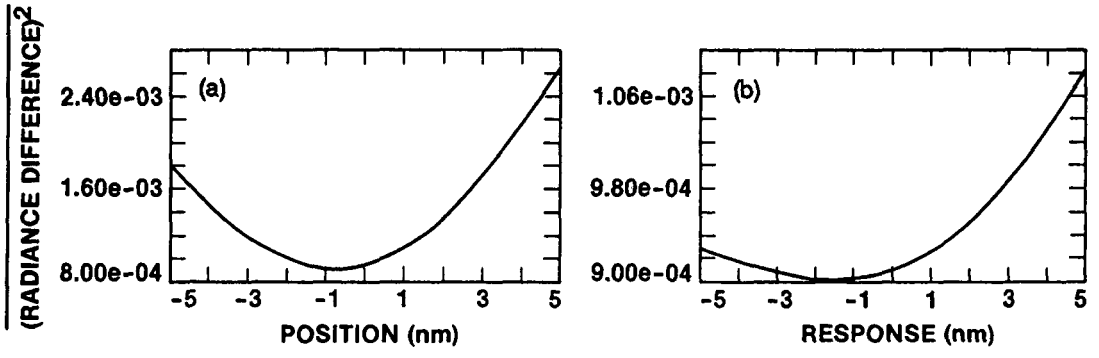


Figure 10. (a) Least squared residual fit for AVIRIS in-flight spectral position as a function of deviation from the pre-flight season laboratory calibration. The wavelength position for spectrometer C is optimized with a 1 nm shift to shorter wavelengths. (b) Residual minimization for spectral response function as deviation from a 10 nm Gaussian. Spectral response is optimal for a full width at half maximum of 9 nm.

minimization algorithm for each of the spectrometers. The plots in Figure 11 show the result of application of the in-flight spectral calibration to the AVIRIS flight data in comparison with the radiance curves obtained from LOWTRAN 7. Compared with Figure 9, an improvement can been seen in terms both of correspondence of wavelength position and resolution of the atmospheric absorption features.

TABLE 3. In-flight spectral calibration.

| Spectrometer | Sampling Int. (nm) | Starting Pos. (nm) | Detector Number | Response Width (nm) |
|---|---|---|---|---|
| A | 9.858 | 396.5 | 0 - 31 | 15 |
| B | 9.579 | 674.2 | 0 - 63 | 17 |
| C | 9.849 | 1240.7 | 0 - 63 | 9 |
| D | 9.859 | 1831.8 | 0 - 63 | 10 |

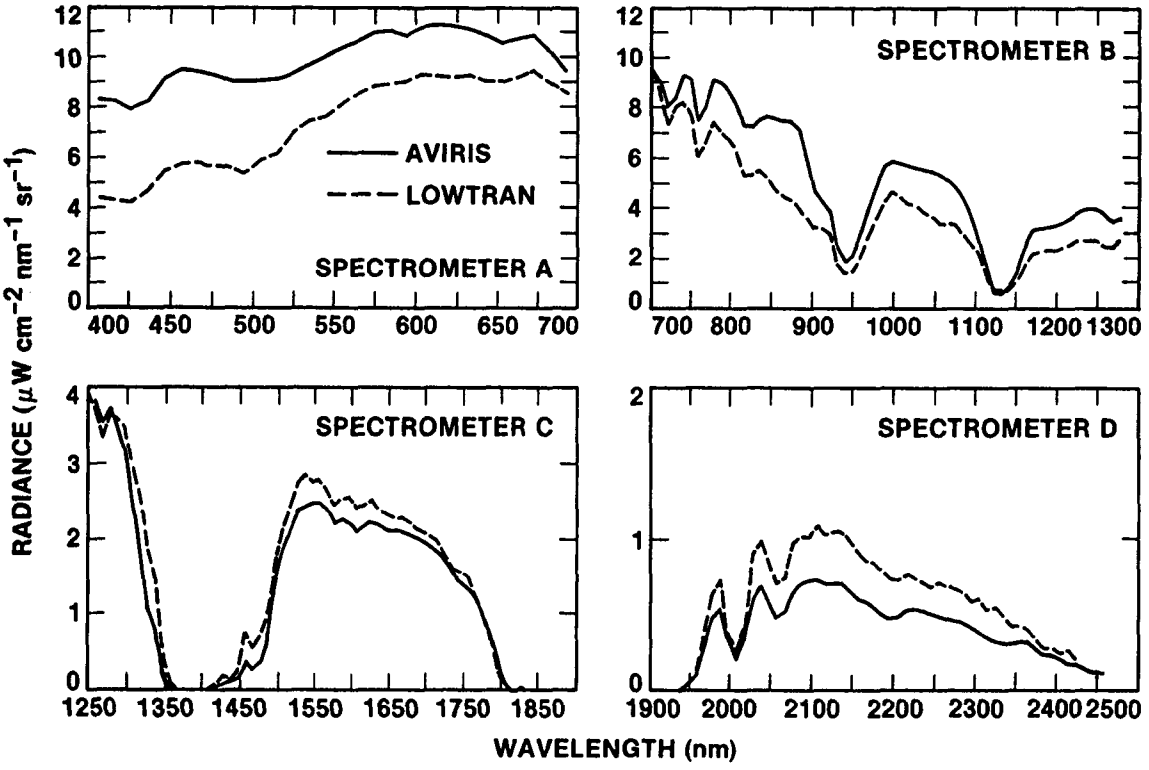


Figure 11. Results of the application of the in-flight determined spectral calibration. The spectral positions of spectrometers B and C are significantly improved as is the spectral resolution of spectrometer B.

## 4.2 Radiometric Performance and calibration.

In Figure 9 some level of disagreement in all four spectrometers between the AVIRIS laboratory calibrated total radiance and the LOWTRAN 7 modeled radiance over Ivanpah Playa is observed. A ratio of these data in Figure 12 shows the LOWTRAN 7 modeled radiance is on the average 1.2 times that of AVIRIS in spectrometer A, 1.4 in B, 0.85 in C and 0.80 in D. The various factors contributing to these discrepancies are discussed by Vane et al. (1988).

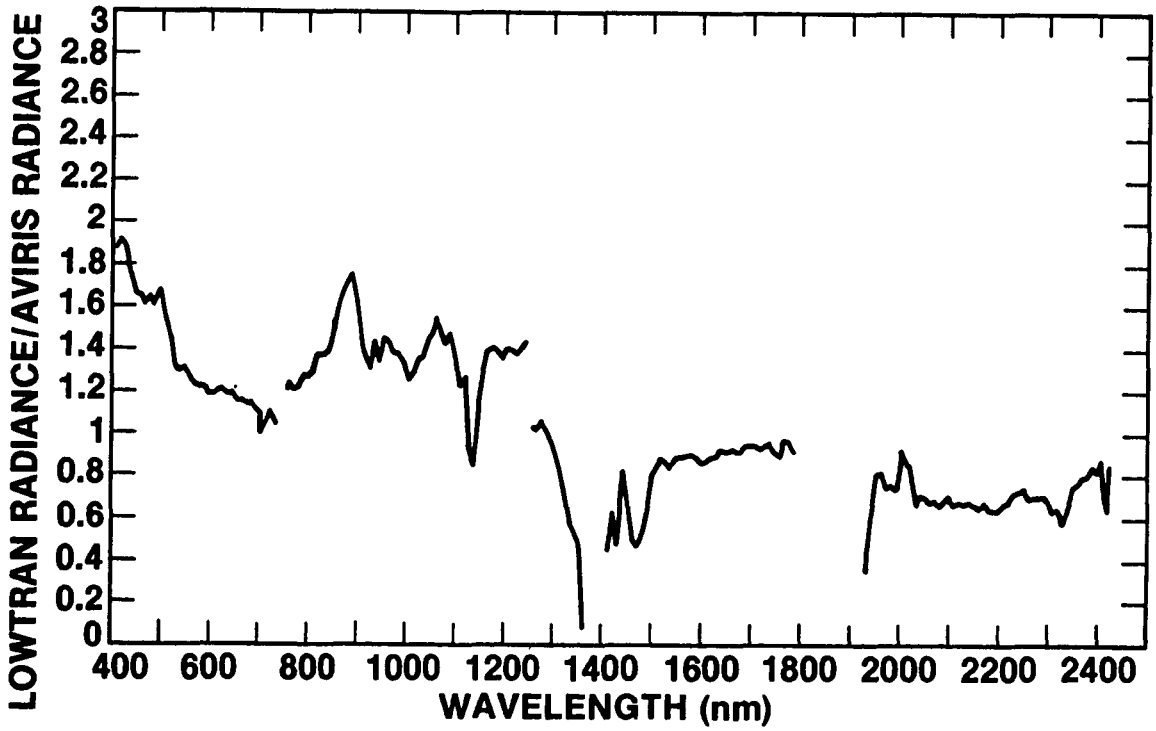


Figure 12. Ratio of LOWTRAN 7 modeled radiance to radiance derived by applying the pre-flight season radiometric calibration to AVIRIS data from Ivanpah Playa. The deviation from a ratio of 1 indicates the amount of disagreement between the laboratory and in-flight radiometric response function of AVIRIS.

Using the LOWTRAN 7 radiance model, an improved in-flight radiometric calibration was achieved by constructing the ratio of LOWTRAN 7 total radiance to AVIRIS in-flight instrument response. These factors for the in-flight radiometric calibration of the Mountain Pass data set, which transform instrument response into radiance, are plotted in Figure 13. This calibration provides a basis for analysis of these AVIRIS data requiring accurate units of total radiance.

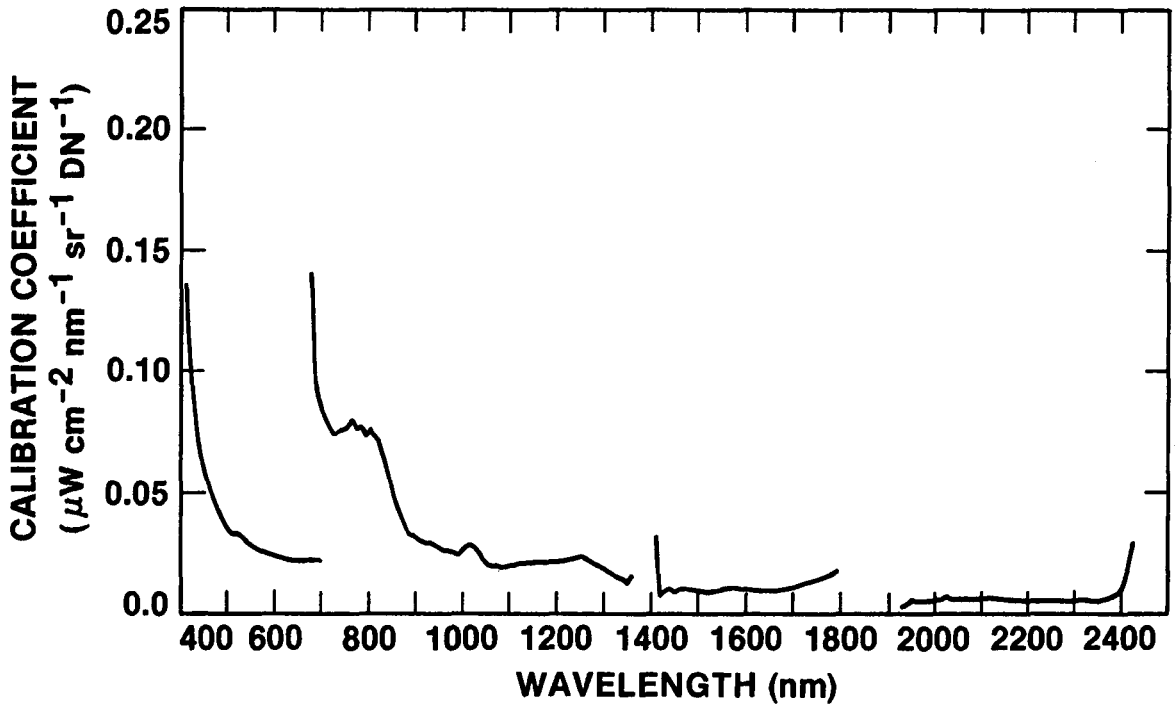


Figure 13. Radiometric calibration factors determined for the Mountain Pass flight data. The coefficients provide an accurate transformation of AVIRIS instrument response in DN to total radiance incident at the instrument.

## 4.3 Spatial Performance

As a preliminary evaluation of spatial resolution and intra-image geometric quality, images of the AVIRIS and TM data were compared over the Mountain Pass site as shown in Figure 14 (slide No. 12). The AVIRIS 10-nm channels were averaged to correspond to the broad TM channels centered at 660, 1650 and 2200 nm; the data are displayed as red, green and blue respectively. The spatially varying geological and cultural surface features provide a basis for comparison of spatial resolution. AVIRIS resolves the two strands of Interstate 15 and the detailed geological stratigraphy to the south of the road which are not as clearly discernable in the TM image. This observed higher spatial resolution of AVIRIS is consistent with the designed 20 m ground instantaneous field of view (GIFOV) and 17 m pixel-to-pixel spacing of AVIRIS, compared to the 30 m GIFOV and 28.5 m pixel-to-pixel spacing of TM. The intra-image geometric fidelity of the AVIRIS and TM images is comparable. The AVIRIS image has had no geometric correction applied to it other than the limited on-board roll correction which is applied in flight (Porter and Enmark, 1987).

AVIRIS

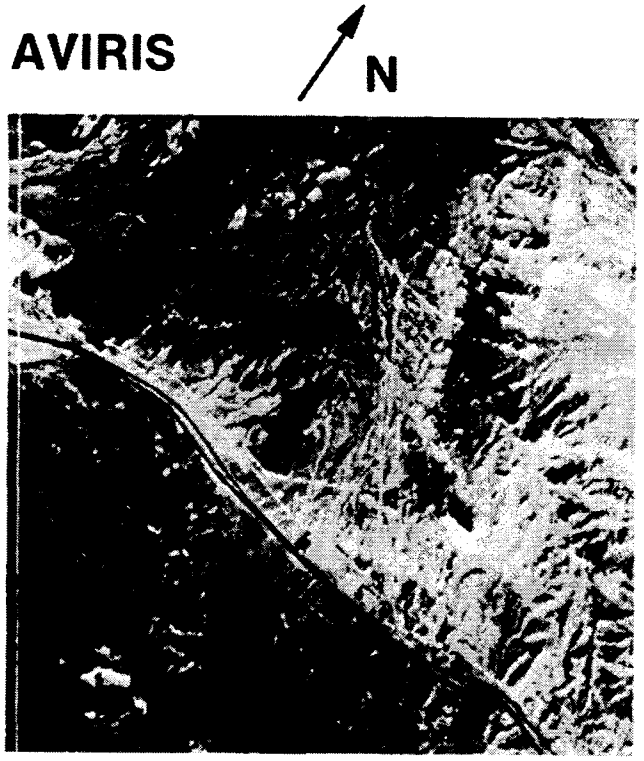

N

THEMATIC MAPPER

| | | | | | |
|---|---|---|---|---|---|
| FLIGHT | 10 | BLUE | 2200 nm | SCENE | 850043 7424 |
| RUN | 2 | GREEN | 1650 nm | PATH | 39 |
| SEGMENT | 3 | RED | 560 nm | ROW | 35 |

Figure 14. Comparison of AVIRIS and Thematic Mapper images of Mountain Pass, CA, at equivalent spectral wavelengths and bandwidths. AVIRIS more completely resolves the two strands of Interstate 15 as well as the fine stratigraphic units and drainage patterns found at the test site (refer to slide No. 12).

## 4.4 Signal-to-Noise Performance.

An in-flight assessment of the noise performance was developed through calculation of the standard deviation of each AVIRIS channel from data acquired over a nearly homogeneous region of the Ivanpah Playa. This analysis relates signal variation over a spatially homogeneous region to in-flight instrumental noise. An independent assessment of noise is found through determining the statistical variation in the dark current measured at the end of each image line. Results from each of these analyses are plotted in Figure 15. In each spectrometer, the variation calculated in the instrument response over the playa is similar in magnitude to the variation in the end-of-line dark current, establishing the dark current statistics as a valid estimator of instrument noise. Accurate determination of noise based solely on the dark current demonstrates AVIRIS noise for these data is independent of the radiance incident at the instrument. These results are consistent with laboratory measurements dark current and integrating sphere signal levels and statistics (Chrien, 1988).

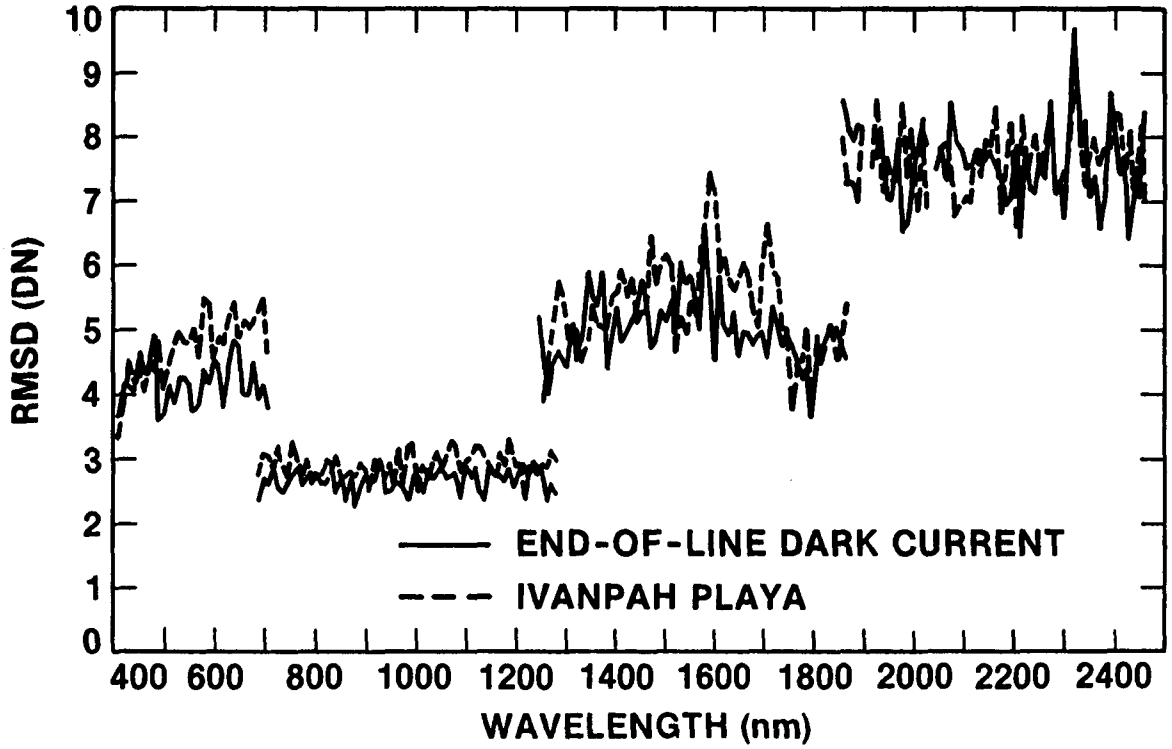


Figure 15. Standard deviation of AVIRIS end-of-line dark current and image data over a homogeneous section of Ivanpah Playa. The statistical variation of the dark current accounts for the variation observed in the data over the playa, demonstrating dark current statistics to be a good estimator of instrument noise.

Determination of in-flight noise without requiring a large homogeneous surface target provides an approach for calculating the signal-to-noise ratio for any region of interest in the AVIRIS data. The ratio of average instrument response, with dark current subtracted, to the standard deviation of the dark current provides a valid estimate.

Because the signal incident at AVIRIS is determined by the solar illumination, surface reflectance, atmospheric attenuation and atmospheric scattering, the directly calculated signal-to-noise is not comparable to determinations under other conditions or in the laboratory. This issue is resolved by scaling the actual instrument response to the AVIRIS reference radiance prior to calculating the signal-to-noise. The reference radiance is constrained by the conditions given in Table 4. A comparison of the AVIRIS reference radiance model and Ivanpah Playa radiance calculated is shown in Figure 16. The Ivanpah radiance values were calculated using LOWTRAN 7 and the PIDAS and atmospheric optical depth data as previously described.

TABLE 4.

Parameters defining the AVIRIS reference radiance.

| | |
|---|---|
| Radiative Transfer Code | LOWTRAN 7 |
| Atmospheric model | Midlatitude summer |
| Atmospheric aerosols | Rural 23 km visibility |
| Observer altitude | 0 km |
| Target altitude | 0 km |
| Target reflectance | 0.50 |
| Date | Summer solstice |
| Hour | Solar noon |
| Latitude | 45 degrees |
| Radiance used | Reflected component |

A signal-to-noise ratio was calculated by forming a ratio of image signal level over Ivanpah Playa, after dark current subtraction, to image noise values derived from end-of-line dark current statistics. To compare the in-flight signal-to-noise ratio for Ivanpah Playa to laboratory and other in-flight determined values, an AVIRIS reference radiance model was used to normalize the Ivanpah signal levels. Both the normalized signal levels and the observed signal levels were then divided by the observed noise to produce the signal-to-noise plots shown in Figure 17. In terms of the reference radiance model, spectrometer A had a peak signal-to-noise ratio of 90 - 100 to 1, B of 60 to 1, C of 40 - 50 to 1, and D of about 20 to 1 on July 30, 1987.

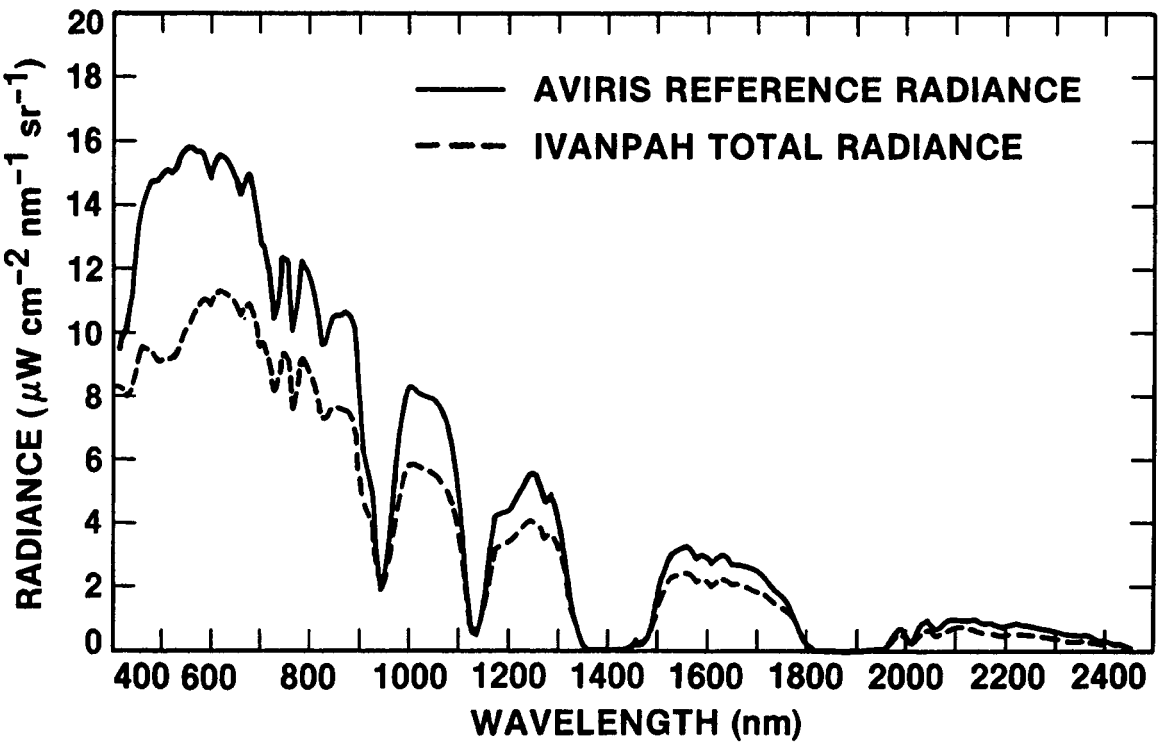


Figure 16. A plot of the AVIRIS reference radiance used to scale actual radiance falling on the instrument for intercomparison of signal-to-noise performance between data sets acquired in flight or in the laboratory.

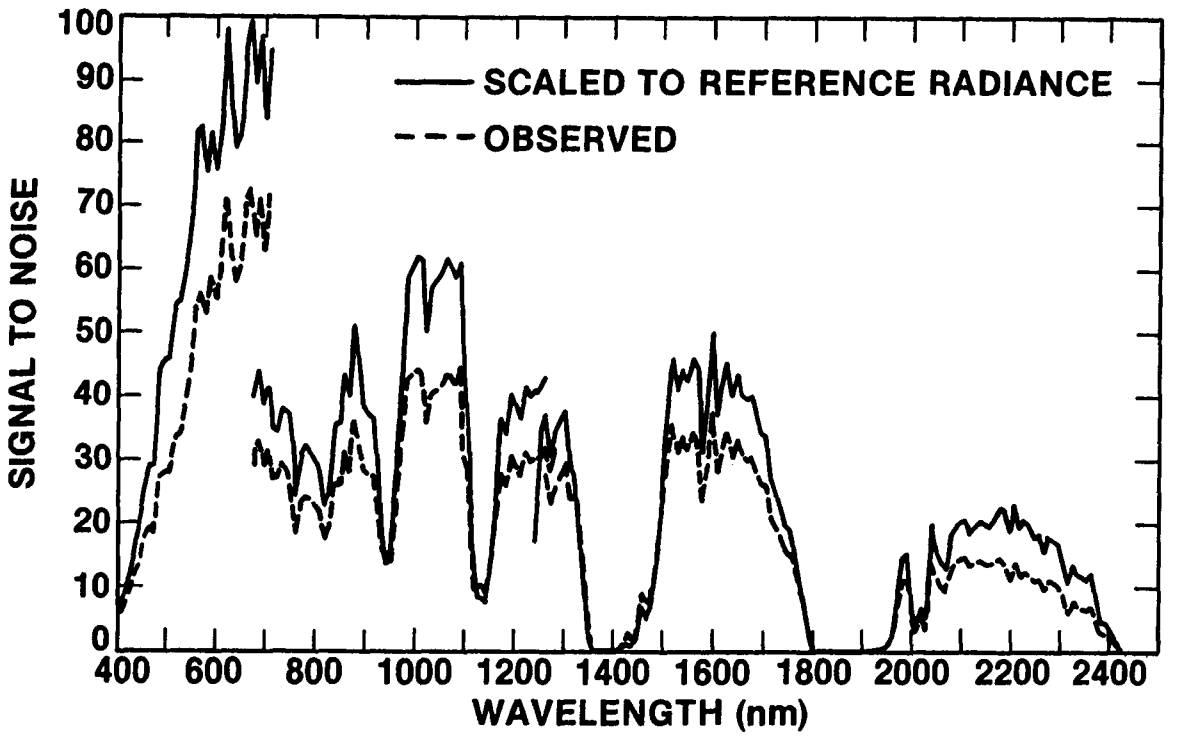


Figure 17. AVIRIS observed signal-to-noise performance over Ivanpah Playa calculated by a ratio of mean signal over the playa to standard deviation of the corresponding end-of-line dark current, and signal-to-noise scaled to the AVIRIS reference radiance. The scaled signal-to-noise can be compared to any other similarly scaled AVIRIS data set to assess stability of the radiometric response function of the instrument.

## 5.0 CONCLUSION

Through the evaluation of the in-flight performance and application of in-flight spectral and radiometric calibrations to the AVIRIS data acquired on July 30, 1987, a number of conclusions are reached. (1) AVIRIS successfully resolves narrow spectral absorption features both on the surface and in the atmosphere. (2) The empirical line algorithm compensates for both additive and multiplicative factors and directly transforms in-flight instrument response to reflectance. (3) Based on both surface and atmospheric absorption features, a shift of several nanometers in spectral position relative to the pre-flight season calibration is shown in spectrometers B and D. (4) Comparison of the modeled atmospheric radiance and the calibrated AVIRIS radiance show a degradation in spectral response function in spectrometers A and B. (5) A least squares residual algorithm minimizing on the LOWTRAN 7 and the pre-season calibrated AVIRIS radiance for both spectral position and

response function generates an improved spectral calibration. (6) In-flight modeled radiance based on concurrent in situ surface and atmospheric measurements predicts higher radiance in spectrometers A and B, with lower radiance in C and D relative to the pre-flight season laboratory calibration, thus demonstrating a corresponding change in radiometric response functions. (7) The modeled radiance provides a direct approach to in-flight radiometric calibration. (8) Comparison of coincident Thematic Mapper and AVIRIS imagery shows AVIRIS is resolving finer surface detail and shows good spatial geometry. (9) Variation in the end-of-line dark current is a valid estimate of noise in the AVIRIS data.

Thus, assessment of the spectral, radiometric, spatial and signal-to-noise properties of AVIRIS can be achieved with a combination of in situ surface and atmospheric measurements in conjunction with a suitable radiative transfer code, providing a tool for sensor in-flight performance evaluation and calibration.

## 6.0 ACKNOWLEDGEMENTS

The authors gratefully acknowledge the helpful discussions and contributions of many individuals during this work: Veronique Carrere, Jack Margolis, Ron Alley, Tom Chrien and Wallace Porter at JPL; Larry Rowen, Jim Crowley and Melvin Podwysocki at the USGS in Reston, Virginia; and Dave Meyer at the EROS Data Center, Sioux Falls, South Dakota.

The work presented in this paper was carried out at the Jet Propulsion Laboratory, California Institute of Technology, under a contract with the National Aeronautics and Space Administration.

## 7.0 REFERENCES

Adams, J. W., "The visible region absorption spectra of rare-earth minerals," The Amer. Min. 50, 356-367, (1965)

Chrien, T. G., personal communication, (1988).

Conel, J. E., R. O. Green, V. Carrere, J. S. Margolis, R. E. Alley, G. Vane, C. J. Bruegge and B. L. Gary, "Mapping atmospheric water vapor with the Airborne Visible/Infrared Imaging Spectrometer (AVIRIS) at Mountain Pass, California," in proceedings of the Airborne Visible/Infrared Imaging Spectrometer (AVIRIS) Performance Evaluation Workshop, G. Vane, Ed., JPL Publication 88-38, pp TBD (1988a).

Conel, J. E., R. O. Green, R. E. Alley, C. J. Bruegge, V. Carrere, J. S. Margolis, G. Vane, T. G. Chrien, P. N. Slater, S. F. Biggar, P. M. Teillet, R. D. Jackson, M. S. Moran, "In-flight radiometric calibration of the Airborne Visible/Infrared Imaging Spectrometer (AVIRIS)," in Proceedings SPIE Conference on Recent Advances on Sensors, Radiometry and Data Processing for Remote Sensing, 924, 168-178, (1988b).

Conel, J. E., R. O. Green, G. Vane, C. J. Bruegge and R. E. Alley, "AIS-2 radiometry and a comparison of methods for the recovery of ground reflectance," in Proceedings of the Third Airborne Imaging Spectrometer Data Analysis Workshop, G. Vane, Ed., JPL Publication 87-30, 18-47 (1987).

Goetz, A. F. H., "The Portable Instant Display Analysis Spectrometer (PIDAS)," in Proceedings of the Third Airborne Imaging Spectrometer Data Analysis Workshop, (ed Vane, G.) JPL Publication 87-30, 8-17 (1987).

Herman, B., A. J. LaRocca and R. E. Turner, "Atmospheric Scattering," in The Infrared Handbook (eds W. L. Wolfe and G. J. Zissis) 4-1-76, Environmental Research Institute of Michigan, (1978).

Kneizys, F. X., E. P. Shettle, G. P. Anderson, L. W. Abrew, J. H. Chetwynd, J. E. A. Shelby, S. A. Clough, and W. O. Galery, "Atmospheric Transmittance/Radiance: computer code LOWTRAN 7," (in press) (1988).

Macenka, S. A. , and M. P. Chrisp, "Airborne Visible/Infrared Imaging Spectrometer (AVIRIS) spectrometer design and performance," in Imaging Spectroscopy II, SPIE 834, 32-49, (1987).

Olson, J. C., D. R. Shawe, L. C. Pray, and W. N. Sharp, "Rare-Earth mineral deposits of the Mountain Pass district San Bernardino county California," Geological Survey Professional Paper 261, 75 (1954).

Porter, W. M., H. T. Enmark, "A system overview of the Airborne Visible/Imaging Spectrometer (AVIRIS)," Proceedings SPIE Conference on Imaging Spectroscopy II (San Diego, CA, 20-21 August, 1987), 834, 22-31 (1987).

Shaw, G. E., J. A. Reagan and B. H. Herman, "Investigation of atmospheric extinction using direct solar radiation measurements made with a multiple wavelength radiometer," J. Appl. Meteorol., 12, 374-380, (1973).

Vane, G., T. G. Chrien, E. A. Miller, J. H. Reimer, "Spectral and radiometric calibration of the Airborne Visible/Infrared Imaging Spectrometer (AVIRIS)," Proc. SPIE Conference on Imaging Spectroscopy II (San Diego, CA, 20-21 August, 1987), 834, 91-106 (1987).

Vane, G., T.G. Chrien, J.H. Reimer, R.O. Green, J.E. Conel, "Comparison on laboratory calibrations of the Airborne Visible/Infrared Imaging Spectrometer and the beginning and end of the first flight season," Proc. SPIE Conference on Recent Advances on Sensors, Radiometry and Data Processing for Remote Sensing, 924, 168-178, (1988).

# Appendix A

## SPIE Papers on AVIRIS 1987 Laboratory and In-Flight Spectral and Radiometric Performance

# Comparison of laboratory calibrations of the Airborne Visible/Infrared Imaging Spectrometer (AVIRIS) at the beginning and end of the first flight season

Gregg Vane, Thomas G. Chrien, John H. Reimer, Robert O. Green, and James E. Conel

Jet Propulsion Laboratory, California Institute of Technology
4800 Oak Grove Drive, Pasadena, California 91109

## ABSTRACT

Spectral and radiometric calibrations of the Airborne Visible/Infrared Imaging Spectrometer (AVIRIS) were performed in the laboratory in June and November, 1987, at the beginning and end of the first flight season. This paper describes those calibrations and the changes in instrument characteristics that occurred during the flight season as a result of factors such as detachment of the optical fibers to two of the four AVIRIS spectrometers, degradation in the optical alignment of the spectrometers due to thermally-induced and mechanical warpage, and breakage of a thermal blocking filter in one of the spectrometers. These factors caused loss of signal in three spectrometers, loss of spectral resolution in two spectrometers, and added uncertainty in the radiometry of AVIRIS. Results from in-flight assessment of the laboratory calibrations are presented. The paper concludes with a discussion of improvements made to the instrument since the end of the first flight season and plans for the future. Improvements include (1) a new thermal control system for stabilizing spectrometer temperatures, (2) kinematic mounting of the spectrometers to the instrument rack, and (3) new epoxy for attaching the optical fibers inside their mounting tubes.

## 1. INTRODUCTION

AVIRIS is a second-generation imaging spectrometer developed at the Jet Propulsion Laboratory (JPL) for use in earth remote sensing studies across a broad spectrum of scientific disciplines, including botany, geology, hydrology, oceanography, and atmospheric science.[1] Design and construction of the sensor and ground data processing facility were begun in 1984 and completed in June 1987. Following a laboratory calibration, flight operations were begun on June 25, 1987. Data were collected for 20 investigators between June and October 1987, after which the instrument was returned to JPL for a post-flight-season calibration and refurbishment. In this paper, we give a synopsis of the procedures used in the laboratory spectral and radiometric calibration of AVIRIS, and show results obtained from the two laboratory calibrations conducted in 1987 and from flight experiments also conducted in 1987 to assess the performance of the instrument. As background, a brief description of the instrument follows. Complete details of the sensor and ground data processing system can be found in Volume 834 of the Proceedings of the SPIE.[2-8]

AVIRIS acquires images in 220 contiguous 10-nanometer (nm) spectral bands in the region between 0.40 and 2.45 micrometers (μm). The instantaneous field of view of AVIRIS is 1 milliradian and the field of view as defined by the scan angle is 30 degrees. This results in images covering a 10.5 km swath composed of picture elements (pixels) that subtend 20 m on the ground from the 20 km altitude of the NASA U-2 and ER-2 aircraft. AVIRIS gathers spectral images in the whisk-broom imaging mode, employing foreoptics with a mirror that scans in one direction, then rapidly returns to the start position for the next scan line. A diagram of the optical configuration is shown in Figure 1. An artist's rendition of the flight hardware is shown in Figure 2. The scan rate and detector readout timing were designed to provide a 17 percent spatial oversampling at sea level in both the cross-track and along-track dimensions in order to assure complete spatial coverage over mountainous terrain. This results in the acquisition of 614 pixels in each scan line. Geometric rectification removes the oversampling, resulting in an image 550 pixels across. Twelve scans are completed per second. During the fly-back portion of each scan cycle, a shutter closes the foreoptics from the rest of the optical system, and a single measurement of the detector dark current for each of the detector elements is recorded.

The foreoptics are connected to four spectrometers with optical fibers (see Figure 1). Spectrometer A contains a 32-element line array of silicon detectors, and spectrometers B, C, and D each employ 64-element line arrays of indium antimonide detectors. While a total of 224 spectral bands are actually acquired, the readout architecture of the detector arrays renders the first band of each array unusable; there are thus 220 usable raw spectral bands. The effective spectral ranges of spectrometers A, B, C, and D are 0.40 to 0.71, 0.68 to 1.28, 1.24 to 1.86, and 1.83 to 2.45 μm, respectively, as aligned for the 1987 flight season. There is an overlap of 3 to 4 spectral bands in coverage of the spectrum between the 4 spectrometers. During radiometric calibration the spectral region covered by the 220 raw spectral bands can, at the request of the investigator, be resampled to remove overlap between spectrometers and equalize the spectral sampling interval across the entire 0.40 to 2.45 μm region. This resampling results in 210 spectral bands over the 0.40 to 2.45 μm region.

Each spectrometer additionally receives input via a second optical fiber from an onboard radiometric and spectral calibration source consisting of a tungsten lamp, a four-position filter wheel containing two neutral density filters, a didymium oxide filter and an opaque position.[2] The neutral density filters provide broad-spectral-band energy at two intensity levels to monitor radiometric stability. The didymium oxide filter provides several spectral absorption features in each of the spectral regions of the four AVIRIS spectrometers to monitor wavelength calibration. The opaque position is used in conjunction with the shutter in the foreoptics to provide a measurement of dark current from each detector. In each of the 4 filter positions, a full scan line of data (614 readouts of the detectors) is acquired.

In the following section of the paper we describe the procedures used in the laboratory to perform spectral and radiometric calibrations of AVIRIS. A summary of the calibration accuracies achieved in the pre-flight-season lab calibration is also given. Following that is a comparison of the pre- and post-flight-season calibrations and an in-flight assessment of instrument performance. Instrument factors that caused a degradation in performance over the course of the flight season are also discussed. We conclude with a discussion of improvements that have been made to AVIRIS over the past winter and spring, and plans for the future.

## 2. LABORATORY CALIBRATION OF AVIRIS

AVIRIS calibration is broken into two major parts, spectral and radiometric. Each requires its own support equipment and procedures, and each has associated with it an error budget that defines the accuracies achieved. The following discussion is a summary of a more detailed discussion found in Reference 9.

*SPIE Vol. 924 pp. 168-178 Recent Advances in Sensors, Radiometry, and Data Processing for Remote Sensing (1988)*

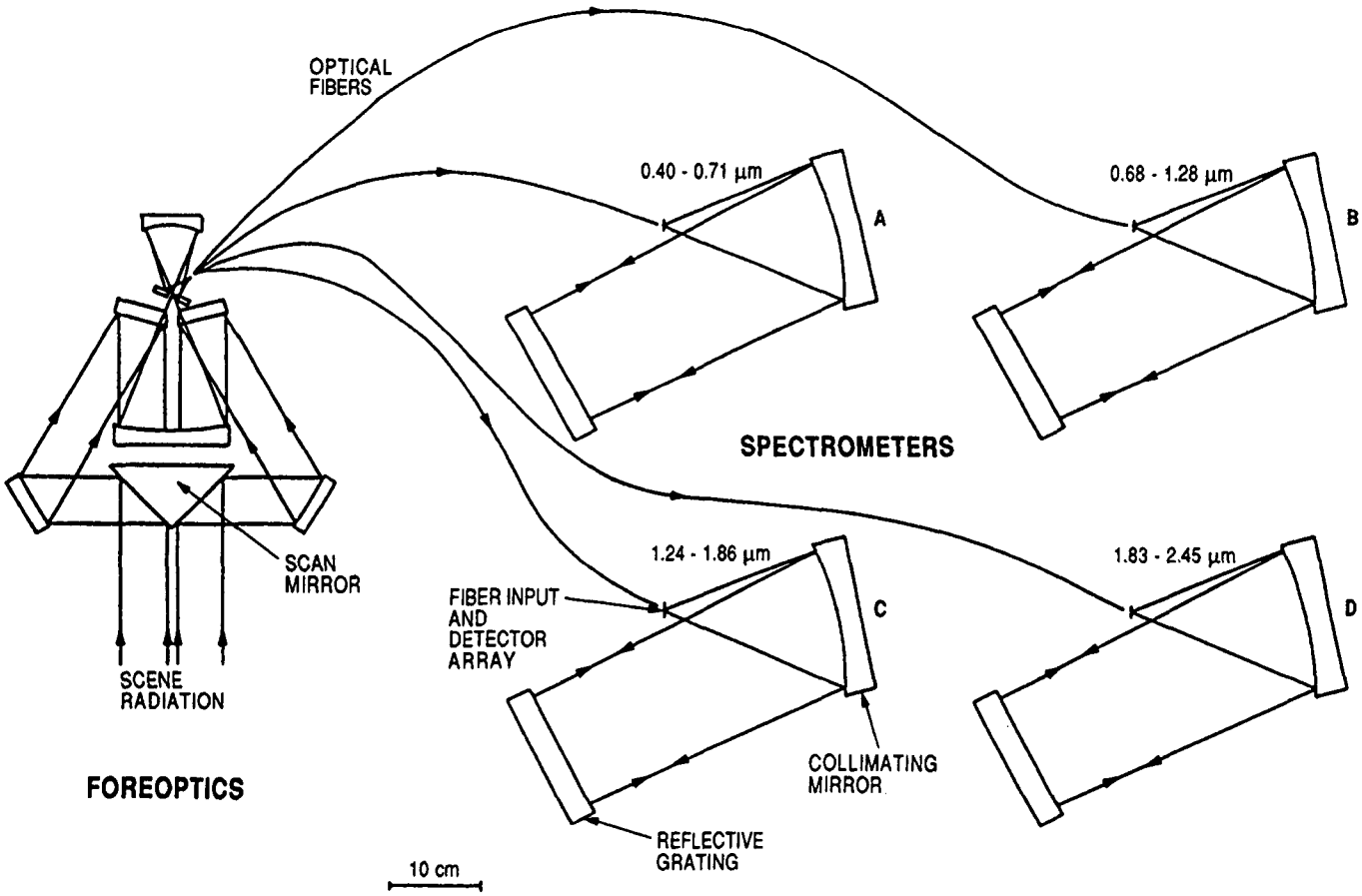


Figure 1. Schematic diagram of the AVIRIS optical configuration. The scanning foreoptics on the right are connected to the four spectrometers on the left with optical fibers.[26]

## 2.1. Spectral calibration

The three goals that must be met in the spectral calibration of an imaging spectrometer are: (1) Mapping of the center wavelength of light falling on each detector element, (2) determination of the wavelength bandwidth falling on each detector element, and (3) determination of the spectral sampling interval of each spectrometer. The purpose of the spectral calibration of AVIRIS is to determine the normalized instrument response function. This function is closely approximated by a Gaussian curve that is completely characterized by the wavelength of maximum response and by the spectral width at half peak height (the so-called full width at half maximum, FWHM). The distance between the maxima of the response functions of adjacent detectors is the spectral sampling interval. The optical setup for performing the spectral calibration is shown schematically in Figure 3. A Jarrell-Ash model 82-487 monochromator and tungsten lamp are used in the calibration. The monochromator is calibrated with a mercury pen lamp using multiple orders of the emission line at 546.1 nm. Three different gratings are used alternately in the monochromator to cover the full spectral range of AVIRIS. The monochromator is calibrated each time a grating change is made. By choosing the widths of the entrance and exit slits of the monochromator, the bandwidth of the exiting light can be tailored as required; typically, a bandwidth of 1 nm is used. The output signal level from a given AVIRIS detector element is recorded as the wavelength output of the monochromator is scanned in steps of 1 nm. This is plotted against the input wavelength as determined from the monochromator calibration, to produce a spectral response curve as shown in Figure 4. Analysis of the spectral response consists of fitting a Gaussian curve to the normalized signal using as the fit parameters the wavelength of maximum response and the FWHM spectral bandwidth. This procedure is followed for several detector elements per spectrometer. A linear fit is applied to the wavelengths of maximum response as a function of detector element number to determine the center wavelength positions of the other detector elements in a given spectrometer for which spectral response curves are not acquired. From the center wavelength positions of the 224 detector elements, the spectral sampling interval is determined. This is also the slope of the line fit to the wavelengths of the maximum response for each spectrometer. The results from the pre-flight-season spectral calibration of AVIRIS are summarized in Table 1.

## 2.2. Radiometric calibration

The goals of radiometric calibration are to establish and apply a set of calibration multipliers which: (1) Convert AVIRIS output digital numbers (DNs) to radiance ($\mu W/cm^2$-sr-nm) accurate to at least 10 percent absolute, and (2) to correct for non-uniformity in the response of the AVIRIS detector elements to at least 0.5 percent. Achieving these goals requires four major steps: (1) Calibration of a spectro-

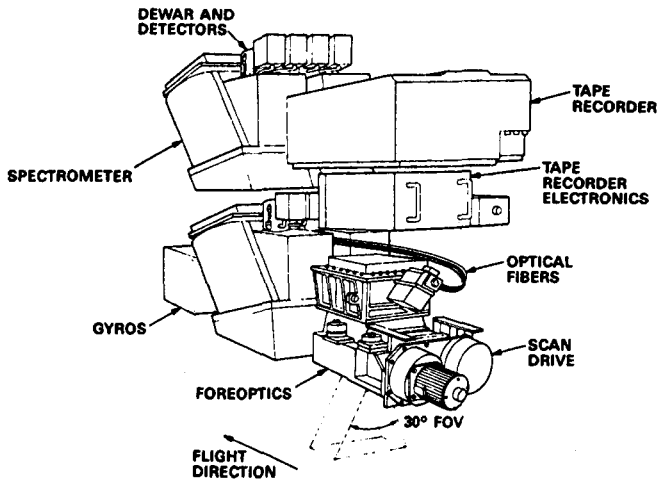


Figure 2. Artist's drawing of the AVIRIS flight hardware showing the physical layout of the major subsystems. The various electronics subassemblies are omitted for clarity.[26]

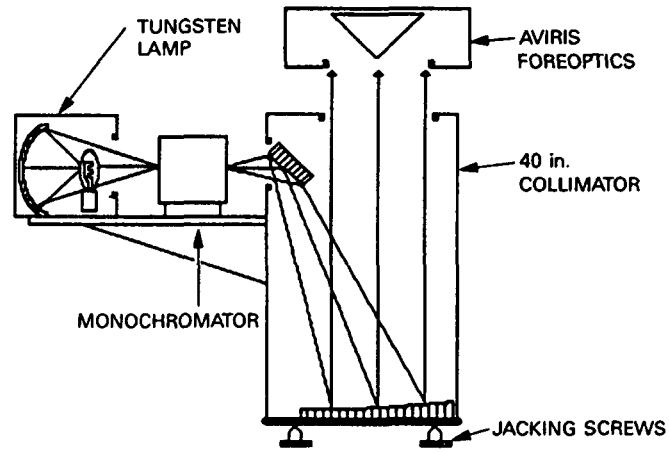


Figure 3. Laboratory setup used in performing the spectral calibration of AVIRIS.[9]

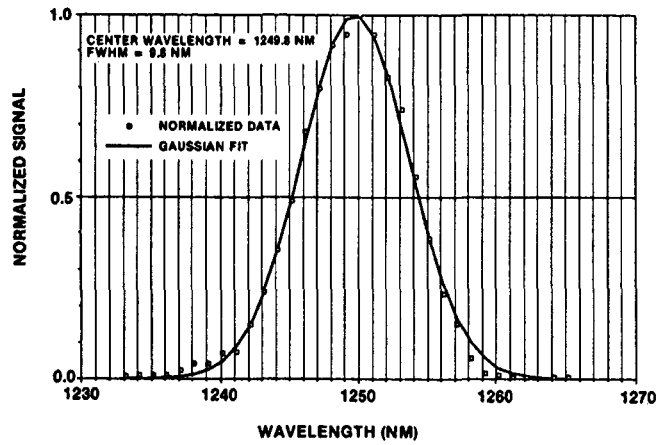


Figure 4. A typical normalized AVIRIS spectral response function for channel 98, Spectrometer C.

Table 1. AVIRIS 1987 Pre-Flight-Season Spectral Calibration[9]

| PARAMETER (IN UNITS OF NM) | SPECTROMETER A | B | C | D |
|---|---|---|---|---|
| AVERAGE BANDWIDTH (FWHM) | 9.7 | 9.7 | 9.0 | 11.6 |
| SPECTRAL SAMPLING INTERVAL | 10.0 | 9.58 | 9.86 | 9.85 |
| STD. DEV. OF LINEARITY MEASUREMENT | 0.71 | 0.60 | 0.58 | 1.84 |
| MONOCHROMATOR CALIBRATION UNCERTAINTY | 0.5 | 0.5 | 0.5 | 1.0 |
| AVIRIS SPECTRAL CALIBRATION ACCURACY | 0.9 | 0.8 | 0.8 | 2.1 |

radiometer against a National Bureau of Standards (NBS) traceable lamp, (2) calibration of an integrating sphere with the calibrated spectroradiometer, (3) acquisition of a file of AVIRIS DNs while viewing the calibrated integrating sphere, and (4) calculation of a table of multipliers tying the AVIRIS DN to the integrating sphere output radiance.

The laboratory setup used in calibrating the spectroradiometer and integrating sphere is shown in Figure 5. An Optronics Laboratories model 746 spectroradiometer is placed on a rotating stage to view alternately a freshly prepared pressed halon target at a 45 degree angle normal to its surface, and a Labsphere, Inc., 40 inch diameter integrating sphere. The halon target is illuminated with a tungsten lamp calibrated as a standard of irradiance by Optronics Laboratories against an NBS-calibrated lamp. The irradiance standard is powered by an Optronics calibrated constant-current power supply. A file of spectral radiance values for the standard lamp-halon target-spectroradiometer configuration in Figure 5 is calculated using the expression

$$L(\lambda) = E(\lambda)\, R(\lambda)\, (50\ \text{cm})^2 / \pi\, (D\ \text{cm})^2 \qquad (1)$$

where $L(\lambda)$ is the radiance viewed by the spectroradiometer, $E(\lambda)$ is the irradiance of the calibrated lamp provided by the manufacturer, $R(\lambda)$ is the reflectance of the halon target,[10] 50 cm is the distance at which the lamp was calibrated, and D is the distance between the lamp and the halon target in the setup in Figure 5. This file is used subsequently to convert spectroradiometer output DN to radiance when calibrating the Labsphere, Inc., integrating sphere.

In an earlier paper[9], there was incorrectly included a cos 45 term in the numerator of the right hand side of the above equation; this term was correct for an earlier calibration setup in which the halon target was 45 degrees to the calibrated lamp and normal to the spectroradiometer. In the configuration shown in Figure 5 and used in calibrating the spectroradiometer for AVIRIS calibrations, the cos 45 term does not apply.

After the spectroradiometer has been calibrated, it is rotated to a position for viewing the 16 inch output port of the integrating sphere. After a 30 minute warmup period, data are acquired from the integrating sphere at several output levels. The intensity of the integrating sphere output is controlled by changing fixed apertures located between the tungsten lamps and the interior of the sphere. The uniformity of output across the 16 inch output port was measured and found to be uniform to within 1% across the port for those aperture settings used in calibrating AVIRIS. Calibration of successive integrating sphere output levels is alternated with repeated calibration of the spectroradiometer. The radiance output of the integrating sphere has been measured to be constant to within 1.1% over a typical calibration period.

To calibrate AVIRIS, the integrating sphere is positioned so that the plane of the output port of the sphere is 12 inches beneath the AVIRIS foreoptics. The same baffles are used in this setup as shown in Figure 5. The U-2 hatch window, a 16-inch-diameter, 1-inch-thick piece of water-free quartz, is positioned above the integrating sphere output port at the same distance from the AVIRIS foreoptics as in the aircraft. Twenty consecutive sets of data are recorded by AVIRIS from two integrating sphere output levels chosen to provide adequate light levels across the full AVIRIS spectral region. Linearity of response of AVIRIS was confirmed by viewing the integrating sphere at 12 output intensities; thus, a single output level in combination with the zero point on the radiance versus DN plot is adequate for constructing the calibration file. In practice, the highest output level (AAAA, in the integrating sphere nomenclature) and the zero point on the radiance/DN curve are used to calibrate the first half of the spectral range of spectrometer A, while a lower output level (EEEE) and the zero point are used for the remainder of the AVIRIS spectral range.

The calibration file used to convert AVIRIS DN values into radiance values is a set of multipliers consisting of 32-bit real numbers generated from the laboratory calibration data. These data consist of two components: radiance measurements of the two integrating sphere intensity levels taken with the spectroradiometer, and data taken with AVIRIS while viewing the integrating sphere at the same two intensity levels. The first step in generating the calibration file is subtraction of the dark current from the AVIRIS data. The next step is to associate the 614 cross-track mean DN values of every spectral band with the corresponding radiance value for that spectral band, computed by resampling the spectroradiometer measurements to match the spectral spacing of the AVIRIS detector elements. The final set of multipliers, M(s,b), is computed as follows:

$$M(s,b) = L(b) / DN(s,b) \qquad (2)$$

where s is the cross-track sample number, b is the spectral band number, L(b) is the radiance of the integrating sphere, and DN(s,b) is the signal level recorded by AVIRIS. This set of 224 x 614 multipliers is saved as the calibration file and used in the radiometric calibration of all subsequent AVIRIS data.

The radiometric calibration of AVIRIS flight data converts 10-bit DN values to 32-bit real-number radiance values in units of $\mu W/cm^2$-nm-sr and linearly scales the values to 16-bit integers. In the process, dark current subtraction, detector equalization, resampling to account for detector readout delays, and, optionally, reconstruction of the full spectrum accounting for spectral band overlap and varying spectral spacings between spectrometers are performed. One dark current value for each detector element is recorded at the end of each scan line. Dark current subtraction is done using a sliding mean of 101 dark current values such that the dark current correction for a given scan line is the mean of the dark current recorded at the end of that scan line and the dark current values recorded at the ends of the 50 scan lines before and after that scan line. The next step is detector response compensation, which corrects for the non-uniformity of responses of the 224 detector elements. Using the multipliers stored in the calibration file, DN values are converted to 32-bit radiance values. Application of the multipliers at this point also removes the cross-track response asymmetry caused by foreoptics vignetting. Resampling to correct for detector readout delays is performed next. These delays occur because the detector elements in the line arrays are read sequentially. This results in the last element of an array acquiring a signal from a spot on the ground approximately one pixel further across the scan than that acquired by the first element. Linear interpolation is performed between successive pixels within a scan line. Following this, the full spectrum is reconstructed. Resampling is performed in the spectral direction to correct for spectral band overlap between spectrometers and to create a spectrum with uniform spacing of spectral band center wavelengths. The first detector element in each spectrometer is bypassed during the interpolation for reasons discussed earlier. (The spectral resampling in this step in radiometric correction processing was performed routinely on all data processed from the first flight season; it is now being offered as an option for the benefit of those investigators wishing un-resampled data.) The spectral resampling step produces 210 spectral bands from 0.4000 to 2.4482 μm with 9.8 nm spectral sampling. Finally, the 32-bit real-number radiance values are converted to 16-bit integers by multiplying each radiance value by a factor of 100 and rounding to the nearest integer value.

The error budget for the AVIRIS pre-flight-season laboratory radiometric calibration is summarized in Table 2. Details of the error analysis are given in Reference 9. Briefly, the integrating sphere calibration accuracy was determined through a propagation-of-errors analysis[11] of measured and estimated uncertainties associated with the calibration of the spectroradiometer and integrating sphere; the thermally induced drift in AVIRIS signal output was measured in the lab through repeated calibrations over time; the vibrationally induced output drifts were determined from the same data; the polarization sensitivity represents the worst case scenario of 100% polarization, which does not occur on the earth's surface, and was measured using visible and infrared polarizing filters; the radiometric effect of uncertainty in the spectral calibration of AVIRIS was calculated using data from Table 1; and spectral and spatial stray light were measured using the calibrated monochromator and collimator as shown in Figure 3. The total AVIRIS radiometric calibration accuracy was calculated by taking the square root of the sum of the squares of the values of all these factors. In the laboratory environment at the start of the flight season, the achieved accuracy of 7.3% exceeded the requirement of 10% absolute radiometry.

## 3. COMPARISON OF CALIBRATION OVER TIME

During the course of the 1987 flight season, assessment of AVIRIS performance in flight was conducted by the AVIRIS project and by several investigators selected and funded by NASA. Results of these investigations are reported in Reference 12. We will summarize here the work done by the AVIRIS project on in-flight performance analysis and the post-flight-season laboratory calibration.

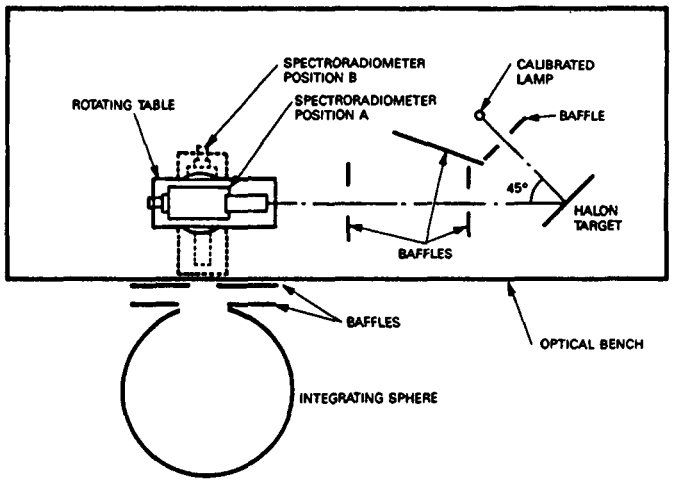


Figure 5. Laboratory setup used in calibrating the AVIRIS spectroradiometer and integrating sphere. All components except the integrating sphere are bolted to an optical bench.[9]

Table 2. AVIRIS 1987 Pre-Flight-Season Radiometric Calibration Error Budget[9]

| PARAMETER | MAGNITUDE (%) |
|---|---|
| INTEGRATING SPHERE CALIBRATION ACCURACY | 3.1 |
| AVIRIS THERMALLY INDUCED OUTPUT DRIFT | 2.4 |
| AVIRIS VIBRATIONALLY INDUCED OUTPUT DRIFT | |
| LOW FREQUENCY | 2.0 |
| HIGH FREQUENCY | 0.7 |
| POLARIZATION SENSITIVITY | 5.0 |
| RADIOMETRIC EFFECT OF SPECTRAL CALIBRATION UNCERTAINTY | 0.5 |
| SPECTRAL STRAY LIGHT | 2.0 |
| SPATIAL STRAY LIGHT | 2.0 |
| AVIRIS RADIOMETRIC CALIBRATION ACCURACY | 7.3 |

### 3.1. Spectral performance over the first flight season

In-flight assessment of the spectral calibration using data acquired at the start of flight operations in June, 1987, confirmed the laboratory calibration summarized above. An example of a full AVIRIS spectrum is shown in Figure 6, which is an average of a 10 by 10 pixel area in the center of Stonewall Playa, Nevada, near the Cuprite Mining District. The playa is a large, uniform surface with only minor spectral structure due to the presence of small amounts of clay, water and $Fe^{+3}$. The spectral features are thus primarily those of the sun and the atmosphere. The locations and apparent widths of the major atmospheric absorption features were used to assess AVIRIS spectral performance. The spectral wavelength positions of the features were determined using the JPL-developed analysis software SPAM (Spectral Analysis Manager).[13] The first wavelength number is from the AVIRIS data as determined using SPAM; in parentheses are the LOWTRAN 6[14] positions for the features and the atmospheric constituent(s) responsible for the absorption. The figure shows that the AVIRIS and LOWTRAN 6 wavelength positions agree to within 5 nm or better. The widths of the atmospheric absorption features are approximately those that would be expected for an atmospheric spectrum sampled at a 10 nm spectral bandwidth (see following discussion and figures). Thus the in-flight spectral performance of AVIRIS in this early data set agrees well with the laboratory performance.

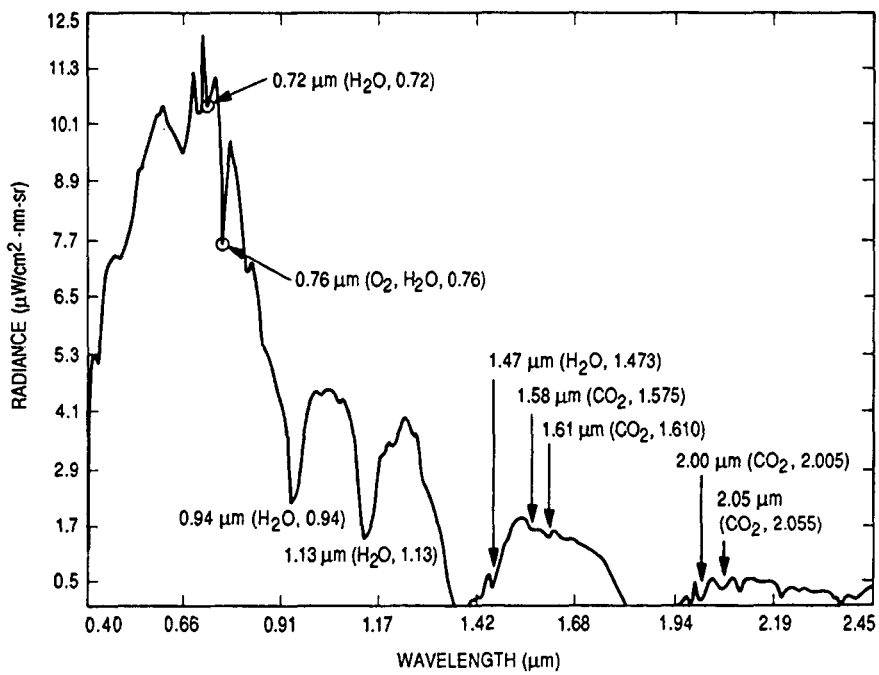


Figure 6. Full spectrum of a 5 by 5 pixel area in the center of Stonewall Playa, Nevada. The data have been radiometrically corrected. The wavelength positions of several atmospheric absorption features are indicated. The first number is the wavelength position derived from the AVIRIS data. In parentheses are the wavelength position of that feature from LOWTRAN 6, and the atmospheric constituent(s) responsible for it (adapted from Reference 26).

During the flight season, the optical fibers carrying the signal from the foreoptics became detached at Spectrometers A and B. A post-flight-season inspection showed that insufficient epoxy had penetrated into the ends of the hypodermic needles holding the fibers at the focus of the spectrometers; mechanical stress from repeated cooling and warming of the instrument during flight operations probably caused the fibers to pull loose and move out of focus. The effects of the defocus are shown in Figure 7, comparing the spectral response functions for each spectrometer measured in the pre- and post-flight-season laboratory calibrations. The FWHM in the post-flight-season calibration for Spectrometers A and B are greater than those of the pre-flight-season calibration, while those of Spectrometers C and D remained unchanged. Their fibers did not detach. Also, the wavelength position of maximum response has shifted by more than 1 nm, which is the measurement threshold in the laboratory, in 3 of the spectrometers. The detached fibers in spectrometers A and B probably explain the wavelength shift in those spectrometers, while warpage of Spectrometer D induced by distortion of the instrument rack probably explains the change in wavelength position of that spectrometer. Table 3 summarizes the laboratory pre- and post-flight-season calibration results for spectral bandwidth and wavelength position.

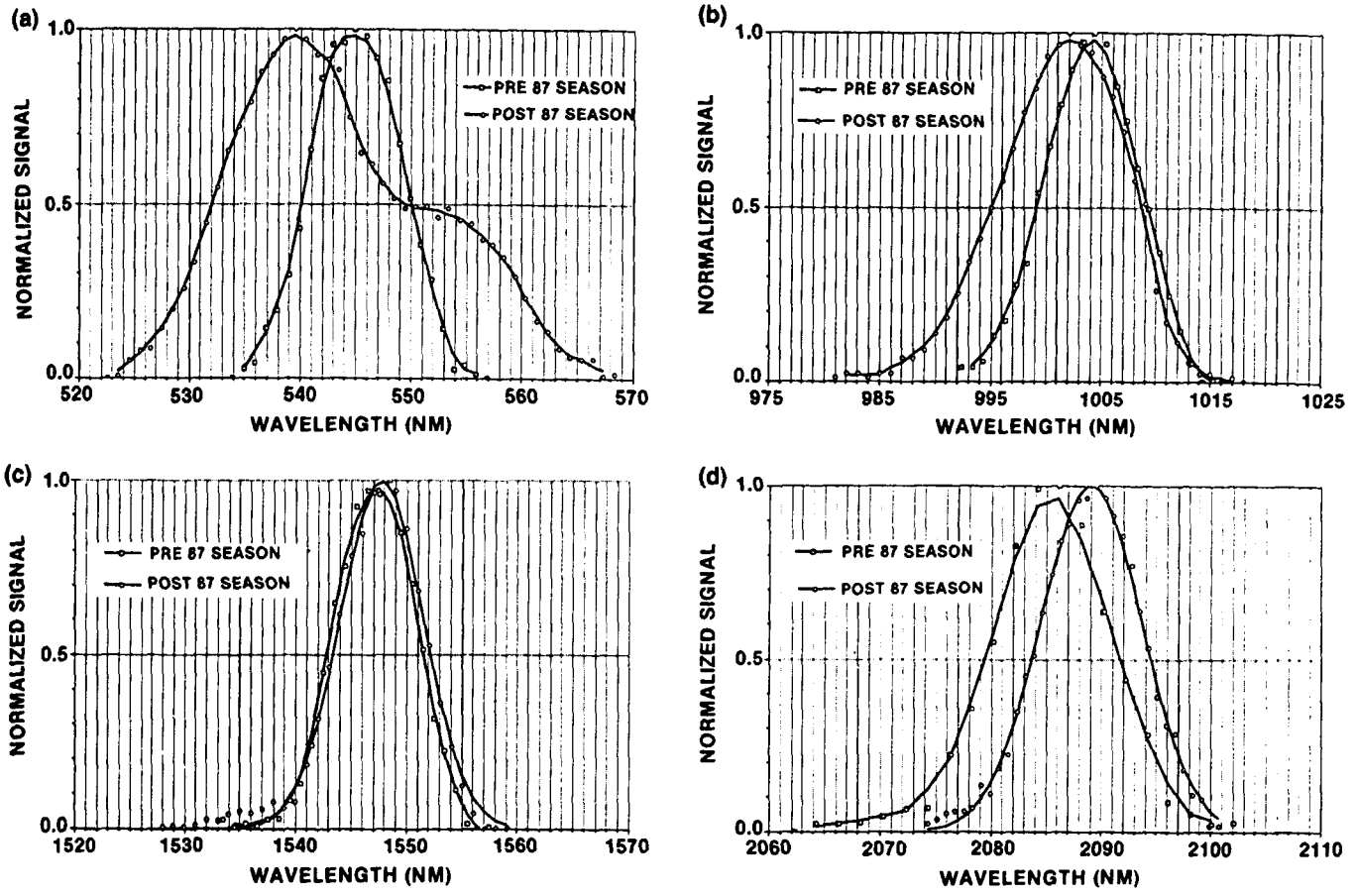


Figure 7. Normalized spectral response functions measured from 4 channels, one from each of the 4 AVIRIS spectrometers, in the 1987 pre- and post-flight-season laboratory calibrations. (a) Spectrometer A, channel 16, (b) Spectrometer B, channel 67, (c) Spectrometer C, channel 128, and (d) Spectrometer D, channel 187.

Table 3. AVIRIS 1987 Pre- and Post-Flight-Season Spectral Response Characteristics

| SPECTROMETER (CHANNEL) | FWHM (nm) | | λ OF MAXIMUM RESPONSE (nm) | |
|---|---|---|---|---|
| | PRE-SEASON | POST-SEASON | PRE-SEASON | POST-SEASON |
| A (16) | 10 | >17 | 545 | 539 |
| B (67) | 10 | 14 | 1004 | 1002 |
| C (128) | 9 | 9 | 1547 | 1548 |
| D (187) | 11 | 11 | 2086 | 2089 |

A quantitative assessment of the in-flight spectral FWHM and wavelength positions from later in the flight season is shown in Figure 8, comparing atmospheric spectra acquired with Spectrometers B, C and D over Ivanpah Playa, California, on July 30, 1987, with LOWTRAN 6 spectra at full resolution ($\Delta\lambda < 1$ nm) and resampled at the indicated bandwidths. Resampling was done using a Gaussian function with the indicated half-maximum spectral bandwidths. The figure shows that by July 30, 1987, Spectrometer B had become defocussed. A shift in spectral alignment of as much as 10 nm is also suggested. Spectrometers C and D show performance equivalent to that expected for the bandwidths measured in the lab. The spectral alignment of Spectrometer C agrees well with the laboratory calibration

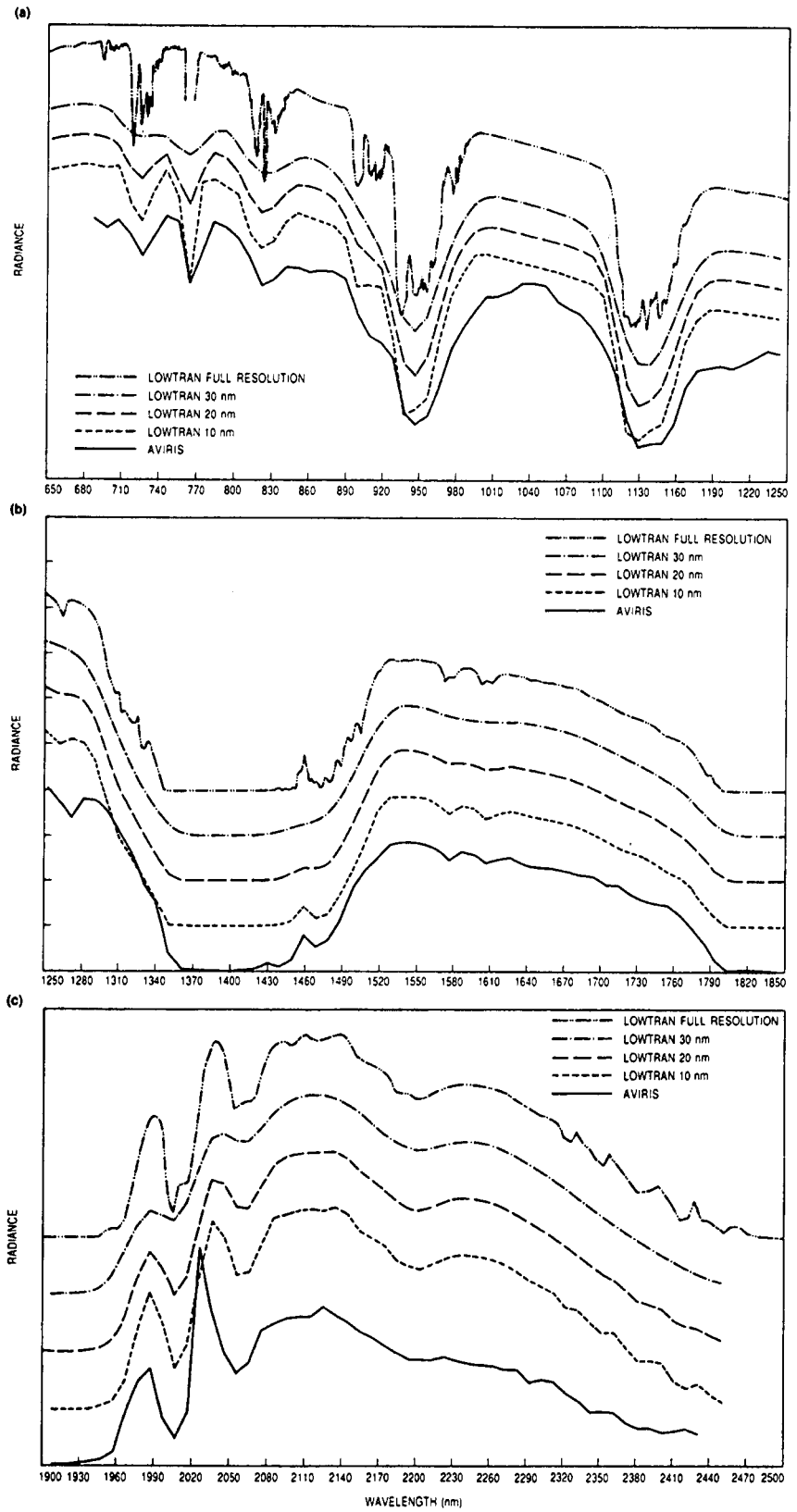


Figure 8. Comparision of AVIRIS atmospheric spectral features over Ivanpah Playa, CA, with LOWTRAN 6 at full resolution, and LOWTRAN 6 resampled at 10, 20, and 30 nm spectral bandwidths. The curves are offset to facilitate comparison between them. (a) Spectrometer B, (b) Spectrometer C, and (c) Spectrometer C.

in these data, while a shift in wavelength of as much as 5 nm in Spectrometer D is suggested. Although the bandwidths and wavelength positions derived from comparison of in-flight data with the LOWTRAN 6 model do not agree precisely with either the pre- or post-flight-season laboratory spectral calibrations, it should be remembered that (1) the instrument response was changing during the flight season, and (2) derivation of spectral performance from assessment of atmospheric absorption features is not as precise as laboratory determinations.

In-flight assessment of the bandwidth and spectral alignment of Spectrometer A is difficult because of the lack of sharp atmospheric absorption features over its region of spectral coverage. An experiment is planned for 1988 using mineral absorption features in this spectral region associated with the carbonatite mine located at Mtn. Pass, California. The Mtn. Pass carbonatite is rich in rare earth elements such as neodydium that contribute several sharp absorption features to the visible portion of its reflectance spectrum.

### 3.2. Radiometric performance over the first flight season

Detachment of the optical fibers at Spectrometers A and B affected radiometric performance by causing a loss of signal at the detectors. Several other instrument factors also degraded the absolute radiometry of AVIRIS. The thermally-induced warpage to the spectrometer bodies was discussed earlier and found to cause instability in output signal levels of from 2.4% to 7.7% in the laboratory environment.[9] In the much colder aircraft environment, larger instabilities were noted but cannot be quantified due to instabilities in the onboard calibrator in the flight environment. Further, the instrument rack to which the spectrometers are mounted was deformed during the flight season, causing a distortion in the spectrometer bodies that resulted in a loss of optical alignment. This caused an additional loss of signal. Finally, in the post-flight season inspection of AVIRIS, it was discovered that the thermal blocking filter in Spectrometer B had broken during the flight season.

Spectrometer B, which covers the 0.68 to 1.28 μm spectral region, is equipped with two filters[4], a bandpass filter with short- and long-wavelength cutoffs of approximately 0.6 and 2.7 μm, respectively, and a thermal-blocking filter which is opaque to energy beyond 2.0 μm. This dual filter approach was chosen for Spectrometer B because it was not possible to manufacture a bandpass filter with cutoff wavelengths to match its spectral range. Such filters were obtainable for the other 3 spectrometers; hence they each employ a single filter. The short-wavelength cutoff of the bandpass filter assures that no higher order diffracted electromagnetic radiation will be present over the spectral region of interest, while the long-wavelength cutoff of the filter blocks the thermal radiation to which AVIRIS is sensitive. The filters are mounted directly over the detectors on the dewar cold fingers to assure that they are at 77 K to block the thermal background radiation and to minimize their own thermal emissions. The chief source of thermal background radiation in AVIRIS is the spectrometer body itself, which subtends a large portion of the total field of view of the detectors. The spectrometer bodies are thermally controlled to about 300 K and radiate very little energy short of 2.7 μm. Moreover, at a given temperature, the same thermal energy falls on the detector whether it is in the image or dark current readout mode. Hence, subtraction of the detector dark current value which is recorded at the end of each AVIRIS scan will correct for the small thermal background contribution to the signal. However, if the spectrometer body temperature varies between the time of the detector dark current and image acquisition, dark current subtraction does not adequately compensate for the thermal background contribution to the image signal. The original thermal control system for the AVIRIS spectrometers was designed to maintain their temperatures between 296 and 300 K. Our calculations show that a 4 K change in the spectrometer body temperature between the times of the detector readout of the image and dark current, an improbably large change over 1/12 of a second for the massive spectrometer body, would cause an added uncertainty in instrument radiometry of about 2%, if wavelengths as great as 2.7 μm were allowed to fall on the AVIRIS detectors. It was decided to employ an additional blocking filter in spectrometer B to minimize the thermal contributions short of 2.7 μm. A filter cut from a crystal of $KH_2PO_4$ (KDP) was recommended because of its high transmission over the operating region of spectrometer B and its cutoff wavelength of 2.0 μm. However, it has been subsequently learned that KDP undergoes a solid-state phase transition at about 130 K,[15] and the mechanical stress which results from using it at 77 K in the AVIRIS dewar was the cause of the filter breakage. Some of the cracks in the filter were over the detector array, allowing additional light to fall on the detectors. We also observed during subsequent failure testing of a KDP filter that the phase transition caused a noticeable variation in the transmission properties across the filter which varied each of several times the filter was thermally cycled. After the filter cracked, each piece varied in transmission and each piece came to a different state with each successive thermal cycle. We conclude that KDP is not a suitable filter material for use at temperatures below 130 K. We discuss the solution for Spectrometer B in the next section of the paper.

The changes in AVIRIS radiometry resulting from all these effects are shown in Figure 9, where the percentage change between pre- and post-flight-season radiometric calibration multipliers are shown. The multipliers convert DN to radiance through the relation given in Equation 2. If the instrument response were the same at the time of both calibrations, the percent change between the two sets of multipliers would be 0. This is indeed the case for Spectrometer C (spectral channels 97 through 160), which alone of the 4 spectrometers appears not to have suffered degradation during the flight season. For Spectrometer A (channels 1 through 32), the post-flight-season calibration multipliers are from 90% to 180% greater than the pre-flight-season multipliers, indicating a correspondingly lower signal output from the spectrometer for the same radiance input. The Spectrometer B multipliers (channels 33 through 96) are larger for the second calibration by about 100% to 120%, but in addition, there is variation in the percent change in the multipliers across the spectral region of Spectrometer B. This is almost certainly due to solid phase transition-induced variations in transmission and light leakage through the broken KDP filter. Spectrometer D multipliers (channels 161 through 224) are about 20% higher uniformly across its entire spectral region, except for spikes at channels 170, 181, and 210, which are noisy detectors. Although the optical fiber did not detach in this spectrometer, its base was warped by distortion of the instrument rack to which it is mounted, shifting part of the signal off the detectors. A slight shift in wavelength calibration was noted earlier.

On September 14, 1987, a field radiometric calibration experiment was performed at Rogers Dry Lake, California, to assess the validity of the laboratory calibration of AVIRIS.[16] Extinction measurements of the atmosphere were taken by observing the sun from the test site at 5 to 15 minute intervals from sunrise until solar noon, the time of the AVIRIS overflight, using solar radiometers. Total precipitable atmospheric water was measured with a spectral hygrometer. The ratio of direct to diffuse radiation incident at the surface was determined using a hand-held ratioing radiometer (HHRR).[17] On the surface of the dry lake bed, reflectance measurements were made simultaneously with the overflight using the JPL Portable Instantaneous Display and Analysis Spectrometer (PIDAS),[18] and the University of Arizona Barnes Modular Multispectral 8-channel Radiometer (MMR)[19] and Exotech Model 100-AX radiometer.[20] Five different atmospheric

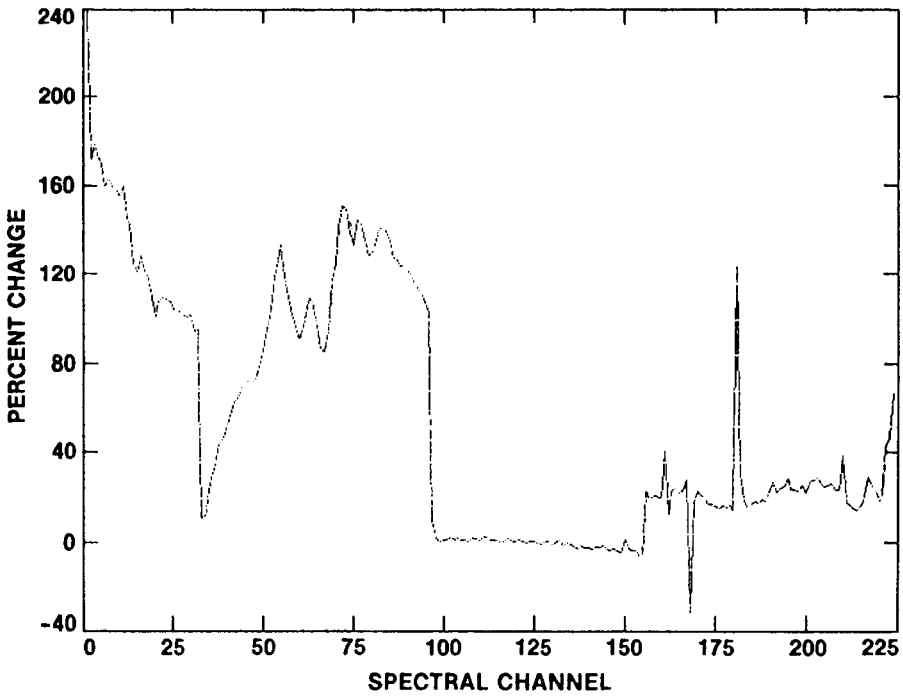


Figure 9. Percent change in the AVIRIS radiometric calibration multipliers, pre- and post-flight-season. Percent change = $(M_{post} - M_{pre})/M_{pre} \times 100$.

models, LOWTRAN 6,[14] LOWTRAN 7,[21] Herman-Browning,[22] Diner-Martonchik,[23] and the 5S code of Tanre et al.[24], were employed. The latter four account for multiple scattering. The measured surface reflectance and atmospheric optical depth were used to particularize the models for flight conditions, and the radiance from the dry lake bed at the instrument was calculated. Good agreement over most of the wavelength region of AVIRIS was found between the 5 models. Figure 10 shows the comparison between the Herman-Browning, Diner-Martonchik, and LOWTRAN 7 generated results, and the AVIRIS-predicted radiance for both the pre- and the post-

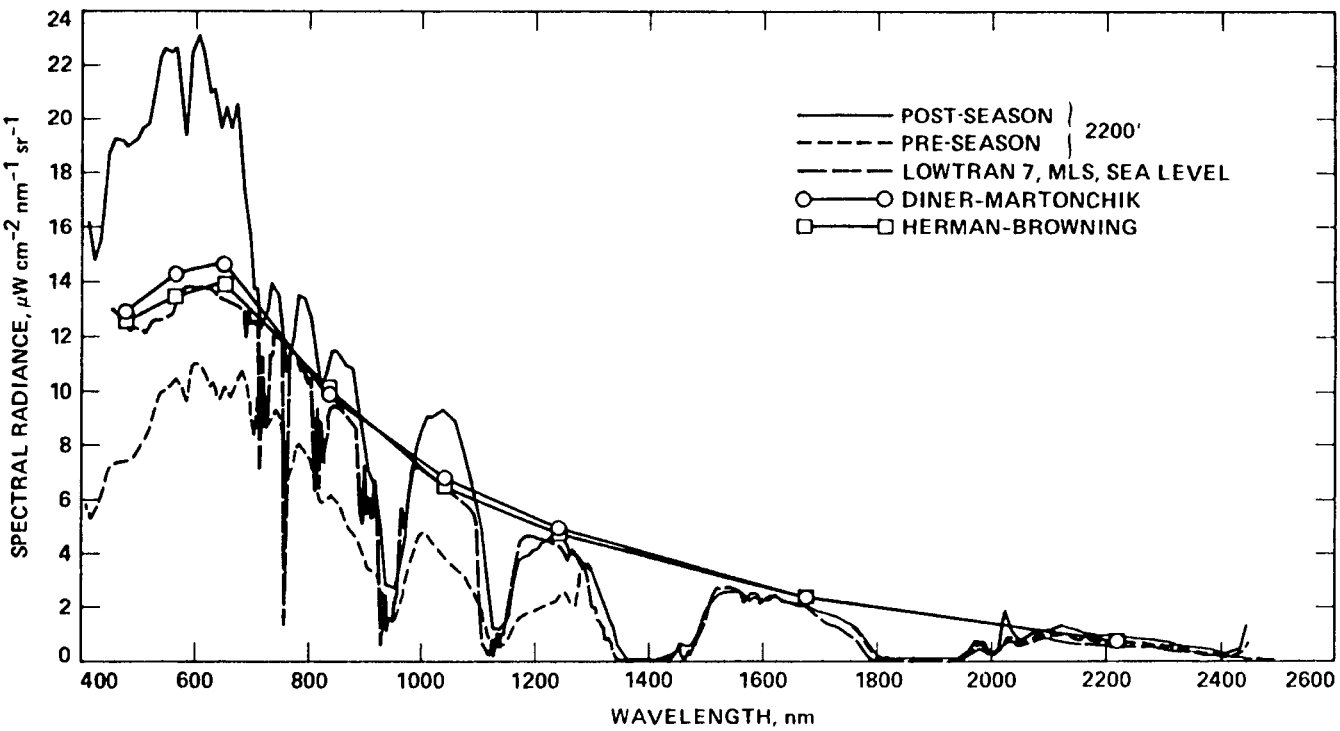


Figure 10. Comparison of three code-generated sets of radiance for Rogers Dry Lake, CA, with the AVIRIS-generated radiance using the pre- and post-flight-season radiometric calibration multipliers.[16]

flight-season calibration multipliers. There is very good agreement between the code-generated and AVIRIS-predicted values over the range of Spectrometer C for both the pre- and post-flight-season calibrations. The discrepancies over the other spectral regions of AVIRIS indicate that instrument response at the time of the overflight was not adequately characterized by either the pre- or post-flight-season calibrations, a reflection of the dynamic nature of instrument performance during the flight season. For a thorough discussion of the field calibration experiment and the results obtained, see Conel et al.[16]

The conclusions from this work are: (1) The validity of the laboratory calibration methodology appears to be confirmed through the agreement achieved over the wavelength range of Spectrometer C between the atmospheric model-generated and the AVIRIS-generated radiance values, but (2) the dynamic nature of the response of the other 3 spectrometers over the course of the 1987 flight season renders the AVIRIS-generated radiance values accurate to no better than 25% to 65% over those spectral regions, depending on the spectrometer and the flight date.

## 4. IMPROVEMENTS TO AVIRIS AFTER THE FIRST FLIGHT SEASON

All of the known factors that adversely affected AVIRIS spectral and radiometric performance during the first flight season have been resolved as a result of engineering upgrades to the instrument over the past several months. The thermal instability of the spectrometers has been resolved by replacing the thermal control system with a much more sophisticated approach.[25] The system used during the first flight season employed three heater strips on each spectrometer barrel that were commanded to turn on when the spectrometer barrel reached about 296 K and to turn off when the temperature reached 300 K. The new system consists of 24 small heater strips placed evenly over the entire spectrometer body, including the grating and collimator mirror housings and the dewar nose piece. The heaters are on constantly when the temperatures of the spectrometers are at or less than 300 K (room temperature in the calibration laboratory is kept at about 293 K to assure that the heaters are on during spectrometer alignment and focus and during instrument calibration). The output level of the heaters is controlled by a new circuit designed to keep the spectrometer bodies isothermal and at about 300 K plus or minus 0.1 K. The stabilized temperature varies among spectrometers but all are controlled at that temperature to within 0.1 K. Each spectrometer was tested in a cold chamber where it was thermally cycled from room temperature (293 K) to flight temperature (273 K) and back to room temperature. Spectrometer body temperatures were monitored at several places on the structure and a constant optical signal was put into the detectors. Detector output was found to be constant to within 2% over the entire thermal cycle and the spectrometer bodies were found to be isothermal and stable to within the desired tolerance.

To alleviate the effects on the spectrometers of warpage of the instrument rack, the spectrometers have been mounted kinematically on vibration isolators. Spectrometers A, B, and C are on three-point mounts, while Spectrometer D is on a four-point mount because of mechanical packaging constraints. It is expected that this new mounting approach will also provide additional isolation from the instrument and aircraft vibrational environment, and will greatly reduce the heat flow from the spectrometer bodies to the instrument rack, which will aid the effort to keep their temperatures stable.

The tight control on the spectrometer body temperatures achieved with the new heater and controller configuration has made it possible to remove the thermal blocking filter (i.e., the KDP filter) from Spectrometer B. Analysis has shown that if the temperature of the spectrometer body were to vary by as much as 0.1 K between the times of dark current and image acquisition, which is the worst case, the resulting degradation in radiometric precision would be less than 0.1%. Thus the bandpass filter provides adequate blockage of thermal background.

The optical fiber detachment problem has been resolved by using a new epoxy which is less viscous, allowing thorough capillary penetration into the fiber holder. It also has greater holding strength than the epoxy previously used. To verify the improved capillary penetration of the new epoxy, several test fibers were cemented into stainless steel hypodermic needles identical to those used in the AVIRIS spectrometers. After the epoxy had cured, the needles were sectioned in increments of 1 mm. It was found on all the test fibers that the epoxy had penetrated to about 6 mm, which is the desired distance. A new flight fiber package and backup for the foreoptics and the onboard calibrator were made using the new epoxy.

Confirmation of the effectiveness of these changes to the flight hardware is still required. Pre- and post-flight-season laboratory calibrations will be performed on AVIRIS in September and November, 1988, and field radiometric calibration experiments will be conducted in conjunction with the laboratory calibrations. In-flight performance of AVIRIS will also be continuously monitored during the 1988 flight season. Results of our studies of these data will form the basis of a future report on AVIRIS in-flight performance.

## 5. ACKNOWLEDGEMENTS

The work described in this paper was carried out at the Jet Propulsion Laboratory, California Institute of Technology, under a contract with the National Aeronautics and Space Administration.

## 6. REFERENCES

1. Vane, G., M. Chrisp, H. Enmark, S. Macenka and J. Solomon, "Airborne Visible/Infrared Imaging Spectrometer: an advanced tool for earth remote sensing," *Proc. 1984 IEEE Int'l. Geoscience and Remote Sensing Symposium*, ESA SP215, 751-757 (1984).

2. Chrisp, M.P., T. Chrien and L. Steimle, "Airborne Visible/Infrared Imaging Spectrometer (AVIRIS) foreoptics, fiber optics and onboard calibrator," *Proc. SPIE Conference on Imaging Spectroscopy II* (San Diego, CA, 20-21 August, 1987), 834, 44-49 (1987).

3. Porter, W.M., and H.T. Enmark, "System overview of the Airborne Visible/Infrared Imaging Spectrometer (AVIRIS)," *Proc. SPIE Conference on Imaging Spectroscopy II* (San Diego, CA, 20-21 August, 1987), 834, 22-31 (1987).

4. Macenka, S.A., and M.P. Chrisp, "Airborne Visible/Infrared Imaging Spectrometer (AVIRIS) spectrometer design and performance," *Proc. SPIE Conference on Imaging Spectroscopy II* (San Diego, CA, 20-21 August, 1987), 834, 32-43 (1987).

5. Bailey, G.C., "Visible and infrared linear detector arrays for the Airborne Visible/Infrared Imaging Spectrometer (AVIRIS)," *Proc. SPIE Conference on Imaging Spectroscopy II* (San Diego, CA, 20-21 August, 1987), 834, 50-54 (1987).

6. Miller, D.C., "Airborne Visible/Infrared Imaging Spectrometer (AVIRIS) scan drive design and performance," *Proc. SPIE Conference on Imaging Spectroscopy II* (San Diego, CA, 20-21 August, 1987), 834, 55-62 (1987).

7. Bunn, J.S., Jr., "Signal chain for the Airborne Visible/Infrared Imaging Spectrometer (AVIRIS)," *Proc. SPIE Conference on Imaging Spectroscopy II* (San Diego, CA, 20-21 August, 1987), 834, 63-68 (1987).

8. Steinkraus, R.E., and R.W. Hickok, "Airborne Visible/Infrared Imaging Spectrometer (AVIRIS) on-board data handling and control," *Proc. SPIE Conference on Imaging Spectroscopy II* (San Diego, CA, 20-21 August, 1987), 834, 69-78 (1987).

9. Vane, G., T.G. Chrien, E.A. Miller and J.H. Reimer, "Spectral and radiometric calibration of the Airborne Visible/Infrared Imaging Spectrometer (AVIRIS)," *Proc. SPIE Conference on Imaging Spectroscopy II* (San Diego, CA, 20-21 August, 1987), 834, 91-106 (1987).

10. Weidner, V.R., and J.J. Hsia, "Reflection properties of pressed polytetrafluoroethylene powder," *J. Opt. Soc. Am.*, 71(7), 856-861 (1981).

11. Bevington, P.R., *Data Reduction and Error Analysis for the Physical Sciences,* McGraw Hill, New York, 336 pp. (1969).

12. Vane, G. (ed.), *Proceedings of the Airborne Visible/Infrared maging Spectrometer (AVIRIS) Performance Evaluation Workshop, JPL Publication,* Jet Propulsion Laboratory, Pasadena, CA, in preparation (1988).

13. Mazer, A.S., M. Martin, M. Lee and J.E. Solomon, "Image processing software for imaging spectrometry data analysis," *Remote Sensing of Environment,* 24(1), 201-210 (1988).

14. Kneizys, F.X., E.P. Shettle, W.O. Gallery, J.H. Chetwynd, Jr., L.W. Abrew, J.E.A. Shelby, S.A. Clough and R.W. Fenn, "Atmospheric transmittance/radiance: Computer code LOWTRAN 6," AFGL-TR-83-0187, AFGL Hanscom AFB, MA, 200 pp. (1983).

15. Cook, W.R., Jr., "Thermal expansion of crystals with $KH_2PO_4$ structure," *J. Applied Physics,* 38(4), 1637-1642 (1967).

16. Conel, J.E., R.O. Green, R.E. Alley, C.J. Bruegge, V. Carrere, J.S. Margolis, G. Vane, T.G. Chrien, P.N. Slater, S.F. Biggar, P.M. Teillet, R.D. Jackson and M.S. Moran, "In-flight radiometric calibration of the Airborne Visible/Infrared Imaging Spectrometer (AVIRIS)," *Proc. SPIE Conference on Recent Advances in Sensors, Radiometry and Data Processing for Remote Sensing,* (Orlando, FL, 4-8 April, 1988), 924, in press (1988).

17. Whitney, G., M. Abrams and A.F.H. Goetz, "Mineral discrimination using a portable ratio-determining radiometer," *Econ. Geol.,* 78(4), 688-698 (1983).

18. Goetz, A.F.H., "The Portable Instant Display and Analysis Spectrometer (PIDAS)," in *Proc. of the Third Airborne Imaging Spectrometer Data Analysis Workshop* (G. Vane, *ed.*), *JPL Publication 87-30,* Jet Propulsion Laboratory, Pasadena, CA, 8-17 (1987).

19. Robinson, B.F., M.E. Bauer, D.P. Dewitt, L.F. Silva and V.C. Vanderbilt, "Multiband radiometer for field research," *Proc. of the SPIE,* 196, 8-15 (1979).

20. Slater, P.N., S.F. Biggar, R.G. Holm, R.D. Jackson, Y. Mao, M.S. Moran, J.M. Palmer and B. Yuan, "Reflectance- and radiance-based methods for the in-flight absolute calibration of multispectral sensors," *Remote Sensing of Environment,* 22, 11-37 (1987).

21. Kneizys, F.X., E.P. Shettle, G.P. Anderson, L.W. Abrew, J.H. Chetwynd, J.E.A. Shelby, S.A. Clough and W.O. Gallery, "Atmospheric transmittance/radiance: Computer code LOWTRAN 7," in press (1988).

22. Herman, B.M., and S.R. Browning, "The effect of aerosols on the earth-atmosphere albedo," *J. Atmos. Sci.*, 32, 1430-1445 (1975).

23. Diner, D.J., and J.V. Martonchik, "Atmospheric transfer of radiation above an inhomogeneous non-Lambertian reflective ground: I. Theory," *J. Quant. Spectros. Radiat.Transfer.*, 31, 97-125 (1984).

24. Tanre, D., C. Deroo, P. Duhaut, M. Herman, J.J. Morcrette, J. Perbos and P.Y. Dischamps, "Effets atmospheriques en tele-detection-logical de simulation du signal satellitaire dans le spectra solaire," *Proc. Third Int'l. Colloq. on Spectral Signatures of Objects in Remote Sensing,* ESA SP247, 315-319 (1985).

25. Porter, W.M., T.G. Chrien and G. Vane, "Improvements in the Airborne Visible/Infrared Imaging Spectrometer (AVIRIS) since the first flight season," in preparation (1988).

26. Vane, G., "First results from the Airborne Visible/Infrared Imaging Spectrometer (AVIRIS), *Proc. SPIE Conference on Imaging Spectroscopy II* (San Diego, CA, 20-21 August, 1987), 834, 166-174 (1987).

# IN-FLIGHT RADIOMETRIC CALIBRATION OF THE AIRBORNE VISIBLE/INFRARED IMAGING SPECTROMETER (AVIRIS)

James. E. Conel, Robert O. Green, Ronald E. Alley, Carol J. Bruegge, Veronique Carrere, Jack S. Margolis, Gregg Vane, and Thomas G. Chrien
Jet Propulsion Laboratory, California Institute of Technology, Pasadena, California 91109

Philip N. Slater, Stuart F. Biggar, and Phil M. Teillet
University of Arizona, Tucson, Arizona 85721

Ray D. Jackson and M. Susan Moran
United States Department of Agriculture, Phoenix, Arizona 85040

## ABSTRACT

A reflectance-based method was used to provide an analysis of the in-flight radiometric performance of AVIRIS. Field spectral reflectance measurements of the surface and extinction measurements of the atmosphere using solar radiation were used as input to atmospheric radiative transfer calculations. Five separate codes were used in the analysis. Four include multiple scattering, and the computed radiances from these for flight conditions were in good agreement. Code-generated radiances were compared with AVIRIS-predicted radiances based on two laboratory calibrations (pre- and post-season of flight) for a uniform highly reflecting natural dry lake target. For one spectrometer (C), the pre- and post-season calibration factors were found to give identical results, and to be in agreement with the atmospheric models that include multiple scattering. This positive result validates the field and laboratory calibration technique. Results for the other spectrometers (A, B and D) were widely at variance with the models no matter which calibration factors were used. Potential causes of these discrepancies are discussed.

## 1. INTRODUCTION

We present here an updated analysis of the in-flight radiometric performance of the Airborne Visible/Infrared Imaging Spectrometer (AVIRIS)[1,2]. AVIRIS is a scanning imager (400 - 2450 nm) that employs four spectrometers connected to common foreoptics by optical fibers. The spectrometers employ linear detector arrays and are labeled A (400-710 nm with 32 detectors), B (680-1280 nm, 64 detectors), C (1240-1860 nm, 64 detectors), and D (1830-2450 nm, 64 detectors). A test flight was carried out in mid-September 1987, over a field site at Rogers Dry Lake, California (Edwards Air Force Base) with the following objectives: (1) develop radiometric and spectral calibrations for the instrument; (2) determine in-flight signal/noise characteristics; (3) compare various methods of reducing the data to ground reflectance. To support these studies, the following field measurements were made simultaneously with the overflight: (1) atmospheric optical depth using solar radiometers; (2) total precipitable water (in cm) with a spectral hygrometer; (3)

the ratio of direct to diffuse radiation incident at the surface using a hand-held ratioing radiometer (HHRR[3]). Spectral reflectance factor measurements were made of the bright playa surface using the Portable Instantaneous Display and Analysis Spectrometer (PIDAS[4]), a Barnes Modular Multispectral 8-Channel Radiometer (MMR[5,6]) and an Exotech Model 100-AX radiometer[6].

To meet the first objective we used a surface reflectance-based method[6] and compared the solar radiance at the instrument reflected from the playa target as determined from a laboratory calibration of AVIRIS[7], with the radiance predicted from that target according to an atmospheric model. Previously we used the LOWTRAN 6 code[8] for these comparisons, recognizing by so doing that we could only account for a single order of scattering in the predicted radiance. In the present work, we employed the LOWTRAN 7 code[9], which provides a description of multiple scattering (with Rayleigh and aerosol contributions) together with gaseous absorption, we also used multiple scattering codes developed by Herman and Browning[10], and Diner and Martonchik[11]. The latter two codes also account for multiple scattering and absorption effects, but rely on user inputs to quantify these at each wavelength. No spectral gaseous absorption databases are included within the codes themselves.

In addition to incorporation of improved scattering codes in the analysis, we compared the results of pre- and post-flight season laboratory calibrations of the instrument using the Rogers Lake data. Apart from sound procedure, the relevance of this comparison stems from the post-1987 flight season discovery[7] of the detachment of optical fibers connecting the foreoptics to spectrometers A and B. The point in time of this occurrence during flight operations during the summer of 1987 is not known. But these comparisons, together with a reanalysis of the laboratory radiometric calibration procedure itself, has helped to sort out explanations for the substantially reduced radiometric performance of AVIRIS previously reported[7].

We also present comparisons of independent atmospheric optical depth and surface reflectance measurements by the Jet Propulsion Laboratory (JPL), University of Arizona (UA), and United States Department of Agriculture (USDA) groups. The field data obtained agree closely and serve to reduce or eliminate the possibility that discrepancies between the AVIRIS calibrations were due to errors in the field measurements.

## 2. TEST SITE AND FIELD MEASUREMENTS

### 2.1 Site, flight and image data

Rogers Dry Lake (Lat. 34° 55′N; Long. 117° 50′W) is a playa located 104 km north of Los Angeles, California, at an elevation of 692 m above sea level. The surface consists of silty mudstone which, from X-ray diffraction analysis, contains quartz, plagioclase feldspar, kaolinite, (abundant) analcime, and calcite. The visible and infrared reflectance is however dominated by the presence of hydrated iron oxides that are not detectible in the X-ray diffraction data. During the summer and fall months, the playa is dry and the surface is patterned with narrow dessication cracks. Intermittent streams have dissected the eastern half exposing a series of varicolored brown and tan strata beneath the surface layer. Such erosion has lead to broad patchiness in the exposed surface. Nevertheless, large areas of relatively uniform surface properties remain; these constitute the standard targets employed in our studies.

AVIRIS overflew the test site on September 14, 1987, around 10:20 AM Pacific Standard Time (18:20 hr UT) at an altitude of 20 km above terrain. AVIRIS has a one-milliradian instantaneous field-of-view and a 30-degree scan angle[1], which determines a 20 m pixel size and 10.5 km swath width of the ground. The test flight took place under cloud-free, but hazy atmosphere conditions. The calculated visibility was 26 km.

The image data contain periodic noise, and at least three spatially distinct patterns are present. The most prominent of these has a period of about 10.3 lines per cycle (0.097 $line^{-1}$) normal to the banding which trends at an angle of about 18° to the scan direction. A second band set has a period 12.8 lines per cycle (0.78 $line^{-1}$) at an angle of about 65 degrees; the third periodic variation is manifested within the second set with a period of one line per cycle (1 $line^{-1}$) along the flight direction. A complete analysis of the noise characteristics of the data will be presented elsewhere.

## 2.2 Spectral reflectance measurements

Coincident with the time of aircraft overflight, we measured the spectral reflectance of the playa target with PIDAS and with the broadband MMR and Exotech filter radiometers. PIDAS covers the spectral range 425-2500 nm with sampling intervals of 0.88 nm between 450 and 900 nm, and 4.7 nm between 900 and 2500 nm. The MMR has filters matched to Thematic Mapper (TM) band widths with central wavelengths of 486, 571, 661, 838, 1677, 2223 nm, and an additional band centered at 1254 nm.

The field sampling strategy employed by the UA and USDA groups has been described in detail by Slater *et al.*[6] A rectangle – 4 × 16 pixels in size (20 m per pixel) – was marked on the surface, its length being parallel to the flight line. Cross patterns of 16 measurements were made within each pixel, and averages and the scatter in each were computed individually and for the total 1024 measurements. The field reference was a $BaSO_4$ panel. These reflectance factor measurements were traceable to the National Bureau of Standards diffuse reflectance standard by calibration with respect to a pressed halon surface[12]. With PIDAS, four measurements were made at the center of each pixel and combined to secure an average from 256 measurements. In practice, about 50 measurements were lost, and the averages were computed from 200 spectra. The field reflectance standard was a portable pressed halon surface prepared to NBS specifications.

Figure 1 shows that there is good agreement between the determinations of the spectral reflectance of the playa target measured by PIDAS and by the MMR. The PIDAS reflectance data depict mean values ±1 standard deviation of the observations. The scatter results from at least two sources, real variations in the surface reflectance, and a variation in the number of shadowed cracks present in the spectrometer field-of-view from place to place. The gap in reflectance between 1800 and 1900 nm arises from saturation of the atmospheric water band over that interval. The jagged spectrum seen beyond 1700 nm results from noise (since corrected) introduced by the second of two amplifiers covering the infrared spectral region. The higher value at 2220 nm returned by the MMR is more nearly correct judging by the general concordance between these values and the hemispherical directional reflectance of a surface sample determined with laboratory ratioing spectro-radiometers.

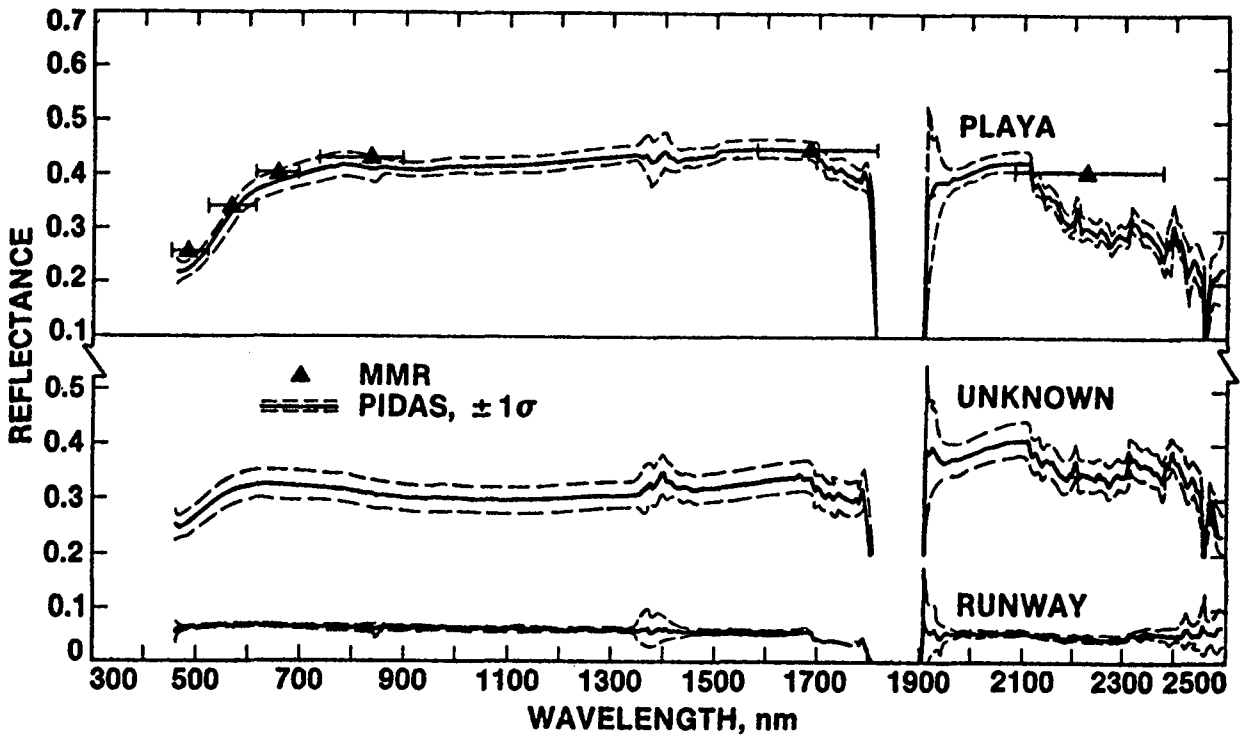


Figure 1 Surface reflectance of playa calibration target on September 14, 1987. Solid line is spectral reflectance given by PIDAS ±1 standard deviation, representing an average of 200 spectra. Triangles are reflectance determined over TM bandpasses with MMR, representing averages of about 1500 measurements.

### 2.3 Measurement of optical depth

Measurements of incident solar illumination at ten wavelengths (370, 400, 440, 520, 610, 670, 780, 870, 940 and 1010 nm) were made with two Reagan-type solar radiometers.[13] These observations were carried out between approximately 7:00 AM and 12:30 PM Pacific Standard Time. Optical depths were derived independently from slopes of conventional Langley plots of the solar IR radiance versus the secant of the solar zenith angle. The data for the two Reagan instruments are shown in Figure 2 and compared there to optical depths obtained from the transmittance functions of the standard mid-latitude summer (mls) LOWTRAN 6 model.

## 3. LABORATORY RADIOMETRIC CALIBRATION OF AVIRIS

### 3.1 Definitions and procedure

The laboratory radiometric calibration of AVIRIS was described in detail by Vane *et al.*[2] The purpose of this calibrations was to obtain a set of functional relationships (one for each of 224 detectors) between radiance incident at the instrument, and instrumental output. If L is the radiance (in $\mu Wcm^{-2}nm^{-1}sr^{-1}$) and DR (digital response) the representation of instrument output, the relationship is

$$L = DR/G \qquad (1)$$

where G represents a "gain" factor ($G^{-1}$ = inverse responsivity[14]). In writing

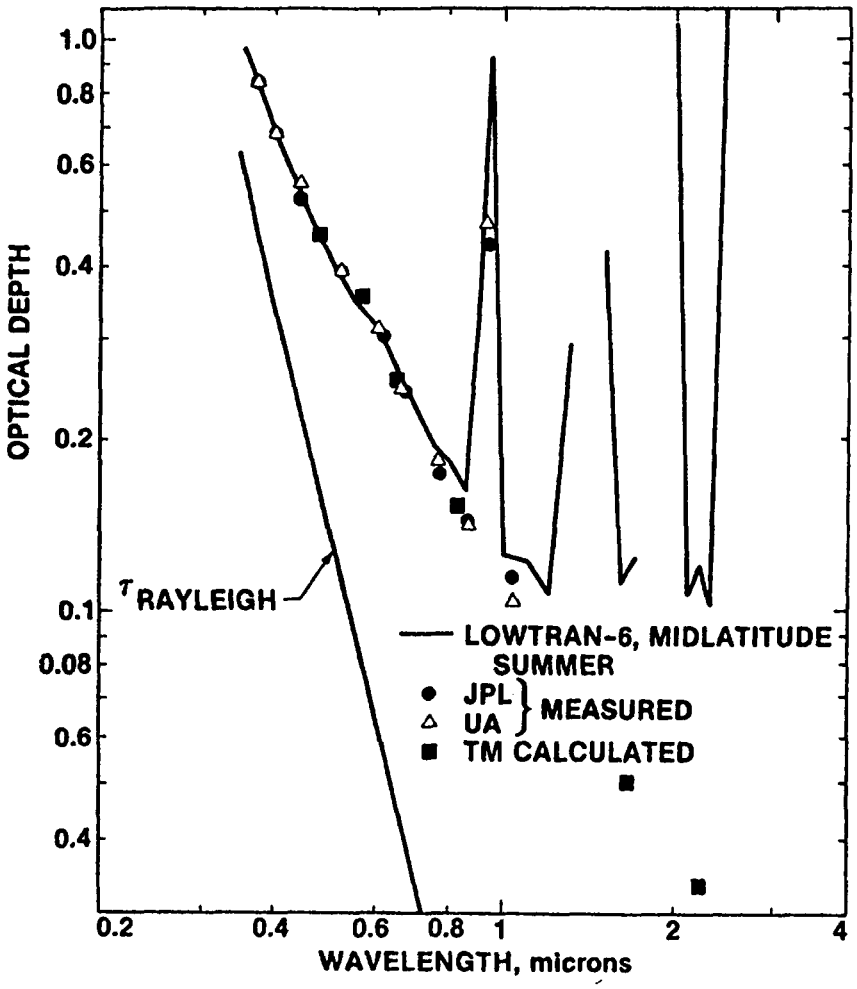


**Figure 2** A comparison of optical depths measured by JPL (•) and University of Arizona (Δ), September 14, 1987, Rogers Dry Lake. Optical depths at TM wavelengths (■) are calculated from the (Δ) data points.

Eqn.(1), it was assumed that detector dark responses were accounted for, *i.e.*, zero instrument output for zero radiance input.

The procedure for instrument calibration involved four steps: 1) radiometric calibration of a spectroradiometer against a standard lamp, traceable to a National Bureau of Standards lamp; 2) production of light transfer curves (radiance *vs.* wavelength) for the AVIRIS radiance calibration source (40-inch diameter $BaSO_4$-coated integrating sphere) using a calibrated spectroradiometer; 3) acquisition of AVIRIS DR output files as a function of integrating sphere radiance; and 4) generation of lookup tables of AVIRIS response *vs.* radiance for each detector at each wavelength. In practice, a linear relationship (Eqn. 1) was assumed and the lookup file generated from a single integrating sphere determination, thus determining a value of G. The radiometric calibration converted 10-bit DR values to 32-bit floating point radiance values.

We briefly recapitulate here the laboratory method used in (1) above because the equation employed by Vane *et al.*[2] for calculation of spectral radiance seen by the standard spectroradiometer is incorrect. For its calibration the

spectroradiometer views a standard halon panel at an angle of 45°. The panel is illuminated at normal incidence by a standard irradiance source at a calibration distance $D_{CAL}$ above its surface. The irradiance E(CAL) at the standard panel is

$$E(CAL) = E(STD)(D_{STD}/D_{CAL})^2 \quad (2)$$

where E(STD) is the irradiance of the standard lamp provided by the manufacturer measured at the calibration distance $D_{STD}$. Assuming Lambertian diffuse reflectance from the halon panel with reflectance $\rho$, the radiance L(CAL) uniformly outward from the panel is

$$L(CAL) = \rho E(CAL)/\pi. \quad (3)$$

Combining Eqns. (2) and (3) gives the radiance of the spectroradiometer in terms of the irradiance of the standard lamp. This result is greater than that of Vane *et al.*[2] by a factor of $1/\cos(45^\circ)$, or $\sqrt{2}$. The radiance of the integrating sphere $L_{IS}$ is then determined in terms of the radiance emergent from the halon and the standard lamp irradiance from the relation,

$$L_{IS} = L(CAL)A_{SR}\Omega_{SR}\left[\Phi_{SR}(IS)/\Phi_{SR}(CAL)\right]/A_{SR}\Omega_{SR} \quad (4)$$

where $\Phi_{SR}(IS)$ and $\Phi_{SR}(CAL)$ are respectively the radiant fluxes observed by the spectroradiometer from the integrating sphere and from the calibration source. $A_{SR}$ and $\Omega_{SR}$ are the area of the entrance aperture of the spectroradiometer and its solid angular field-of-view. The etendue $A_{SR}\Omega_{SR}$ is of course common to the spectroradiometer for both the integrating sphere path and standard source path, but is included to emphasize that the determination is made from the total radiant flux received in each path.

The absolute accuracy of the radiometric calibration was calculated to be about ±7%[2] across the spectral interval 1800-2450 nm, where the response of AVIRIS was observed to be most stable. Over the interval 400 to 1800 nm, additional uncertainties of a few percent are introduced because of thermal distortions (discussed below).

### 3.2 Pre- and post-season instrument status and determination of G

The initial laboratory calibration of AVIRIS was carried out in early June, 1987, before the 1987 flight season. During this calibration, it was discovered that the output signal level from the four spectrometers varied with time in the presence of a stable input radiance. The instability was traced to thermally induced distortions from on-off cycling of heaters within the spectrometer barrels. The distortions produced a reduction in signal level without change in wavelength distribution of the energy. The magnitudes of these variations in signal output were: spectrometer A, 3.5%; spectrometer B, 7.7%; spectrometer C, 4.2%; spectrometer D, 2.4%. During subsequent engineering test flights, variations of twice these magnitudes were observed that also correlated with on-off cycling of the spectrometer heaters, and with distortion of the spectrometer base and instrument rack in-flight.

After termination of the flight season (October, 1987), inspection revealed that the optical fibers connecting spectrometers A and B to the foreoptics had come loose from their mountings. Additionally, a longer wavelength blocking filter had fractured. The exact timing of the mishaps is not known.

A second post-flight season laboratory calibration of AVIRIS was carried out in October, 1987. In Figure 3, we compared the responsivities G (= DR/L) obtained from the pre- and post-season AVIRIS calibrations. The largest changes were seen to have occurred in spectrometers A and B with the post-season numbers smaller by factors varying between 0.36 and 0.91, compared to pre-season. Spectrometer C proved to be stable. The gain factor for spectrometer D decreased by a factor of about 0.8.

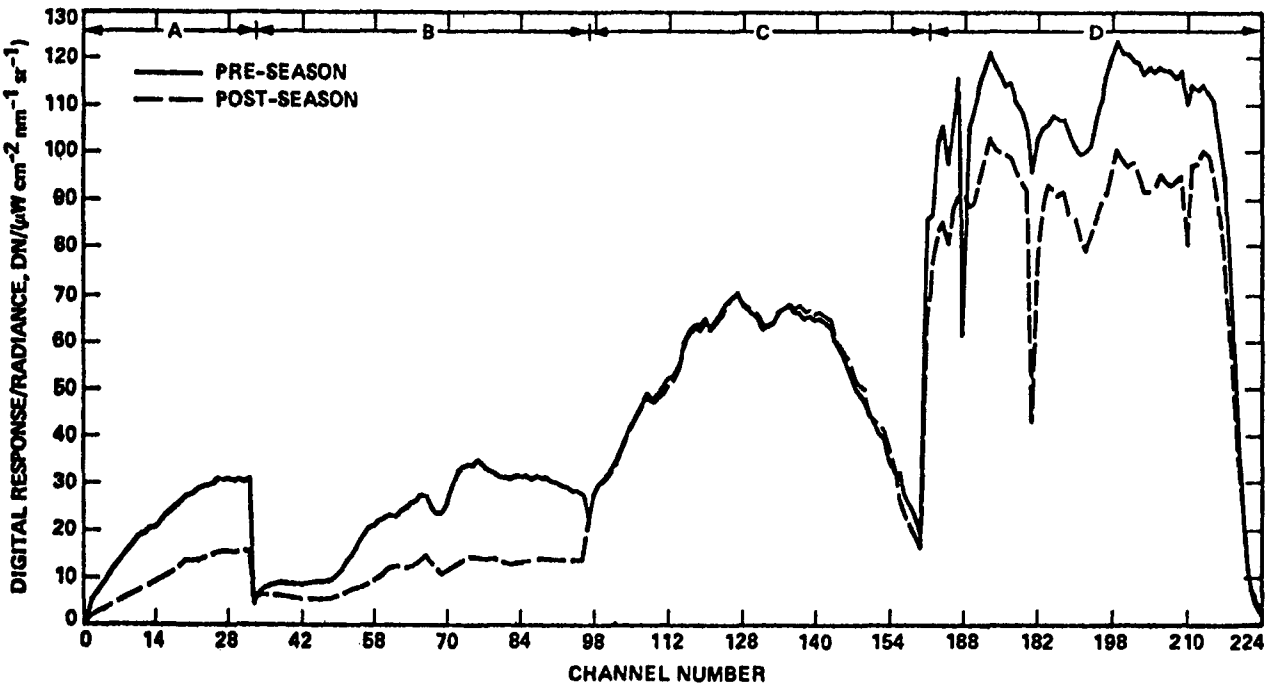


**Figure 3** Comparison of the pre- and post-season responsivities (gain factors G) for AVIRIS determined from the laboratory calibrations.

## 4. COMPARISON BETWEEN AVIRIS- AND MODEL-GENERATED SOLAR RADIANCES

An important test of the validity of the laboratory radiometric calibration for flight conditions is the calculation of solar radiance at the instrument reflected from a target of known reflectance, when account has been taken of the atmosphere, as compared to the radiance predicted from the instrument response. In this section, we present: (1) the responses implied by the two AVIRIS laboratory calibrations; (2) the results of atmospheric modelling using the measured surface reflectances and atmospheric optical depths; and (3) a comparison of these various results.

### 4.1 Radiances predicted from AVIRIS using pre- and post-season calibrations

In Figure 4 are presented the spectral radiances produced for the playa target from the pre- and post-season laboratory radiometric calibrations. For each the ±1 standard deviation lines refer to scatter introduced because of natural

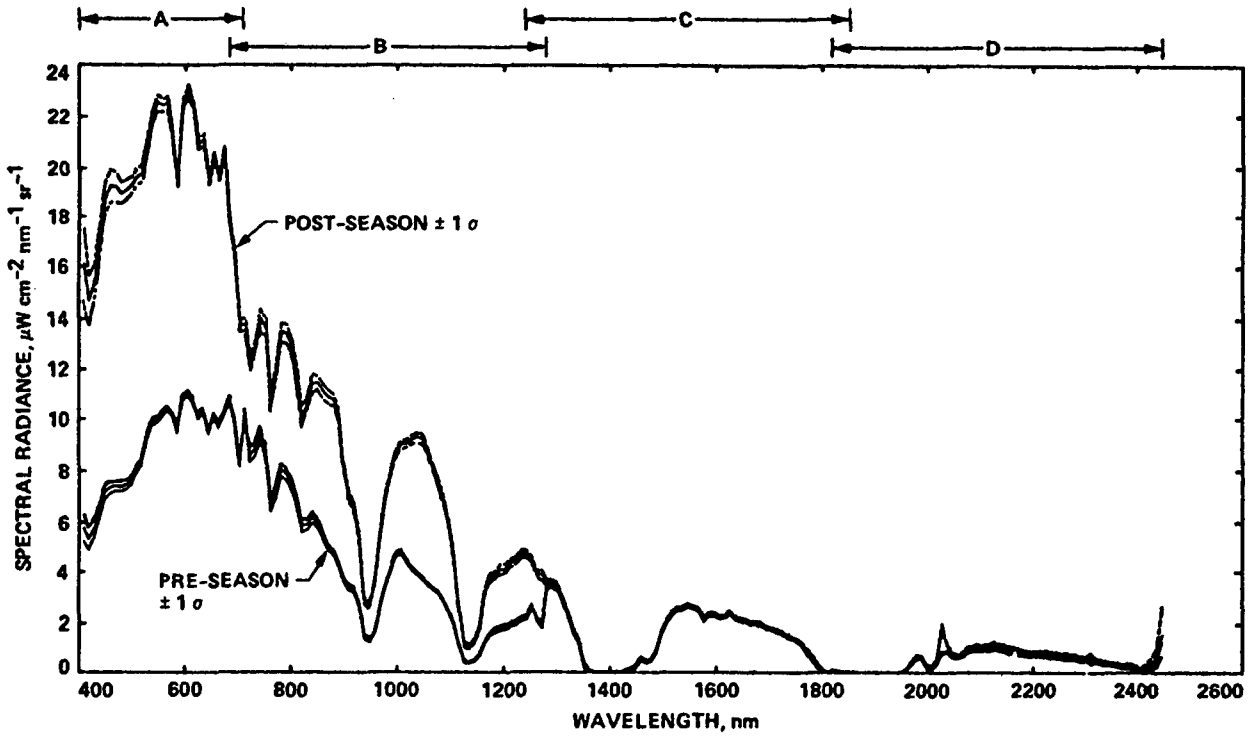


Figure 4 Spectral radiances predicted for the Rogers Day Lake target from AVIRIS from the pre- and post-season radiometric calibrations.

variations in reflectance over the 64 pixels used in the sample and to instrumental noise. As implied by the changes in responsivity shown in Figure 3, the post-season calculated radiance for this target was greater over the spectral regions covered by spectrometers A, B and D, and essentially unchanged in the region of C.

### 4.2 Radiances predicted by atmospheric models

We have employed four atmospheric radiative transfer (RT) codes in these studies. The results from each are compared below:

(1) LOWTRAN 6[8] calculates atmospheric transmittance and radiance for a given atmospheric path. The code includes molecular absorption and single scattering from aerosols and molecules. The spectral resolution of 20 $cm^{-1}$ is sufficiently greater than the spectral sampling interval of AVIRIS (10 nm) to provide a very useful basis for wavelength calibration and effective spectral response for the instrument under flight conditions. The standard mid-latitude summer model was employed, and the geographic and solar conditions were the same as for other codes used, as given in Table 1.

Single scattering was accounted for using the following equation,

$$L_{total} = L_{scattered} + L_{reflected} \qquad (5)$$

where $L_{scattered}$ is the radiance from single scattering in the atmosphere above any ground elevation, and $L_{reflected}$ is the ground-reflected direct radiance reaching the sensor. Two problems exist with the single scattering option in LOWTRAN 6.

First, only a single target reflectance is accepted at all wavelengths in the unmodified code. We modified the program to allow for ground reflectance that varied with wavelength as given by PIDAS. Second, the program does not compute ground reflected radiance unless the target is at sea level. To circumvent this difficulty, the downward and upward transmitted parts from the target elevation were computed separately, and multiplied by the surface reflectance. The equation is

$$L_{reflected} = (E_{\odot}\mu_o/\pi)T_{dn}T_{up}R_{PIDAS} \quad (6)$$

where $E_{\odot}$ = exoatmospheric solar irradiance, $\mu_o$ = cosine of the solar zenith angle, $T_{dn}$ = transmittance of downward path, $T_{up}$ = transmittance of upward path, and $R_{PIDAS}$ is the reflectance of the (horizontal) surface returned by PIDAS.

(2) The principal improvement provided by the LOWTRAN 7[9] code, from our standpoint, is the inclusion of multiple scattering, although it has not yet proved possible to modify the program to account for ground reflectance at any elevation except sea level. This code has been changed to account for variable surface reflectance as given by PIDAS.

(3) The UA RT code by Herman and Browning[10] has been used extensively in the in-flight calibration of Landsat providing internally consistent results to within 2.5%[15]. The code uses Mie theory to compute aerosol scattering functions for a specified size distribution, and the Gauss-Seidel iterative technique to solve the equation of radiative transfer. The aerosol phase function is sampled at discrete angular intervals.

(4) The 5S code of Tanré *et al.*[16] was modified at the University of Arizona to allow user specification of terrain elevation and sensor altitude, including other changes. The 5S code makes extensive use of analytical expressions and preselected atmospheric models, resulting in a very short execution time. The code has proven to be significantly more accurate than models with fast or moderate execution times (Royer, *et al.*[17]).

(5) The JPL code[11] also computes aerosol scattering functions from Mie theory and employs the Gauss-Seidel method, but traces spatial Fourier components of the radiation field, and represents the aerosol phase function as a 24-term Legendre series. The JPL code is believed, in theory, to have the same degree of certainty as the UA code, but has only recently been tested against field data.

The results of calculations for these five models are given in Figure 5. Vertical bars on the JPL model points represent approximately the variation in calculated radiance from the variation in surface reflectance as determined with PIDAS (Figure 1). The spectral radiance generated by LOWTRAN 6 and 7 were for the standard mid-latitude summer model[8]. The spectral radiance generated by the JPL, UA and 5S codes were for the geographic, solar and atmospheric conditions summarized in Table 1. Note that the LOWTRAN 7 result refers to an atmospheric path from Sun-to-sea level to an altitude of 20 km. Removing the lower 690 m of atmosphere, corresponding to the actual elevation of Rogers Lake, can be expected to increase the computed radiance somewhat, because of decreased attenuation, but to decrease the scattered component because of the reduction in scattering volume. The net result might be expected to resemble more closely the Herman-Browning radiance, since this code accounts for molecular absorption through the 5S code, at the proper elevation. The LOWTRAN 6 result, which represents the sum of directly transmitted radiation reflected by the ground and singly scattered radiation in the

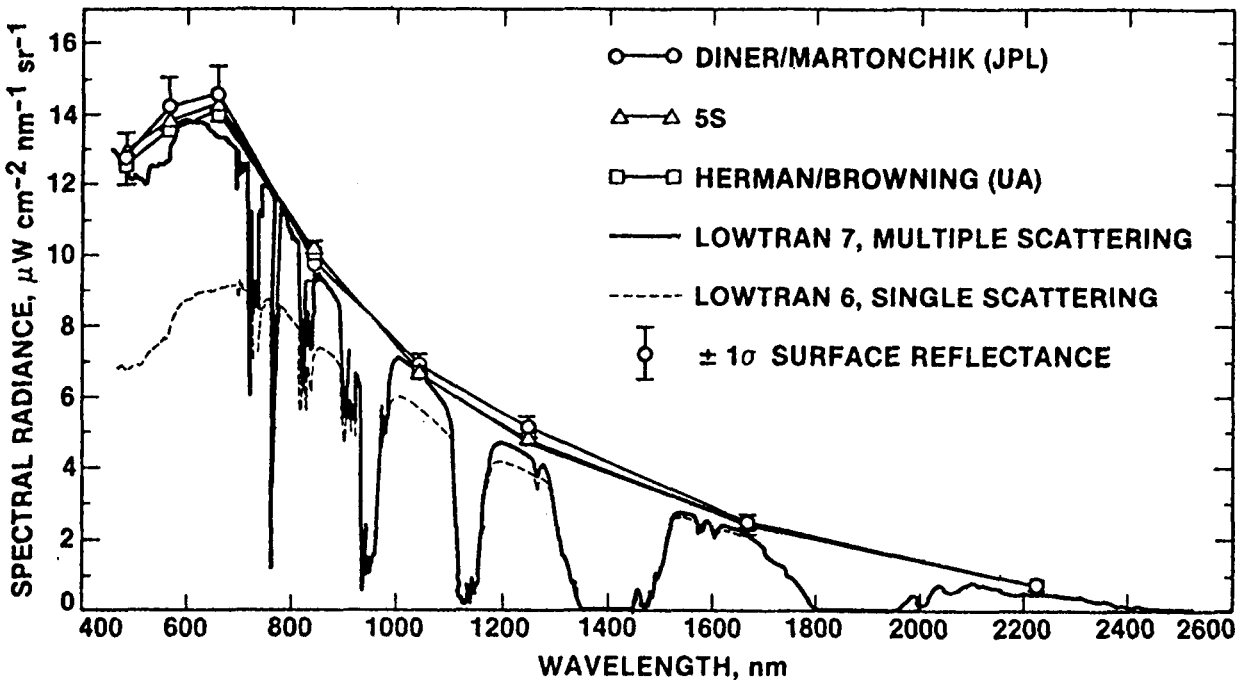


Figure 5 Comparison of radiances generated by atmospheric RT models: (1) LOWTRAN 6, single scattering; (2) LOWTRAN 7, multiple scattering; (3) UA code; (4) 5S code; and (5) JPL code.

TABLE 1

MODEL CONDITIONS EMPLOYED WITH UA, 5S AND JPL RT CODES FOR ROGERS DRY LAKE, CALIFORNIA SEPTEMBER 14, 1987

| | |
|---|---|
| SOLAR ZENITH ANGLE: 37.3 | JUNGE SIZE DISTRIBUTION: 3.46 |
| SOLAR AZIMUTH ANGLE: 142.9 | AEROSOL SIZE RANGE: 0.02 - 5.02 μm |
| SOLAR DISTANCE, AU: 1.0058 | REFRACTIVE INDEX: 1.54 - 0.01i |
| LATITUDE: 34° 59.7' | PRESSURE: 920.4 mb |
| LONGITUDE: 117° 52.4' | TEMPERATURE: 21°C |
| ELEVATION: 694 m 2276' | $H_2O$ CONTENT: 0.729 g/cm²/km |
| AIRCRAFT ALT.: 20 km 65620' | INTEGRATED PATH $H_2O$: 1.76 g/cm² |
| TIME OF OVERPASS: 18:21 UT | OZONE CONTENT: 0.376 cm-atm |
| CALCULATED VISIBILITY: 26 km | NADIR VIEWING ANGLE: <5° |

| THEMATIC MAPPER BAND | 1 | 2 | 3 | 4 | | | 5 | 7 |
|---|---|---|---|---|---|---|---|---|
| CENTRAL WAVELENGTH (nm) | 486.3 | 570.6 | 660.7 | [illegible] | 1050[a] | 1250[a] | 1677.0 | 2223.0 |
| OPTICAL DEPTH | | | | | | | | |
| AEROSOL | 0.299 | 0.237 | 0.191 | 0.135 | 0.0958 | 0.0706 | 0.049 | 0.032 |
| RAYLEIGH | 0.148 | 0.077 | 0.042 | 0.016 | 0.0065 | 0.0032 | 0.0010 | 0.0003 |
| GAS TRANSMITTANCE, (5S)[b] | 0.988 | 0.920 | 0.962 | 0.964 | 0.999 | 0.9965 | 0.990 | 0.979 |
| SURFACE REFLECTANCE | 0.253 | 0.335 | 0.395 | 0.430 | 0.416 | 0.426 | 0.446 | 0.409 |
| SOLAR IRRAD., $Wm^{-2}\,\mu m^{-1}$ | 1883.84 | 1799.95 | 1533.35 | 1011.00 | 658.19 | 464.49 | 221.13 | 71.26 |
| NORMALIZED CODE RAD.[11] | .06797 | .07985 | .09622 | .1076 | 0.1046 | 0.1082 | .1120 | .1029 |
| RADIANCE, $Wm^{-2}\,\mu m^{-1}\,sr^{-1}$ | | | | | | | | |
| UA[10] | 126.3 | 135.6 | 140.6 | 101.6 | 66.9 | 48.6 | 24.2 | 7.1 |
| 5S[16] | 128.7 | 139.3 | 144.1 | 103.0 | 67.2 | 48.7 | 24.3 | 7.2 |
| JPL[11] | 128.0 | 143.7 | 147.5 | 100.2 | 68.69 | 49.86 | 24.2 | 7.0 |
| PERCENT DIFFERENCE | | | | | | | | |
| 100 x (JPL - UA)/JPL | 1.4 | 5.6 | 4.7 | -1.4 | 2.6 | 2.5 | 0.0 | -1.4 |
| 100 x (JPL - 5S)/JPL | -.52 | 3.8 | 2.3 | -2.8 | 2.2 | 2.3 | -0.3 | -2.9 |
| 100 x (5S - UA)/UA | 1.9 | 2.7 | 2.5 | 1.4 | 0.4 | 0.2 | 0.4 | 1.4 |

a MONOCHROMATIC VALUES
b CALCULATED FROM A RT CODE OF TAURE et al.[16] USED HERE FOR DETERMINING GASEOUS TRANSMITTANCES

atmosphere is about 35-40% lower at shorter wavelengths than the results from the other codes. The reasons are twofold, LOWTRAN 6 ignores the diffuse irradiance of the sky on the target and the upward atmospheric path radiance. The distinction between the results for LOWTRAN 6 and LOWTRAN 7 essentially disappears at wavelengths greater than about 1300 nm.

The JPL, UA, and 5S models have been exercised at the TM band wavelengths only. The numerical differences in output for these three models are summarized in Table 1. In general the differences are greatest in the region of strongest scattering and may arise in the method of describing the phase function. In particular, for the Herman-Browning and JPL codes, the differences disappear for the case of a purely Rayleigh atmosphere (J. Martonchik, personal comm.). Close agreement is also found between the continuum LOWTRAN 7 radiance and the model-computed radiance in the TM bands. A better overall fit between these envelopes could be achieved with with closer spacing of the computed points. Two additional points at 1050 and 1250 nm have been added to realize this in part.

### 4.3 Comparison of AVIRIS-generated and model-generated radiances

The AVIRIS-generated radiance for the playa target using the pre- and post-season gain factors is compared to the three model-generated spectral radiance distributions in Figure 6. To be definite in the comparison, we will regard the UA, 5S, and JPL codes as more accurately describing the radiance to be expected in TM bands 1-4 (spectrometers A and B) from a perfectly functioning and perfectly calibrated instrument because, as we have mentioned, the LOWTRAN 7 simulation does not account properly for the actual elevation of the site. In bands 5 and 7 (spectrometers C and D), atmospheric scattering is diminished as shown in Figure 5, and we can regard comparison with the LOWTRAN 7 model in a better light. The

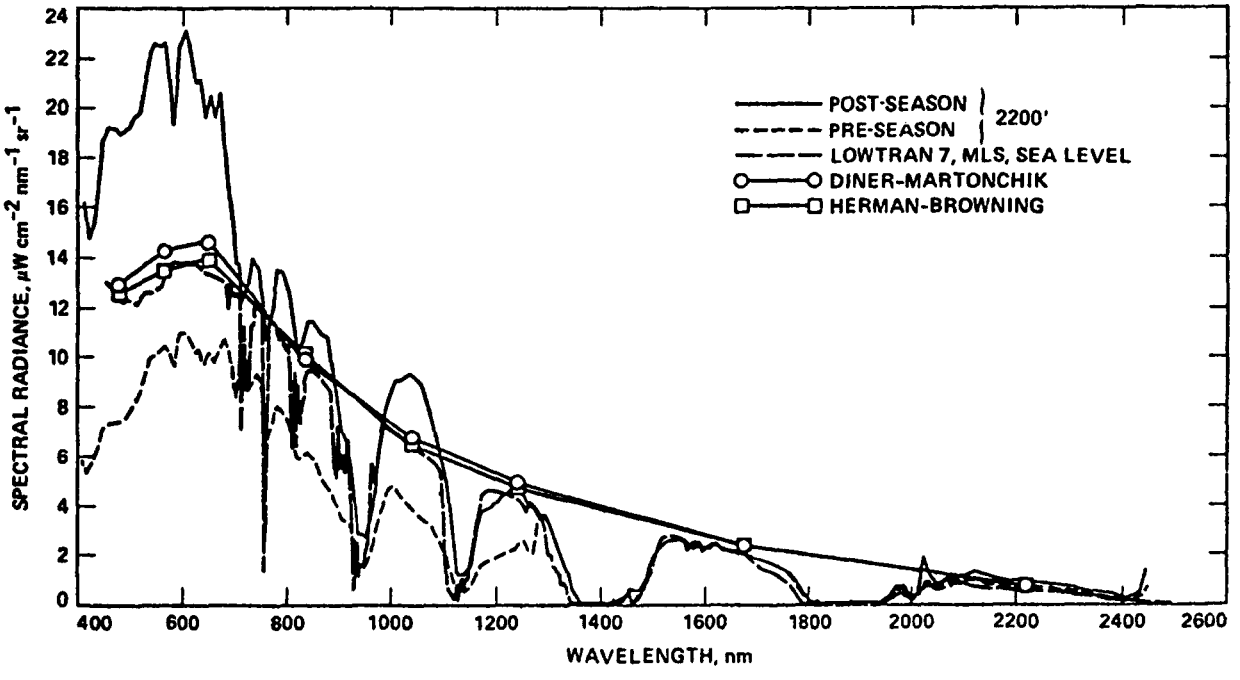


Figure 6 Comparison of RT code results with radiance for the playa target as determined from AVIRIS according to the pre- and post-season radiometric calibrations.

differences between observed and the JPL- and UA-modelled radiances at TM band wavelengths, where these code radiances were unambiguously determined, are given in Table 2.

TABLE 2

Comparison (in %) of observed and modelled radiances at wavelengths of TM bands. (+) or (-) values designate observed radiance greater or less than % of the model radiance. (A) indicates TM band falls within region of spectrometer A, etc.

| | Pre-season | | Post-season | |
|---|---|---|---|---|
| Band | JPL | UA | JPL | UA |
| 1 (A) | -43 | -40 | +47 | +52 |
| 2 (A) | -27 | -23 | +58 | +67 |
| 3 (A) | -32 | -27 | +40 | +47 |
| 4 (B) | -37 | -41 | +13 | +12 |
| 5 (C) | ~-15 | ~-15 | ~-15 | ~-15 |
| 7 (D) | 0 | 0 | ~+30 | ~+30 |

The comparison with LOWTRAN 7 is given in Figure 7. Here, for spectrometer C, the agreement between AVIRIS-derived and model radiance in the continuum region is within (-)5%, for both pre- and post-season calibrations. For spectrometer D, the pre-season result is about 25% higher and the post-season 50-75% higher than the model. The result for spectrometer C is encouraging and leads us to believe in the general correctness of the laboratory and model comparisons attempted here, despite unfavorable comparisons in the other spectrometers.

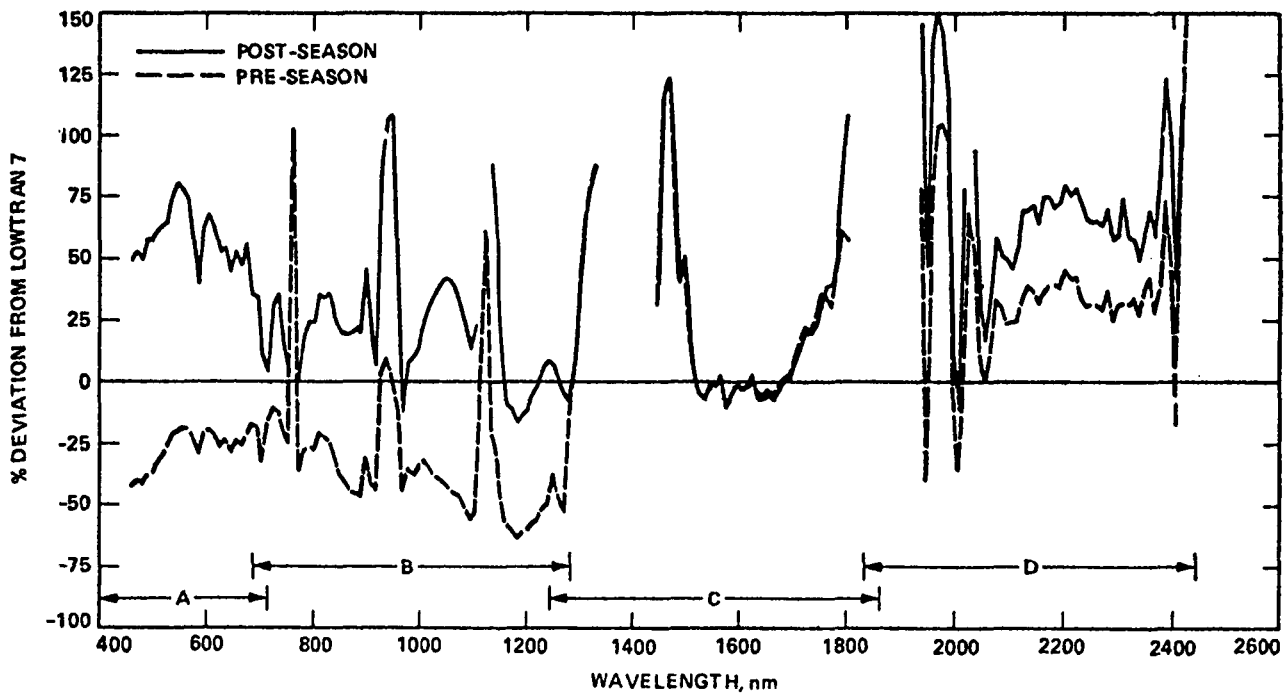


Figure 7 Percentage difference 100 (LOWTRAN-AVIRIS)/LOWTRAN for the playa target and pre- and post-season calibrations. Code used is LOWTRAN 7.

The region 450-1050 nm, covering all of the A and part of the B region is presented scale-expanded in Figure 8 and compared to the LOWTRAN 7 result which provides the spectral continuity required to interpret (in detail) the AVIRIS spectrum. Possibly excepting the concave upward portion of the observed AVIRIS spectrum between 450-550 nm, which may represent the $Fe^{+3}$ band seen in the playa reflectance (Figure 1), the additional features present were introduced by the instrument or are noise. Compare this result with that reported by Vane[18] (his Figure 6) at Stonewall Playa, Nevada, in which similar features are present. Note also the prominent discontinuity near 700 nm introduced between the spectral regions of A and B by the post-season calibration.

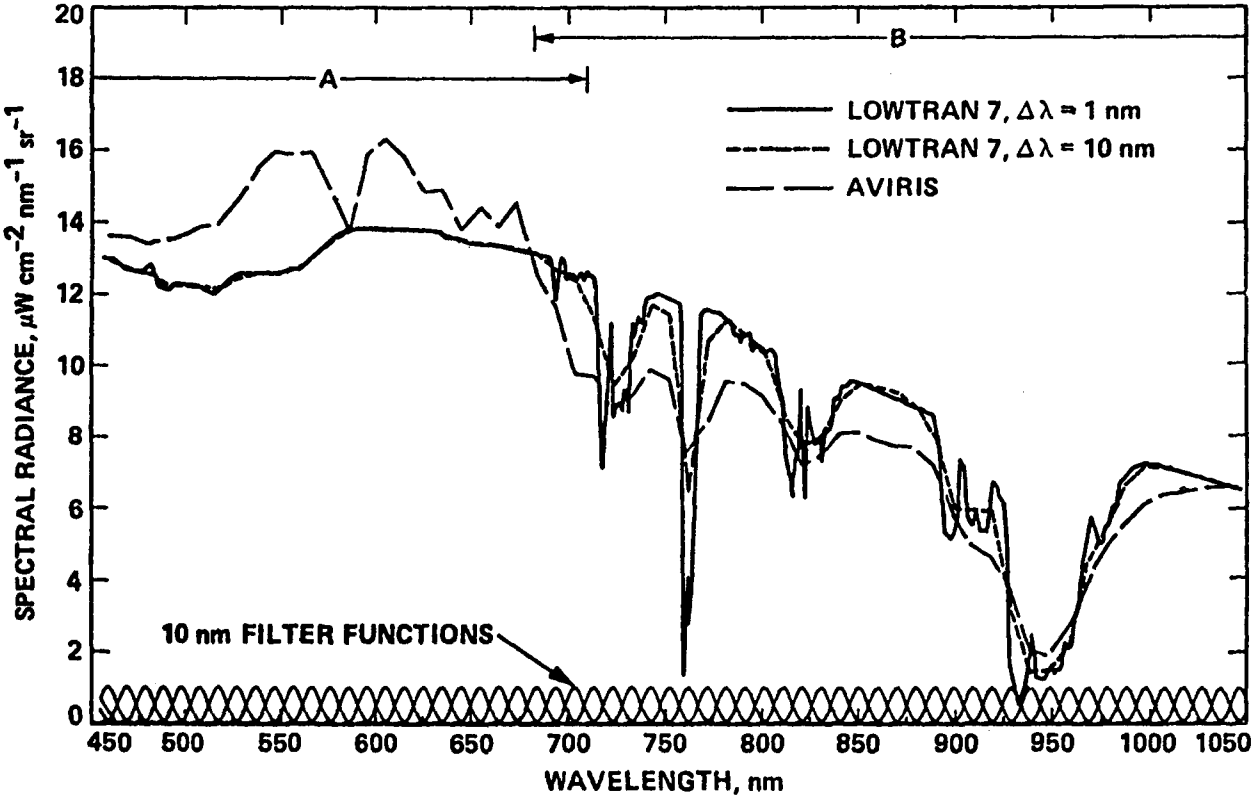


**Figure 8** Comparison of LOWTRAN 7 and AVIRIS-predicted radiances for the spectral region 450-1050 nm. The degraded LOWTRAN spectrum calculated from Eqn (7) using FWHM $\Delta\lambda$ = 9.58 nm in Eqn (8). Post-season calibration.

## 5. EFFECTIVE IN-FLIGHT SPECTRAL RESOLUTION

We can use the AVIRIS spectra of Figures 6 and 8 to provide estimates of the effective in-flight spectral "resolution", and by inference the spectral sampling interval. By spectral resolution, we mean the detection of separate radiance minima associated with neighboring absorption bands, arising, in this case, in the atmosphere. The spectral sampling interval is obtained qualitatively by dividing the wavelength interval covered by each spectrometer by the number of detectors covering the interval.

An improved evaluation of the spectral sampling properties of AVIRIS can be obtained by examining the spectral response function. For each detector located provisionally at wavelength $\lambda_i$, the signal $s(\lambda_i)$ generated by the incident spectrum $L(\lambda)$ is

$$s(\lambda_i) = \int_o^\infty f(\lambda_i - \lambda)L(\lambda)d\lambda \qquad (7)$$

where $f(\lambda_i - \lambda)$ is the spectral response or spread function of the system at $\lambda_i$ from the radiance at wavelength $\lambda$. In practice, this is evaluated by restricting $L(\lambda)$ to a narrow band of wavelengths $\Delta\lambda$ at successive wavelengths $\lambda'$ to secure approximately

$$s(\lambda_i - \lambda') \approx f(\lambda_i - \lambda')L(\lambda')\Delta\lambda \qquad (8)$$

The spectral response curves for a number of AVIRIS detectors have been determined by Vane *et al.*[2] using $\Delta\lambda = 1$ nm. The function

$$f(x) = \exp(-h^2x^2) \qquad (9)$$

proves to be a good representation for the normalized response $s(\lambda_i - \lambda)/L(\lambda)\Delta\lambda$ (Figure 9). The central wavelength of the channel is taken to be the maximum of $f(x)$, thus fixing $\lambda_i$, and the full width $\Delta\lambda_i$ at half maximum height (FWHM) as the effective channel spectra width of sampling interval. This gives $h = 1.665/\Delta\lambda_i$. The spectral sampling intervals for AVIRIS for all spectrometers have been determined by Vane *et al.*[2] as follows: spectrometer A, 10.0 nm, spectrometer B, 9.58 nm, spectrometer C, 9.86 nm; spectrometer D, 9.85 nm.

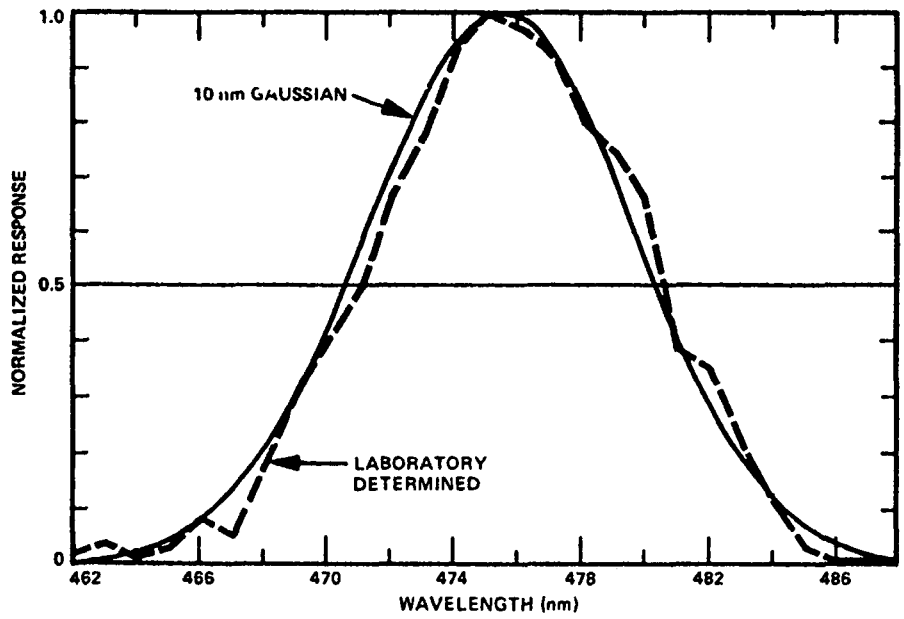


Figure 9 Comparison of laboratory-measured spectral response with approximation of the single-channel normalized spectral response by the function $f(x) = \exp\left(-h^2x^2\right)$ (smooth curve).

In principle, the resolution is determined from the sampling interval and Nyquist's sampling theorem. If the frequency of sampling is $1/\delta\lambda_s$ $nm^{-1}$, then the sampling interval $\Delta_s = 1/2\delta\lambda_s$. Thus, for $\delta\lambda_s = 10$ nm, $\Delta_s = 20$ nm; that is, narrow bands in adjacent channels will produce a single minimum in radiance and are not distinguished unless separated by ≥20 nm.

We now use these results to examine the implied resolution throughout the spectrum. From Figure 6, at 2050 nm (spectrometer D), the pair of $CO_2$ bands are separated by 50 nm, and are clearly resolved, thus establishing a resolution <50 nm for that spectrometer. At 1600 nm (spectrometer C), the atmospheric $CO_2$ bands there are separated by 30 nm and are also resolved.

An improved description of the in-flight spectral resolution is possible taking account of the functional form of the spectral response curves, Eqn (9). For AVIRIS, a single detector sees a signal that is represented by Eqn (7), which can be used with Eqn (9) to calculate a degraded full-resolution LOWTRAN 7 equal to that of AVIRIS. By comparing the degraded LOWTRAN spectrum to the observed AVIRIS spectrum and using h as a variable parameter the effective AVIRIS spectral resolution can be deduced. This comparison is shown in Figure 8 using FWHM = 10 nm (h = 0.1665), which represents the expected AVIRIS spectrum if the instrument were actually sampling at the laboratory-determined estimated sampling interval. A better match (Figure 10) is provided by doubling the width of the Figure 9 spectral response curve so that the full sampling width at half-maximum is 20 nm. This is in accord

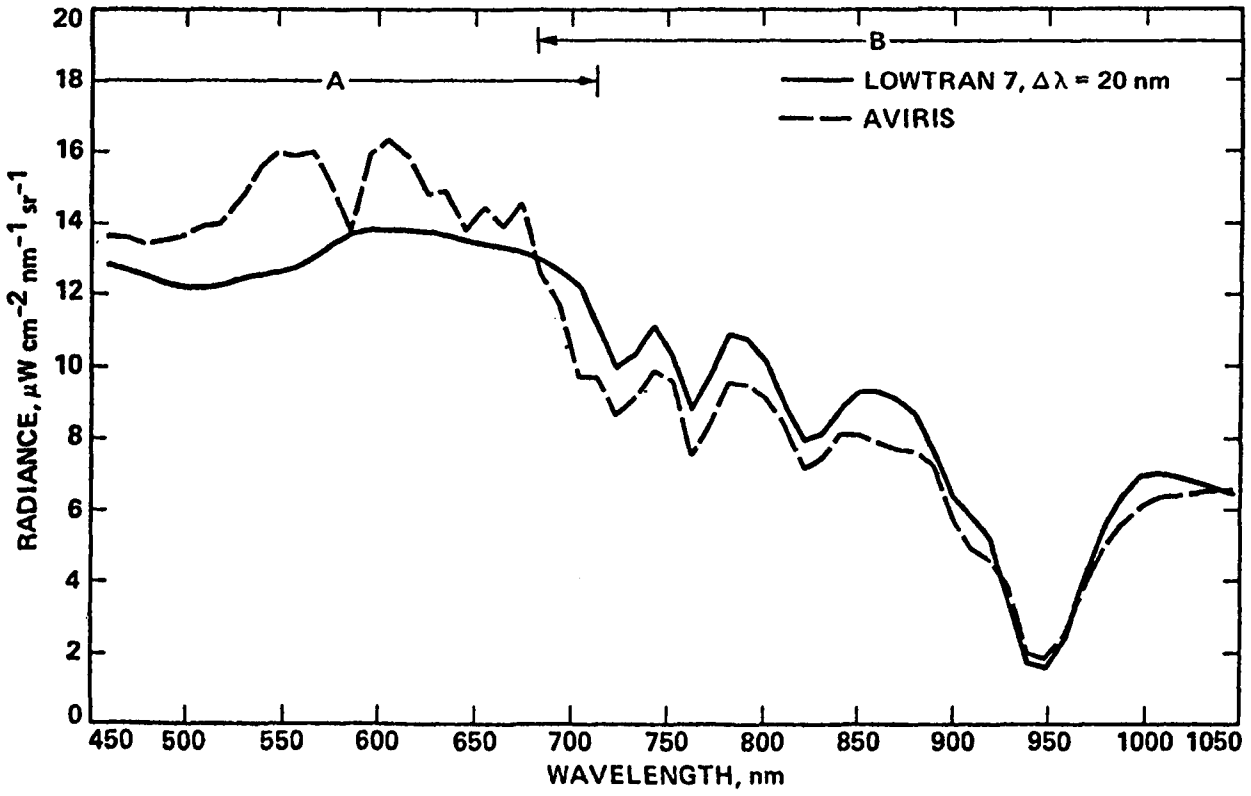


Figure 10 Comparison of the observed AVIRIS spectrum and LOWTRAN 7 spectrum degraded using FWHM Δλ = 20 nm in Eqn (8). Post-season calibration.

with the post-season spectral calibration of AVIRIS, which revealed that, because of the detachment of optical fibers in spectrometers A and B and the resulting defocussing, the spectral FWHM of these two spectrometers was 18-20 nm compared to 9-10 nm in the pre-season calibration. Spectrometers C and D were found to have remained unchanged.

## 6. SUMMARY

Data from an AVIRIS overflight of a field test site at Rogers Dry Lake, California have been analyzed to characterize the in-flight radiometric and spectral performance of the instrument. The combined field data sets of the UA, USDA and JPL groups, consisting of spectral reflectance observations of the playa and optical depth measurements of the atmosphere, are presented. Results of the measurement programs agreed closely (a few percent for reflectance, 1% for optical depth determinations). Results of two laboratory radiometric calibrations of AVIRIS, pre- and post-season are presented. Significant differences in gain factors were found between the two calibrations, varying from reductions of as much as a factor of 2.8 in performance (spectrometer A) to essential stability (spectrometer C). Employing a reflectance-based method, we compared the AVIRIS-generated response to five separate atmospheric RT models. Reasonable and encouraging agreement was found between the instrument-produced radiance using the post-season calibration data, and the three multiple scattering RT models employed, particularly for spectrometer C. A scenario that may explain much of the variable behavior of the other spectrometer is as follows: (1) instrument was calibrated pre-season; (2) optical fibers detached during flight season prior to September 14 calibration flight; (3) instrument was re-calibrated post-season with fibers detached but not necessarily in positions occupied during the September 14 calibration flight. While the fiber detachment problem may partly account for the variable performance of AVIRIS relative to that expected, a complete story must include the effects of in-flight thermal and mechanical distortion, since the flight environment is drastically different from that of the laboratory. There seems to be no way of separating these effects for the past data sets because AVIRIS has since been refurbished. We must therefore rely on future test flights to explore such questions.

## 7. ACKNOWLEDGMENTS

We thank Eric Laue and John Appleby of JPL for their assistance. Research described here was carried out by Jet Propulsion Laboratory, California Institute of Technology, under contract with the National Aeronautics and Space Administration.

## 8. REFERENCES

1. Vane, G. (*ed.*) (1987), Airborne Visible/Infrared Imaging Spectrometer (AVIRIS): A description of the sensor, ground data processing facility, laboratory calibration and first results. *JPL Publication 87-38*, Jet Propulsion Laboratory, Pasadena, CA, 97 pp.
2. Vane, G., T. G. Chrien, E. A. Miller and J. H. Reimer (1987), Spectral and radiometric calibration of the Airborne Visible/Infrared Imaging Spectrometer, *Proceedings of SPIE Conference on Imaging Spectroscopy II* (San Diego, CA, 20-21 August, 1987), 834, 91-105.
3. Whitney, G., M. Abrams and A. F. H. Goetz (1983), Mineral discrimination using a portable ratio-determining radiometer, *Econ. Geol.*, 78(4), 688-698.

4. Goetz, A. F. H. (1987), The Portable Instant Display and Analysis Spectrometer (PIDAS), in Proceedings of the third Airborne Imaging Spectrometer data analysis workshop (G. Vane, *ed.*), *JPL Publication 87-30*, Jet Propulsion Laboratory, Pasadena, CA, 8-17.
5. Robinson, B. F., M. E. Bauer, D. P. Dewitt, L. F. Silva and V. C. Vanderbilt (1979), Multiband radiometer for field research, *SPIE*, 196, 8-155.
6. Slater, P. N., S. F. Biggar, R. G. Holm, R. D. Jackson, Y. Mao, M. S. Moran, J. M. Palmer and B. Yuan (1987), Reflectance- and radiance-based methods for the in-flight absolute calibration of multispectral sensors, *Rem. Sens. Envir.*, 22, 11-37.
7. Conel, J. E., G. Vane, R. O. Green, R. E. Alley, V. Carrere, A. Gabell, and C. J. Bruegge (1988), Airborne Visible/Infrared Imaging Spectrometer (AVIRIS): In-Flight radiometric calibration and the determination of surface reflectance, presented at 4$^{e}$ Colloque International Signatures Spectrales D'Objets en Teledetection (Aussois, France, 18-22 January).
8. Kneizys, F. X., E. P. Shettle, W. O. Gallery, J. H. Chetwynd, Jr., L. W. Abrew, J. E. A. Shelby, S. A. Clough and R. W. Fenn (1983), Atmospheric transmittance/radiance: Computer code LOWTRAN 6, AFGL-TR-83-0187, AFGL Hanscom AFB, MA, 200 pp.
9. Kneizys, F. X., E. P. Shettle, G. P. Anderson, L. W. Abrew, J. H. Chetwynd, J. E. A. Shelby, S. A. Clough and W. O. Gallery (1988), "Atmospheric transmittance/radiance: Computer code LOWTRAN 7 (*in press*).
10. Herman, B. M. and S. R. Browning (1975), The effect of aerosols on the Earth-atmosphere albedo, *J. Atmos. Sci.*, 32, 1430-1445.
11. Diner, D. J. and J. V. Martonchik (1984), Atmospheric transfer of radiation above an inhomogeneous non-Lambertian reflective ground: I. Theory, *J. Quant. Spectros. Radiat. Transfer.*, 31, 97-125.
12. Jackson, R. D., M. S. Moran, P. N. Slater and S. F. Bigger (1987), "Field calibration of reference reflectance panels", *Rem. Sens. Env.*, 22, 145-158.
13. Shaw, G. E., J. A. Reagan and B. M. Herman (1973), Investigations of atmospheric extinction using direct solar radiation measurements made with a multiple wavelength radiometer, *J. Appl. Meteorol.*, 12, 374-380.
14. Wyatt, C. L. (1978), *Radiometric calibration: theory and methods*, Academic Press, New York, 200 pp.
15. Slater, P. N., S. F. Bigger, R. G. Holm, R. D. Jackson, Y. Mao, M. S. Moran, J. M. Palmer and B. Yuan (1986), Absolute radiometric calibration of the Thematic Mapper, *SPIE*, 660, 2-8.
16. Tanre, D., C. Deroo, P. Duhaut, M. Herman, J. J. Morcrette, J. Perbos and P. Y. Dischamps (1985), "Effets atmospheriques en télédétection-logical de simulation du signal satellitaire dans le spectra solaire", Proc. Third Int. Colloq. on Spectral Signatures of Objects in Remote Sensing, ESA SP-247, pp. 315-319.
17. Royer, A., N.T. O'Neill, A. Davis, and L. Hubert (1988), Comparison of radiative transfer models used to determine atmospheric optical parameters from space, *SPIE*, 928, in press.
18. Vane, G. (1987), First results from the Airborne Visible/Infrared Imaging Spectrometer (AVIRIS), *SPIE*, 834, 166-174.

# Appendix B

## Workshop Agenda

# AGENDA

## AVIRIS PERFORMANCE EVALUATION WORKSHOP

## JUNE 6, 7, 8, 1988

JPL BUILDING 167 CONFERENCE ROOM

MONDAY, JUNE 6, 1988

8:00 Shuttle Bus Leaves Pasadena Holiday Inn for JPL

8:30 Check-In at JPL Visitor Control Center

9:00 JPL Welcome, Building 167 Conference Room: Charles Elachi, Assistant Laboratory Director, Office of Space Science and Instruments

9:15 NASA Headquarters Welcome: Diane Wickland, Manager, Terrestrial Ecosystems Program, Earth Science Division, NASA

9:30 Workshop Overview and AVIRIS Project Status: Gregg Vane, AVIRIS Experiment Scientist and Manager

10:00 Break

10:30 AVIRIS Instrument Status: Wallace Porter, AVIRIS Instrument Engineer

11:00 AVIRIS Laboratory Calibration Status: Thomas Chrien, AVIRIS Optics and Calibration Engineer

11:30 AVIRIS Ground Data Processing: John Reimer, AVIRIS Ground Data Processing System Manager

12:00 LUNCH

1:00 Spectral Analysis Manager (SPAM) Software Status: Alan Mazer and Greg Cooper, SPAM Development Group

1:30 U-2 Operations: Gary Shelton and Ron Williams, NASA Ames High Altitude Branch

2:00 AVIRIS field radiometric and spectral calibration and studies of the atmosphere and surface by model and observational methods: James Conel, Robert Green, Carol Bruegge, Jack Margolis, Ron Alley, Gregg Vane, Veronique Carerre, Philip Slater, and Ray Jackson

2:30 BREAK

3:00 Radiometric performance of AVIRIS: Assessment for an arid region geologic target: Hugh Kieffer and Kevin Mullens

3:30 Calibration of AVIRIS images to reflectance: J.B. Adams, M.O. Smith, A.R. Gillespie, D. Sabol, and D.A. Roberts

4:00 A quick-look assessment of AVIRIS radiometic quality over water: James Mueller

4:30 DISCUSSION

5:00 ADJOURN

5:15 Shuttle Bus Departs JPL for Pasadena Holiday Inn

6:00 RECEPTION at the Pasadena Holiday Inn (Piazza Room)

TUESDAY, JUNE 7, 1988

8:00 Shuttle Bus Leaves Pasadena Holiday Inn for JPL

8:30 Zones of information in the AVIRIS spectra: Paul Curran and Jennifer Dungan

9:00 Assessment of AVIRIS data for characterizing a northern forest: John Ranson

9:30 Evaluation of ozone injury in Ponderosa pine forests using AVIRIS: Brian Curtiss, Susan Ustin and Scott Martens

10:00 BREAK

10:30 Calibration and evaluation of AVIRIS data: Roger Clark

11:00 Automated extraction of absorption features from Airborne Visible/Infrared Imaging Spectrometer (AVIRIS) and Geophysical Environmental Research Imaging Spectrometer (GERIS) data: Fred A. Kruse and Wendy M. Calvin

11:30 Preliminary analysis of Airborne Visible/Infrared Imaging Spectrometer (AVIRIS) data for mineralogical mapping at sites in Nevada and Colorado: Fred A. Kruse and Dan L. Taranik

12:00 LUNCH

1:00 Assessment of AVIRIS data from vegetated sites in the Owens Valley, California: Barry Rock and Chris Elvidge

1:30 Examination of the spectral features of vegetation in 1987 AVIRIS data: Chris Elvidge

2:00 AVIRIS data quality for coniferous canopy chemistry: Nancy Swanberg

2:30 BREAK

3:00 Evaluation of AVIRIS data for stratigraphic analysis of the Wind River/Bighorn Basin area, Wyoming: Harold Lang, Veronique Carerre and Earnest Paylor

3:30 AVIRIS data characteristics and their effects on spectral discrimination of rocks exposed in the Drum Mountains, Utah: Results of a preliminary study: Brian Bailey, John Dwyer, and Dave Meyer

4:00 King/Kaweah ophiolite melange: A first look: John F. Mustard and Carle M. Pieters

4:30 DISCUSSION

5:00 ADJOURN

5:15 Shuttle Bus Leaves JPL for Pasadena Holiday Inn

WEDNESDAY, JUNE 8, 1988

8:00 Shuttle Bus Leaves Pasadena Holiday Inn for JPL

8:30 Characterization of rice field habitat quality using AVIRIS data: Byron W. Wood, Kenneth J. Weinstock, Robert K. Washino and Paul D. Sebesta

9:00 Analysis of AVIRIS spectra of California wetlands: M. F. Gross, V. Klemas and S. Ustin

9:30 An assessment of AVIRIS spectra acquired over the Goldfield Mining District, Nevada: Michael Abrams and Veronique Carerre

10:00 BREAK

10:30 Assessment of AVIRIS inflight performance over the Mtn. Pass Carbonatite, California: Larry Rowan, Jim Crowley and Dave Meyer

11:00 Assessment of AVIRIS inflight performance over the Mtn. Pass Carbonatite, California: Gregg Vane and Robert Green

11:30 LUNCH

1:00 Workshop Summary, Recommendations from the Performance Evaluation Investigators to NASA Headquarters and the AVIRIS Project at JPL

2:30 BREAK

3:00 SPAM Demonstration, Laboratory Tours (to be arranged)

5:00 Shuttle Bus Leaves JPL for Pasadena Holiday Inn (earlier departure to be arranged if requested by workshop attendees)

# Appendix C

## Workshop Attendees

# AVIRIS WORKSHOP ATTENDEE LIST

JOHN ADAMS
DEPT. GEOLOGICAL SCI. AJ-20
UNIVERSITY OF WASHINGTON
SEATTLE, WA 98195

STEVEN ADAMS
JPL
M/S 168-552

PAUL ANUTA
HUGHES AIRCRAFT COMPANY
P.O. BOX 902 MSE52/D220
EL SEGUNDO, CA 90245

GHASSEM ASRAR
NASA HEADQUARTERS
CODE EEL
WASHINGTON, D.C. 20546

G. BRYAN BAILEY
U.S. GEOLOGICAL SURVEY
EROS DATA CENTER
SIOUX FALLS, SD 57198

LEE BALICK
EG & G ENERGY MEASUREMENTS
MS H-02
P.O. BOX 1912
LAS VEGAS, NV 89125

C. BANNINGER
INST. FOR IMAGE PROCESSING
AND COMPUTER GRAPHICS
WASTIANGASSE 6
GRAZ, AUTRIA A-8010

LISA BARGE
JPL
M/S 168-522

SAMUEL BARR
U.S. ARMY ENG. TOPO. LABS
ATTN: SL-TE
FORT BELVOIR, VA 22060-5546

M.J. BARTHOLOMEW
JPL
M/S 183-501

DENNIS BEAVER
BATTELLE PACIFIC NW LABS
P.O. BOX 999
RICHLAND, WA 99352

JOHN L. BERRY
SHELL DEVELOPMENT CO
BRC-GEOPHYSICIST
P.O. BOX 481
HOUSTON, TX 77001

PAMELA BLAKE
SETS, INC.
1110 UNIVERSITY AVENUE #506
HONOLULU, HI 96822

JOE BOARDMAN
CIRES/CSES
CAMPUS BOX 449
BOULDER, CO 80309

J. BODECHTEL
JRC - EUROPEAN COMMUNITIES
ISPRA (VA) ITALY
ISPRA ESTABLISHMENT
ISPRA (VA) ITALY J21020

STEPHEN BRIGGS
BRITISH NATIONAL SPACE CENTER
R16 BUILDING
RAE
FARNBOROUGH, HANTS, UK
GU14 6TD

GEORGE CAMPBELL
BOEING AEROSPACE
P.O. BOX 3999 M/S 84-19
SEATTLE, WA 98124-2499

STEVE CARPENTER
JPL
M/S 168-427

VERONIQUE CARRERE
JPL
M/S 183-501

ROGER N. CLARK
U.S. GEOLOGICAL SURVEY
M/S 964, BOX 25046
FEDERAL CENTER
DENVER, CO 80225

JOE CONLEY
JET PROPULSION LABORATORY
M/S 264-654
PASADENA, CA 91109

MIKE CRAWFORD
ARCO OIL & GAS COMPANY
2300 W. PLANO PKWY
PLANO, TX 75075

ROBERT CRIPPEN
JPL
M/S 300-233

JIM CROWLEY
U.S. GEOLOGICAL SURVEY
NATIONAL CENTER MS 927
RESTON, VA 22092

PAUL CURRAN
NASA, AMES RESEARCH CENTER
M/S 242-4
MOFFETT FIELD, CA 94035

BRIAN CURTISS
CSCS/CIROS
UNIVERSITY OF CO
CAMPUS BOX 449
BOULDER, CO 80303

JEFF DOZIER
JPL
M/S 264-654

NICK DRAKE
DEPT. GEOGRAPHY
UNIVERSITY OF READING
WHITERNIGHTS
READING, ENGLAND

JENNIFER DUNGAN
NASA AMES RESEARCH CENTER
M/S 242-4
MOFFETT FIELD, CA 94035

JOHN DWYER
EROS DATA CENTER
SIOUX FALLS, SD 57198

CHRIS ELVIDGE
DESERT RESEARCH INSTITUTE
P.O. BOX 60220
RENO, NV 89506--0220

WAI-CHI FANG
JPL
M/S 300-329

WILLIAM FARRAND
LUNAR & PLANETARY LAB
UNIVERSITY OF ARIZONA
TUCSON, AZ 85721

SANDRA FELDMAN
MACKAY SCHOOL OF MINES
13820 LEAR BOULEVARD
RENO, NV 89506

HARLON FOOTE
BATTELLE PACIFIC NW LABS
P.O. BOX 999
RICHLAND, WA 99352

JAMES FREW
COMPUTER SYSTEMS LAB
UNIVERSITY OF CALIFORNIA
SANTA BARBARA, CA 93016

ALEXANDER GOETZ
CSES CAMPUS BOX 449
UNIVERSITY OF COLORADO
BOULDER, CO 80309

ROBERT GREEN
JPL
M/S 183-501

MIKE GROSS
MARINE STUDIES
UNIVERSITY OF DELAWARE
NEWARK, DE 19716

FRED B. HENDERSON III
C/O GEOSAT COMMITTEE
601 ELM STREET ROOM 438C
NORMAN, OK 73019

MARK HERRING
JPL
M/S 11-116
PASADENA, CA 91109

JOHN HOM
6330 ALVARADO CT, #208
SAN DIEGO STATE UNIVERSITY
SAN DIEGO, CA 92120-0057

GORDON HOOVER
JPL
M/S 183-501

RAY HUNT
JPL
M/S 183-501

AMY HUTSINPILLER
MACKAY SCHOOL OF MINES
DEPARTMENT OF GEOLOGY
UNIVERSITY OF NEVADA
RENO, NV 89557

JAMIE L. JISA
12152 PENDERVIEW TERRACE#1301
FAIRFAX, VA 22033

G. KAUFMANN
INSTITUTE OF PHOTOGRAMMETRY
AND REMOTE SENSING
7500 KARLSRUHE
ENGLIVITEN, 7
FRG-7500

PETE KEALY
DEPARTMENT GEOLOGICAL SCIENCE
UNIVERSITY OF DURHAM
DURHAM, ENGLAND
UNITED KINGDOM

T.V.V. KING
P.O. BOX 25046-MS964
U.S. GEOLOGICAL SURVEY
DENVER, CO 80225

VIC KLEMAS
MARINE STUDIES
UNIVERSITY OF DELAWARE
NEWARK, DE 19716

BILL KOWALIK
CHEVRON OIL FIELD RSCH CO.
P.O. BOX 446
LA HABRA, CA 90631

B. KOCH
INST. OF LANDSCAPE TECHNICS
UNIVERSITY OF MUNICH
WINZERERSTR. 45
8 MUNCHEN 40
W. GERMANY FRG-8000

GEORG KRITIKOS
DFVLR
INSTITUTE OF OPTOELECTRONICS
WESSLING, W. GERMANY 8031

FRED KRUSE
CIRES/CSES
CAMPUS BOS 449
UNIVERSITY OF COLORADO
BOULDER, CO 80309-0449

HAROLD LANG
JPL
M/S 183-501

FRANK LEHMANN
DFVLR, INSTITUTE FOR
OPTOELECTRONICS
WESSLING, F.R.G. 8031

CRISTINA LINK
JPL
M/S 11-116

KUANG Y. LIU
JPL
M/S 156-246

NADINE LU
JPL
M/S 179-225

BERNARD LUCIANI
CNES DP/OT
2 PLACE M. QUENTIN 75001
PARIS, FRANCE

TOM LUNDEEN
SETS, INC.
1110 UNIVERSITY AVENUE
HONOLULU, HI 96826

JOHN MACDONALD
MACDONALD DETTWILER
3751 SHELL ROAD
RICHMOND, B.C.
CANADA V6X2Z9

A.P. MACHADO
DEPARTMENT OF EARTH SCIENCE
THE OPEN UNIVERSITY
WALTON HALL
MILTON KEYNES
BUCKS, ENGLAND MKF GAA

STEVE MACKIN
DEPARTMENT GEOLOGICAL SCIENCES
UNIVERSITY OF DURHAM
DURHAM, ENGLAND

GIANCARLO MARACCI
JOINT RESEARCH CENTER (J.R.C.)
COMM. OF EUROPEAN COMMUNITY
ISPRA ESTABLISHMENT B127
ISPRA (VA) ITALY 21020

JOHN MELACK
DEPT. OF BIOL. SCI.
UNIVERSITY OF CALIFORNIA
SANTA BARBARA, CA 93106

DAVE MEYER
EROS DATA CENTER
SIOUX FALLS, SD 57105

L.F. MOLINARI
JPL
M/S 264-654
PASADENA, CA 91101

A. GEORGE MOURAD
BATTELLE COLUMBUS DIV.
505 KING AVENUE
COLUMBUS, OH 43201

JAMES L. MUELLER
S10;A-021
UCSD
LA JOLLA, CA 92093

KEVIN MULLINS
U.S.G.S.
2255 N. GEMINI DRIVE
FLAGSTAFF, AZ 86001

JOHN MUSTARD
DEPT. GEOL. SCI.
BOX 1846
BROWN UNIVERSITY
PROVIDENCE, RI 02912

A. OCAMPO
JPL
M/S 183-618

C.E. OLSON, JR.
SCHOOL OF NATURAL RESOURCES
UNIVERSITY OF MICHIGAN
ANN ARBOR, MICHIGAN 48109-1115

BRIAN PACZKOWSKI
JPL
M/S 168-222

HELEN PALEY
JPL
M/S 183/501

IVAN PIPPI
CNR-IROE
VIA PANCIATIEHI, 64
50127 FIRENZE, ITALY

JOHN PENNY
UNOCAL
376 S. VALENCIA AVENUE
BREA, CA 92921

CARLE PETERS
DEPT. GEOLOGICAL SCIENCES
BOX 1846
BROWN UNIVERSITY
PROVIDENCE, RI 02912

MEL PODWYSOCKI
U.S. GEOLOGICAL SURVEY
MAIL STOP 927
RESTON, VA 22092

WALLY PORTER
JPL
M/S 11-116

BILL POWERS
LOS ALAMOS NATIONAL LAB
M/S K723
LOS ALAMOS, NM 87545

BOB RAND
U.S. ARMY ENG. TOPO. LABS
ATTN: CEETL-SL-TE
FORT BELVOIR, VA 22060-5546

JOHN REIMER
JPL
M/S 168/427

MATTHEW REST
100 SOUTH VAN DORN
APT. C309
ALEXANDRIA, VA 22304

GEORGE RIGGS
SCHOOL OF FORESTRY
UNIVERSITY OF MONTANA
MISSOALA, MT 59812

BARRY ROCK
COMPLEX SYSTEMS RESEARCH CNTR.
SCIENCE AND ENGINEERING BLDG.
UNIVERSITY OF NEW HAMPSHIRE
DURHAM, NEW HAMPSHIRE 03824

LARRY ROWAN
US GEOLOGICAL SURVEY
NATIONAL CENTER - 927
RESTON, VA 22092

MARTIN RUZEK
NASA HQ
CODE EEL
WASHINGTON, DC 20546

DON SABOL
17 OAK PARK DR. S.W.
TACOMA, WA 98499

FREDERICK SAFA
9 AV. COLONEL ROCHE
C.E.S.R. 31029
TOULOUSE/FRANCE

P.A. SCHULTEJANN
M/S C-335
LOS ALAMOS NATIONAL LAB
LOS ALAMOS, NM 87545

GARY SHELTON
ARC M/S 240-6
MOFFETT FIELD, CA 94035

MILTON SMITH
DEPARTMENT OF GEOLOGICAL SCI.
UNIVERSITY OF WASHINGTON
SEATTLE, WA 98195

TONY SOELLER
UNOCAL RESEARCH
376 S. VALENCIA AVENUE
BREA, CA 92621

KARL STAENZ
CANADA CENTER FOR REMOTE SENSING
2464 SHEFFIELD ROAD
OTTAWA, ONTARIO
CANADA, K1A OY7

CHARLES STANICH
P.O. BOX 1864
ANN ARBOR, MI 48106

NANCY SWANBERG
NASA AMES RESEARCH CENTER
M/S 242-4
MOFFETT FIELD, CA 94035

ALAN H. STRAHLER
DEPT OF GEOGRAPHY
BOSTON UNIVERSITY
675 COMMONWEALTH AVENUE
BOSTON, MA 02215

GREGG SWAYZE
U.S. GEOLOGICAL SURVEY
MS 964 BOX 25046
DENVER FEDERAL CENTER
DENVER, CO 80225

DAN TARANIK
CAMPUS BOX 449
CIRES/CSES
UNIVERSITY OF COLORADO AT BOULDER
BOULDER, CO 80309

W.J. TODD
O/61-92, B/107
LOCKHEED MISSILES & SPACE CO.
1111 LOCKHEED WAY
SUNNYVALE, CA 94088

ROBERT W. TURNER
BOEING AEROSPACE
P.O. BOX 3999 M/S 84-37
SEATTLE, WA 98124-2499

SUSAN USTIN
DEPT. BOTANY
UNIVERSITY OF CALIFORNIA
DAVIS, CA 95616

JEANNETTE VAN DEN BOSC
STAR RT., BOX 205
SANTA BARBARA, CA 93105

GREGG VANE
JPL M/S 180-703
4800 OAK GROVE DRIVE
PASADENA, CA 91109

RICH WALKER
JPL
M/S 168/522

DIANE E. WICKLAND
NASA CODE EEL
WASHINGTON, DC 2008

T.H. LEE WILLIAMS
CIARS
F-132 ENERGY CENTER
UNIVERSITY OF OKLAHOMA
NORMAN, OK 73019

MARY M. YANG
KAIROS
P.O. BOX 1179
KENDALL SQUARE, MA
CAMBRIDGE, MA 02142

JAN YOSHIMIZU
JPL
168/427

KATHY YOUNG
CIRES/CSES
CAMPUS BOX 449
UNIVERSITY OF COLORADO
BOULDER, CO 80309

DOUG YOUVAN
ROOM 56-213
MIT
77 MASS AVE.
CAMBRIDGE, MA 02139

LINDA ZALL
6812 WILSON LANE
BETHESDA, MD 20817

JOE ZAMUDIO
CIRES/CSES
CAMPUS BOX 449
UNIVERSITY OF COLORADO
BOULDER, CO 80309-0449
**********

# Appendix D

## Slide Captions

| Slide No. | Caption | Senior Author |
|---|---|---|
| 1 | Characteristics of AVIRIS | Vane |
| 2 | (a) Three-color composite image of the Mountain Pass site using 10 nm channels from AVIRIS, 1537 nm (red), 1051 nm (green), 672 nm (blue). The point labeled A locates station where optical depth was determined; point B, a playa target used for inflight calibration of the instrument. (b) generalized topographic map of the site, (c) map of the distribution of precipitable water in cm (color scale at right) determined using the 940 nm atmospheric water band, and the radiance ratio L(940)/ L(870). Stippled region CD marks location of sharp change in mapped water abundance that may represent edge of water vapor boundary layer tapered against the topography. | Conel |
| 3 | A false-color-infrared composite of the Cripple Creek scene. The reflectance at 0.88 m is red, the reflectance at 0.68 m is green, and the reflectance at 0.54 m is blue. | Clark |
| 4 | A Color-Composite-Band-Depth Image (CCBDI): the band depth for the 0.94- m goethite band depth is assigned to red, the 0.68- m lodgepole pine band depth is assigned to green, and the 2.20- m kaolinite band depth is assigned to blue. A band depth of zero is black. The purplish area to the upper left of center is Globe Hill, a region of hydrothermal alteration. | Clark |
| 5 | AVIRIS false-color composite of the test area. Red: b200 (2.21 m); Green: b130 (1.56 m); Blue: b50 (0.8 m). (The bands are only corrected for dark current variations and detector read-out delays.) | Carrere |
| 6 | Example of color composite combining different ratios. Red: Kaolinite (b179/b172); Green: Jarosite (b5/b20); Blue: Alunite (b134/b131). | Carrere |
| 7, 8 | Comparison of AVIRIS spectra and library spectra using SPAM. A: Example of Kaolinite (slide No. 7); B: Example of Alunite (slide No. 8). | Carrere |
| 9 | A: Classified image obtained using the clustering program CLUSAN; B: Examples of classes as determined by CLUSAN. | Carrere |

| Slide No. | Caption | Senior Author |
|---|---|---|
| 10 | Single spectrum residual compared with original atmospheric curve for alluvium calibration target. | Crowley |
| 11 | Comparison between flat field corrected and single spectrum corrected data. | Crowley |
| 12 | Comparison of AVIRIS and Thematic Mapper images of Mountain Pass, CA, at equivalent spectral wavelengths and bandwidths. AVIRIS more completely resolves the two strands of Interstate 15 as well as the fine stratigraphic units and drainage patterns found at the test site. | Green |